2014-04-17

Understanding and Preventing Ni Oxidation in Ni-YSZ Anode-Supported SOFCs

Young, Jason Lee

UNIVERSITY OF CALGARY

Understanding and Preventing Ni Oxidation in Ni-YSZ Anode-Supported SOFCs

by

Jason Lee Young

A THESIS

SUBMITTED TO THE FACULTY OF GRADUATE STUDIES

IN PARTIAL FULFILMENT OF THE REQUIREMENTS FOR THE

DEGREE OF DOCTOR OF PHILOSOPHY

DEPARTMENT OF CHEMISTRY

CALGARY, ALBERTA

APRIL, 2014

Abstract

Ni-yttria-stabilized zirconia (YSZ) anode-supported cell architectures are the current state-of-the-art in solid oxide fuel cells (SOFCs), but their lifetime is too short due to sulphur (S) poisoning, coking and deleterious Ni oxidation. The aim of this work was to understand the mechanisms by which Ni oxidation ('redox cycling') damages the cell and develop solutions to this problem. It was shown that degradation due to air exposure increases as the temperature was increased from 600 to 900˚C and as pO_2 was decreased. The severity of degradation was correlated to the steepness of the NiO gradient in the anode layer. It was also shown that when oxidation is homogeneous in the anode, some NiO particles were pushed out of the air-anode interface. A pre-oxidation cycle, aimed at intentionally forcing NiO out onto the surface, increased the oxidation tolerance at 600˚C from 74% to 80%, but the tolerance at 800˚C was not changed by the process, although the severity of the electrolyte degradation was lowered. Raman spectroscopy was used to quantitatively map the NiO gradient across partially oxidized anodes. It is shown that this technique can quickly and accurately map the NiO distribution through the thickness of a Ni-YSZ anode layer and even showed 20% NiO content in regions of the anode that were not expected to contain any NiO. A reverse bias (a negative bias applied to the Ni-YSZ anode) technique was also used during air exposure to attempt to prevent Ni oxidation. *Ex situ* microscopy showed that Ni adjacent to the electrolyte is protected preferentially. A new technique, *in operando* TGA, that allows electrochemical evaluation while concurrently monitoring cell mass was developed. It was shown that the application of > -1.5 V or > -13 $mA \cdot cm^{-2}$ to a Ni-YSZ electrode during air exposure (800˚C) can prevent a large fraction of Ni oxidation. It was also demonstrated with *in operando* TGA that S-define could be removed by an air exposure with a reverse bias applied, although it may be necessary to oxidize the Ni surface in the region of the electrolyte to fully remove the S.

Acknowledgements

First, I would like to thank my supervisor Dr. Viola Birss, for her guidance and encouragement. I would like to acknowledge my committee members, Dr. Josephine Hill and Dr. Venkataraman Thangadurai, and everyone involved with the SOFC Canada NSERC Strategic Network, especially Sharon Thomas, for many very useful and high level discussions.

The Chemistry Department is also given my appreciation for their contributions to this project, in particular, Mark Toonen, Andy Read, Edward Cairns, Keith Collins, Mike Siewert, Bonnie King and Janice Crawford. I would also like to thank the entire Birss research group, both past and present, for their support. In particular, I am grateful to Dr. Scott Paulson, who is an essential part of a great group (and he knows where everything is hidden), and V. Vedasri.

Special thanks are bestowed to Drs. Offer and Maher at Imperial College London, who hosted me for a three week visit to their lab on two occasions.

I gratefully acknowledge the Natural Sciences and Engineering Research Council of Canada (NSERC) for the support of this work through funding to the NSERC SOFC Canada Strategic Research Network as well as the Strategic Network Enhancement Fund. This work was also supported by an equipment and infrastructure grant from the Canadian Foundation for Innovation (CFI) and the Alberta Science and Research Authority.

I am appreciative of my family, especially my wife Maggie and my children Caalum and Vivian, and my Mom, Audrey, who helped raise our kids while my wife and I both undertook Ph.D. studies.

Table of Contents

List of Figures

List of Tables

List of Symbols

Symbol	Value	Unit	Description
C		F	capacitance
E		V	potential
f		Hz	frequency
F	96485	C/mol	Faraday constant
θ			phase angle (angle between the impedance vectors)
η_{th}		%	efficiency
i	$\sqrt{-1}$		imaginary unit
I		A	current
L		H	inductance
λ		m	wavelength
n			total number of electrons
R	8.31451	J/(K·mol)	gas constant
R		Ω	resistance
R_s		$\Omega \cdot cm^2$	area specific series resistance
R_p		$\Omega \cdot cm^2$	area specific polarization resistance
t		s, min, h	time
T		K, °C	temperature
Z			total impedance

Z’			resistance of the resistor
Z”			resistance due to out-of-phase reactance from the capacitor or inductor
ω	2πf	rad/s	angular frequency

List of Abbreviations

a.c.	alternating current
AFC	alkaline fuel cell
CE	counter electrode
CPE	constant phase element/capacitance
CV	cyclic voltammetry
d.c.	direct current
EDX	energy dispersive X-ray spectroscopy
EIS	electrochemical impedance spectroscopy
LSM	$La_{(1-x)}Sr_xMnO_3$
MCFC	molten carbonate fuel cell
Ni-YSZ	nickel-yttria stabilized zirconia
OCP	open circuit potential
PAFC	phosphoric acid fuel cell
PEMFC	proton exchange membrane fuel cell
RE	reference electrode
SEM	scanning electron microscopy
SOFC	solid oxide fuel cell
TEM	transmission electron microscopy
TPBL	triple phase boundary length

WE	working electrode
XRD	X-ray diffraction
XPS	X-ray photoelectron spectroscopy
YSZ	yttria-stabilized zirconia

Chapter One: **Introduction**

The United Nations Human Development Index shows that almost all measures of quality of life (life expectancy, infant mortality, water availability, years of schooling, gender equality, etc.) are improved when per capita electricity consumption exceeds 2,500 kWh per year. A shortage of water, for example, is not a shortage of water, but a localized shortage of energy. With sufficient energy, water can be pumped from its source to where it is needed, or even better, more freshwater can be produced by the distillation of seawater. Over a billion people still do not have access to adequate electricity.

Locally, some environmental concerns, such as deforestation and pollution, can even be ameliorated. Deforestation, for example, slows as nations become able to provide their citizens with increasing electricity, since the demand for biomass for cooking, heating and even lighting decreases, and reforestation can even begin once local incomes and electricity availability both increase. Pollution is alleviated, since burning biomass for cooking and heating tends to produce a higher yield of pollutants per unit of energy consumed than do modern electrical appliances. Over 2.5 billion people still depend on biomass to fulfill basic needs.

Today, world electricity consumption is over 20,000 TWh per year and this number is expected to double (or even triple) in order to maximize human quality of life. However, there is a justifiable concern that such a large increase in electricity production will dramatically increase pollution and greenhouse gas emissions. The mining, transportation and consumption of coal in a electricity generating plant can increase the release of CO_2, SO_2, NO_x, As, Hg, Cr and Ni compounds into the environment.

However, the pollution from electricity production is inversely proportional to the efficiency of the generator. The present world production of electricity from coal is only ~31% efficient so that most of the energy produced is simply released as heat to the surrounding environment. The production of CO_2 from a coal power plant that is 31% efficient consumes 396 g of pulverized coal and produces 1188 g of CO_2 per kWh of power produced. By doubling the efficiency, the consumption of coal and production of CO_2 would be halved.

Solid oxide fuel cells (SOFCs) (electrochemical devices that can convert hydrocarbon fuels directly to electricity and heat) that run on gasified coal can potentially achieve 67% efficiency during electricity generation because they are not coupled to Carnot efficiency limitations. The waste heat from these devices can be used in cogeneration (to produce more power in a steam turbine, for example) or simply to heat water for domestic use. The use of the waste heat can result in efficiencies of > 95% for some applications.

However, there are many technological limitations that are preventing SOFCs from reaching the marketplace. One challenge relates to the development of materials that can operate at high temperatures (600-1000˚C) without significant performance losses for tens of thousands of hours. At high temperatures, degradation mechanisms can include electrode sintering, interfacial diffusion between fuel cell components, and mechanical stresses due to differing thermal expansion coefficients of adjoined materials.

Lowering the operating temperature of SOFCs has had a significant impact on these degradation rates, allowing the use of less costly materials (stainless steel interconnects, instead of Ni-based alloys or ceramic materials, for example). Anode-supported Ni-yttria-stabilized zirconia SOFC architectures are the current state-of-the-art when it comes to cost and performance. This SOFC design uses the most conductive component of the fuel cell to provide

the mechanical support of the cell and allows the other much less conductive components to be made thin.

However, the lifetime of anode-supported SOFCs is still too short and, while the use of hydrocarbon fuels (CO, CH_4, etc.) is technically feasible, their use can increase the cost of producing a system and shorten the lifetime of the stack. The use of Ni in the anode provides high electrocatalytic activity for the hydrogen oxidation reaction at the anode, but sulphur (S) impurities in the fuel and carbon deposition on the Ni surface due to hydrocarbon cracking can cause significant problems. Further, if there is an emergency fuel shutdown, for example, air can enter the anode chamber through non-hermetic seals or back through the afterburner. Ni oxidation under these conditions is rapid and can cause the electrolyte to fracture due to a large volume expansion (~70%).

In order to extend the lifetime of the cell, S-poisoning, coking and oxidation tolerance of the Ni-based anode must all be improved. Since it is known that S-poisoning and coking can be reversed with exposure to air, then a cell that is oxidation tolerant would be able to remove adsorbed S and deposits of C. Thus, the aim of this study is to attain a better understanding of the degradation mechanisms of Ni-based anode oxidation. This knowledge can then be used to either improve the tolerance of the cell to Ni oxidation or to prevent Ni oxidation altogether. If successful, S-poisoning can then be reversed by exposing a Ni-YSZ anode to air while using these new techniques to protect the cell from the degredation associated with Ni oxidation.

This thesis is divided into 9 chapters. Chapter 2 provides an overview of present SOFC technology and a literature review of Ni oxidation as it relates to the air exposure of Ni-based anodes. In addition, relevant information about the techniques used in this work are reviewed in Chapter 2. Chapter 3 is a summary of the materials and methods used over the course of this

study. In Chapter 4, the mechanism of Ni-based anode-supported SOFC degradation, due to air exposure, is studied. In Chapter 4, it was noted that Ni may be ejected out of the anode-air interface during the anode oxidation, and thus, in Chapter 5, the aim was to prove that NiO ejection out to the anode-air interface is quantifiable and to develop a "pre-oxidation" technique that will improve the tolerance of Ni-based cells to air exposure. In Chapter 6, Raman spectroscopy was used to map the Ni:NiO ratio across an anode layer over the course of Ni oxidation at different temperatures. The goal of this work was to provide a quantitative NiO:Ni ratio through the thickness of an anode, which would provide modellers with the information needed to provide further insight into anode oxidation kinetics.

In Chapters 7 and 8, the application of a reverse bias to the anode, an approach that had shown promise in earlier work in preventing (or slowing) Ni oxidation during air exposure, was examined using a new *in operando* technique. Electrochemical studies carried out using a cell *in operando* in a thermogravimetric analyzer, which enables real-time mass measurements to be carried out, are demonstrated in Chapter 7. The *in operando* technique is then used in Chapter 8 to determine if a reverse bias could be used to slow Ni oxidation while adsorbed S is removed by an air purge. Chapter 9 summarizes the main results of this Ni-based anode oxidation study and suggests some possible future research directions in this area.

Chapter Two: **Background**

Fuel cells are energy conversion devices that convert chemical energy to electricity through electrochemical processes, very similar to batteries. In both cases, an oxidation reaction takes place at the anode, a reduction reaction takes place at the cathode, the electron(s) move through an external circuit from anode to cathode and the electrolyte will transport one of these newly formed ions to the opposite electrode (most commonly from anode to cathode) where it reacts to form a new compound. Finally, individual cells (batteries or fuel cells) can be combined in series to form a "stack" or "pile" to boost the potential.

The primary difference is that, in the case of batteries, once the electrode (which is the reactant) is exhausted in this closed system, the battery is considered "dead" and is either discarded or recharged by reversing the current flow. In a fuel cell, the anode itself is not oxidized (except as a possible intermediate step), but a fuel that is supplied to the anode is oxidized instead. Likewise, the cathode itself is not reduced (beyond any short-lived intermediate phases), but an oxidant that is supplied is reduced instead. Thus, as long as reactants are supplied to the electrodes of the fuel cell, a dc current is generated, and the cell is never "dead" and never needs to be "recharged" (other than "replenishing a fuel cartridge", for example).

2.1 A Brief History of Fuel Cells

The first use of a fuel cell on record was likely by Sir Humphrey Davey in 1802, when he created a simple fuel cell (C | H_2O, HNO_3 | O_2 , C), whereby the carbon was oxidized at the anode and O_2 was reduced at the cathode. As long as the carbon was constantly replenished at

the anode, the cell was never "dead" and it therefore meets the primary definition of a fuel cell. However, it is Sir William Grove who is often referred to as the father of the fuel cell, with his development of a "gas battery" (1). Grove's (2) cell consisted of two platinum strips in an acidic solution, one exposed to H_2 and the other to O_2 and electricity was produced ($Pt, H_2 \mid H_2SO_4 \mid O_2, Pt$). As current flowed, H_2 and O_2 were observed to deplete and it was noted that, with a higher Pt surface area, the gases would deplete faster (3).

It was Friedrich Wilhelm Ostwald in 1894 (4) who first provided much of the theoretical understanding of how fuel cells operate, experimentally determining the interconnected roles of the various components of the fuel cell, including the electrodes, electrolyte, oxidizing and reducing agents, anions, and cations. The thermodynamic advantage of producing electricity from coal directly in a galvanic cell was also demonstrated (as will be discussed further in Section 2.2). While this provided some driving force for further research on fuel cells, research would not escalate significantly until the 1960s. At this time, a reliable and lightweight energy supply, where cost was not a hindrance, was needed for space exploration (5). Batteries had been ruled out due to their size and weight (i.e., their insufficient capacity required larger and, therefore, heavier electrodes, as opposed to the use of compressed gases) and toxicity (the only by-product of fuel cells is potable water when H_2 is used as a fuel) (6).

In the 1990s, energy prices began to rise as cheap and easily accessible conventional supplies began to shrink. In addition, pollution in cities began to increase as the number of cars on the road began to increase and concern regarding CO_2 induced global warming began a push toward a "Hydrogen Economy", whereby H_2 was envisioned as an energy storage medium (i.e., as an alternative to chemical storage batteries). Fuel cells were envisioned as the ideal energy

conversion device to convert the potential energy of stored H_2 back into electricity on demand (7).

Today, while the difficulty of storing H_2 has not been overcome, fuel cells are still recognized by industry and government as a clean energy conversion device for the future and billions of dollars have been spent on research and the commercialization of fuel cell products (8). While fuel cells have been incorporated into a diverse range of applications beyond the space program, including submarines, stationary power, transportation, remote and/or back-up power, and portable power, these devices are still largely utilized where the advantages of fuel cells significantly outweigh the current cost and lifetime issues. For fuel cells to have a positive impact environmentally, they must penetrate more markets and compete directly with other energy conversion devices, especially coal and gas turbines. To achieve this, system costs must be lowered by at least a factor of 5 and lifetime increased by a factor of at least 2 over current designs (8).

2.2 Advantages of Fuel Cells

In Section 2.1, it was revealed that fuel cell research really began when the Apollo program was started because fuel cells have advantages over batteries in their size, weight and toxicity, in addition to providing continuous power without recharging (6). Fuel cells also have advantages over conventional energy conversion devices, which rely on flame combustion to heat a reservoir (Rankine Cycle in a steam power plant) or to directly expand a gas (Brayton cycle in a gas turbine or Otto cycle in a spark ignition engine) to do mechanical work. These advantages arise largely because the fuel and air are separated by an ion conducting barrier layer and the reaction is driven by the chemical potential difference across this electrochemical barrier.

Another advantage, as was stated in Section 2.1, is that the emissions of pollutants to the atmosphere is zero when H_2 is utilized as the fuel (6). When gaseous hydrocarbons (CH_4, CO, H_2, etc.) are used in high temperature fuel cells (fuel limitations for different fuel cell types will be described further in Section 2.3), the emissions of pollutants are still very low, since the operating temperature is too low to produce significant NO_x or O_3 (9). Further, S-containing compounds are typically scrubbed from the fuel before they reach the fuel cell, since, for most fuel cell catalysts, S is a poison (10).

The primary advantage of fuel cells over conventional energy conversion devices, however, is that they are very efficient, thus lowering the overall impact related to electricity production (resource depletion, emissions, etc.). A fuel cell converts the Gibb's free energy change (ΔG) of a chemical reaction into electrical energy according to Equation 2.1, as follows:

$$\boldsymbol{\Delta G = -nFE_r} \qquad \textbf{2.1}$$

where n is the number of electrons, F is Faraday's constant and E_r is the reversible potential of the cell. Under standard conditions (T = 25°C, $pH_2 = pO_2 = 1$ atm, liquid water), E_r is 1.23 V for a fuel cell that reacts H_2 and O_2 ($H_2 + 1/2\ O_2 \rightarrow H_2O$), since ΔG = -237 kJ/mol (11) and n = 2. The theoretical efficiency of the cell is determined by dividing the energy used to produce a potential (ΔG) by the enthalpy (or total heat) of the reaction (ΔH). Since ΔH for the reaction of H_2 and O_2 is -285 kJ/mol (11), the theoretical efficiency, η_{th}, is 83%. For a fuel cell that operates at 1073 K with a gaseous H_2O by-product, as is the case with high temperature fuel cells (described further in Section 2.3), ΔH is -250 kJ/mol, ΔG is -190 kJ/mol (11) and the theoretical efficiency is lowered to 75%.

The most efficient theoretical model for heat engines is the Carnot cycle, so this is the example that is the most commonly used to compare with fuel cells. In the case of the Carnot cycle, the efficiency, η_{th}, is limited by the high, T_H, and low, $T_{L,}$ temperature limits during reversible adiabatic expansion and reversible adiabatic compression, respectively, as shown in Equation 2.2, as follows (12):

$$\boldsymbol{\eta_{th} = 1 - \frac{T_L}{T_H}} \qquad \textbf{2.2}$$

Thus, with a low and high temperature limit of 25 and 800°C, respectively, the maximum theoretical efficiency (η_{th}) that would be possible is 72%.

While it appears that the efficiency of the Carnot cycle is comparable to the efficiency of a fuel cell that operates at 800°C (i.e., 72% versus 75%, respectively), there are three primary factors that give fuel cells a higher theoretical efficiency. First, the Carnot cycle is not practical in a real system (it is the equivalent of a highly efficient car that requires > 100 km to reach a normal cruising speed). Second, a T_H of 1073 K is not possible due to materials constraints and, finally, a fuel cell can utilize the waste heat without suffering a penalty to the overall system efficiency (i.e., T_L increases if the waste heat is used in a Carnot cycle).

In practice, there are many efficiency losses for both systems. In a typical steam power plant, these losses can include the exergy (the energy available for use versus losses due to irreversibility, i.e., increases in entropy) of steam (~94%), the combustion efficiency (~95%), the heat to steam transfer in the boiler (~96%), the friction loss of the turbine (~95%), and more (e.g., power use for coal grinding and pumps, continuous load changes and start-up/shut-down procedures). In practice, the best practical electrical efficiency possible for a sub-critical steam power plant (163 bar, 538°C) that uses the Rankine cycle is ~40% (13). However, the use of a

combined cycle natural gas power plant that combines the Brayton and Rankine cycles (i.e., using the expansion of an expanding gas through a turbine, followed by using the waste heat in a steam turbine) can improve efficiencies to 56% (14). Similarly, by gasifying coal and using the same power plant, the efficiency of a coal combined cycle power plant is lower due to the oxidation of C to CO in the gasification process, but it is still possible to increase the efficiency to 53% (15).

Of course, fuel cells also have losses that lower the efficiency from the theoretical maximum of 75%. In the cell itself, there are activation polarization and resistance losses, and there can also be concentration polarization (poor reactant diffusion) or low fuel utilization losses, and these will be described in more detail in Section 2.7.5. Other losses largely arise from system needs, including air blowers, desulfurizers, fuel pre-reformers/fuel processing, ac/dc inverter losses and more that are dependent on the fuel cell system and type used. Electrical efficiencies as high as 57% have been demonstrated (16), in direct competition with a combined cycle natural gas generating station. When high temperature fuel cells are used in a steam turbine combined cycle, the efficiency increases to 67% and even a small residential unit of only 1-2 kW can achieve up to 83% efficiency when the waste heat of one of these high temperature fuel cells is used for domestic heating (16).

This efficiency of fuel cells is higher than what can be typically attained from conventional power generation, largely owing to the scalability/modularity (size of system) that is possible in fuel cells without affecting their overall efficiency. The problem with conventional power plants is that the power output must be very large, since it takes several gas turbines to provide enough heat for the steam turbine. Fuel cells can be large (MW sized systems) or small (1-2 kW) without suffering a large efficiency penalty (6).

2.3 Types of Fuel Cells

As alluded to in Section 2.2, fuel cells can have many different limitations to the operating temperature, to the diversity of fuel feedstock and to the fuel impurity tolerances. These limitations largely arise from the electrolyte, since the materials that make up this component limits the operating temperature range (for good ion conductivity and stability), the ion that is the mobile charge carrier (for fuel feedstock limitations), and the materials that are compatible with it for the other components (for impurity tolerances). Fuel cells are therefore commonly classified into 5 types that are based on the electrolyte: phosphoric acid fuel cells (PAFCs), alkaline fuel cells (AFCs), polymer electrolyte (sometimes referred to as proton exchange) membrane fuel cells (PEMFCs), molten carbonate fuel cells (MCFCs) and solid oxide fuel cells (SOFCs). The fuel cell type, charge carrier and charge carrier movement direction, reaction and by-product gases, most common electrode materials, and operating temperature are summarized in the schematic presented in Figure 2.1.

It can be seen in Figure 2.1 that AFCs, PEMFCs and PAFCs operate at low temperatures using pure H_2 as the fuel. This low operating temperature has the advantages of faster start-up times and a broader availability of sealing materials, but electrode reaction kinetics are slow. Thus, a precious metal catalyst, usually Pt, must be used in order to achieve acceptable performance (i.e., a high power per unit area, such that a smaller area can be utilized to produce the same amount of power). While the costs of Pt are known to be high, the current costs per kW installed for PEMFCs is only $8 due to minimized Pt loading (17). While the Pt cost is no longer a barrier to commercialization, it is still ~ 37% of the cost of an 80 kW stack (based on

projections that assume 500,000 units per year are installed) (17) and some promising alternatives to precious metals are being studied (18).

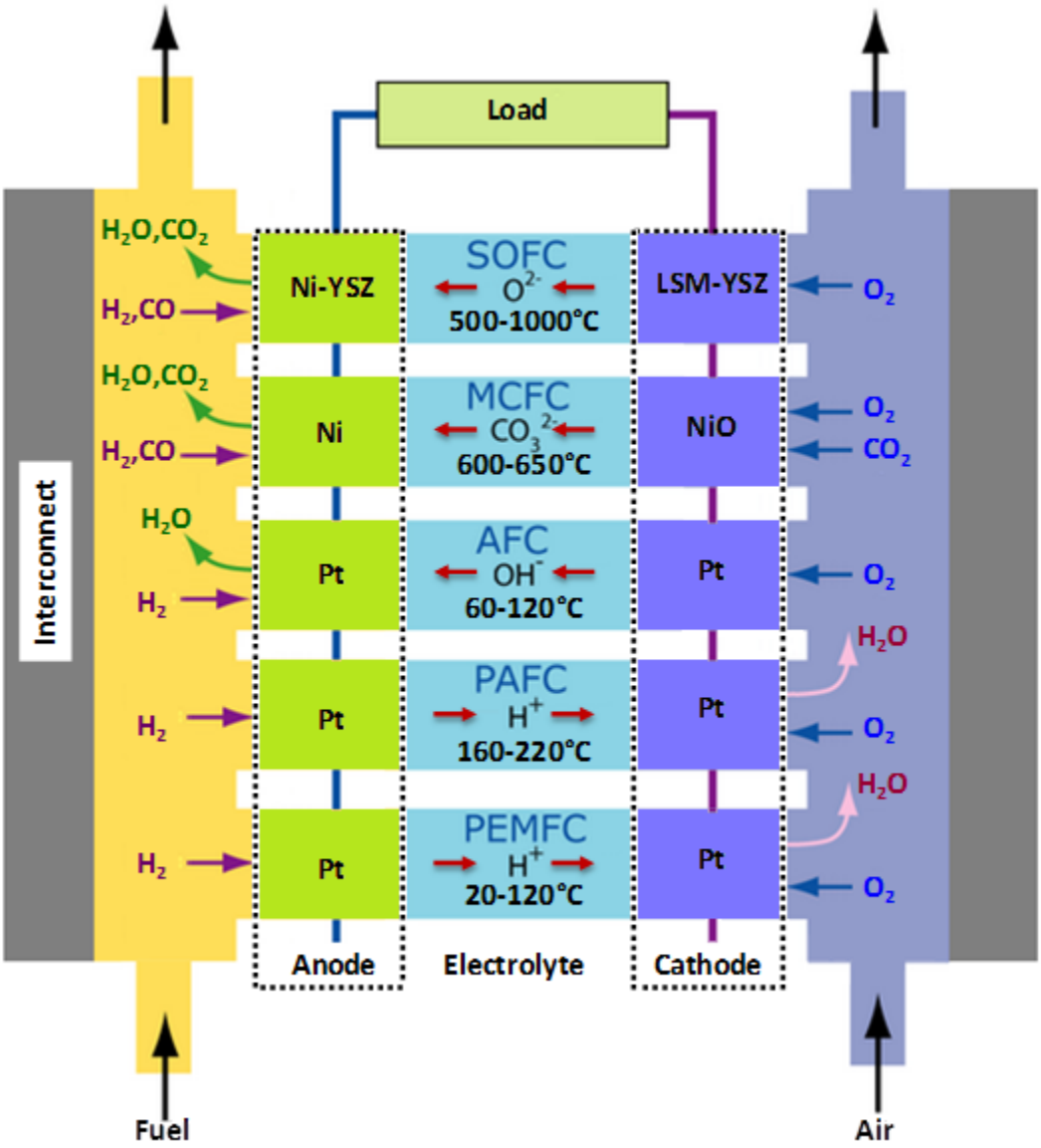

Figure 2.1. Schematic diagram showing the materials, charge carriers, reaction gases and operating temperatures of the 5 most common fuel cell types (19).

PEMFCs have become the most promising and most researched type of low temperature fuel cell, since there are no liquid electrolyte management issues, but alternatives to the current electrolyte material (a polymer material named Nafion^{tm}, which is a sulfonated tetrafluoroethylene based fluoropolymer-copolymer) are desired due to cost and hydration issues (water must be added to the anode to prevent it from drying out and removed from the cathode side to prevent pore flooding). Ideally, an electrolyte with an operating temperature in the range of 150-400°C is desired, since it is thought that this would significantly lower these problems (kinetics, water management, CO catalyst poisoning, carbon current collector corrosion, etc.) (20).

High temperature fuel cells, which include MCFCs and SOFCs, have the disadvantage that a much longer start-up time, due to the need to heat them to > 600˚C slowly to prevent damaging them. However, the high temperature of operation has the advantage that precious metal electrodes are not needed, since the reaction kinetics are fast, the waste heat of these fuel cells can be utilized in a number of applications (as discussed in Section 2.2), and the fuel feedstock can be more diverse, since CO does not poison the catalyst as it does in low temperature fuel cells (21). As will be discussed in Section 2.4.3, there are technological issues associated with the use of hydrocarbon feedstocks, but these hydrocarbons are generally reformed to CO and H_2, shown for methane as follows:

$$CH_4 + H_2O \rightarrow CO + 3\ H_2 \qquad \textbf{(2.1)}$$

In fact, gaseous hydrocarbon fuels can be internally reformed, meaning that methane reacts with steam directly on the surface of the anode, although not without technical difficulties caused by the rapid kinetics of this endothermic reaction on Ni (22).

SOFCs are often considered to be the least mature fuel cell technology (23), but they have some advantages over MCFCs. First, since the electrolyte is a solid, there are fewer issues related to ensuring that there are no discontinuities where air and fuel can intermix, in addition to the fact that the electrolyte of a MCFC must be replaced as quickly as it vaporizes. The molten carbonate electrolyte is also very corrosive to the metals that are typically present in the stack (electrodes and interconnects), thus resulting in dissolution of the components (22).

2.4 Solid Oxide Fuel Cells (SOFCs)

SOFCs have the advantages of a solid electrolyte (no corrosive liquid electrolyte or liquid electrolyte management issues) and high temperature operation (no precious metal catalyst, diversity of fuel feedstock and high quality waste heat), as discussed in Section 2.3, and should have the greatest positive impact on the environment if successfully developed. However, the operating temperature of an SOFC still creates many problems. The need to match thermal expansion coefficients and to minimize chemical interactions of stack materials with the electrolyte prevents the use of materials that would be ideally suited as components (24). Thus, due to cost and reliability issues, SOFCs have not yet successfully penetrated the electricity generation market (except as demonstration projects).

Figure 2.2 is a schematic representation of SOFC operation with H_2 used as the fuel for simplicity. However, in an SOFC, CO will also react with O^{2-} at the anode-electrolyte-fuel interface and the electrons are released to the external circuit, as follows:

$$H_2 + O^{2-} \rightarrow H_2O + 2\ e^- \qquad \textbf{(2.2)}$$

$$CO + O^{2-} \rightarrow CO_2 + 2\ e^- \qquad \textbf{(2.3)}$$

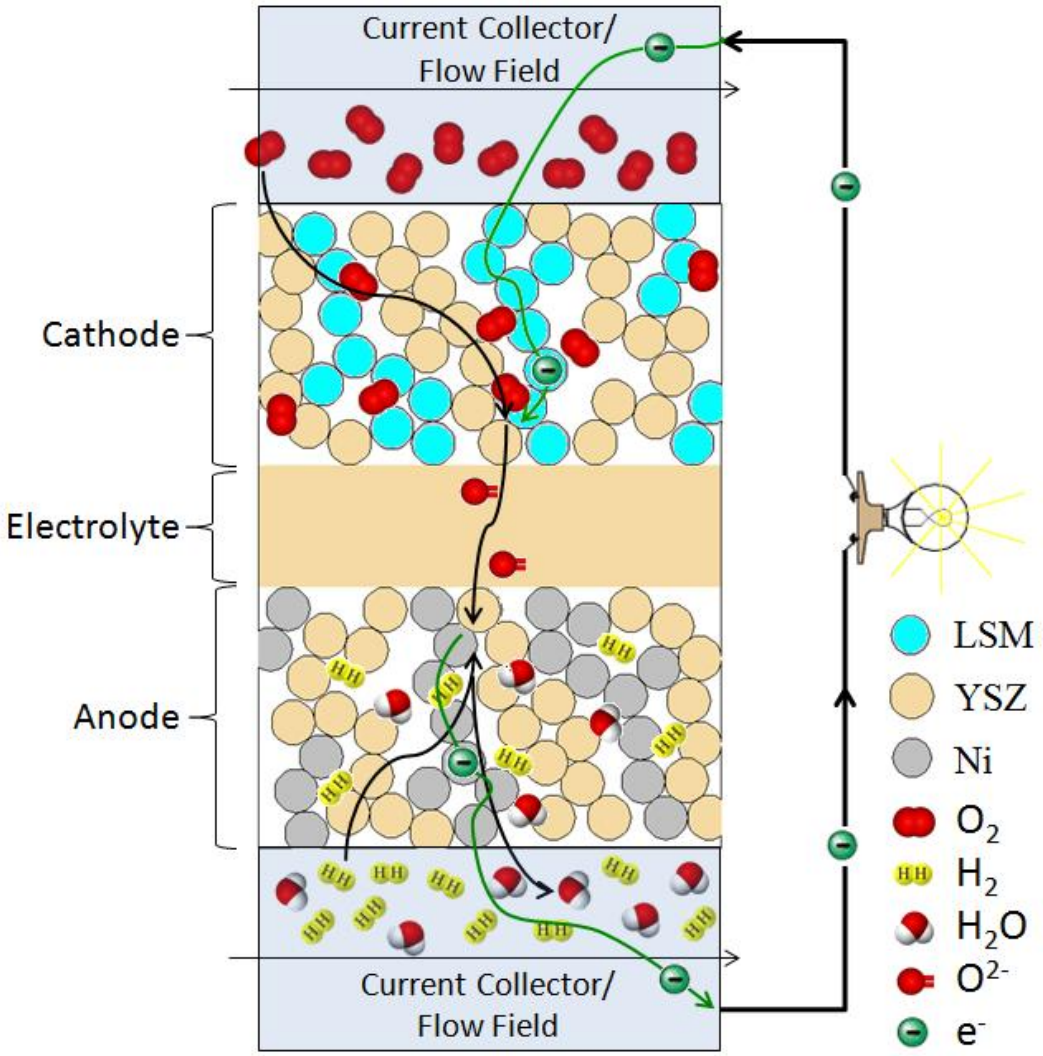

Figure 2.2. Schematic representation of an operating SOFC with H_2 as the fuel.

As illustrated schematically in Figure 2.2, O_2 is first adsorbed and then dissociated on the surface of the cathode. At the cathode-electrolyte-air interface, O_{ads} reacts with electrons to form O^{2-}, as follows:

$$O_{ads} + 2\ e^- \rightarrow O^{2-} \qquad \textbf{(2.4)}$$

which then migrates through the electrolyte by a vacancy defect transport mechanism (25). The materials and function of the SOFC components, which were briefly described in Section 2.3, are described in more detail in Sections 2.4.1 to 2.4.3 for the electrolyte, cathode and anode, respectively.

2.4.1 The Electrolyte

The electrolyte is the key component of a fuel cell, since without a material with a high and selective ionic conductivity (i.e., preferentially conducting one ion) and negligible electronic conductivity, fuel would be consumed without contributing electrons to the external circuit. To ensure that the cell life is long, the material must be stable in both gas environments (pO_2 as high as 5-10 atm at the cathode and as low as ~10^{-22} atm at the anode) and it must be physically and chemically stable with respect to the electrode materials at the operating temperatures. Ideally, the electrolyte material should also have a low sintering temperature, so that interactions with the other components are minimized during fabrication. Otherwise, the fabrication process will become unnecessarily complicated in order to minimize these interactions (i.e., requiring many heating cycles to sinter each component individually, which is costly) (26).

The modern electrolyte material of choice for SOFCs is 8 mol% yttria-stabilized zirconia (YSZ). This material was originally referred to as the “Nernst mass” and was first used in a fuel cell by Baur and Preis (27) in 1937. It was referred to as the "Nernst mass" because, in 1899, it was Nernst who demonstrated that the conductivity of doped zirconia resulted from the mobility of oxygen ions. In the 1920s, Frenkel first described the ion hopping mechanism from filled to defect (or vacancy) sites, which is the mechanism of O^{2-} mobility that makes YSZ ionically conducting (28).

Yttria was initially added to zirconia in order to 'stabilize' the cubic phase of the material (zirconia is only cubic at > 2370°C), in order to avoid the large volume changes that occur during the monoclinic to tetragonal phase change at 1170°C. This structure, seen in Figure 2.3 (25), is commonly referred to as a cubic fluorite-type structure and, while tetragonal zirconia also has good ionic conductivity, materials with the cubic crystal structure tend to have low O^{2-} hopping activation energies (29). In addition, yttria acts as a dopant, increasing the O^{2-} vacancy concentration of the material, represented in Kröger-Vink notation as follows:

$$Y_2O_3 \xrightarrow{ZrO_2} 2\,Y'_{Zr} + 3\,O_O^x + V_O^{\bullet\bullet} \qquad \textbf{(2.5)}$$

Thus, it is shown that, when 2 Y(III) replace 2 Zr(IV) ions, a vacancy in the O^{2-} lattice ($V_O^{\bullet\bullet}$) is created that further enhances O^{2-} conductivity.

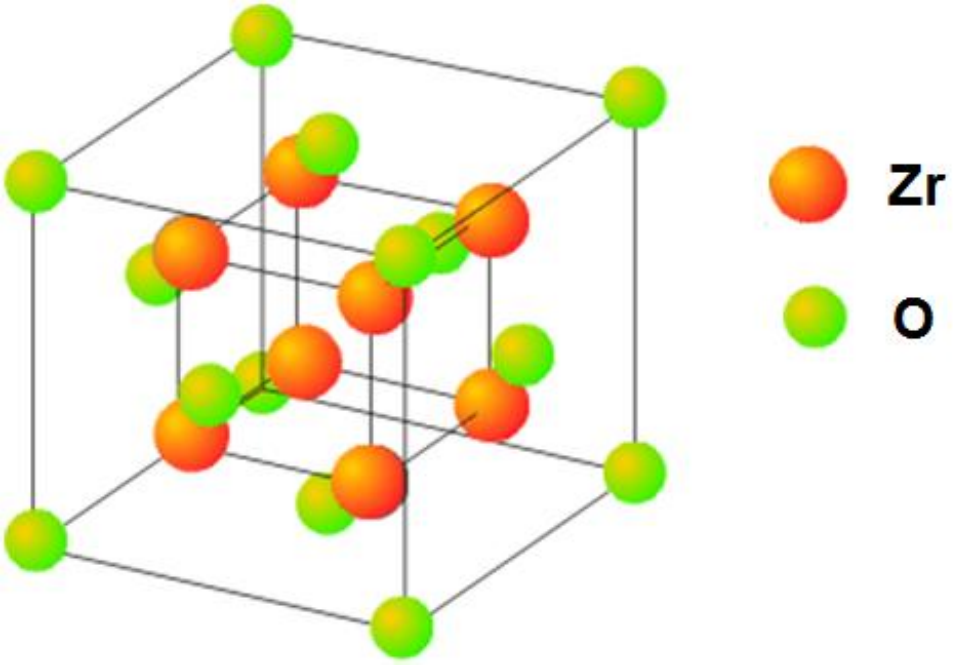

Figure 2.3. Cubic fluorite-structure of stabilized zirconia (30).

The cubic structure can also be stabilized (and vacancy concentration improved) by the addition of CaO, MgO, Sc_2O_3 and certain rare earth oxides(29). YSZ is still the most favoured electrolyte material because it has the best combination of properties (stability, conductivity, cost, manufacturability, etc.). However, there has also been significant interest in calcia-doped zirconia (29), due its low cost and, more recently, in scandia-doped zirconia (31), due to its higher ionic conductivity.

Other materials with the cubic fluorite-type structure, including CeO_2, Bi_2O_3, ThO_2 and HfO_2, can also be doped to enhance their oxygen anion conductivity (29). Of these, doped ceria and bismuth oxide have received the most significant interest due to their high conductivity at lower temperatures (500-600°C), but they have been largely limited by their poor stability in a reducing environment. Ceria, for example, experiences a 3% volume change when reduced from Ce(IV) to Ce(III) (32) in a H_2 environment, and becomes an n-type semiconductor (33).

2.4.2 Cathodes

A suitable cathode material has been difficult to develop due to the oxidizing environment at this electrode (noble metals are too expensive and non-noble metals will oxidize) and the sluggish oxygen reduction kinetics at most ceramic materials. Ceramic semiconductor materials from the perovskite oxide class of ionic solids, which have a general ABO_3 structure, as seen in Figure 2.4, became the favored material class for cathode materials research because of the high conductivity that they can have at high temperatures. The A-site is occupied by a lanthanide or alkaline earth atom with a +2 or +3 charge that is 12-fold coordinated with O. The B-site is occupied by a transition metal with +3 or +4 charge that is 6-fold coordinated with O. The advantage of this class of material is that both the A-site and B-site can be doped (A_xA_{1-}

$_xB_yB_{1-y}O_{3\pm\delta}$) to tailor the properties of the oxide (i.e., to improve conductivity, stability, thermal expansion coefficient, etc.) (34).

LSM ($La_{0.7}Sr_{0.3}MnO_{3-\delta}$) was first studied as a cathode material by Rohr et al. (5) in 1973 and this materials system was preferred for more than 20 years (between 1973 and the late 1990s), despite the fact that it was known that there were reactions with YSZ that form resistive interlayers (35). Significant research during this time period on alternative cathode materials with better performance and lower reactivity with YSZ at both the high operating (1000°C) and sintering (>1200°C) temperatures was largely unsuccessful. Many perovskite materials were found to have either stability or performance, but not both (25).

An improved understanding of how the triple-phase boundary length (TPBL), i.e., the length of all junctions where the electrolyte, the electrode and the gas phase all meet, affects the performance of the electrode led to improvements in cell performance by mixing YSZ and perovskite material in the active area of the cathode (34). However, advances in cell fabrication and architecture (described in Section 2.4.4), which lowered the operating temperature to < 800°C and removed the need to sinter the cathode at high temperatures, was the driving factor that led to an improved cathode performance. This was primarily due to the fact that perovskite-phase materials that had previously been rejected due to their reactivity with YSZ, such as $(La,Sr)(Co,Fe)O_3$ (LSCF), could now be considered (34).

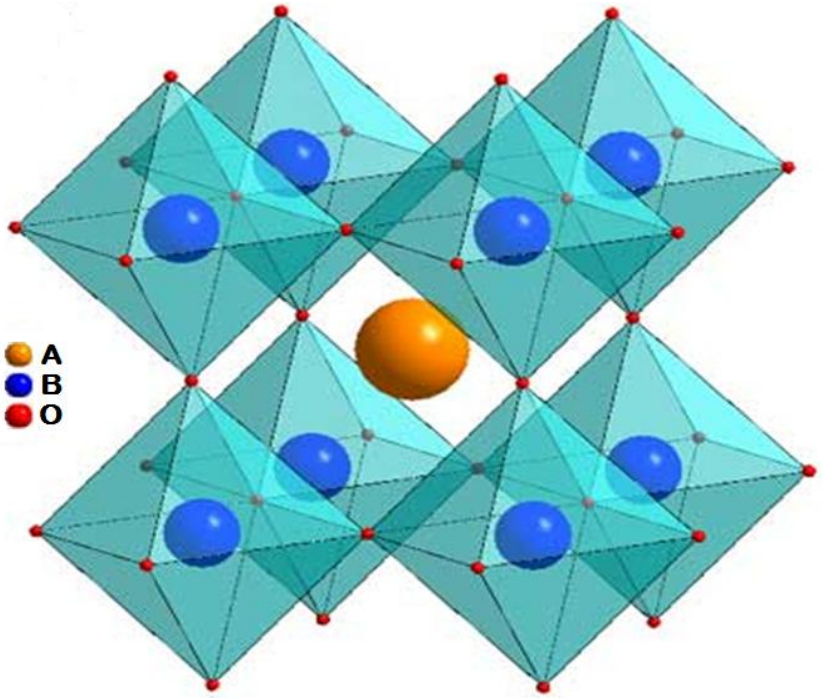

Figure 2.4. Crystal structure of a perovskite (ABO_3) type semiconductor (36).

2.4.3 Anodes

The Ni-YSZ ceramic-metal composite (or cermet) was established as an anode material very early in SOFC development (1964) by Spacil (37). Ni was identified as having good performance, but due to its rapid sintering rate at high operating temperatures (~1000°C) and its high thermal expansion coefficient, it was not considered to be ideal. By mixing NiO and YSZ particles together, these two limitations could be eliminated, and, further, the TPBL was improved by mixing the two phases. This cermet is still in widespread use as an SOFC anode material due to its many advantages, including ease of fabrication, the *in situ* development of high porosity after reducing the NiO (which is present because the SOFC is sintered in air), good

chemical and physical stability in reducing environments, and excellent electrocatalytic activity for hydrogen oxidation (26).

There are, however, two key problems associated with the use of Ni in SOFC anodes: coking and S-poisoning. Coking is the deposition of carbon on the anode surface by methane cracking reaction or by the Boudouard reaction, as follows:

$$CH_4 \rightarrow C + 2\ H_2 \qquad \textbf{(2.6)}$$

$$2\ CO \rightarrow CO_2 + C \qquad \textbf{(2.7)}$$

While C deposition has no immediate deleterious effects on cell performance, it can slowly block pores with time, which slowly decreases gas transport through the anode layer. To prevent coking, it is simply a matter of using a fuel humidifier to maintain a high steam to carbon ratio (up to 2:1) in the presence of Ni, but this high steam to carbon ratio can significantly impact system efficiencies (38).

S-poisoning involves the adsorption of S on Ni, with S serving to block Ni surface sites for H_2 adsorption and oxidation (39). This is a much more instantaneous problem than coking, as a sharp decline in cell performance is observed within minutes of exposure to H_2S concentrations as low as 1 ppm (at $\geq$ 700°C) (40), followed by a more gradual deterioration with time. Tolerance to S in the fuel decreases as the temperature is lowered (to 700°C) (41) and as the cell voltage is increased (i.e., the power output of the cell is lower) (39). Most of the performance loss is slowly recovered after S has been removed from the fuel, but there is a permanent loss to the performance that is speculated to be the result of strongly adsorbed S (S_{ads}) (10), Ni morphology changes due to sintering (42), and/or to the migration/depletion of Ni in the anode due to volatilization (43).

With respect to the use of the existing fuel infrastructure (from natural gas to diesel), a desulphurizer must be used to remove S-species prior to the SOFC stack. The use of a desulphurizer in a SOFC system is not complicated but it adds to the cost and complexity of the system design. Further, the occasional "slip" of S-impurities, resulting from desulphurizer failure/saturation, should be anticipated.

In the case of both coking and S-poisoning, the problems can both be ameliorated with an additional system component. However, this increases the cost of the system and decreases its efficiency and, despite the overall good performance of Ni-YSZ, the coking and S-poisoning problems have driven research into alternative anode materials and materials additions to Ni-YSZ. Cu, Co and some perovskites (44; 38), for example, have been investigated to replace Ni completely. To date, the combination of performance, cost and manufacturability of these new materials cannot match that of Ni-YSZ and, further, developers are hesitant to replace Ni-YSZ with a new materials system that would require years of trials and validation, since this would be a costly delay to market penetration.

Alternatively, improving the coking and S-tolerance of Ni-YSZ anodes with materials additions, such as doped ceria (38; 45), BaO (46) and some perovskites (44; 38), should lessen the validation and development time. For example, using infiltration techniques to add materials is a much less radical change to the materials system (e.g., in comparison with the use of all ceramic anodes), allowing existing manufacturing processes to be used (i.e., infiltration is carried out after co-sintering the cell) and nano-structured materials can be added to further enhance anode performance (47). However, additional development and validation time would still be required to establish if these modified anodes are stable within the existing materials system and if they retain their coking and S-tolerance during long term operation.

2.4.4 Recent Progress in SOFCs: Manufacture and Architecture

Solid oxide fuel cells are very difficult to fabricate, since ceramic materials typically have very high melting points. The sintering temperatures of most materials is approximately $T > 0.5T_m$ K, so those materials with high melting points (T_m) require high sintering temperatures to densify (48). A high sintering temperature can result in the formation of a resistive interlayer (e.g., $La_2Zr_2O_7$ when LSM and YSZ are sintered together), or if the high sintering temperature of one component (YSZ electrolyte) exceeds the decomposition temperature of another component (LSM cathode), the finished product will not contain the desired crystalline phase (49). This difference in sintering temperatures can also have a negative impact on the final density that results. The electrolyte, for example, must ideally be completely crack and pore free, whereas the electrodes require ~30% porosity in order for the reaction gases to penetrate to the reactive sites and for the products to leave the pore structure.

It is recognized that thin electrolytes (< 50 μm) are advantageous because they lower the ohmic resistance of the cell. However, if the electrolyte is not pore- or crack-free, anode and cathode gases can intermix, not only making the fuel cell less efficient, but causing local heating, which can severely damage the cells. Many of the techniques capable of producing thin membranes are slow and expensive (electrochemical vapor deposition, electrophoretic deposition and sputtering), and those that are rapid and inexpensive are not capable of producing adequately thin and dense membranes (CVD, plasma spray) (50). Plasma spray techniques have advanced the most, recently, especially with modern supersonic spray techniques and improvements in powder feedstocks. However, more work is still necessary to improve yields (i.e., fewer flawed

components and consistent performance over MWs of components) and reliability (cracks and > 5% porosity can result) of plasma sprayed thin films (51).

Conventional ceramic processing is an inexpensive method of producing membranes that, after calcining the powder to produce the desired phase, consists of mechanical methods of refining the powder size, including stirring in water, ultrasonic agitation, ultrasonic probe disruption or ball milling. However, a powder with a wide particle size distribution or that contains large agglomerates, which is often the result of these techniques, is inadequate for producing thin (~10 μm), dense membranes. The presence of large particles or agglomerates necessitates higher firing temperatures and much thicker layers to make pore-free components (52). However, the computer age has resulted in a substantial development of a number of inexpensive deposition techniques. Improvements in colloidal suspensions (53) and sol-gel techniques (54) have dramatically improved particle size distributions, which minimizes agglomeration dramatically, such that lower sintering temperatures can now be used and thin electrolytes (< 15 μm) can now be formed using conventional techniques.

Many different cell architectures have been studied (25; 55) to take advantage of the new fabrication techniques as they developed. In general, there are two main architectures: planar and tubular. The planar design has the advantages of low cost manufacturing, since conventional or 'line of sight' ceramic processing techniques can be used, and a lower overall stack resistance, since electron pathways are shorter. In addition, the interconnect, which is an electrically conductive stack component that conducts electrons from the anode of one cell to the cathode of the next cell, and separates the fuel and air compartments in the stack, can be composed of lower cost materials, such as stainless steel.

The disadvantage of planar cells is a short lifetime due to high oxidation rates of the stainless steel interconnect (38). The lifetime of the stack can be extended through the use of coatings, although this also adds to the cost of the stack(56). Another disadvantage of planar cells is that the material used to seal between the manifolds, the interconnects, and the cells must be able to withstand high temperatures (600-800˚C). Glass seals are typically hermetic, but they tend to embrittle over time and are reactive with the cell materials. Compressive ceramic seals will not typically react with the cell components, but because they are not hermetic, a lower efficiency and greater safety concerns can result (57). The monolithic stack was considered as a separate architecture by many in the past (58), but these stacks are essentially planar cells co-sintered with ceramic interconnects into a single stack component to overcome the sealing and interconnect issues of planar cells. However, due to thermal shock issues and the formation of reactive interlayers during co-sintering, this planar design is no longer in development.

Tubular SOFC designs have the advantage that the seals can be kept in the cold zone of the stack and that the cell and ceramic interconnect are sealed during the manufacturing process. Due to the stability of the seals and the interconnect, system incorporating the tubular design have a very long lifetime (> 50,000 h) (59). However, the disadvantage of these cells is that inexpensive line of site conventional ceramic techniques are difficult to implement in a tubular component and, thus, the cost of manufacturing is high. Plasma spraying, as discussed above, could potentially lower these costs substantially, although improvements in the process are still needed (60).

Another disadvantage of tubular cells is that the conductive pathway is much longer than in a planar cell and, even with thick (> 50 μm) electrodes (59), the power output is limited to ~250 $mW \cdot cm^{-2}$ (60). The segmented-in-series design, whereby each tube is a stack of cells (i.e.,

many small tubular cells are connected in series along the length of a tube), overcomes the high resistive losses of the standard tubular cells, although as with monolithic stacks, manufacturing can be complicated (61).

Along with cell architectures (tubular and planar), there has also been an evolution in cell design, specifically relating to which component provides the mechanical support of the fuel cell. YSZ has very good strength and it is therefore still used by many developers as the support layer (25; 55). However, thin (< 10 μm) YSZ electrolyte layers are desired, so another component must be used to provide strength to the cell. For example, Westinghouse (60) originally used a porous alumina tube to support a 50 μm thick cathode and a thin (10 μm) electrolyte (and a 50 μm thick Ni-YSZ anode). This tubular cell had long life, but the cost was high, not only due to the expensive electrolyte deposition technique used (electrochemical vapor deposition), but primarily due to the low performance (which requires many more cells to produce an equivalent amount of power). Utilizing the cathode as a supporting layer is difficult due to the interactions between YSZ and the ceramic cathode and due to the typically low decomposition temperatures of many perovskite ceramics, as discussed in Section 2.4.2.

In 1993, Cassidy et al. (62) and Minh and Gibson (63) first presented the concept of anode-supported cells, as seen in Figure 2.5B (as compared with an electrolyte-supported cells, as seen in Figure 2.5A). These were produced by tape casting and then screen printing (62) or tape calendaring the electrolyte onto the anode (63) and then co-firing the anode and electrolyte at 1350°C in one firing step. In addition to the ease of manufacture (the anode and electrolyte could be fired in a single step), this design architecture also exhibits excellent performance at ≤ 800°C due to the thin electrolyte (10 μm versus > 200 μm for electrolyte-supported cells) and excellent anode support layer (ASL) conductivity.

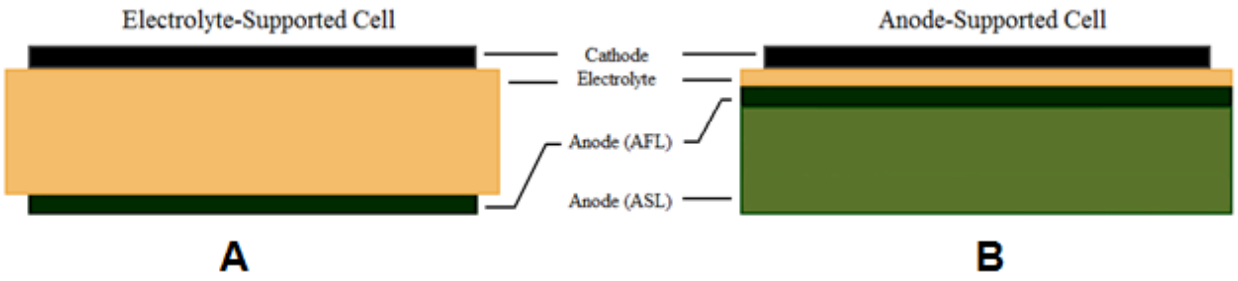

Figure 2.5. Schematic diagram of (A) an electrolyte-supported cell and (B) an anode-supported cell that contains both an ASL and AFL.

Further refinements, including the addition of an anode functionalized layer (AFL) between the ASL and the electrolyte, as shown in Figure 2.5B. The AFL is functionalized by lowering the NiO and YSZ particle sizes from 1 μm, as is used to fabricate the ASL, to 0.5 μm, and this improves the TPBL and, thus, the Ni-YSZ anode performance. Further, since the operating temperature is now lower (< 800°C) and the cathode can be applied after co-sintering the anode and the electrolyte and can even be sintered *in situ* (64), many cathode materials with superior performance (but previously rejected due to their chemical reactivity with YSZ) can now be used, as was discussed in Section 2.4.2. Thus, within the period of a few years from the development of anode-supported architectures, the maximum cell output power of cells increased from between 0.25 and 0.5 $W \cdot cm^{-2}$ at 1000°C to 1.9 $W \cdot cm^{-2}$ at 800°C (65).

Alternative architectures, such as planar metal-supported (61) (using porous stainless steel support layers) and planar electrolyte-supported (66) (using scandia-doping, which has a higher conductivity than YSZ) SOFCs, are currently being pursued. However, the state of the art performance is obtained from anode-supported cell architectures within planar, tubular, or

flattened tubular designs. This clearly indicates that the development of anode-supported cells was a very significant advancement in SOFCs.

The use of Ni as an anode material, unfortunately, still has limitations with respect to coking and sulphur poisoning (Section 2.6.2) and sintering(67). Further, the use of a thick anode layer makes internal reforming even more difficult to accomplish due to an even higher surface area at the cell inlet for steam-methane reforming (Reaction (2.1)) to take place (22). Some of these problems can be mitigated with the design of the balance of plant, such as the use of a high steam to carbon ratio to prevent coking and through the use of a desulfurizer and a reformer to process the fuel before it reaches the stack. However, these components lower the net electrical efficiency and increase the cost of the system.

2.5 Degradation in Ni-YSZ Anode-Supported SOFCs Due to Air Exposure

Immediately following the development of Ni-YSZ anode-supported architectures, questions arose (68) about the mechanical stability of a cell constructed from a very thick anode and a thin electrolyte. This was due to the large volume changes that are associated with the reduction of NiO and the oxidation of Ni, as follows:

$$NiO + H_2 \rightarrow Ni + H_2O \qquad \textbf{(2.8)}$$

$$Ni + \tfrac{1}{2} O_2 \rightarrow NiO \qquad \textbf{(2.9)}$$

An examination (68) of both the reduction of NiO (~41% volume decrease) and the oxidation of Ni (~70% volume increase) indicated that the reduction step does not result in any deleterious cell stresses, but if the Ni in an anode-supported SOFC is oxidized, serious degradation to the cell would result. Further studies (69; 70; 71; 72) have now demonstrated that Ni in a porous

SOFC anode oxidizes at rapid rates at operating temperatures of 600-1000°C, thus severely damaging the cell in a very short period of time.

In the case of electrolyte-supported cells, the anode layer is very thin in comparison to the electrolyte, so the volume change should not cause the electrolyte to crack, although sintering-related degradation (see Section 2.5.2) has been reported after over 12 oxidation/reduction cycles (73). Thus, a degradation mechanism that had not previously been studied, since it is specific to anode-supported architectures, now requires investigation. Since NiO subsequently reduces back to Ni when H_2 is returned to the anode chamber, the Ni oxidation/reduction cycle is often referred to as a "redox" cycle.

There is significant difficulty related to the study of redox cycling. The volume and flow rate of air into the anode chamber is unknown, since there many different stack and system designs that can each have different sources of air. It is thought (68; 74; 75) that air could enter the anode chamber through non-hermetic seals or by returning from the afterburner (where excess fuel is combusted and waste heat is used to preheat reactants) when there is an emergency fuel loss incident or even during a simple system shutdown process. Further, it is now thought that, by flowing air periodically through the anode chamber, any S- or C-species present could be removed, as will be discussed in Section 2.6.2.

2.5.1 Mechanisms Ni Oxidation at Intermediate Temperatures (600-1000°C)

Upon exposure to air, it is known that the initial stages of Ni oxidation are anisotropic. Oxygen on the exposed Ni {100} and {110} surface planes will quickly increase its surface coverage until a complete oxide monolayer is formed, whereas on the {111} Ni surface plane Ni^{2+} and O^{2-} ions migrate to form epitaxial pyramidal structures (76). Since the {111} plane has

the closest packing in a face-centered-cubic crystal structure, it is the most stable surface plane. Thus, for high surface area particles of Ni, these epitaxial pyramidal structures would be the expected oxidation initiation mechanism.

Once the surface of the Ni is fully covered with NiO, the mechanism of scale growth then changes to solid-state defect transport mechanisms, as illustrated schematically in Figure 2.6. Electron conductivity does not limit the scale growth in this reaction, as NiO is an intrinsic p-type semiconductor due to the high concentration of Ni^{3+} that is formed in the structure (76), which results in a conductivity of 1 x 10^{-2} $S \cdot cm^{-1}$ (E_a = 34.8 $kJ \cdot mol^{-1}$) (77). The oxygen anion diffusion coefficients at 600 and 1000°C, respectively, are ~10^{-19} and ~10^{-16} $cm^2 \cdot s^{-1}$ (78), while cation diffusion coefficients at 800 and 1000°C are ~10^{-9} and ~10^{-6}, respectively (79).

Thus, the Ni oxidation reaction follows parabolic reaction kinetics, which are typically observed for metal oxidation when the rate is limited by cation migration. In contrast, logarithmic kinetics typically result for metals, such as Al, where electron transport is the rate determining step (80). Cation vacancies are created at the air/NiO interface, which then allow Ni^{2+} cations that are produced at the Ni/NiO interface to migrate to the NiO/air interface (by a vacancy hopping mechanism), as shown schematically in Figure 2.6.

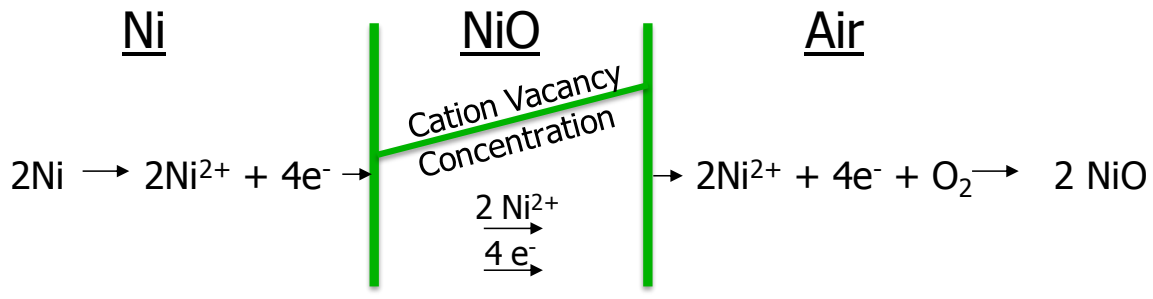

Figure 2.6. Schematic diagram of NiO scale growth during Ni oxidation.

However, it has been demonstrated (81) that NiO scale growth deviates from parabolic kinetics at intermediate temperatures (600 to 900°C). This is likely because NiO is produced with a duplex morphology, consisting of a porous "cellular" 6-30 μm thick structure that is covered by a dense outer NiO scale layer. For the oxidation of small Ni particles (1-3 μm in diameter), an aggregate or cellular NiO structure typically results (82; 83), since the diameter of NiO never exceeds 6 μm.

It is known (84) that a build up of compressive stresses within the NiO scale as it forms can cause spalling or oxide grain ejection. It is therefore thought (81) that this structure may be caused by O^{2-} anion transport into the film through the grain boundaries, which have a diffusion coefficient that is ~10^8 times greater than the bulk O^{2-} duffusion coefficient (78). While this anion transport is normally negligible in relation to the cation mobility in the bulk at intermediate temperatures, it could be sufficient to cause stresses within the NiO scale, causing particles of NiO to be pushed out of the scale, which would cause a cellular appearance to develop.

2.5.2 Mechanism of NiO Reduction at Intermediate Temperatures (600-1000°C)

Like Ni oxidation, the reduction of pure NiO is also very well understood and has even recently been observed inside an environmental transmission electron microscope by Jeangros et al. (85). The stages of NiO reduction are summarized in Figure 2.7. The first phase (Figure 2.7A) consists of an induction period that can last up to 2 min (86), where oxygen vacancies, which favor H_2 adsorption by lowering the energy to break the H-H bonds, are created (87). The induction period increases in length as the temperature decreases and as the ratio of pH_2O:pH_2 increases and, at 600-1000°C, this induction period is negligible (86).

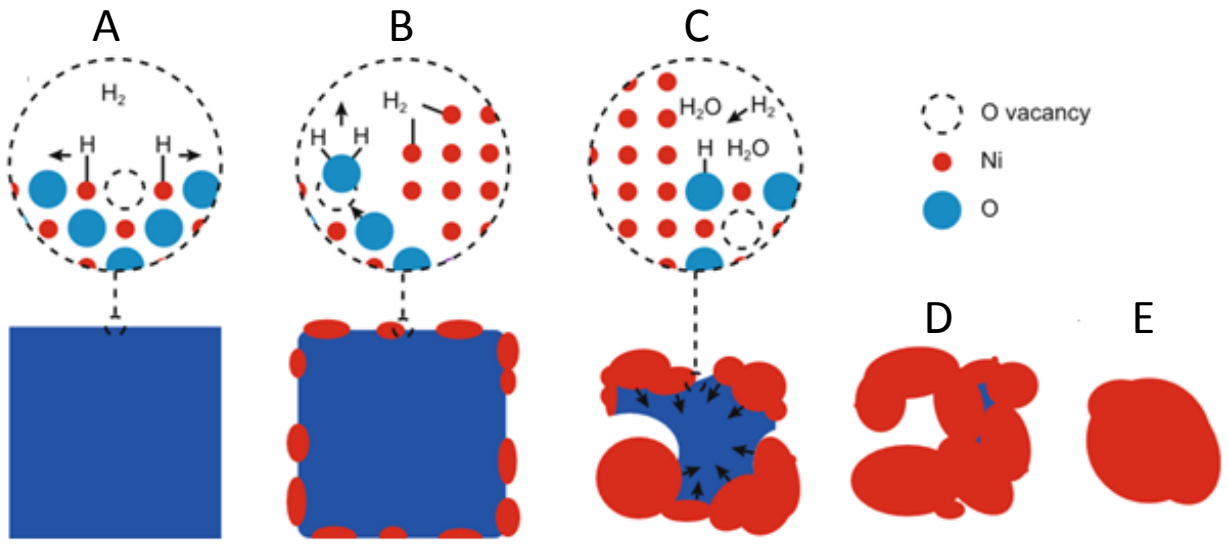

Figure 2.7. Model for NiO reduction and Ni densification, showing (A) the initial formation of oxygen vacancies, (B) Ni nucleation, (C) Ni crystallite growth with increasing H_2O transport limitations, (D) NiO trapped within Ni grains and, (E) finally, the completion of NiO reduction and continued Ni sintering with time (85).

Once Ni nanoclusters nucleate on the NiO surface (Figure 2.7B and C), the reduction reaction proceeds at a higher rate because H_2 can rapidly dissociate on the Ni surface. The kinetics of the reaction at this stage are pseudo-first order with respect to NiO, since there is a large excess of hydrogen (i.e., rate=[kp·(H_2)]·(NiO)). This process is also referred to as an interface-controlled reaction, because NiO reduction takes place at the interface between Ni and NiO and since the reaction rate is autocatalytic, in that the rate is proportional to the interfacial area (86).

In the final phase of NiO reduction (Figure 2.7D), the process deviates from first order, suggesting that the reaction changes from an interface-controlled reaction to some other rate limiting step (87). This likely results from the sintering of Ni crystallites, which increasingly block H_2 access to NiO and prevent H_2O from escaping through the Ni layers (86; 87). This sintering effect can significantly alter the NiO reduction rate at intermediate temperatures. For example, the rate of reduction actually slows for NiO pellets (88) or large particles (~1 mm NiO particles produced by CVD) (89) as the reduction temperature is increased from 600 to 900°C, when, logically, the rate should be increasing. Once NiO is fully reduced, Ni sinters to its lowest energy state (Figure 2.7E)

As can be seen in Figure 2.7, the change from one rate determining mechanism to another is not based solely on the proportion of NiO that is already reduced, but rather on both the pH_2O:pH_2 ratio and the NiO morphology (pellet versus powder). Richardson et al. (86) summarized the activation energies reported from different studies of pure NiO reduction and established that activation energies that are affected more by chemical resistance are between 65 and 98 kJ mol^{-1}. Low activation energy values are affected by gas transport through a growing Ni phase and high values are caused by a high pH_2O:pH_2 ratio.

2.5.3 Mechanisms of Ni-YSZ Anode-Supported Cell Degradation During Air Exposure

In theory, if a SOFC anode has 20 to 30% porosity after manufacture (in its oxidized state), the porosity will increase to 30 to 40% after reduction, due to the density difference between Ni and NiO (8.91 $g \cdot cm^{-3}$ and 6.67 $g \cdot cm^{-3}$, respectively) (76). Thus, when the Ni in a SOFC anode is re-oxidized, there should be enough pore volume to accommodate the volume increase due to Ni re-oxidation without damaging the cell, but damage is severe (68). Local

tensile stresses of ≥ 1000 MPa have been measured during Ni oxidation (90) (the yield strength of 8YSZ is only 300 MPa (91)). Sarantaradis and Atkinson (75) determined that, if the cell exceeds 0.1% strain, as measured by a dilatometer, then a 10-15 μm thick YSZ electrolyte will crack.

A model of redox cycling degradation has been expounded by Klemenso et al. (92), whereby upon initial *in situ* reduction in H_2, the Ni metal reorganizes by sintering mechanisms. As described in Section 2.5.2, Ni crystallites that form on the NiO surface will rapidly sinter to form larger particles and, as described in Section 2.4.3, the YSZ in the anode layer prevents the Ni particles from sintering too much. Nonetheless, larger Ni agglomerates can form, which upon re-oxidation in air, cannot return to their original distribution and, thus, the YSZ matrix in the anode and the YSZ electrolyte are subjected to high stresses.

It is therefore clear that mechanical stress on the thin electrolyte is the most significant contributor to cell degradation during a redox cycle. Other mechanisms of Ni oxidation degradation have also been investigated, including loss of conductivity (or loss of Ni interconnectivity), loss of TPBL (or loss of Ni surface area), and cumulative mechanical damage with multiple redox cycles (i.e., if a cell survived one oxidation cycle, but failed the second cycle due to larger agglomerates forming after a second reduction cycle) (74; 93; 64; 94). In each of these cases, the degradation is caused (or made worse) by Ni agglomeration. Thus, since NiO reduction will result in the formation of small, high energy Ni crystallites during each reduction cycle, it was speculated that, with each subsequent reduction cycle after the initial one, Ni sintering could accelerate, forming larger agglomerates after each cycle.

However, studies aimed at determining the extent to which Ni sintering mechanisms are enhanced by each reduction cycle have had varied results. For example, when measuring the Ni-

YSZ conductivity, Grahl-Madsen et al. (93) observed an increase after one oxidation cycle, while Kim et al. (95) observed a decrease in conductivity over 20 oxidation cycles. Likewise, when measuring anode performance, Kong et al. (96) observed a large increase in polarization resistance (R_p) after an oxidation cycle, while Laurencin et al. (73) noted only a slight decrease in performance after an oxidation cycle (using electrolyte-supported cells).

Young et al. (74) found that, the conductivity of Ni-YSZ anodes increased following an oxidation cycle when the anode porosity was high (38%) and decreased when the anode porosity was low (32%). In the case of the low porosity sample, the degradation was severe, with cracks propagating through the entire thickness of the anode after one oxidation cycle. Likewise, the R_p was observed to decrease (i.e., the performance increases) unless the mechanical degradation was severe (i.e., in the low porosity sample). Thus, the loss in performance was primarily due to loss of interconnectivity due to cracks that physically separated Ni to Ni interconnectivity.

It would be expected that, if there is an increase in agglomeration with each reduction cycle due to enhanced sintering rates, an increase in the severity of degradation should be apparent after several oxidation cycles. However, no cumulative or increased damage is generally observed after multiple oxidation cycles (74), unless there is insufficient pore space to accommodate for the Ni to NiO volume expansion, in which case, severe cracking is the result (97). Minor YSZ cracks in the anode (when pore volume is sufficient) do not prevent the YSZ in the anode from functioning to prevent further agglomeration, but once the YSZ in the anode begins to crack severely (i.e., the cracks propagate), it is no longer pinning Ni particles in the structure and Ni is more free to agglomerate.

The exothermic nature of Ni oxidation also increases the possibility that thermal effects are leading to degradation. Thermal shock occurs because a thermal gradient causes different

parts of an object to expand by different amounts, while creep is the tendency of a solid material to slowly and permanently deform during mechanical stress at high temperatures. Both thermal shock (74) and creep (98) could contribute to the mechanical stresses on the electrolyte during oxidation. However, no evidence has been found showing conclusively that either of these mechanisms are playing a role in the observed degradation.

Thus, it is concluded that, as long as the porosity of the anode is high (75; 99; 74), mechanical stress, caused by the volume expansion of the Ni-NiO reaction, and the resulting electrolyte cracking, is the primary source of degradation in Ni-YSZ anode-supported cells. If the cracks propagate through the full thickness of the anode layer, then the continuous pathway for electron conduction is broken and the cell performance degradation is catastrophic (74). Otherwise, the conductivity and performance will temporarily improve (94) due to alterations to the Ni morphology (i.e., through enhanced Ni interconnectivity and Ni surface roughening). Cumulative agglomeration after multiple oxidation cycles does not occur, unless the YSZ in the anode is severely mechanically damaged (74).

2.6 Preventing the Degradation Resulting from the Redox Cycling of SOFC Anodes

Ideally, anode-supported cells should have redox cycling tolerance, which is the ability of a cell to be exposed to O_2 with little or no degradation in performance, and several studies have focussed on improving cell tolerance. Waldbillig et al. (100), for example, contended that the lower porosity of the AFL was likely causing most of the observed cell degradation, modified the NiO content in the AFL. Adjacent to the ASL, the NiO content was 57% by weight (~10 μm thick) and, adjacent to the electrolyte, the NiO content was 40% by weight (~10 μm thick), in comparison with a standard 20 μm thick AFL that has 57% by weight NiO. Grading the Ni

content in the AFL results in a slightly improved oxidation tolerance, but the performance decrease due to a diminished TPBL was significant.

Pihlatie et al. (101), on the other hand, simply increased the porosity of the anode so that there was more pore volume available for the Ni to NiO volume expansion. Similar to the results obtained using a graded AFL (100), the initial performance of the cell, when compared to an anode with normal porosity, was significantly lower. Even though there were improvements observed in the redox tolerance of the cell, the performance loss was too significant for this microstructure to be considered for use in a commercially viable SOFC system.

Other cell modifications to minimize the damage caused by redox cycling have been proposed, such as decreasing Ni particle agglomeration during the first NiO reduction step by dispersing ceramic particles of CaO, MgO and TiO_2 into the Ni phase (72). While these modifications did slow oxidation rates and decrease the observed YSZ cracking, there has been no cited use of these in a commercial SOFC. This is largely due to a reluctance by commercial developers to increase the complexity of the powder preparation and sintering steps, or to add materials that could have interactions that could potentially affect the long-term performance of the cells.

System operating procedures are therefore the present method used to prevent air from entering the anode chamber, primarily by purging with N_2. However, purging consumes a high volume of N_2, making this approach impractical in remote locations, and purging during emergency fuel loss situations would require storage of large volumes of N_2 on site (102). As discussed early in Section 2.5, sources of O_2 primarily result from leakage through non-hermetic seals and back-flow from the afterburner. Thus, O_2 exposure could be prevented simply by using a valve that will work in the hot zone of an SOFC system, similar to the approach used by Delphi

Technologies (27), and using hermetic glass seals. Unfortunately, as discussed in Section 2.4.4, glass seals are problematic (57).

Wood et al. (102) summarized many key system solutions that could be used to protect an SOFC stack from O_2 exposure, including purging with steam, anode gas recirculation, sacrificial or reversible O_2 scavengers in the manifolds, or even thermally cracking a stored fuel source. It was found (102) that a steam purge was capable of protecting a cell for over 12 h, although the steam supply was likely H_2-saturated, since the steam source used in the study was from the normal fuel humidification infrastructure. Stathis et al. (70) found significant degradation due to steam flow through the anode, since, in this case, the steam source was likely O_2-saturated.

Another possible solution involves cooling the cell immediately after the emergency fuel loss incident. It was found (103) that, by cooling the cell rapidly from the operating temperature (750 or 800°C) to 250°C immediately after air ingress at a cooling rate of ≥ 3°C/min, cracking was prevented for a 5 x 5 mm test cell. However, some systems, especially those with large cell sizes, will be unable to achieve sufficiently rapid cooling rates to prevent critical levels of oxidation at the air ingress points.

2.6.1 Reverse Cell Bias During Air Exposure for the Prevention of Ni Oxidation

As was discussed in Section 2.5.1 (see Figure 2.6) (76), Ni oxidation involves the production of Ni^{2+} cations, which migrate across a growing NiO membrane and react with oxygen. In the case of SOFC anodes, however, Ni oxidation is taking place adjacent to an oxygen anion conductor. Thus, another approach to reversing or significantly slowing the rate of Ni oxidation involves applying a negative current to the Ni-YSZ electrode during air exposure (104), which will reduce Ni, as follows:

$$NiO + 2\,e^- \rightarrow Ni + O^{2-} \qquad \textbf{(2.10)}$$

Ni is reduced and the applied bias will cause the O^{2-} ion to migrate to the opposite electrode. Thus, the process must involve the application of a sufficiently negative potential to reduce Ni^{2+} and a sufficiently high current to remove oxygen.

Previously, cyclic voltammetry has been used to study the initial phases of the electrochemical oxidation/reduction of Ni/NiO and, in these studies (105; 106; 107), a cathodic peak was seen (NiO reduction) at -655 mV vs. a Pt crack-free at high temperatures (950°C) and in a high vacuum ($pO_2 = 10^{-13}$ atm). This result matches with thermodynamic data (E_r = -675 mV) (11), which also shows that, at 800°C, the potential applied to begin reversing Ni oxidation should be -750 mV. However, since it is uncertain if the potential of the reference electrode could be affected by the gas environment and other conditions used in these studies (105; 106; 107), it is not clear how large the negative potential must be in an operating SOFC system to reduce Ni^{2+}.

There are practical limitations to the quantitative study of the effect of reverse biasing a Ni-YSZ anode, however, due to difficulties in assessing the state of the electrode during air exposure with a bias applied. In order to determine if Ni is protected from oxidation in an anode, the cell must be inspected after the trial is complete. Ideally, anode-supported cells would be used for this study, since this is the type of cell that requires protection, and then the cell could be inspected for electrolyte cracks upon the completion of the cycle. However, when applying a Pt ink counter electrode on a pre-fired electrolyte, the outer edges of the electrolyte must be left uncoated to avoid short circuiting the cell across the 10 μm thick electrolyte. In these uncoated regions, it is uncertain whether current flow is sufficient to keep the Ni reduced and, as a result,

it would be impossible to determine if any cracks observed had initiated in the uncoated portion of the electrolyte or if the bias was insufficient to protect the cell.

In an electrolyte-supported cell, the working and counter electrodes can be fabricated to avoid these problems. However, it is then difficult to determine if Ni was oxidized, since a thin anode will not generate enough stress to crack a thick electrolyte and since changes to the Ni microstructure after a redox cycle are subtle. Delamination is the most common redox cycling degradation mechanism in electrolyte-supported cells, but delamination does not consistently take place, even after many oxidation cycles (74; 73).

With electrolyte-supported cells, however, it has been observed that the open circuit R_p in humidified H_2 usually decreases (74) and the conductivity of the anode usually increases (74; 94) after the Ni-YSZ anode is oxidized (and re-reduced). It is speculated that this is due to changes in the Ni morphology, arising from a redox cycle, that result in a larger TPBL and an improved interconnectivity in the anode. Therefore, the goal of our earlier work on reverse bias (108) was to determine if this performance enhancement could be prevented during an air exposure period with a reverse polarization applied. If the anode performance remained unchanged, it could then be inferred that Ni had been protected from oxidation by the negative polarization.

By monitoring the EIS spectra before and after air exposure, it was found (108) that, after a negative potential bias of up to -350 mV (vs. reference electrode) was applied to the Ni-YSZ electrode, R_p decreased and the anode therefore did not appear to have been protected. In contrast, the application of a constant cathodic current density of -6.5 mA/cm^2 did not result in a lower R_p and, thus, it appears that this negative current density was sufficient to prevent Ni oxidation. This was a promising result, as electrochemical reduction during air exposure of a Ni-

based anode would have significant advantages over other techniques, primarily owing to its simplicity and rapidity of implementation.

However, there were clues that the Ni in the WE may not have been fully protected in this study (108). With a low cathodic potential applied (-150 mV vs. RE), the measured current density dropped to zero immediately after air exposure began, while at a higher potential (-350 mV vs. RE), the current density slowly decreased during the full period of air exposure, but was never zero. Likewise, at -6.5 mA/cm^2, the potential was constantly increasing with time (108). In both cases (a decreasing measured current or an increasing measured potential), the results suggest that the Ni was still slowly oxidizing and it was therefore not possible to confirm from the EIS data if NiO formation had been prevented or not.

In the earlier cyclic voltammetry work (106), using Ni/NiO working and counter electrodes with a YSZ electrolyte (briefly discussed above), it was demonstrated that there were diffusion limitations associated with NiO reduction. Specifically, O^{2-} diffusion through Ni is slow (105; 109) and, for the electrochemical reduction of NiO during cyclic voltammetry, a thin metallic phase quickly forms between the NiO and YSZ. Once this metallic phase forms, diffusion of O^{2-} through this layer becomes the limiting step in the reaction.

Ideally, the onset of a redox cycle will be predicted, so that when the reverse bias is applied, the Ni in the anode should still be fully reduced (with no NiO in the structure). Then, as air enters the anode chamber, much of this oxygen will be removed before forming bulk NiO. However, it would be expected that those portions of Ni that are not adjacent to the ion conducting phase will be slowly oxidized over time, since the diffusion of O^{2-} through Ni is slow. In this case, the electronic conductivity of the anode would slowly decrease, since NiO has a lower conductivity than does Ni.

2.6.2 Reversing Coking and Sulphur Poisoning of Ni-YSZ Anodes with Air Exposure

As discussed in Section 2.4.3, coking and S-poisoning are serious technological obstacles to the use of Ni-YSZ anodes in SOFCs, although they can be mitigated through the use of a humidifier and a desulfurizer, respectively. Because these components add cost and complexity to the SOFC system and as there is a high likelihood of component failure (i.e., due to water loss in the humidifier or due to adsorbant saturation in a desulphurizer, respectively) during the lifetime of the SOFC system, the anode should ideally be coking and S-tolerant, meaning that the performance degradation is small or non-existent. However, as discussed in Section 2.4.3, most alternative materials used to prevent coking or S-poisoning are inferior to Ni-YSZ when comparing performance, cost and manufacturability.

When anodes are accidentally exposed to fuels containing H_2S, followed by normal (desulphurized) fuel flow, the performance is slow to recover to near normal performance and there is a small permanent loss to cell performance is seen (40). When anodes are inadvertently exposed to conditions suitable for coking, the C deposits that form are stable once normal (humidified) fuel flow ensues, although a high steam flow (20% in He) at > 800°C has been shown (110) to be able to remove the C.

An alternative method of fully removing both C (111) and S (112; 113) from the surface of Ni-based anodes is the use of an air purge. However, one problem that has been anticipated is that the quantity of air necessary to successfully remove all or most of the coke or S from the Ni surface in the active area of the entire cell (which is often > 10 x 10 cm) may be enough to cause extensive NiO formation, leading to cell degradation, as described in Section 2.5.3. Therefore, the approaches developed to minimize cell damage caused by redox cycling, such as a reverse

bias (Section 2.6.1 and Chapter 7), will be used in conjunction with an air purge in order to avoid cell degradation while reversing S-poisoning, as will be discussed in Chapter 8.

2.7 Background Related to Experimental Techniques

2.7.1 Microscopy

Microscopy is an indispensible materials characterization tool with a long history (114). A profile or "top down" image of a sample surface can be viewed or the sample can be prepared by sectioning (and possibly polishing) and viewing the "cross-section". For a typical fully reduced Ni-YSZ anode attached to an electrolyte, for example, a profile image involves either imaging the surface of the electrolyte or the outer surface of the anode, while a cross-sectional image shows the anode and/or the electrolyte from the side.

When a sample is viewed with a microscope (optical, SEM, etc.), a 2-d image is seen, which can then be used to give a 3-d rendering of the phase content with one of three techniques (114). The Delesse technique (area percent equals volume percent), the Rosiwal technique (lineal percent of randomly drawn lines equals volume percent), and the point counting technique (a grid of points are drawn on an image and the percentage of points on a phase equals volume percent) have all been used to estimate phase contents (114). While the Delesse technique fell out of favor due to the difficulty of quantifying phases having odd shapes, modern image analysis software, which counts pixels within a range of color or contrast, made this determination much easier and it is now the most commonly used of these techniques.

However, using images from any source (Optical, SEM, etc.) for determining phase content in SOFC anodes results in many problems that stem from the geometry of the samples. First, Ni-YSZ anodes have a high "natural variability". By randomly intermixing NiO and YSZ

particles and then sintering at high temperatures, the initial 1 μm particles agglomerate. After sintering, NiO and YSZ particles range in diameter from 2 to 5 μm and 1 to 3 μm, respectively, and, after reduction, Ni particles range from 1.5 to 3.7 μm in size (115). Second, when the Ni particle is partially oxidized, it results in two concentric spheres and, when these spheres are cross-sectioned, the Delesse technique volume results will be biased in favor of the dominant phase (116). Finally, NiO occupies 70% greater volume than the same Ni due to the Ni-NiO density differences (76).

2.7.1.1 Optical Microscopy

An image arises in optical microscopy due to light that is reflected from the sample surface and through multiple lenses to allow a magnified view of the sample. Material phases can be distinguished by the differing contrast of light that arises due to differences in light absorption or by refraction (if the refractive index of the materials on the surface vary). In black and white cross-sectional images of Ni-YSZ anodes, a relatively even distribution of white (metallic phase), grey (YSZ and shallow pores) and black (deep pores) phases are seen through the thickness of the cell. When the Ni is oxidized, a fourth phase appears (NiO) and it appears green or, in a black and white image, as a darker shade of grey relative to YSZ. Achieving image contrast that can distinguish between NiO and YSZ is difficult in an anode containing polished Ni, since Ni that is polished to a mirror finish is very bright in comparison. Therefore, past studies (103; 117) using optical microscopy have focussed on the relative amount of shiny (Ni) areas in light microscopy images to qualitatively compare the amount of Ni that is in the metallic state throughout the anode.

While better light microscopes are available for some applications, the diffraction limit to resolution of a standard metallurgical optical microscope is approximately 0.2 micrometres (118). This resolution limit is insufficient for quantitatively determining the oxidation depth of a Ni-YSZ anode, since some features can be smaller than this limit. In Figure 2.8, it can be seen that the change in the total radius of the Ni/NiO particle (black) linearly increases with oxidation depth, while the Ni radius and NiO thickness do not change linearly. This results in a NiO layer thickness that does not exceed the microscope resolution limit until more than 30 at% of the Ni is oxidized and a Ni particle radius that does not change significantly until more than 60 at% of the Ni is oxidized.

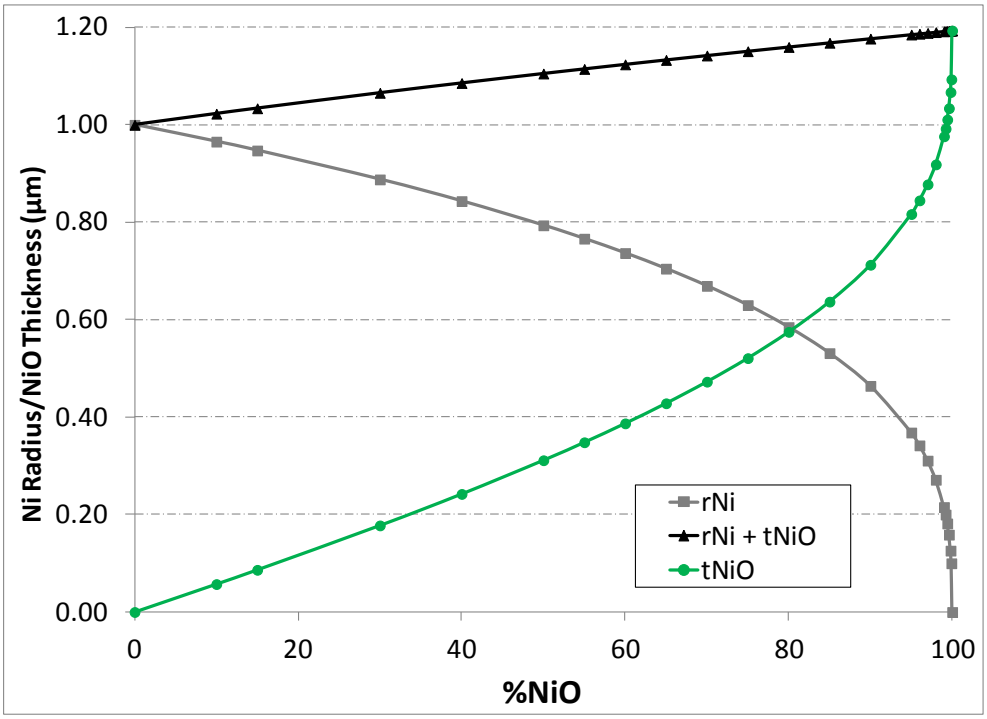

Figure 2.8. Radius of Ni and thickness of NiO as a 2 µm diameter Ni particle is oxidized, showing the decrease in the radius of Ni and increase in the NiO scale thickness with oxidation depth (percentage of Ni oxidation).

2.7.1.2 Scanning Electron Microscopy (SEM)

The use of SEM has many advantages over light microscopy, including a much higher resolution (SEM can achieve resolution better than 1 nm, but 10 nm is typical) and a much higher depth of field (118). This allows much higher magnification images to be collected and improved microstructure characterization. In SEM, a focused beam of high-energy electrons is directed at the specimen. The interaction of the electrons with the specimen surface can result in a number of different electron-sample interactions, producing secondary electrons, backscattered electrons, Auger electrons, cathodoluminescence (visible light), characteristic x-rays and Bremsstrahlung x-rays (118).

Images are produced by moving the focussed electron beam over the surface of the sample in a raster pattern and either secondary electrons or backscattered electrons are detected (by separate detectors). In the case of secondary electrons, electrons are expelled from an atom when an incident electron excites an electron in the sample. Due to the low energy of the secondary electrons, only those produced near the sample surface are released to the detector and the number of secondary electrons released is mostly the result of the incidence angle of the electron beam (although atomic mass also has an effect). Thus, image contrast is largely the result of sample topography and secondary electron SEM is largely used for characterizing the morphology of material surfaces.

Backscattered electrons result when high energy electrons (from an electron beam) are reflected or backscattered out of the specimen. Since the production of backscattered electrons varies directly with the specimen's atomic number, higher atomic number elements (bright) can be distinguished from lower atomic number elements. For Ni-YSZ anodes, Ni and YSZ are typically indistinguishable from one another, while NiO typically appears grey and pores appear

dark grey or black. In Chapter 4, it will be shown that the analysis of oxidation depth is carried out in a similar fashion to optical microscopy. Contrary to the case with optical microscopy (Section 2.7.1.1), where the shiny Ni was qualitatively tracked across the anode surface, in backscattered electron SEM, the dark NiO phase was qualitatively compared across the anode cross-section.

2.7.1.3 Energy Dispersive X-ray Spectroscopy (EDX).

As discussed in Section 2.7.1.2, the focussed electron beam used in SEM analysis also results in the emission of characteristic x-rays. A photon with an energy that is characteristic of each element is produced when a higher energy level electron replaces one that was removed when a secondary electron was released. In energy dispersive x-ray spectroscopy (EDX or EDS), the composition of the specimen can be quantified from the number of x-rays produced with an energy that is characteristic of each element (118).

EDX has been applied in past studies (103) in an attempt to determine the extent of Ni oxidation across the thickness of a Ni-YSZ anode. Characteristic x-ray peaks for Ni, Y, Zr and O were seen with each spectra. Ni, Y and Zr should be relatively constant throughout the anode thickness and only the O content should change across the anode thickness. These results are only qualitative, however, since the large natural variability in the microstructure of the anode (as discussed in Section 2.7.1), which causes variability in the amount of YSZ (vs. Ni/NiO) present in the sampled area, thus altering the background O detected in each spectra. Further, errors in EDX are known to be high and are the highest for light elements such as oxygen (118).

2.7.2 X-ray Photoelectron Spectroscopy (XPS)

X-ray photoelectron spectroscopy (XPS) is based on the photoelectric effect that was discovered by Hertz in 1887 (119) when it was noted that electrons are emitted from elements when they absorb energy from light. It was Prof. Kai Siegbahn who first improved the equipment and demonstrated the potential of XPS to not only identify atoms, but also compounds (120). Today, XPS is recognized as a surface sensitive technique that can determine the elemental composition down to the parts per thousand range, in addition to determining the chemical and electronic state of the element within the material.

In XPS, X-ray radiation (1-15 keV) bombards and ionizes the sample, releasing electrons not only from the outer shells, but also from core levels. Only those electrons that escape the sample and reach the detector in the high vacuum environment (10^{-10} atm) are measured. There are many different interactions that these photo-emitted electrons can undergo, such as inelastic collisions or recombination, which can reduce the number of escaping photoelectrons. These effects drop off exponentially as the depth into the sample surface increases, thus resulting in a very thin (~10 nm) sampling depth and making XPS a surface analysis technique (121).

The kinetic energy of each photoelectron that reaches the spectrometer detector can be measured to an accuracy of ± 0.1-0.2 eV. Using the kinetic energy, E_{Kin}, of the emitted x-rays (aluminum K_α X-rays, E_{ph} = 1486.7 eV) and the instrument work function, ϕ, a correction factor, the binding energy, $E_{B.E.}$, can be determined as follows:

$$E_{B.E.} = E_{ph} - (E_{Kin} + \phi) \qquad \textbf{2.3}$$

A wide energy survey spectrum is produced by all of the photoelectrons that are detected, from which the characteristic binding energies associated with the peaks can be used to identify the elements and their oxidation state. By fitting the peaks and correcting for the background

intensity, the relative element sensitivity factors, and the inelastic mean free path, the elements and compounds that are present can be quantified.

2.7.3 Raman Spectroscopy

The principles of Raman spectroscopy were discovered by Sir Chandrasakara Raman in Calcutta, India in 1921 (122) when using sunlight focussed with a telescope to study the scattering of light through a transparent medium. It was noted that the diffuse radiation from the source was "accompanied by a modified scattered radiation of degraded frequency" (122). Today, using Raman spectroscopy, a monochromatic light source, such as a laser, is focussed on a specimen, which causes electrons in the material to be excited to a "virtual" state from its ground electronic state. As the electrons relax back to their ground state, a photon that is either Rayleigh or Raman scattered is emitted.

Rayleigh scattered light is elastically scattered light that returns to its original ground state and releases a photon that has the same wavelength and energy as the incident beam. However, Raman scattered light is inelastically scattered, such that it either has a lower energy and longer wavelength (Stokes radiation) or it has a larger energy and a shorter wavelength (anti-Stokes radiation). The energy change is related to the vibrational energy levels in the ground state of the molecule, and as such, the observed Raman shift of the Stokes and anti-Stokes features are a direct measure of the vibrational energies of the molecule. A change in the polarization potential, or deformation of the electron cloud with respect to the vibrational energy level, is required for a molecule to exhibit a Raman effect (123).

Scattered light that returns through the objective lens is filtered to remove Raleigh scattered light, which has a high intensity. The beam then passes through an interferometer or

monochromator and the Raman shifted radiation is detected with a CCD. The Stokes and Anti-Stokes lines are equally displaced from the Raleigh line, with the Anti-Stokes lines having less intensity than the Stokes lines. The intensity of the anti-stokes lines are typically lower, since the electrons would need to be induced into an excited state prior to measurement in order to produce a higher intensity at the Anti-Stokes lines, so the more intense Stokes spectra are typically used in Raman spectroscopy. The spectra can now be utilized to determine the chemical composition and quantify the sample constituents.

NiO has a rock-salt-type structure (NaCl) with antiferromagnetic domains, which are accompanied by a weak rhombohedral distortion and a Neel temperature of 523 K (124). When using a 514 nm incident laser, the principal mode is seen to have a Raman shift of 1100 cm^{-1}, whereas the magnon mode is seen to have a Raman shift of 1500 cm^{-1} (125; 126). If the temperature is raised above the Neel temperature, the 1500 cm^{-1} magnon Raman peak will disappear (126). In addition, it has been shown (125) that the ratio of the principal and magnon peaks can change, depending on the orientation of the twin domain patter (i.e. the rhombohedral distortion).

2.7.4 Thermogravimetric Analysis

Thermogravimetric analysis (TGA) is a form of temperature programmed reduction (TPR) or oxidation (TPO). In TPR/TPO, it is common to expose a material to a stimulus, such as a change in temperature or gas environment, and any change in chemical composition will cause a change in the system (pressure, gas composition, etc.) that can be measured (pressure gauge, mass spectrometer, etc.). The use of a TGA is advantageous, since the mass of the sample, which is hanging in a crucible inside the furnace while being exposed to the gas composition at the

temperature of interest, is monitored by a very sensitive balance (± 2 μg) that is located outside of the furnace. Some common applications of TGA include materials characterization through analysis of characteristic decomposition patterns, studies of degradation mechanisms and reaction kinetics, the determination of the organic content in a sample, and the determination of the inorganic content in a sample (127).

2.7.5 Electrochemical Performance of SOFC Electrodes

As was discussed in Section 2.2, the output voltage of a H_2/O_2 fuel cell is ideally 1.23 V (25˚C, 1 atm, liquid water), which falls to approximately 0.98 V at 800˚C (11). However, the use of full cells in typical SOFC research is difficult due to the need to seal the anode and cathode environments and, as will be seen in Chapters 7 and 8, it is not possible to separate two gas environments in the *in operando* TGA apparatus. Cyclic voltammetry (CV) and electrochemical impedance spectroscopy (EIS) are therefore carried out using a half-cell configuration, whereby both the working (WE) and counter (CE) electrodes are exposed to the same gas environment within a single furnace chamber. A 3-electrode configuration with a WE, CE and a reference electrode (RE) is preferred, since one electrode (the WE) can then be isolated to determine its performance (25). However, due to size limitations in the *in operando* TGA apparatus, only a 2-electrode configuration was used for the purpose of the work described in Chapters 7 and 8.

2.7.5.1 Cyclic Voltammetry

In 2-electrode, half-cell CV, the output current is measured while the potential between the WE and CE is changed at a constant rate between two specific potentials, and because it is a 2-electrode configuration, the summed losses at both electrodes are measured. Due to the half-

cell configuration used, the initial potential difference is typically zero, which then initially increases exponentially. This is typically followed by a linear relationship between current and potential with a slope that depends largely on the ohmic resistance of the electrolyte. At very high potential differences, the current will no longer increase with increasing potential due to the onset of diffusion limitations. These three cell losses are due to polarization, which can be broken down into three categories, which are kinetic (activation) polarization, resistance polarization, and concentration polarization, respectively (128; 129).

2.7.5.2 Electrochemical Impedance Spectroscopy (EIS)

When two materials meet at an interface, the physical properties (crystal structure, mechanical stress, chemical potential and electrical properties) can be significantly different, which will lead to charge transfer (polarization). Each system will polarize in its unique way, but the rate that a polarized region will change with a change in the applied voltage is characteristic of the type of interface. It will typically (although there can be exceptions) be slow for electrochemical reactions at an electrode-electrolyte interface, for example, but fast across grain boundaries in YSZ (130; 131).

By applying a single frequency a. c. voltage (2 to 20 mV) to the interface, the impedance can be measured directly from to the phase shift and amplitude of the resulting current at that frequency. The impedance of an R-C circuit can be described by the following equation(130):

$$Z = \frac{R}{1 + i\omega CR} \qquad \textbf{2.4}$$

where ω is the angular frequency, 2πf, i is an imaginary number ($\sqrt{-1}$), C is the capacitance at the interface and R the resistance of the process at the interface. The real and imaginary components of the impedance are as follows(130):

$$Z = Z' + iZ" \quad \textbf{2.5}$$

Z' is the real part of the impedance, as follows:

$$Z' = \frac{R}{1 + (\omega CR)^2} \quad \textbf{2.6}$$

Z" is the imaginary part of the impedance, as follows:

$$Z" = \frac{\omega CR}{1 + (\omega CR)^2} \quad \textbf{2.7}$$

and ϕ is the phase angle, as follows:

$$\tan\phi = -\frac{Z"}{Z'} \quad \textbf{2.8}$$

If the frequency is then varied over a wide range (normally 0.1 to 100,000 Hz), Z" vs. Z' can be plotted in a "Nyquist" plot, as is seen in Figure 2.9A (130).

The number of semicircles in the Nyquist plot depends on the number of time constants present, with each time constant representing a different process or reaction step within the cell. The results are then often compared to the expected response of a best-fit equivalent circuit, as seen in the inset of Figure 2.9A. This allows quantitative values of the circuit elements to be determined, such as the two resistors, R_s and R_p, the capacitor, C, and the inductor, L (Figure 2.9A). R_s is commonly referred to as the series resistance and typically includes all of the ohmic (non-Faradaic) resistances, such as the electrolyte, the wires and the contacts. R_1 is the resistance

(inverse of rate) of the reaction that the impedance arc represents. The sum of the resistors in the impedance arcs is commonly referred to as the polarization resistance, R_p (130).

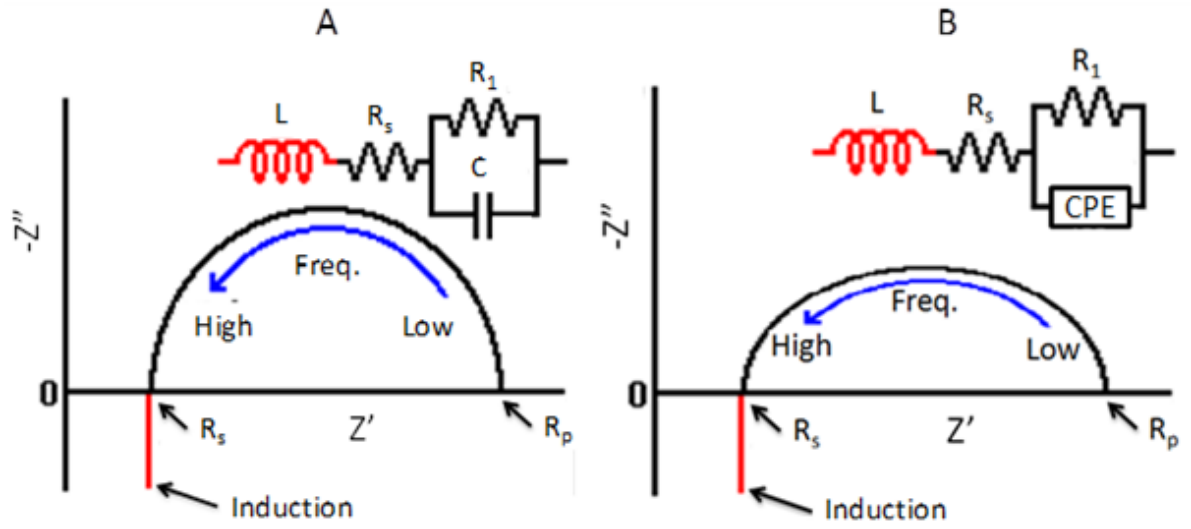

Figure 2.9. An example of Nyquist plots obtained from the equivalent circuits shown (inset), where (A) is a Nyquist plot for a circuit containing an ideal capacitor and (B) is a Nyquist plot from the same circuit, but containing a CPE. Both circuits contain two resistors (R) and an inductor (L).

While electrode/electrolyte interfaces exhibit capacitive properties, often this behaviour is not ideal, as is seen in Figure 2.9B, and a CPE (constant phase element) is substituted for the C. Many variables in a real system can generate a CPE, including surface roughness, porosity, chemical inhomogeneities or impurities, or other non-ideal geometries (130; 132). The CPE is used to represent this non-ideal response, as follows:

$$Z'' = \frac{1}{CPE \cdot i\omega^n} \qquad \textbf{2.9}$$

where n varies between 0 and 1. Depending on the value of n, Equation 2.9 can represent a perfect resistor (n = 0), a perfect capacitor (n = 1) or a Warburg diffusion impedance (n = 0.5) (132).

Chapter Three: **Materials and Methods**

Over the course of the studies presented in Chapters 4 to 8, two cell architectures, anode-supported planar cells and electrolyte-supported planar cells (discussed in Section 2.4.4) were used for the purpose of the studies. The manufacturing techniques used to construct them are described in Section 3.1. Instrumentation and the general experimental procedures used in the course of these studies are detailed in Section 3.2, while analysis techniques that were used to examine cells or components of cells before and after electrochemical or thermogravimetric analysis (TGA) studies are described in Section 3.4.

3.1 Cell Fabrication

3.1.1 Ni-YSZ Anode-Supported SOFC Comprising a Co-Fired YSZ Electrolyte (ASC-1)

The anode-supported samples used for the majority of the experiments carried out in Chapters 4 to 6 consisted of a 17 mm diameter (post-sintering) Ni-YSZ anode support layer (ASL, 1 mm thick), a Ni-YSZ anode functional layer (AFL, 20 μm thick), and a thin, dense YSZ electrolyte layer (10 μm), as shown in Figure 3.1. The electrolyte side of the sample was not coated with a cathode or CE layer, since this configuration was useful for mass measurements in TGA. It was also useful for quickly examining the electrolyte surface in order to determine the extent of its cracking, for example, after exposure of the samples to a range of conditions (temperature or pO_2). These cells are designated as 'ASC-1' for the purpose of this thesis.

ASC-1 samples were prepared by first tape casting and drying a 1 mm thick Ni-YSZ ASL (using 1 μm diameter NiO and YSZ particles) and then screen printing two layers of Ni-YSZ paste to form the AFL (functionalized by the use of finer 0.5 μm diameter NiO and YSZ particles) onto the tape cast ASL. After this, two layers of a dense YSZ electrolyte layer (10 μm final thickness) were sequentially screen-printed onto the AFL, followed by drying at 80°C after the deposition of each screen printed layer, and then co-firing at 1450°C for 2 h.

Both the ASL and AFL contained 57% (by mass) NiO and 43% YSZ, although the ASL was fabricated with a 1 μm average NiO and YSZ particle size versus 0.5 μm for the AFL. Prior to NiO reduction, the ASL and AFL had a porosity of 30% and 22%, respectively, while after NiO reduction, the ASL porosity increased to 38% and the AFL porosity to 30%. Porosities were determined using AnalySIS software.

Figure 3.1. Schematic diagram of ASC-1 samples that contain an ASL, AFL and YSZ electrolyte.

3.1.2 Ni-YSZ Anode-Supported SOFC Comprising a Co-Fired YSZ Electrolyte and a Ni-YSZ Counter Electrode (ASC-2)

The second anode-supported cell, used primarily in the work presented in Chapter 4, comprised a 13 mm diameter (post-sintering) Ni-YSZ ASL (1 mm), a Ni-YSZ AFL (20 μm), a thin, dense YSZ electrolyte layer (10 μm), and another Ni-YSZ anode functional layer on the

counter electrode side (AFL-CS, 20 μm thick), as shown in Figure 3.2. This geometry was useful for quantifying the severity of cracking during air exposure at a range of temperatures and, due to their reproducible mass, they were superior for comparing Ni oxidation kinetics in cells exposed to air at a range of temperatures. These cells are designated as 'ASC-2' for the purpose of this thesis.

ASC-2 cells were prepared by first tape casting a 1 mm thick Ni-YSZ ASL (using 1 μm diameter NiO and YSZ particles) and then screen printing two layers of Ni-YSZ paste to form the AFL (functionalized by the use of finer 0.5 μm diameter NiO and YSZ particles) onto the dried tape cast ASL. After this, two layers of a dense YSZ electrolyte layer (10 μm final thickness) were sequentially screen-printed onto the AFL, followed by the application of two more layers of Ni-YSZ AFL paste to the counter electrode side of the electrolyte. Drying at 80°C was carried out after the application of each screen printed layer, and then the cell was co-fired at 1450°C for 2 h.

As with the ASC-1 cells described in Section 3.1.1, the ASL and both the AFL and AFL-CS layers contained 57% (by mass) NiO and 43% YSZ, although the ASL was fabricated with a 1 μm average NiO and YSZ particle size versus 0.5 μm for the AFL and AFL-CS. Prior to NiO reduction, the ASL and AFL had a porosity of 22% and 14%, respectively, while after NiO reduction, the ASL porosity increased to 38% and the AFL porosity to 30%. Porosities were determined using AnalySIS software.

Figure 3.2. Schematic diagram of ASC-2 samples that contain an ASL, AFL, YSZ electrolyte and another AFL on the counter electrode side of the cell.

3.1.3 YSZ Electrolyte-Supported SOFC Containing Ni-YSZ and Pt Electrodes (ESC-1)

These cells, shown schematically in Figure 3.3, contain a 30 μm thick Ni-YSZ WE, a 0.5 mm thick self-supported YSZ electrolyte and a Pt CE. The YSZ disks (0.5 mm thick) were manufactured by pressing the YSZ powder (TOSOH) and firing at 1500°C for 2 h. To fit into the *in operando* TGA test apparatus, as discussed in Section 3.2.5, the 17 mm YSZ disks were sectioned into four smaller (~7 x 7 mm) pieces.

The 0.4 cm^2 WE was prepared by mixing 56 wt% NiO (99% metal basis, Alfa Aesar) and 44 wt% 8 mol% YSZ (TOSOH) with ethanol (1:10 ratio by mass) and ball milling with a high energy planetary ball mill (Fritsch Planetary Ball Mill - Classic Line, 250 rpm for 4 h) with 0.55 cm diameter zirconia balls in a zirconia jar. After drying the powder, the WE was deposited by screen-printing a paste of powder and glycerol and firing at 1350°C for 2 hours.

For the preparation of the 0.4 cm^2 CE, a Pt adhesion layer was sputtered onto the YSZ disc with a mask carefully applied to ensure that the CE was not offset from the placement of the WE (on the opposite side of the electrolyte). Pt paste (Ferro 4082) was then painted on top of the sputtered Pt layer, the mask was removed, a Pt mesh (Alfa Aesar, 100 mesh, 0.0762 mm, 99.9%

metals basis) was affixed to both electrodes with Pt paste, and then the CE was sintered at 1000°C for 2 h.

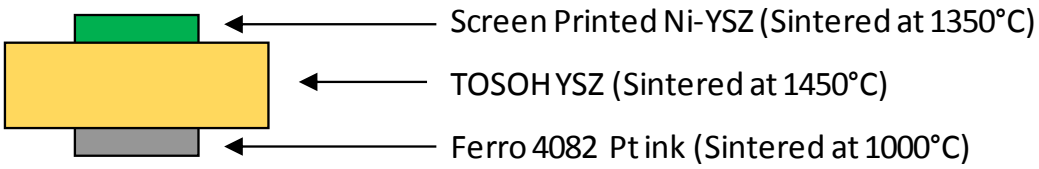

Figure 3.3. Schematic diagram of the ESC-1 cell used in this study.

3.2 Thermogravimetric Analysis

In Chapters 4 to 8 of this thesis, oxidation and reduction cycles were carried out under various conditions in a Setaram TAG 16 TGA/DSC symmetrical balance. In performing these experiments in a TGA, the sample mass at any time during the experiment could always be determined and, thus, the extent of Ni oxidation/NiO reduction within the Ni-YSZ anode layers could also always be determined accurately.

3.2.1 Gas Atmosphere in TGA Experiments

The Setaram TGA requires an inert backing gas to protect the balance components from reactive gases and, thus, all gas concentrations included a He flow that contained more than 50% of the total gas flow. As the most important gas concentration for these experiments was the oxidizing gas, the flow of oxygen was set to the desired level and the remaining gas compositions depended on the backpressure set for oxygen and the composition of the supplied gas cylinder.

For all oxidation cycles, air was simulated by mixing O_2 (99.6%) with a He (99.995%) backing gas in an approximately 1:5 ratio to achieve a 20% O_2-He composition. For reducing and inert conditions, the backpressure was kept the same as for O_2 for both pure H_2 (99.99%) and pure N_2 (99.998%), resulting in gas compositions of approximately 10% H_2-He and 20% N_2-He, respectively, as estimated from the use of a rotameter. For the work described in Chapters 7 and 8, the gas composition was humidified by redirecting the He supply through a water bubbler. In addition, the H_2 and H_2S cylinders contained 10% H_2-He (99.99%) and 5 ppm H_2S-10% H_2-He, respectively. Thus, the gas compositions contained 2.5% H_2O-20% O_2-He ("air"), 2.5% H_2O-20% N_2-He ("N_2"), 2% H_2-2.5% H_2O-He ("H_2"), and 1 ppm H_2S-2% H_2-2.5% H_2O-He, respectively.

3.2.2 Full Ni Oxidation-Reduction Cycling at 0.1, 20 and 50% pO_2 Inside the TGA

Fragments of the ASC-1 cells (80 to 250 mg, formed by sectioning pieces from the full disc specimen) or complete ASC-2 cells (850 to 950 mg) were placed (electrolyte down) in a shallow 100 μL Pt crucible in the TGA. As seen in the schematic of Figure 3.4, the sample was raised to the temperature of interest (600-900°C) at 5°C·min^{-1} in simulated air and then subjected to its first reduction cycle (after a 15 min N_2 purge). Reducing (10% H_2-He) and oxidizing (0.1, 20 or 50% O_2 in He) atmospheres were cycled, with intermittent 15 min N_2 purges used for safety, for 1 to 10 cycles. Time periods during the oxidation and reduction cycles in Figure 3.4 varied between 3 and 12 h in each reaction gas depending on the temperature used and the partial pressure of the reaction gases.

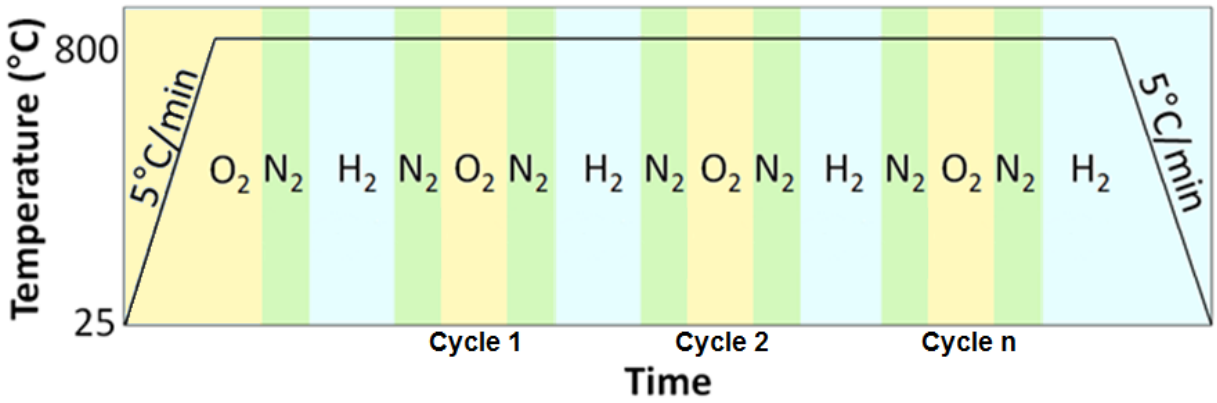

Figure 3.4. Thermal and gas environment profile used for redox cycling a Ni-YSZ anode in the TGA (shown for 800˚C). The time period of each gas cycle is contingent on the goals of the investigation, temperature and gas environment.

3.2.3 Partial Oxidization of Ni-YSZ Anodes Inside the TGA

Fragments of the ASC-1 cells (180 to 220 mg, formed by sectioning pieces from the full disc specimen) were placed (electrolyte down) in a shallow 100 μL Pt crucible. For partial oxidation, as illustrated in Figure 3.5, samples were first heated to 600, 700, 800 or 900°C in 20% N_2-He at 5°C/min, and held in N_2 for 15 min while the temperature stabilized. H_2 (10% H_2 in He) was then switched on (and N_2 off) and held at temperature for up to 12 h to ensure full (≥ 99%) reduction. Samples were then exposed to 20% O_2-He (after a 10 min N_2 purge) for up to 20 min (the time of air exposure was chosen such that ~50% of the Ni in the anode would oxidize). The samples were then immediately cooled to room temperature at 7.5°C/min in 20% N_2-He for further analysis.

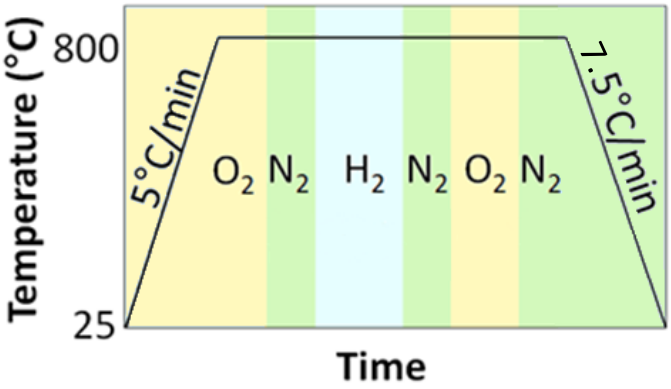

Figure 3.5. Thermal and gas environment profile used for partially oxidizing a Ni-YSZ anode in the TGA (shown for a partial oxidation at 800˚C). The time period of each gas cycle is contingent on the goals of the investigation, temperature and gas environment.

3.2.4 Pre-Oxidation Cycling Inside the TGA

Pre-oxidation (described in Chapter 5) cycling was carried out on fragments of the ASC-1 cells (180 to 220 mg, formed by sectioning pieces from the full disc specimen) that were placed electrolyte down in a shallow 100 μL Pt crucible. As illustrated in Figure 3.6, samples were first heated to 600 or 800°C in 20% N_2-He at 5°C/min and then held there for 15 min to allow the temperature to stabilize. The H_2 (10% H_2 in He) flow was switched on for up to 12 h to ensure full (> 99%) reduction of NiO. Samples were then exposed to 20% O_2-He (after a 10 min N_2 purge) for various time periods to achieve the controlled partial oxidation of the Ni component of the AFL and ASL. The samples were then immediately exposed to 20 or 50% N_2-He and cooled to room temperature at 7.5°C/min. After microscopic characterization, the cell was then re-inserted into the TGA and heated to 600 or 800°C, re-reduced, and then subjected to the next oxidation cycle.

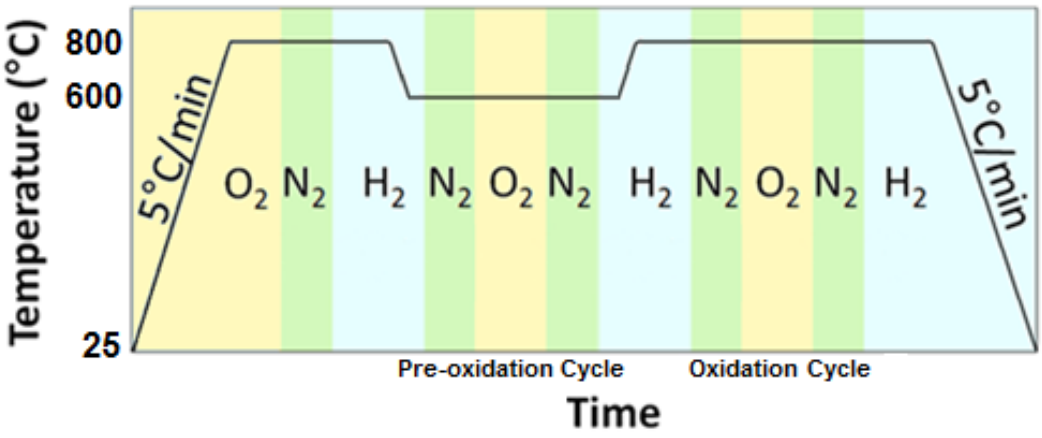

Figure 3.6. Thermal and gas environment profile used for a pre-oxidation cycle, followed by a full oxidation cycle of a Ni-YSZ anode in the TGA. The time period of each gas cycle is contingent on the goals of the investigation, temperature and gas environment.

3.2.5 In Operando TGA

All *in operando* reduction and oxidation cycles were carried out in a Setaram TAG 16 symmetrical balance (TGA), allowing the cell mass to be monitored while half-cell electrochemical testing was being carried out. The TGA required some modifications to allow *in operando* testing. The He (carrier gas) supply tubing was re-routed through a water bubbler, as was detailed in Section 3.2.1. In addition, a hanging module was designed to hold the cell upright while allowing the Pt wires and Pt mesh to be affixed to the electrodes for current collection. Figure 3.7 shows a photograph of a 1 x 1 cm, 200 μm thick 3YSZ electrolyte-supported cell that is seen suspended upright the Pt wires and the cell support stand of the hanging module. The Pt CE can be easily seen in the photograph (Ferro 4082 Pt paste) with a Pt mesh current collector

attached, while the Ni-YSZ electrodes is on the opposite side, also with a Pt mesh current collector affixed. A schematic diagram of the hanging module is also shown in Figure 3.7 to better illustrate the components in the apparatus.

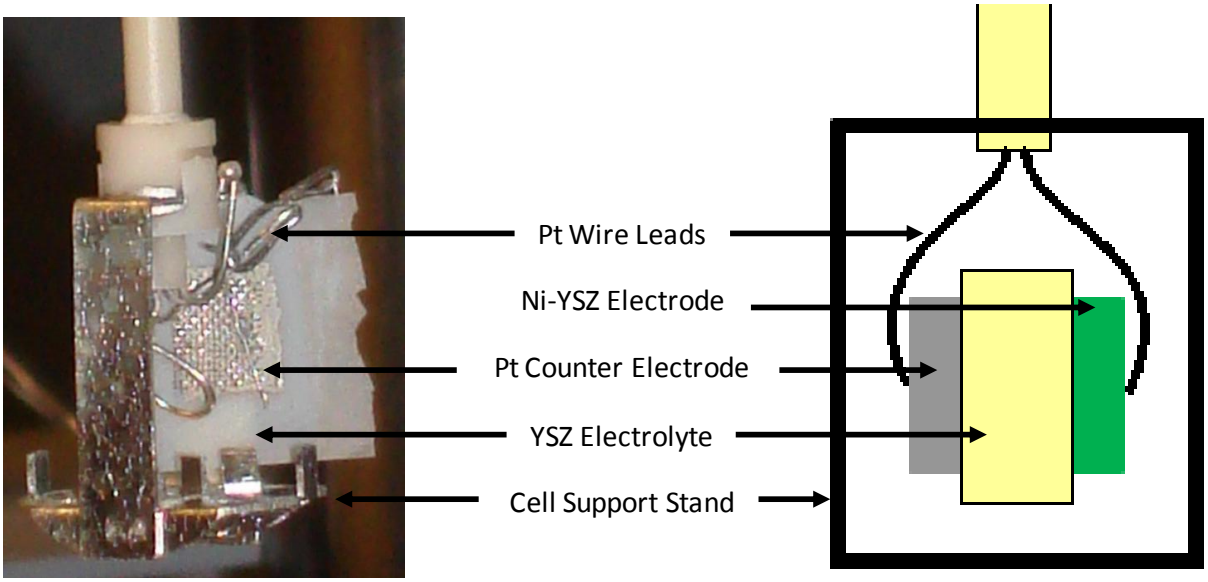

Figure 3.7. A photograph (left) and schematic diagram (right) of the setup used for 2-electrode half-cell studies for *in operando* TGA.

The ESC-1 cell, as described in Section 3.1.3, was first heated to 1000°C in air (in the TGA) to sinter the Pt paste so that the Pt current collector was bonded to the Pt leads. Samples were then cooled to inspect the contacts and then heated to 800°C in H_2 at 5°C/min and held there for 15 min to allow the temperature to stabilize. H_2 was switched on for 2 h, as shown in Figure 3, for NiO reduction and the baseline performance of the cell (EIS and CV) was determined, as described in Section 3.3.

The desired constant applied current or potential was then applied to the cell (Figure 3.8) and after 15 min, the furnace chamber was purged with N_2 for 30 min, exposed to air for 1 h, purged again (N_2) for 30 min, and then returned to the initial H_2 composition. The current or potential was then switched off and the new cell performance (EIS, CV) was measured for comparison with initial cell performance.

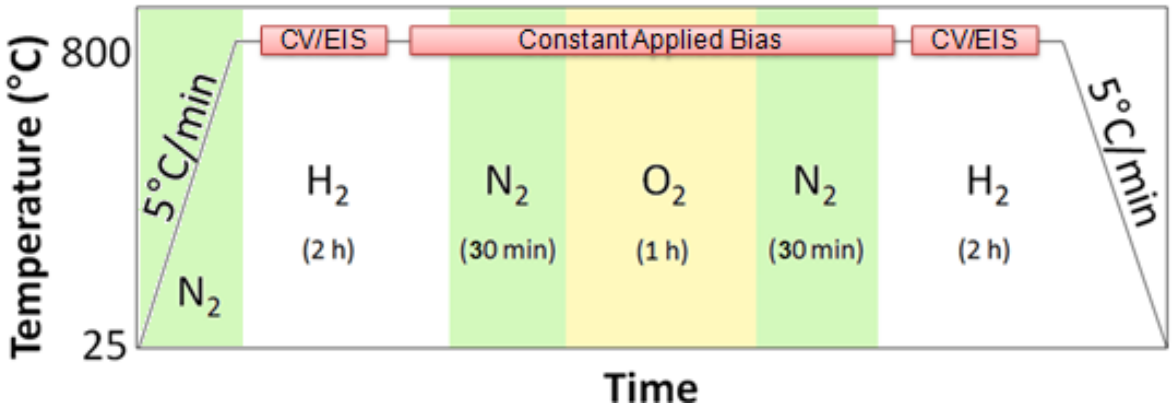

Figure 3.8. Temperature and gas environment profile used for reverse bias experiments (under both constant current and constant potential conditions).

3.2.5.1 *In Operando* TGA S-Poisoning Study

Once the NiO in the WE was fully reduced and the initial performance (EIS) of the ASC-1 cells were determined, H_2S was switched on and the poisoning cycle started. Poisoning cycles were carried out for up to 72 h, either at the OCP or with a 1 V anodic bias applied to the WE. Following the 65 h poisoning cycle, normal reducing conditions (H_2) were continued for 24 h at the OCP in order to clear the supply lines of H_2S. The electrochemical performance of the "poisoned" cell was determined (EIS), an oxidation cycle was then carried out (Figure 3.9),

whereby a cathodic potential of -4 V was applied to the Ni-YSZ WE, and then the oxidation cycle was commenced. After a N_2 purge for 30 min, samples were then exposed to air for 1 h, purged again, and then returned to a H_2 environment (Figure 3.9) following another purge. The constant current or potential was then stopped and the new baseline performance (EIS) was measured and compared with the initial and poisoned performance of the cell.

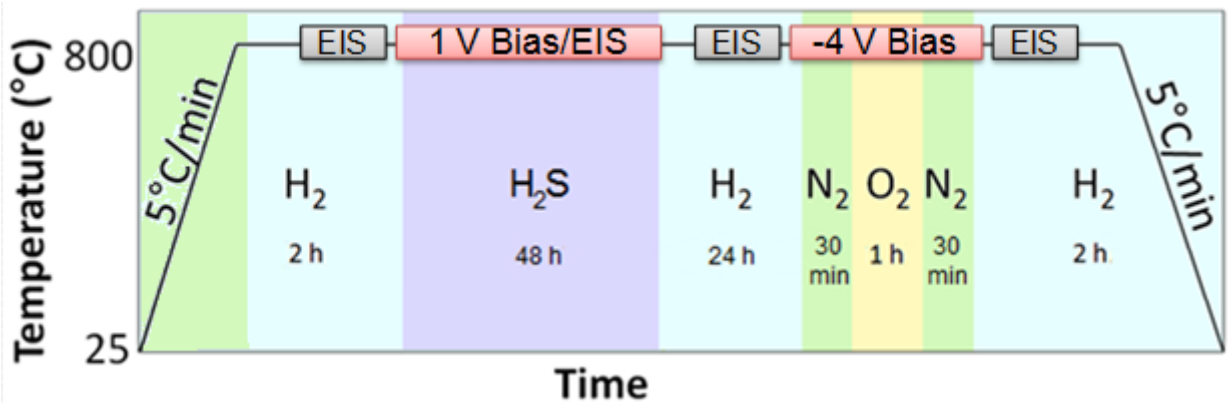

Figure 3.9. Temperature, gas environment profile and biases applied to the Ni-YSZ WE during S-poisoning and reverse bias experiments.

3.3 Electrochemical Testing

EIS measurements were carried out using a Solartron 1255 frequency response analyzer coupled with a Solartron 1287 potentiostat. Data were collected using Corrware (Version 2.7a, Scribner Associates) and Zplot software (Version 2.8, Scribner Associates). The applied frequency range was typically 0.1 Hz to 100 kHz. Measurements were obtained by scanning from high to low frequencies and vice-versa to ensure that there was no drift in activity of the

electrode material over time. A polarization amplitude of 10 mV was employed at the OCP all vs. the CE (2-electrode half-cell configuration). The EIS data were analyzed and fitted using Zview software (Version 2.4a, Scribner Associates).

Cyclic voltammetry (CV) experiments were carried out using a Solartron 1287 potentiostat, with control and data collection achieved using Corrware software (Version 2.7a, Scribner Associates) and imaging/data analysis achieved using Corrview software (Version 3.0, Scribner Associates). CVs were collected at 10 $mV \cdot s^{-1}$ using a maximum non-IR corrected potential range of -2 to +2 V.

3.4 Characterization

3.4.1 SEM and Optical Analysis

Cell imaging was carried out using a Nikon OPTIPHOT metallurgical microscope (uncoated sample) or a Philips FEI XL-30 environmental scanning electron microscope (SEM, 20 kV, 10 mm working distance) in vacuum mode (gold-coated). Cross-sections of the cell were prepared by sectioning (with a diamond saw or by simply breaking the sample) and then affixing the cell perpendicular to a stub covered with double-sided carbon tape so that the fresh break was facing upwards. Alternatively, the samples were mounted in epoxy with the fresh break facing upwards, followed by polishing (320 and 600 grit emery paper 3 μm diamond paste and then 0.01 μm alumina suspension).

3.4.2 XPS Analysis

A Physical Electronics PHI VersaProbe 5000-XPS (X-ray photoelectron spectroscopy) instrument was used to record the XPS spectra. The spectra were collected using a

monochromatic Al source (1486.6 eV) with a beam diameter of 200.0 μm. The binding energies were reported relative to the C1s peak at 285 eV. All samples were mounted after full oxidation without further treatment and pumped down from atmospheric pressure to ultrahigh vacuum (10^{-10} Torr). A wide energy survey was carried out (0 to 1400 eV) using a 187 eV pass energy to identify and quantify all the elements in the sample. A narrow energy spectrum (10 to 30 eV) was then acquired with a pass energy of 23 eV (for improved energy resolution) to determine the chemical state of the elements in the sample.

ASC-1 samples were analyzed with this technique to determine the relative amount of NiO ejected out of the outer anode-air interface (bottom up in Figure 3.1) in Chapter 5. Cross-sections of ASC-1 samples that were partially oxidized (Chapter 4) were also analyzed with XPS to provide additional evidence of NiO in the inner low NiO content region of the cell cross-section (into the page in Figure 3.1) to confirm results of the Raman analysis in Chapter 6. The epoxy mounted samples (used in Chapter 4) were re-polished (0.01 μm alumina) to remove the Au coating prior to XPS. The area of the most intense peak for each element was divided by the element-specific sensitivity factor, and normalized to 100% to obtain the normalized at% for each of the elements present in the sample.

3.4.3 Raman Spectroscopy Analysis

Raman spectroscopy was then carried out on the cross-sections of ASC-1 using a Renishaw RM-2000 CCD spectrometer (Blackett Labs, Department of Physics, Imperial College London). A 514 nm wavelength laser was used for the analyses and integration times varied between 1 and 10 s with both a 20X and 50X objective lens used for the preliminary surface analysis. ASC-1 samples that were characterized by SEM in Chapter 4 were analyzed with

Raman Spectroscopy in Chapter 6 to provide a quantitative representation through the thickness of a cell cross-section (into the page in Figure 3.1). The epoxy mounted samples (used in Chapter 4) were re-polished (0.01 μm alumina) to remove the Au coating prior to Raman spectroscopy analysis.

For the purpose of mapping of the anode layer NiO composition through the 1 mm anode thickness, one Raman spectrum was acquired at 5 μm intervals laterally across the anode, using a 1 s integration time and a 20X objective lens that resulted in a 2.5 μm diameter spot size. Spectra were collected from the epoxy mounted samples (in air, at room temperature) in raster mode over an area of 200 μm × 1200 μm, which was split into 10 lines with a 20 μm spacing between them. As a result, over 2000 spectra were collected throughout the cross-section of each sample. The areas that were analyzed (2.5 μm spot size, 5 μm spacing, and 20 μm between raster lines) did not overlap, with each sample map requiring > 2 h to acquire.

3.5 Error Analysis

The TGA instrument used for this study has a high precision (± 2 μg) due to the use of a symmetrical furnace chamber and a dummy hanger. The use of a symmetrical TGA prevents large perturbations during gas buoyancy changes, thus allowing precise measurements to continue even during gas environment changes. The temperature calibration of the TGA was carried out using the melting points of certified pure metals (In, Zn, Al, Au and Pd) and was checked periodically with Al (the metal with the melting point closest to the temperatures used in these experiments). Errors in the mass measurements could also theoretically arise from the presence of more than one Ni oxidation state. All experiments were carried out with multiple trials to increase data reproducibility. The gas composition was measured with a rotameter

(supplied by and calibrated by Setaram Instrumentation, Inc.) and has an error of 0.5 $ml \cdot min^{-1}$, which results in high errors when low flow-rates were used.

Errors resulting from the measurement of the current and potential values were estimated to be within ± 0.2%, while the frequency response analyzers has a 10 μHz frequency resolution, with ± 1% error in the DC bias. Errors were also introduced in the data analysis and fitting process. The error in fitting of EIS data is estimated to be ± 5% for most low frequency arcs, and up to ± 30% for high frequency arcs.

Errors can arise in microscopy, related to the difference in volume occupied by Ni and NiO and in quantifying concentric spheres, as was discussed in Section 2.7.1. Errors arising from SEM analysis are related primarily to the magnification (~1%) (133) and to "artifacts" in the surface of the sample that can distort what is seen (118). For example, an artifact can arise when a fresh break is made in a sample, as it will likely fracture preferentially through the weakest material, giving the impression that one element is more prevalent than it really is. By polishing, this error can be removed. However, in the case of a fully reduced Ni-YSZ anode, for example, Ni, which is relatively soft, can smear across the sample and deposit in a different location. This would give the appearance that Ni surrounds the YSZ, which will not move around because of its relative rigidity. To avoid these artifacts, a low viscosity epoxy was used, which can penetrate into the pores better.

Errors can arise in XPS analysis due to low signal to noise ratios when element concentrations are low, a low accuracy of relative sensitivity factors, a low accuracy of the correction for the electron transmission function, surface volume homogeneity, a low accuracy of the correction factor for energy dependence of the electron mean free path, and the degree of sample degradation due to analysis. Overall, the accuracy of XPS results can be affected by

many processes, resulting in errors that are typically 5 to 10 at%, depending on the signal to noise ratio (121; 134; 135). This agrees well with the Versaprobe manual (136) provided by Physical Electronics, which states that "the error in quantification is about 1:2 (± 0.1) is included when a molar ratio of 1:2 is obtained".

When using Raman spectroscopy to quantitatively analyze materials, there are several sources of error, including differing scattering efficiencies for different species, contaminated calibration standards, poor spatial resolution (i.e., a defocussed beam if the sample is not flat), and a small sample area for heterogeneous samples (137). As with XPS analysis, discussed in Section 3.4.2, peak fitting (or deconvolution) can be subject to errors of 5 to 10% when the signal to noise ratio is good, but samples without a high signal to noise ratio can result in errors of < 10% if the data are smoothed prior to peak fitting (138).

Chapter Four: **Crack severity in Relation to Non-Homogeneous Ni Oxidation in Anode-Supported Solid Oxide Fuel Cells**[*]

4.1 Introduction

It was noted in early studies (74; 139) involving full redox cycles of Ni-YSZ anodes (100% of the Ni was oxidized and reduced) that the extent of degradation was less (fewer cracks and narrower crack widths) at lower (600˚C) vs. higher (800˚C) oxidation temperatures. Changes in internal stress within the anode layer are therefore likely playing a role in the observed degradation. It was uncertain, however, if thermal effects (thermal shock and creep) were playing an important role and whether a highly porous (ca. 38%) anode support layer, deposited on top of a less porous (30%) anode functional layer would be equally susceptible to redox cycling damage. In this chapter, a careful thermogravimetric analysis (TGA) study was therefore carried out, comparing the mass gain vs. time data with scanning electron and optical microscopy observations. The primary goal was to better understand the mechanism of Ni-YSZ oxidation as a function of the air exposure temperature so that future degradation of anode supported cells could be minimized.

4.2 Experimental Methods

For the purpose of the work in this chapter, ASC-1 and ASC-2 cells were used, as described in Sections 3.1.1 and 3.1.2, respectively. All redox cycles were carried out in a TGA,

[*] Published as J.L. Young and V.I. Birss, Journal of Power Sources, 196, 2011, 7126-7135, although the abstract, introduction, and experimental sections have been removed.

as detailed in Section 3.2, while Section 3.4.1 describes the surface analysis that was carried out by SEM and optical microscopy in this work.

4.3 Results and Discussion

4.3.1 TGA Study of Ni-YSZ Anode Oxidation During Multiple Redox Cycles

The TGA oxidation profiles of newly manufactured 13 mm ASC-2 button cells that were isothermally oxidized and reduced at 700 and 800°C in 5 successive full redox cycles are shown in Figure 4.1A and B, respectively. The data have been normalized to the theoretical mass of oxygen (12.1%) in NiO in a fully oxidized NiO-YSZ anode. It should be noted that the apparently incomplete oxidation in Ox 1 after long times at all temperatures arises from the incomplete NiO reduction in the first reduction cycle (not shown, as summarized in Table 4.1). In fact, the anode is fully oxidized after the completion of each subsequent oxidation step in Figure 4.1. Figure 4.1 also shows that, as expected, it takes longer to completely oxidize the Ni-YSZ anodes at lower temperatures. Further, at 700°C (Figure 4.1A), it takes the same amount of time to oxidize 75% of the sample in all 5 cycles, while at 800°C (Figure 4.1B), the oxidation process becomes more rapid with each cycle until the fifth cycle, when the mass gain/time curves begin to overlap.

To explain the changes in the TGA mass/time profiles with cycling time, the Ni morphology was examined by SEM, as shown in Figure 4.2 for the first and fifth full reduction steps at 700°C (Figure 4.2A and B, respectively) and at 800°C (Figure 4.2C and D, respectively). The atypically large agglomerates seen in Figure 4.2 show that the Ni grains (within the agglomerates) have increased in size (from ~0.5 μm in the as-reduced sample to ~0.75 μm after redox cycling). Additionally, the Ni grains are more spheroidized and some nanocrystallites of

Ni have appeared on the surface of the Ni agglomerates after redox cycling. At 700°C, the grains are more coherent, due to slightly less sintering than at 800°C, although the differences are not dramatic. Overall, the Ni morphology does not change significantly after 5 full redox cycles at 700°C (Figure 4.2). Therefore, despite large changes in the oxidation rates with cycle number in Figure 4.1, at least at 800°C (Figure 4.1B), changes in the Ni morphology likely do not contribute to the differences in the mass/time profiles. It will be shown below that the increased Ni oxidation rate with multiple redox cycling is more likely due to O_2 penetration into the inner anode regions through cracks that develop in the YSZ electrolyte, especially at higher oxidation temperatures.

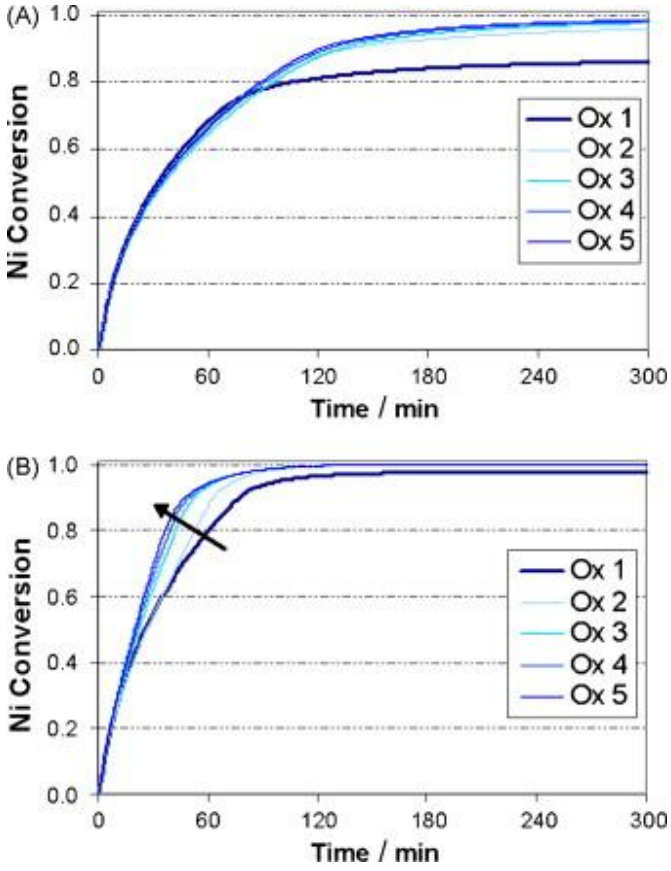

Figure 4.1. Thermogravimetric analysis data in successive Ni-YSZ full oxidation steps during redox cycling of an ASC-2 cell (Figure 3.4) at (A) 700°C and (B) 800°C.

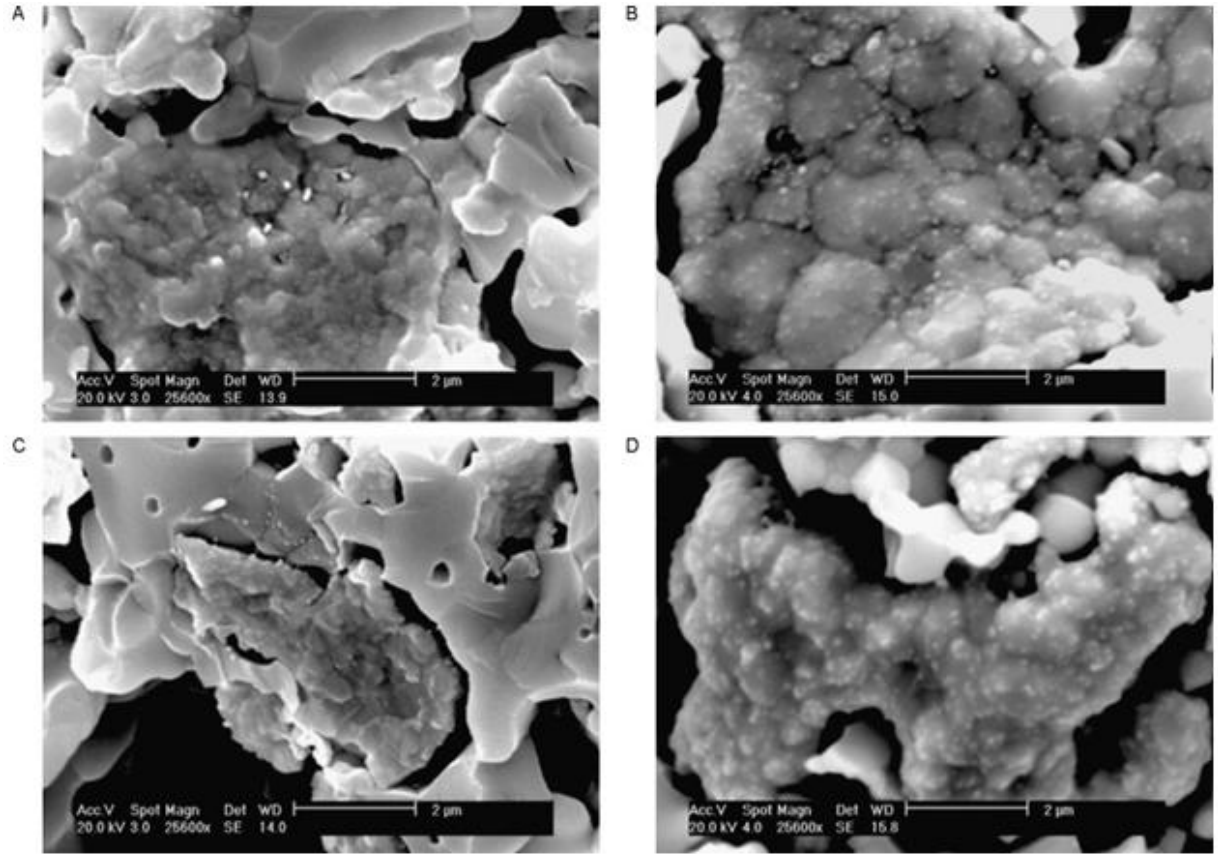

Figure 4.2. SEM micrographs of Ni-YSZ in the anode-support layer of an ASC-2 cell in a fully reduced state after (A) first reduction at 700°C, (B) 5 redox cycles at 700°C, (C) first reduction at 800°C, and (D) 5 redox cycles at 800°C.

4.3.2 Effect of Redox Cycling Temperature on Fully and Partially Oxidized Ni-YSZ Anodes

Optical microscopy and SEM analysis were used to establish the effect of the temperature at which Ni-YSZ anodes were both fully and partially oxidized on the resulting degree of crack damage. The exposed surface of the electrolyte layer of ASC-1 cells (Figure 3.1A), the Ni-YSZ

layer on the cathode side of ASC-2 cells (Figure 3.1B), as well as cross-sections of both cell types, were examined to determine the extent and type of cracking observed (Table 5.1).

Table 4.1. Extent of NiO-YSZ reduction at various stages of TGA analysis (from Figure 4.1).

Temperature (°C)	Completion of linear reduction region (%)[1]	Extent of NiO reduction (%) and time required[#]	Completion of linear reduction region (%)[*]	Extent of NiO reduction (%) and time required[*]
650	12	83 (10 h)	48	95 (10 h)
700	25	86 (10 h)	58	99 (10 h)
750	37	88 (8 h)	67	99.5 (6 h)
800	50	98 (4 h)	75	100 (4 h)

[#] In first redox cycle.
[*] In subsequent redox cycles.

In the first set of experiments, all of the anodes were fully oxidized, but at different temperatures (600-900°C). The impact of temperature was found to be quite extreme, as shown by SEM analysis in Figure 4.3A-D after oxidation at 900-600°C, respectively, and as also summarized in Table 4.2. Severe cracks were observed after full oxidation at >700°C (Figure 4.3A and B), while at temperatures below this (Figure 4.3C and D), the degree of cracking of the electrolyte was much less extensive, similar to what has been reported previously (139).

In Figure 4.3A and B, the ASC-1 cells subjected to 2 full redox cycles at 900 and 800°C, respectively, also show “buckling” of the electrolyte surface, where it appears that entire electrolyte fragments have been pushed out from the electrolyte plane. The associated severe

electrolyte cracking would likely then allow O_2 to access the anode through the electrolyte side of the cell during redox cycling. This may then be responsible for the increase in oxidation rates seen with successive redox cycles in the TGA experiments at 800°C in Figure 4.1B. In contrast, the much less severe cracking (lower quantity and narrower cracks) seen at 700 and 600°C in Figure 4.3C and D would not allow significant O_2 to pass through to the anode, consistent with the relatively non-changing TGA mass/time profile with repeated redox cycles at 700°C in Figure 4.1A.

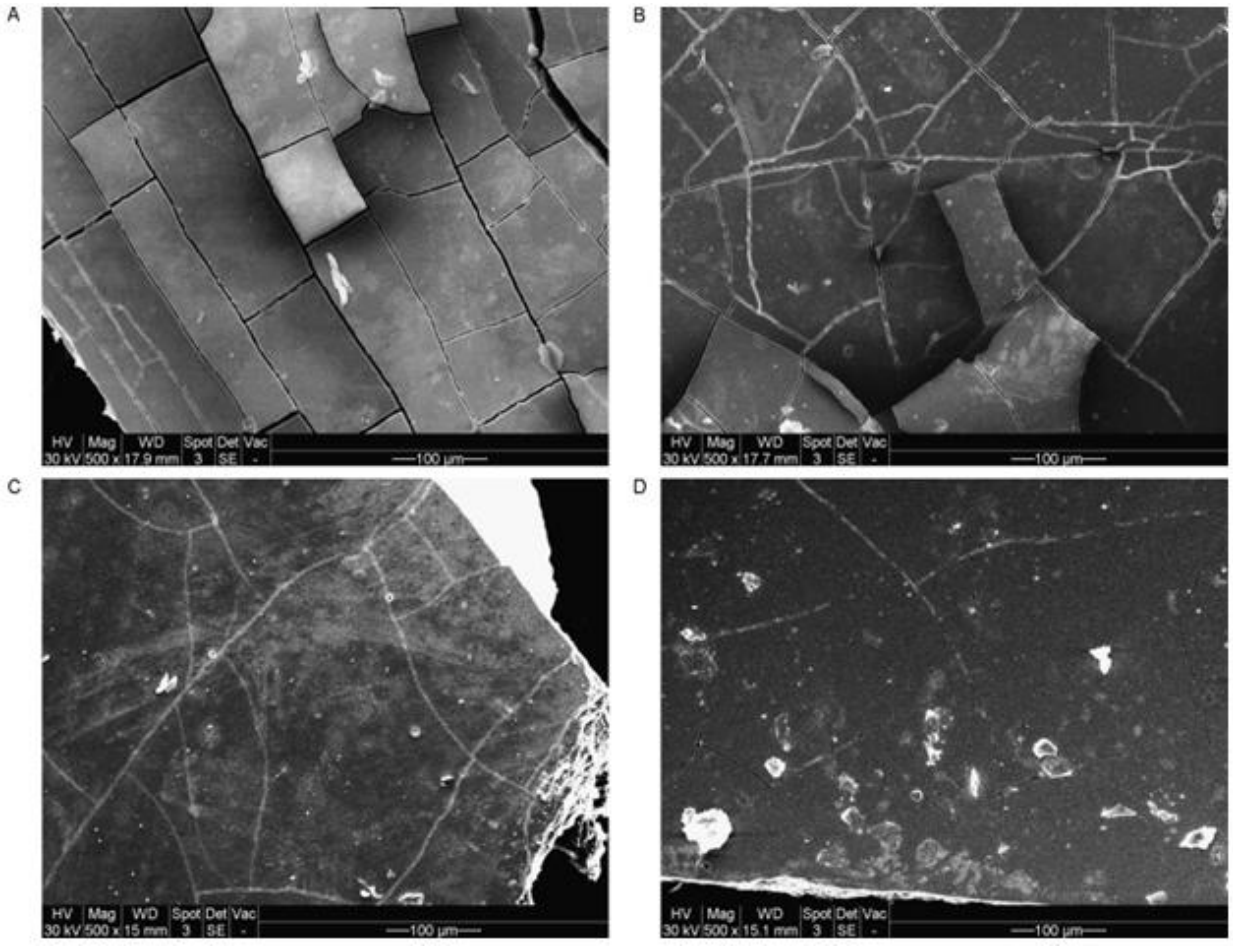

Figure 4.3 SEM images of the electrolyte of an ASC-1 cell, showing the cracks that form after 2 full redox cycles at (A) 900°C, (B) 800°C, (C) 700°C, and (D) 600°C.

Table 4.2. Cracking observed in ASC-2 cells after 5 redox cycles at various temperatures.

Temperature (°C)	Electrolyte cracks·mm^{-1} (from cross-section)[#]	Cracks penetrating AFL[*] (ASC-2 cells only)	Parallel edge cracks (Figure 4.4, 20% pO_2)
650	4.5	No	No
700	6.5	Yes	No
750	13.2	Yes	Yes
800	18.5	Yes	Yes

[#] Cracks·mm^{-1} is the number of the cracks observed in the cross-section of the electrolyte (7-10 mm wide samples), as viewed by SEM.

[*] The presence of cracks through the AFL is an indication of the severity of cracking.

To better understand the differences in cracking seen at different temperatures (Figure 4.3), cells in which the anodes were only partially oxidized (≥50%) were also examined. At 800°C (Figure 4.4A), the first cracks to develop on the surface of the electrolyte after 61% of the Ni in an ASC-1 cell was oxidized at 800°C were seen by optical microscopy to be near, and parallel to, the cell edges (where air is able to easily penetrate the porous anode region, especially adjacent to the electrolyte). With further oxidation (to 73%), cracks perpendicular to the cell edge develop, with some propagating to the middle of the cell, as shown in Figure 4.4B. As the cell was oxidized still further, an increasing number of cracks propagated to the middle of

the cell until a maximum was reached at ~90% oxidation (Figure 4.4C), very similar to the 100% oxidized sample (Figure 4.4D).

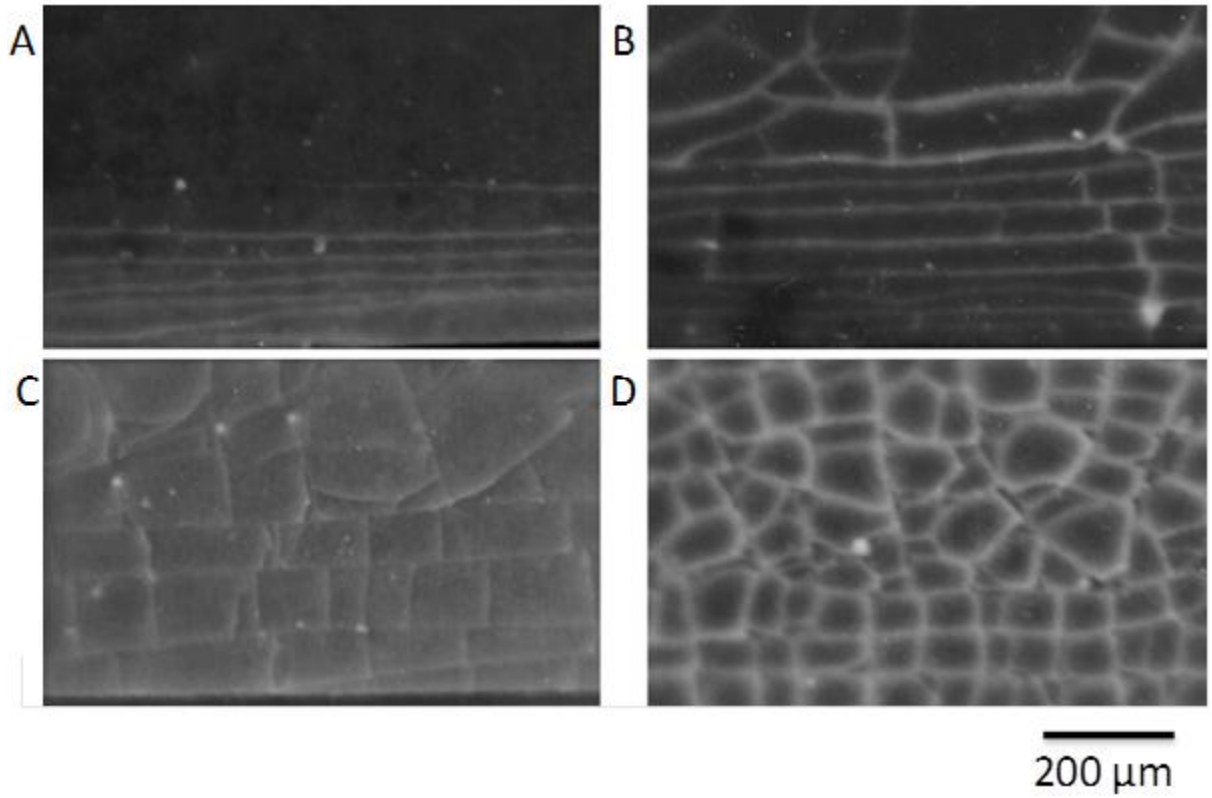

Figure 4.4. Optical microscopy images (20× magnification) of electrolyte cracks after 5 redox cycles of an ASC-1 cell when the cell was partially oxidized at 800°C to (A) 61%, (B) 73%, (C) 90% and (D) 100% of the total Ni in the anode layer.

The development of cracks was seen to be very different at temperatures ≤700°C, with no cracks seen parallel to the edges of the cell (as in Figure 4.4A) and only cracks that randomly propagate across the electrolyte observed after oxidizing more than 80% of the Ni in the anode. Thus, there is a clear transition in the character of Ni oxidation between 700 and 750°C, below

which the parallel cracks do not occur and above which they do. This also correlates with the transition between minor and severe cracking (in terms of crack width and electrolyte buckling), as seen in Figure 4.3.

Anode layers that were only 50% oxidized, but at different temperatures, were then closely examined by SEM analysis. Figure 4.5A and B, involving samples that were oxidized to 50% NiO at 900 and 800°C, respectively, show a compilation of backscattered electron (BSE) images along the entire thickness of the anode layer. These demonstrate that NiO (grey) is highly prevalent in the outer half of the anode layer, but that Ni (white, and indistinguishable from YSZ) is dominant in the inner (electrolyte side) half of the anode. In Figure 4.5C, at 700°C, however, this gradient in the NiO/Ni content is much less clear, and at 600°C (Figure 4.5D), Ni appears to be oxidized homogeneously throughout the entire anode-support layer.

Thus, these results show clearly that a gradient in the Ni/NiO composition of the anode layer (and hence in the Ni oxidation rate), seen here after partial oxidation at 800°C, correlates with extensive electrolyte cracking for both partially and fully oxidized cells. The pronounced gradient in composition at 800°C was also predicted by the linear TGA mass/time data at this temperature in Figure 4.1B, indicative of mass transport controlled conditions (and related gradients in the O_2 concentration) during Ni oxidation.

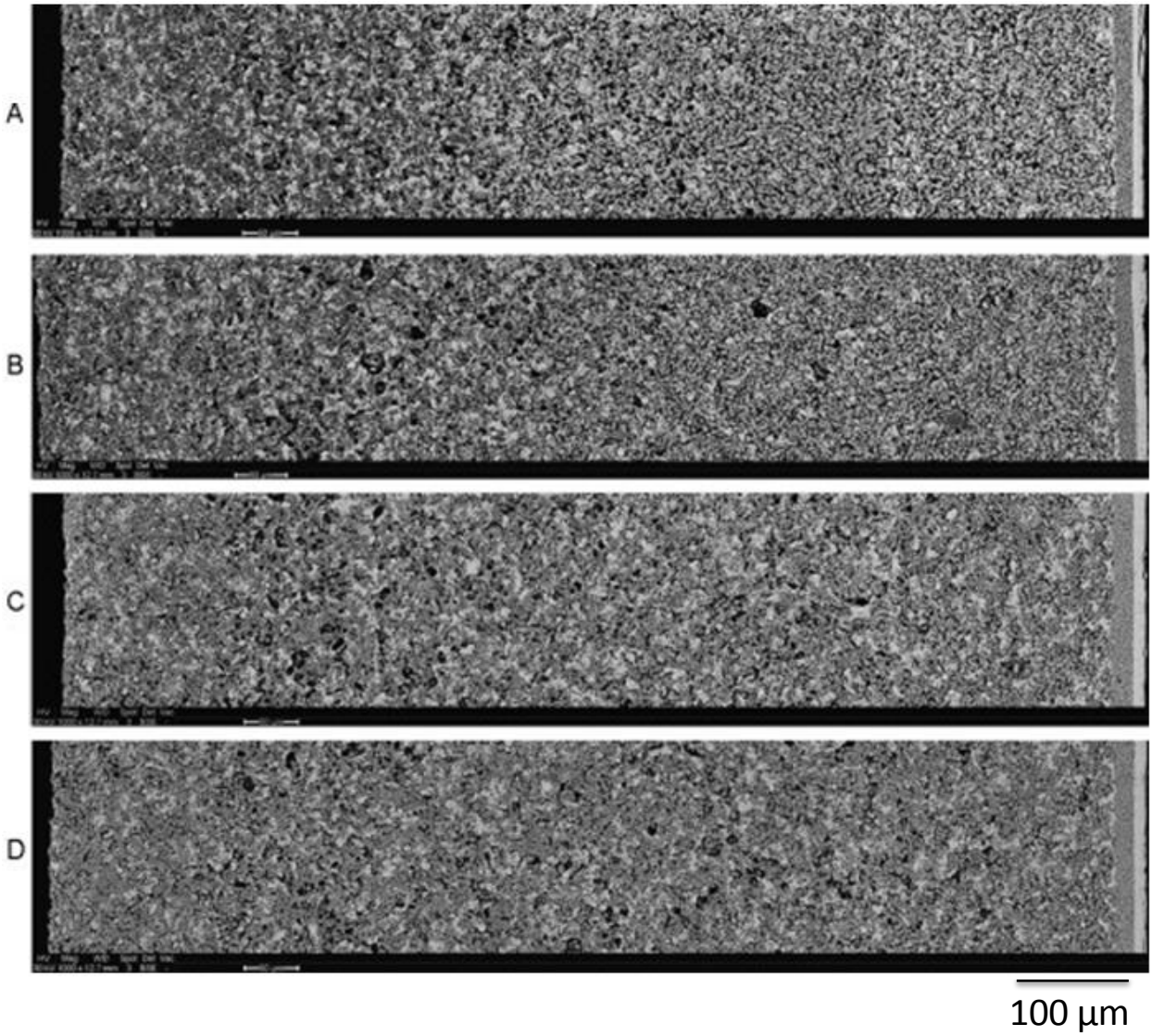

Figure 4.5. Compilations of SEM BSE images of an ASC-1 cell partially oxidized (~50%) at (A) 900°C, (B) 800°C, (C) 700°C and (D) 600°C. NiO is dark grey, while Ni and YSZ are both white and thus indistinguishable. At high temperatures (>700°C), NiO is the dominant phase near the anode/air interface (left), while adjacent to the electrolyte (right), Ni and YSZ are the major phases present. At lower temperatures (≤700°C), NiO is much more evenly distributed throughout the anode layer cross-section. Gamma settings have been altered to enhance contrast between phases.

4.3.3 Effect of Variable pO_2 on Electrolyte Cracking Due to Redox Cycling: Further Evidence for Impact of Graded NiO Content

In order to test the hypothesis that a graded NiO content, formed in the porous Ni-YSZ anode layer during redox cycling, exacerbates the severity of cracking, and that thermal shock or high temperature creep (98) are not responsible for cracking, a variable pO_2 was used for redox cycling of fresh fragments of ASC-1 samples at 800°C. Figure 4.6 shows the TGA results obtained during the first and fifth oxidation steps at normal O_2 concentrations (~20% O_2-He), higher pO_2 (~50% O_2-He), and very low O_2 concentrations (~0.1% O_2-He). Based on the linear mass/time profile at low pO_2 (Figure 4.6), it is clear that O_2 is reacting with Ni as quickly as it enters the pore structure. Analogous to the 800°C data in Figure 4.1, the low pO_2 data in Figure 4.6 predict that extreme O_2 and NiO/Ni concentration gradients should be present and that cracking should be severe. In contrast, at 20 and 50% O_2, there is more evidence for parabolic mass/time behavior (Figure 4.6), and thus less cracking damage would be expected.

Indeed, after 5 full redox cycles, the severity of the damage to the cell was found to be the most significant at the lowest pO_2. While it would be tempting to attribute the degradation to the much longer time at temperature after 5 redox cycles, most of the degradation in low pO_2 environments occurred after the first cycle, while a cell exposed to 5 cycles under 20% pO_2 is exposed to oxygen over a much longer time period. The cracks are large, deep and visible to the eye (Figure 4.7A), as compared to the case in 20 and 50% O_2 (Figure 4.7B and C, respectively). Cracks in the electrolyte parallel to the edge of the cell (similar to Figure 4.4A) were noted. Additionally, at the lowest pO_2, the cell became warped (convex to the electrolyte) after 5 full redox cycles in the TGA. This result is very similar to what was observed by Stathis et al. (70), who oxidized a Ni-YSZ anode using only steam (at a low pO_2). The reaction rate was linear with

time during oxidation in their case as well, corroborating that, at low pO_2, the reactant is quickly exhausted as it enters the porous anode layer, thus leading to significant internal concentration gradients. At 20 and 50% O_2, the degradation is much less severe than at low pO_2. At 50% O_2 (Figure 4.7C), the cracks are the narrowest, and there are no parallel cracks seen on the electrolyte at the edges of the cell.

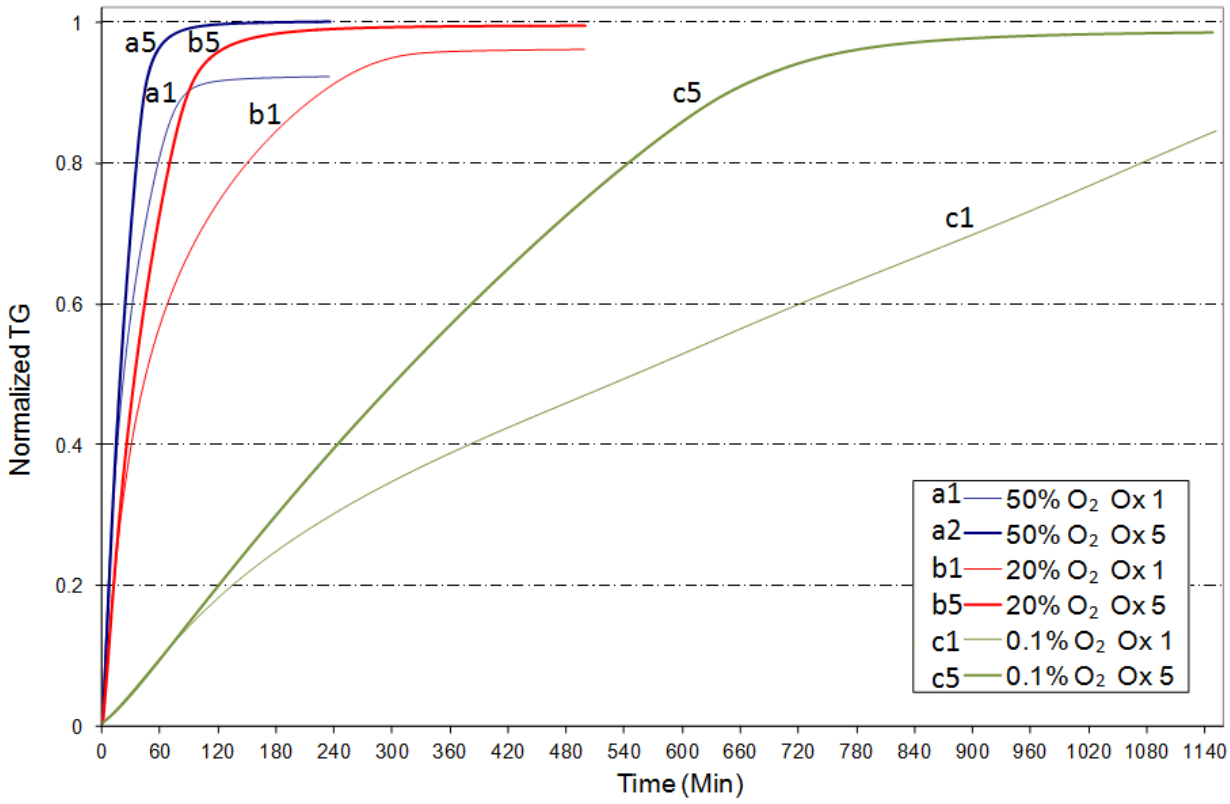

Figure 4.6. Measured mass gain of Ni-YSZ anode at 800°C in a fresh ASC-1 cell (a1, b1 and c1) and in the fifth oxidation cycle (a5, b5 and c5) during oxidation in (a1 and a5) 50% O_2-He, (b1 and b5) 20% O_2-He and (c1 and c5) 0.1% O_2-He.

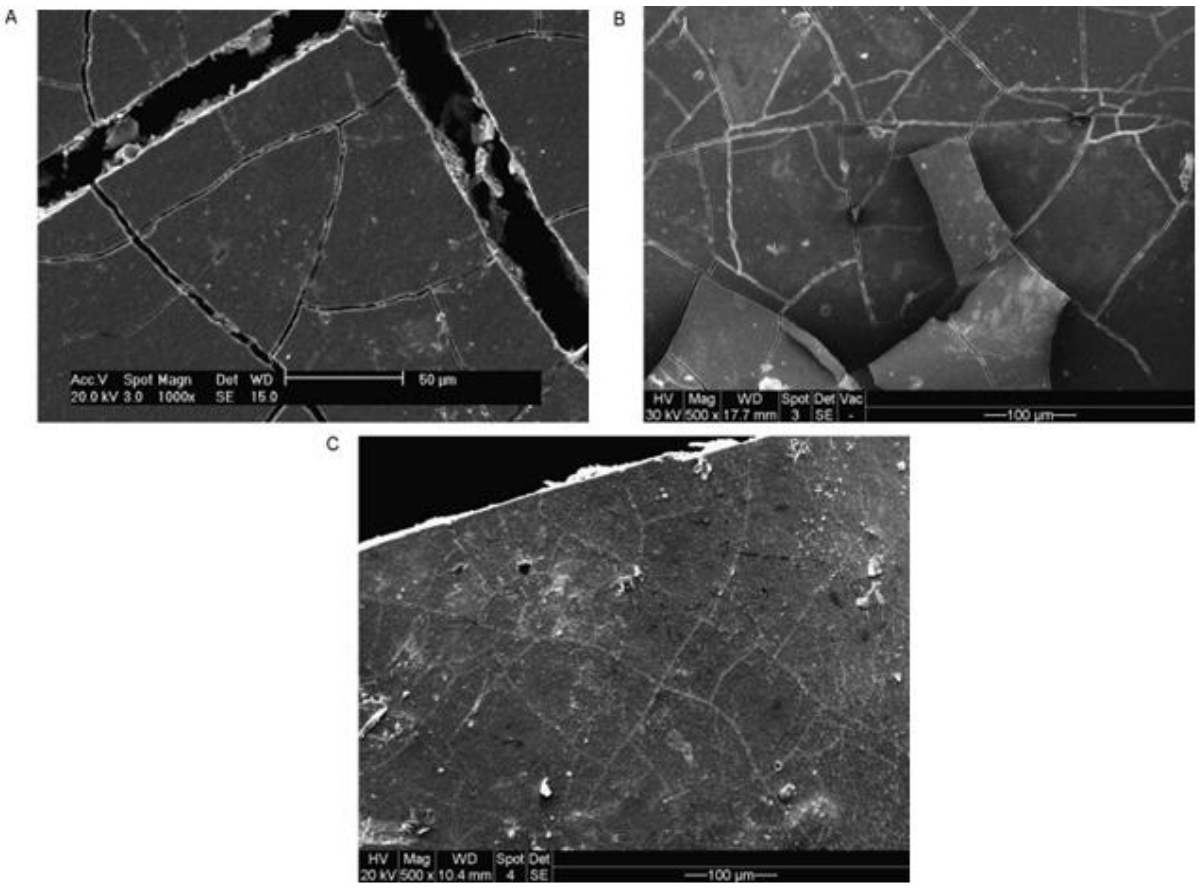

Figure 4.7. SEM (secondary electron) images of the electrolyte of an ASC-1 cell after full oxidation at 800°C in (A) 0.1% O_2-He, (B) 20% O_2-He and (C) 50% O_2-He.

To further verify that the presence of gradients in the NiO and Ni content of the anode layers correlates with the severity of degradation observed, 50 ± 5% of the Ni in the anode was oxidized in a 0.1, 20 and 50% O_2 environment at 800°C and then oxidation was stopped in each case. Figure 4.8 shows the cross-sectional compilation images, demonstrating the presence of a significant gradient in the NiO and Ni content in the anode at the lowest O_2 concentration (Figure 4.8A), but much less so after oxidation in 20% (Figure 4.8B) and 50% O_2 (Figure 4.8C).

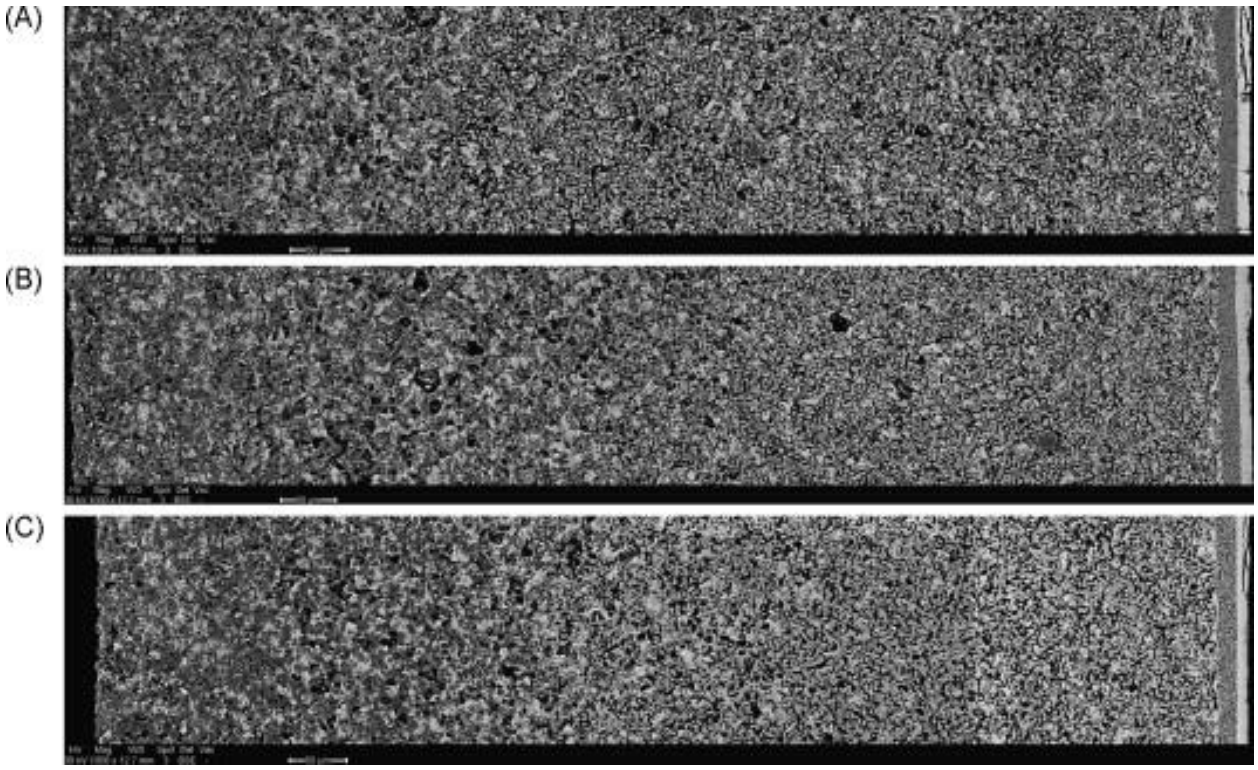

Figure 4.8. SEM backscattered electron compilation images of the anode layer of an ASC-1 cell in which the Ni phase was ~50% oxidized at 800°C in (A) 0.1% O_2-He, (B) 20% O_2-He and (C) 50% O_2-He, showing the non-isotropic distribution of NiO (dark grey) formation through the anode layer. Gamma settings have been altered to enhance contrast between phases.

Higher magnification SEM images of the outer region of the ASL (near the ASL/air interface) of each of the 50% oxidized anode are shown in Figure 4.9, indicating that, at low pO_2 (Figure 4.9A), the Ni particles in this region have been completely converted to NiO. In 20% O_2 (Figure 4.9B), Ni is seen in the core of some of the NiO particles, while at 50% O_2, Ni (surrounded by dark regions of NiO) is seen to be quite abundant in this region of the anode.

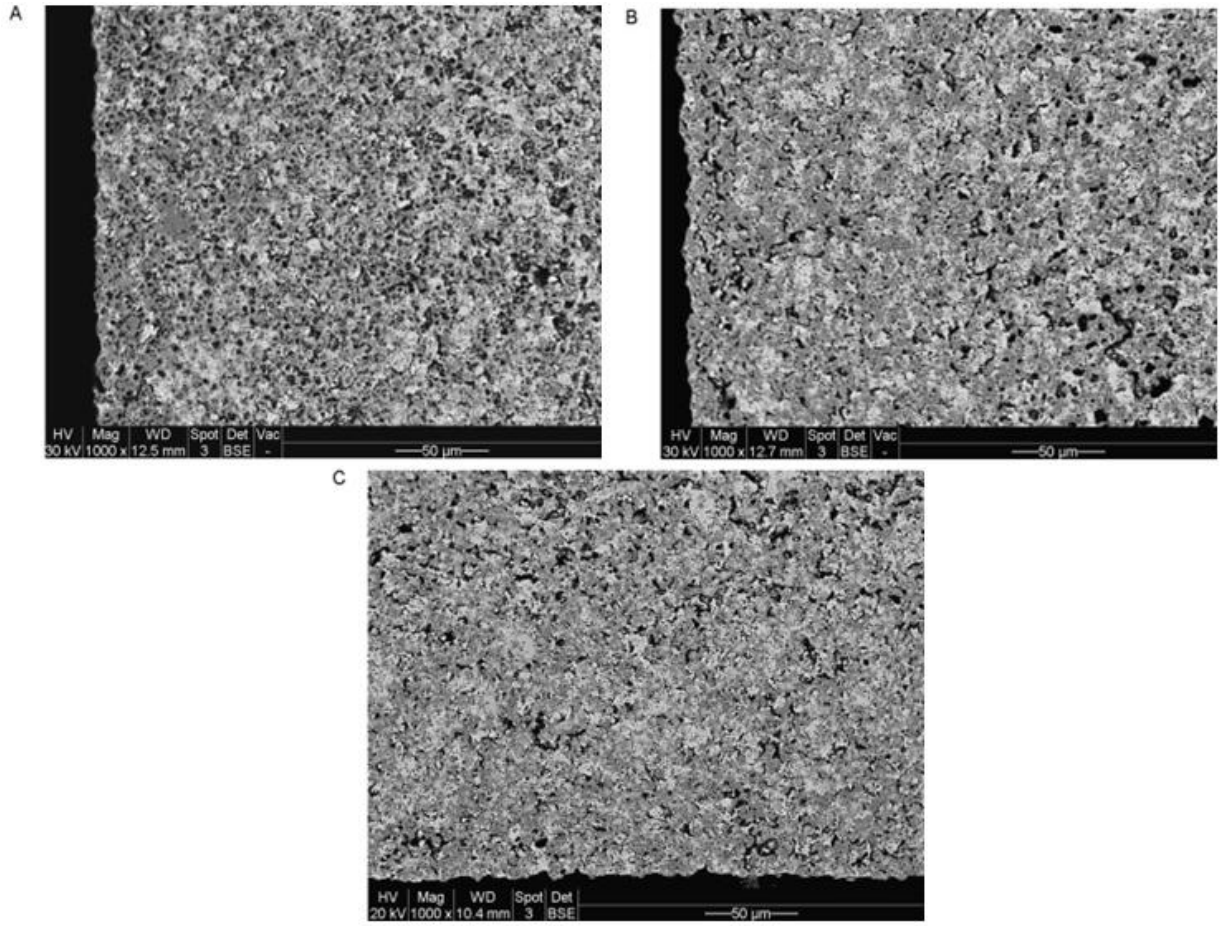

Figure 4.9. SEM backscattered electron images of the ASL cross-section at the outer edge (ASL/air interface) after oxidation of 50% of the Ni in (A) 0.1% O_2-He, (B) 20% O_2-He and (C) 50% O_2-He. The lightest shade of grey is YSZ, the darkest shade of grey is NiO, and the intermediate shade of grey (primarily observed in C) is Ni, seen to be surrounded by a dark grey NiO coating. Gamma settings have been altered to enhance contrast between phases.

Overall, it is clear that lowering the pO_2 results in a significant gradient in the NiO content in the anode layer when the anode is partially oxidized, as was also the case when the temperature of oxidation was increased. For example, the NiO gradient (Figure 4.5A) and the

extent of electrolyte cracking (Figure 4.3A) at 900°C and 20% O_2 is comparable to what is seen after exposure of the anode to a low pO_2 at 800°C. In both cases, the anode layers are highly oxidized in the outer regions of the anode (near the anode/air interface) and much less oxidized deeper in the anode, thus leading to similarly severe cracking. As was stated previously (139) and is confirmed here, the rate of permeation of air through the anode layer relative to the rate of Ni oxidation are the key factors determining whether Ni oxidation is isotropic or non-isotropic.

4.3.4 Model of Enhanced Degradation of Ni-YSZ Anodes Caused by Non-Isotropic Oxidation During Redox Cycling

The TGA oxidation data (Figure 4.1) demonstrated that the mass gain/time profile of anode-supported cells (Figure 3.4) is essentially linear at 800°C, but not at 700°C, suggesting that Ni oxidation is diffusion controlled at high temperatures (>700°C). This, in turn, implies that substantial O_2 concentration gradients, and hence NiO (and Ni) gradients, are present in the anode layer at the higher temperature conditions. In Section 4.3.2, these predictions were verified, with cross-sectional compilation images of partially oxidized anodes showing a distinct gradient in NiO content through the full thickness of the ASL at 800°C that was not as prevalent for anodes oxidized at 700°C. Importantly, anodes that were fully oxidized at higher temperature conditions showed significantly more severe electrolyte cracking (Figure 4.3). In Section 4.3.3, it was shown that lowering of the pO_2 also leads to mass transport controlled Ni oxidation, along with significantly increased cell degradation, with cross-sectional images of partially oxidized anodes confirming the presence of a gradient in the Ni and NiO content through the full thickness of the ASL.

The conclusion reached from these results is that the presence of a gradient in NiO content during anode oxidation exacerbates damage due to cell cracking. A similar conclusion was also reached by Ettler et al. (139), who investigated the redox stability of a 25 cm × 50 cm cell under varying cell temperature, direction of gas flow, and gas flow rate conditions. The mechanism for the increased degradation in the presence of NiO gradients was suggested (139) to involve the development of a high compressive stress in the oxidized part of the anode, causing the cell to warp. This makes sense, as the direction of warp was concave to the electrolyte, while the present results, and those in other studies (70), show that warping is convex to the electrolyte surface.

Other explanations for the increased cracking severity when the Ni/NiO gradients are more pronounced include thermal shock (due to the rapid increase in local temperature) and thermal stress (due to thermal expansion of the hotter oxidizing region vs. the rest of the anode layer). Others have speculated that creep (98) is responsible for the damage caused by non-isotropic Ni oxidation during redox cycling, resulting from the increase in temperature during the exothermic Ni oxidation reaction. These mechanisms (thermal shock, thermal stress, and creep) all require a higher local temperature in the oxidizing regions of the anode. However, in the case of Ni oxidation at the lowest O_2 content studied here (0.1% O_2), the rate of oxidation is constant for the >14 h required to fully oxidize the anode (Figure 4.6). Therefore, the temperature increase (above 800°C) should be negligible and yet the degradation patterns are the same as what is seen at 900°C (parallel cracks starting at the edge of the cell, then propagating across the electrolyte and into the anode layer). In fact, the degradation observed at low pO_2 is the most severe of all, with cell warping and electrolyte cracks easily detected visually (Figure 4.7A). Thus, the results show that cell cracking results from stress build-up as a consequence of the presence of a NiO

concentration gradient (high concentration near air/anode interface and low near the anode/electrolyte interface) in the anode layer, rather than from thermal effects.

The following model, which links the extent of cracking with the presence of gradients in the Ni/NiO content into the depth of the anode layer, is therefore proposed. Considering the extreme case when Ni in the outer region of the anode layer (near the anode/air interface at the anode base and at the edges of the cell (Figure 4.4A)) becomes fully oxidized before O_2 penetrates further (e.g., at low pO_2 or at high temperatures), the outer region of the anode can relieve stress only by expanding into the most accessible pores deeper in the ASL. The NiO particles that form will then be rigidly fixed in place, since they will have filled the local pores. As the oxidation "front" proceeds deeper into the ASL with longer times of exposure to O_2, the newly formed NiO can only continue to grow in towards the electrolyte layer to reduce the stress. With increasingly fewer options available for Ni to NiO volume expansion as the oxidation front moves deeper, the stress increases in magnitude as the cell is oxidized further and, ultimately, can only be relieved by cracking the electrolyte. In extreme cases, the stress is very large and this leads to electrolyte warping and the propagation of cracks into the ASL.

Thus, it is suggested that, when the anode layer is homogeneously oxidized (no NiO concentration gradients present within the ASL, as during oxidation at high pO_2 and low temperatures), the stress that NiO formation causes within the anode layer is isotropic. Under these conditions, the expansion due to NiO growth will occur equally in all directions, resulting in NiO being ejected out of the anode layer at the ASL/air interface and into the anode layer's unoccupied pores. This, in turn, may prevent the formation of parallel cracks at the edges of the cell, since there would be a lower compressive force applying tension to the electrolyte.

SEM images of the anode/air interface should therefore provide an indication of how homogeneous Ni oxidation is through the anode layer. Figure 4.10A and B show that, as predicted, more NiO is ejected outwards at the ASL/air interface after oxidation in 50% O_2-He than what was observed at 20% O_2-He, respectively, both at 600°C. To compare the effect of the Ni oxidation temperature, Figure 4.10A and C show that more NiO protrudes at the ASL/air interface at 600 than at 800°C, respectively (both in 20% O_2), indicative of the less damaging and more homogeneous oxidation conditions within the ASL.

As the present experiments were carried out using a single anode-support layer morphology, the question arises as to how the cell cracking characteristics would be affected by a change in anode porosity. Ettler et al. (139) showed that, even when using a high porosity anode, the electrolyte continued to crack after a single redox cycle, although the quantity and characteristics of these cracks were not reported. In fact, it is expected that the effect of increased porosity would be similar to the impact of decreased operating temperature, since the gas transport to oxidation rate ratio will be diminished in both cases. Thus, parallel cracks should be less likely to occur and crack severity should be further reduced, all at constant temperature and pO_2.

For an operating SOFC stack, it has been speculated that air leakage may be quite slow during a redox event. Based on the present work, this is the worst possible scenario, as these conditions would be expected to significantly increase the gradient in NiO content in the anode layer, in turn increasing the extent of degradation. To prevent severe degradation to the cell, it should therefore be cooled to a temperature that will minimize the Ni/NiO gradients, e.g., below 700°C in atmospheric pO_2. As stated above, in a situation in which the outer regions of the anode are oxidized preferentially, and the inner regions remain metallic, a subsequent full oxidation of

the remaining (inner) Ni particles will result in severe mechanical stress and damage to the electrolyte. This, however, will only prevent electrolyte cracking until more than ~80% of the Ni is oxidized. Thus, the temperature of the cell should be lowered to below 500°C if the redox event is prolonged.

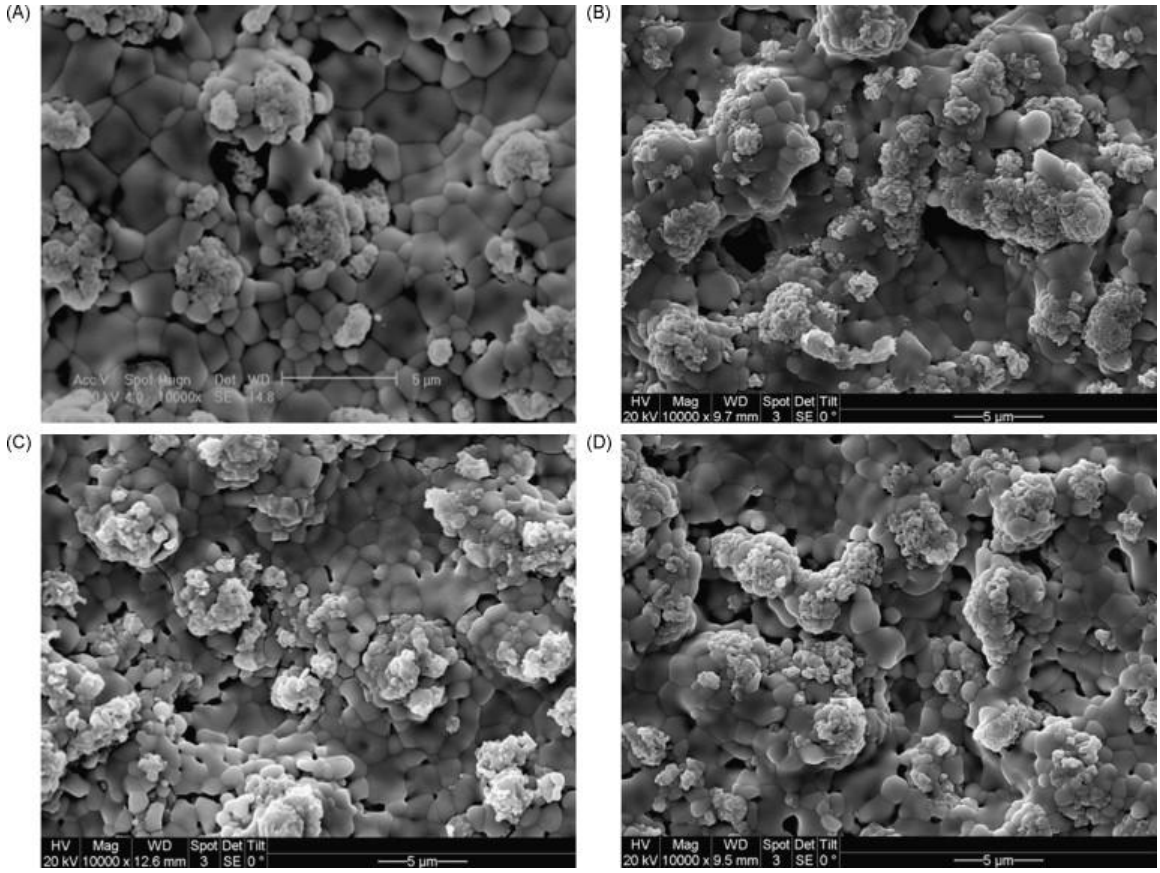

Figure 4.10. SEM secondary electron images of the base of the ASL (ASL/air interface) after full oxidation (1 cycle) at 600°C in (A) 20% O_2-He and (B) 50% O_2-He, and at 800°C in (C) 20% O_2-He and (D) 50% O_2-He.

4.4 Summary

In this work, it is shown that non-homogeneous oxidization of Ni-YSZ anode-support layers, which results from oxygen exposure at high temperatures, enhances the severity of electrolyte cracking. This is consistent with the thermal gravimetric analysis data, which demonstrated that, at higher temperatures (>700°C), the mass/time profiles are linear up to 90% oxidation after the first cycle. This indicates that gas diffusion in the pores is rate limiting, i.e., that O_2 is reacting as rapidly with Ni as it enters the pores of the anode. Under these conditions, a concentration gradient of O_2 is present into the depth of the anode layer and that the anode layer also contains a gradient of Ni and NiO, with more NiO in the outer regions of the anode and less deep inside the pores. At lower temperatures, the mass/time data are parabolic, indicative of the slow step in Ni oxidation being ion transport through the thickening NiO layer.

Optical microscopy and SEM analysis have confirmed that the extent of cracking of the cells is more severe when anodes are fully oxidized at higher temperatures, with entire electrolyte fragments pushed out from the electrolyte plane. Anodes that were only partially oxidized to ≥50% showed that, at 800°C, the first cracks are near, and parallel to, the cell edges (allowing air to easily penetrate the porous anode region and enhance oxidation rates), while cracking is much less extensive at lower temperatures. SEM analysis confirms that, at high temperatures, NiO is highly prevalent in the outer regions of the anode layer, but that Ni is dominant closer to the electrolyte. At 700°C, however, the NiO/Ni gradient is much less distinct and Ni is more homogeneously oxidized throughout the anode layer.

Lowering of the O_2 concentration (to 0.1% O_2) is also shown here to result in a significant gradient in the NiO content in the anode layer when the anode is partially oxidized, with the anode layer again being highly oxidized in the outer regions of the anode (near the

anode/air interface) and much less oxidized deep inside the anode. This correlates with a linear mass gain in TGA experiments and very severe cracking and cell damage seen at these low pO_2 conditions. Importantly, as the rate of Ni oxidation at the lowest O_2 contents is constant for the many hours required to fully oxidize the anode, the local temperature increase should be negligible. This therefore rules out thermal shock, thermal stress, and creep as primary causes of cell cracking, which all require a higher local temperature in the oxidizing regions of the anode.

Thus, these results show that cell cracking results from stress build-up as a consequence of the presence of a NiO concentration gradient (high concentration near air/anode interface and lower near the anode/electrolyte interface) in the anode layer, rather than from thermal effects. The NiO formed in the outer regions of the anode will be rigidly fixed in place in the local pores, and therefore NiO that forms at longer times of oxidation can only grow inwards towards the electrolyte layer to reduce the stress. With increasingly fewer options available for Ni to NiO volume expansion as the oxidation front moves deeper, the stress is ultimately relieved by cracking of the electrolyte. Therefore, to prevent severe degradation due to cracking of the cell, efforts should be made to avoid gradients in the NiO/Ni content during oxygen exposure of Ni-YSZ anode-supported cells while at high temperatures.

Chapter Five: **The Effect of 'Pre-Oxidation Cycles' on the Oxidation Tolerance of Ni-YSZ Anodes in SOFCs**[†]

5.1 Introduction

In Chapter 4, it was noted that electrolyte cracking during Ni oxidation cycles was more severe (crack width and total number of cracks) as the isothermal oxidation temperature was increased. It was also noted that there appears to be an increased NiO content on the outer surface of the anode after a redox cycle. This suggested that the expulsion of some of the NiO particles at this interface occurs in order to relieve some of the internal stresses in the anode and minimize YSZ electrolyte cracking. The aim of the work in this chapter is, therefore, to confirm the enrichment of NiO at the Ni-YSZ anode/air interface under these safer air exposure conditions, and to determine if this Ni would remain on the outer surface of the anode layer in subsequent redox cycles. Thus, the key goal of this work was to determine if an anode could be pre-treated in such a way as to force some of the NiO out of the anode layer, thus making it more resistant to damage in future redox cycles.

5.2 Experimental Methods

For the purpose of the work described in this chapter, ASC-1 cells were used, as described in Section 3.1.1. All redox cycling was carried out in a TGA, as detailed in Section

[†] To be published: J.L. Young, H. Molero and V.I. Birss, TBA. Dr. Molero carried out XPS analysis of the pre-treated Ni-YSZ anodes, did peak deconvolution, and provided useful input on the interpretation of the XPS results.

3.2, and Sections 3.4.1 and 3.4.2 describe the analysis that was carried out by SEM and XPS, respectively.

5.3 Results and Discussion

5.3.1 Conditions Leading to Damage Due to Ni Oxidation of Ni-YSZ Anode-Supported Cells

In Chapter 4, high porosity (39%) Ni-YSZ anode support layers, covered with a thin Ni-YSZ AFL and then a thin YSZ electrolyte (20-30 mm^2 in area, no cathode layer attached, Figure 3.1), were repetitively oxidized and reduced inside a TGA, with the primary goal being to better understand the mechanism of Ni oxidation and cell degradation. It was demonstrated in Chapter 4 that the oxidation of a Ni-YSZ ASL resulted in more damage in the overlying thin YSZ electrolyte layer if the oxidation conditions led to an inhomogeneous NiO distribution throughout the ASL over the course of the oxidation process. Specifically, the more extreme the difference in NiO content between the outer and inner regions of the anode layer (Figure 5.1), a condition that can be achieved at high temperatures (> 700˚C) or in low pO_2 (0.1% O_2) environments, the higher the degree of degradation. Under these conditions, cracks in the thin electrolyte were seen at an oxidation depth (percentage of total Ni in the anode that has been oxidized) of only 40%.

Conversely, the severity of degradation (YSZ electrolyte crack width and crack frequency) was lower when the oxidation rate of the Ni, and hence the distribution of NiO into the depth of the anode layer, was homogeneous. This was achieved when the temperature of air exposure is low (≤ 700°C), although the temperature for homogeneous oxidation was shown (Chapter 4) to increase as the pO_2 was increased (e.g., a 50% O_2-He atmosphere results in homogeneous oxidation at 800˚C). Under conditions that lead to homogeneous Ni oxidation, the electrolyte will not crack until an oxidation depth of ≥ 74% is reached.

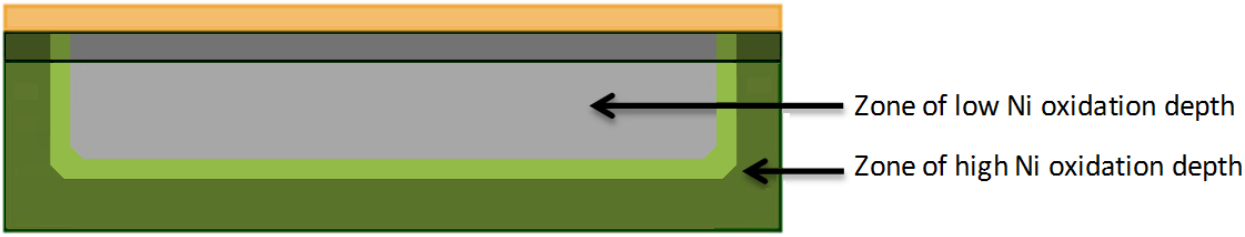

Figure 5.1. A schematic showing the ASC-1 sample (Figure 3.1) after partial oxidation as a very extreme case of inhomogeneous oxidation (e.g., at 900˚C or 0.1% O_2). Here, the partially oxidized Ni-YSZ ASL and AFL have a very high degree of Ni oxidation (dark green) near the anode/air interfaces (bottom and sides only, since the electrolyte at the top prevents air ingress), a transition zone from high to low degree of Ni oxidation (light green), and a low NiO content in the inner regions of the anode layer (grey).

However, less cracking of the thin YSZ electrolyte (seen following air exposure using conditions that result in uniform Ni oxidation throughout the Ni-YSZ anode thickness) only indicates that the tensile stresses on the electrolyte lower when the oxidation temperature is lowered. Other mechanisms could also lead to a lower stress inside the anode layer, such as a change in NiO morphology. This would imply that the NiO, formed when it is exposed to high temperature/low pO_2 conditions, has a lower density from what results when the anode is exposed to the safer low temperature/high pO_2 conditions. Thus, including pores that form within the NiO agglomerates at higher temperatures, the total volume expansion may be > 70%, which would then exert greater stress on the underlying YSZ electrolyte layer. Thus, if a dense Ni phase is forming a NiO phase with a porosity that is dependent on the oxidation temperature, the overall volume expansion, and tensile stress, would depend on the resultant NiO porosity.

Figure 5.2A and B show SEM images of the air-side of a Ni-YSZ ASL after 100% oxidation of the Ni component at 600 and 800°C, respectively, in a single oxidation cycle. It can be seen that, in both cases (Figure 5.2A and B), a cellular structure results. However, it is also seen that the NiO formed at 600°C (Figure 5.2A) has a smaller average particle size (~0.4 μm) than that formed at 800°C (~0.6 μm) and that the NiO formed at higher temperature may be somewhat less porous. As this porosity trend would result in higher stresses at low Ni oxidation temperatures, the opposite of what is actually seen (Chapter 4), it is likely that other processes are responsible for electrolyte cracking at higher oxidation temperatures.

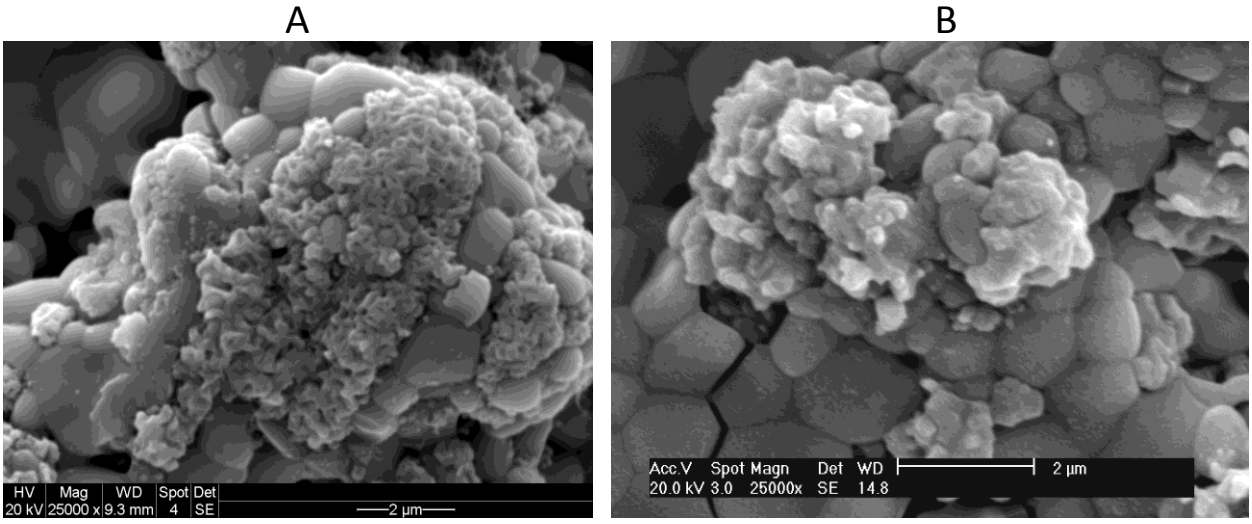

Figure 5.2. SEM images of air-side of Ni-YSZ support layer after full oxidation of Ni component at (A) 600 and (B) 800°C. NiO is distinguishable from YSZ by its finer grained structure and apparent roughness in comparison with YSZ.

Another mechanism by which the stress on the YSZ electrolyte during the oxidation of the Ni phase within a Ni-YSZ ASL could be lowered involves the ejection of some of the NiO

particles out of the anode-air interfacial region towards the outer surface. It has been demonstrated *in situ* in an environmental SEM that, during the high temperature oxidation of a Ni-YSZ anode, NiO particles will push into voids within the anode layer and out of the ASL surface (6) . It is suspected that the ejection of some of the NiO particles leads (after reduction to Ni) to improved electrical contact to the current collectors and may also explain the increase in the conductivity of the ASL after Ni oxidation (74; 140).

A schematic diagram, shown in Figure 5.3A to 4I, depicts the ejection of NiO particles during Ni-YSZ anode layer oxidation. Figure 5.3A shows the Ni-YSZ anode in its initially reduced state and also gives a legend explaining the color scheme used in all of the diagrams in Figure 5.3 for the different particles. All of the particles shown in Figure 5.3 are drawn to scale based on the amount of oxidation of each particle, where the radius increases from 1 μm for Ni particles to 1.2 μm for NiO (resulting in 70% volume increase). YSZ has a constant radius of 1.1 μm in each of these schematic drawings (Figure 5.3).

The case when the oxidation conditions have resulted in a uniform Ni/NiO distribution throughout the anode layer is shown in Figure 5.3B to E (left side), while the case when the oxidation conditions have produced a gradient in NiO distribution into the depth of the anode layer is shown in Figure 5.3F to I (right side). In each diagram (Figure 5.3), the total oxidation depth (percent of NiO) of the anode that is portrayed is equal to the fraction of NiO (green) vs. Ni (grey) in the different particles, depicted as oxidized to different extents. Thus, Figure 5.3B (homogeneous) and 4F (graded) both represent an anode layer in which 25% of the Ni is oxidized. The oxidation depth for both the homogeneous (Figure 5.3B to E) and graded (Figure 5.3F to I) cases increase by 25% in each diagram until the anode layer is fully oxidized (Figure 5.3E and I).

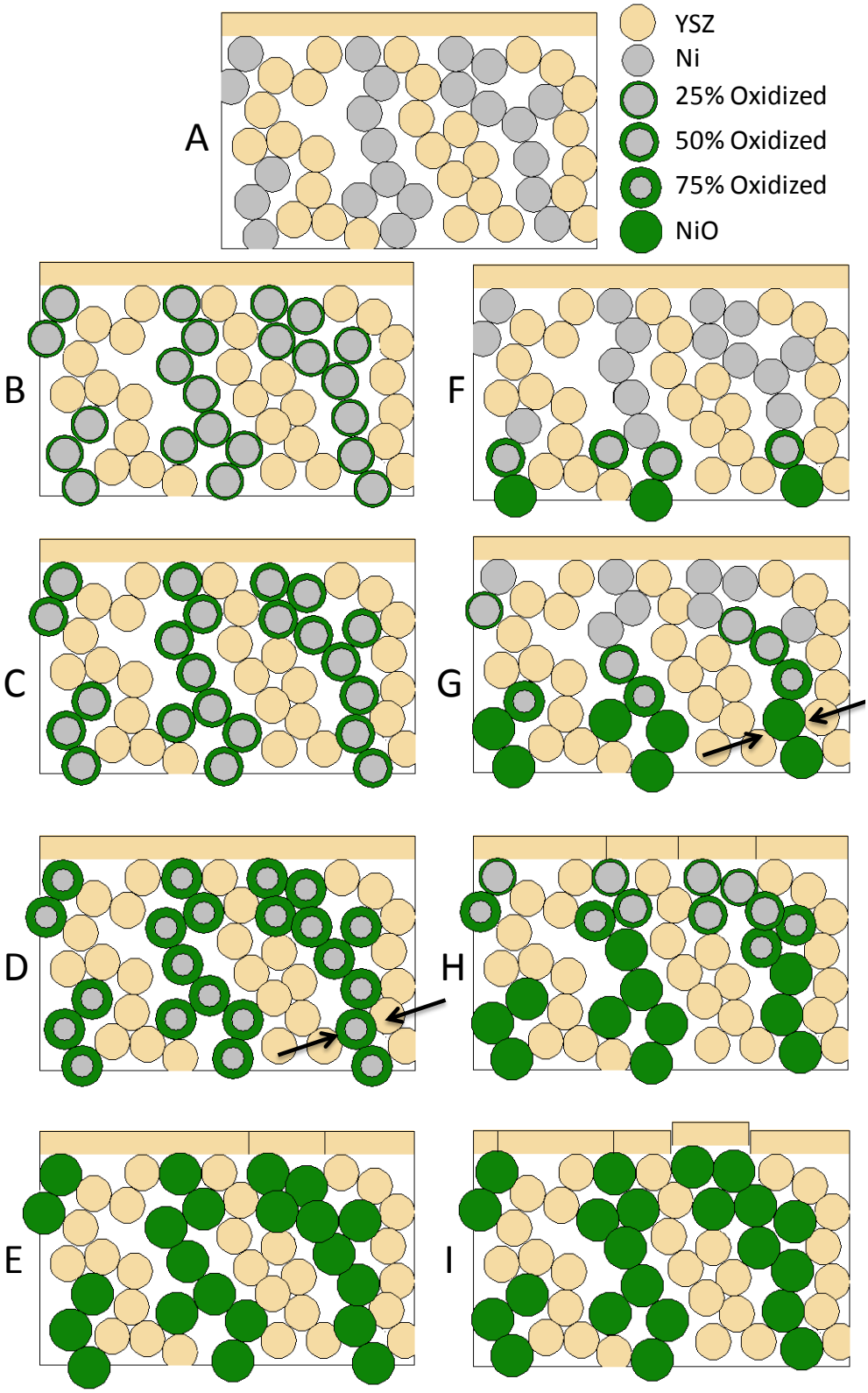
A
YSZ
Ni
25% Oxidized
50% Oxidized
75% Oxidized
NiO
B
F
C
G
D
H
E
I

Figure 5.3. Schematic showing (A) a single Ni-YSZ anode microstructure in which the anode layer is oxidized, either homogeneously (B, C, D, E) or with a gradient (F, G, H, I), to an extent of (B,F) 25%, (C,G) 50%, (D,H) 75% and (E,I) 100% of the full Ni content. In the homogeneous case (B to E), as individual Ni particles reach 75% oxidation (D), they push against the YSZ particles (indicated by arrows), becoming pinned, preventing further ejection of NiO to the surface. In the graded case (F to I), this pinning occurs at a lower anode oxidation depth (G) and thus fewer NiO particles are pushed out of the anode/air interface (base of diagrams).

It can be seen that, as the oxidation depth of the anode in the homogeneous case progresses from 25% in Figure 5.3B to 75% in Figure 5.3D, the interconnected Ni/NiO particles on the right side of the diagram, for example, are not pushing against the particles in the YSZ skeleton until ~75% of the total Ni content is oxidized, as indicated by the arrows in Figure 5.3D. By this time, local stresses within the anode layer have already served to eject a substantial amount of NiO out of the anode surface plane, which is designated by the line at the base of Figure 5.3E.

However, in the graded case (Figure 5.3F to I), the outer air-exposed edges and face of the anode are preferentially oxidized first and then these same Ni/NiO particles (designated by the arrows in Figure 5.3G) push against the YSZ skeleton in the Ni-YSZ anode when between 25% in Figure 5.3F and 50% in Figure 5.3G of the total Ni content has been oxidized. Thus, after only 50% of the Ni is oxidized, no more NiO would be ejected out onto the outer anode surface. As Ni oxidation proceeds, less NiO will be expelled from the Ni-YSZ anode at the anode/air

interface (Figure 5.3I) and, as a result, which results in more NiO pushing inwards towards the thin YSZ electrolyte and increasing the tensile stress on it.

5.3.2 Confirmation of Ni Ejection at Anode/Air Interface Using XPS

In Figure 5.2 (and in Chapter 4), more NiO is seen on the surface after oxidation of a Ni-YSZ layer at 600°C versus at 800°C. However, the natural variability of the morphology of these anodes is very high and the changes in the amount of NiO that present on the outer surface are subtle. As it is difficult to conclusively determine if there is a reliable trend in the SEM micrographs, other techniques must be used to demonstrate these differences more clearly.

To verify the enrichment of NiO at the anode layer/air interface after air exposure at different temperatures, X-ray photoelectron spectroscopy (XPS) of the outer anode surface was employed here. XPS has the advantage that it can be used to determine the NiO surface content over a large area, which minimizes the inherent surface morphology variability that is a result of the fabrication process used. In XPS, only a shallow depth (1 - 6 nm), from which photoelectrons are able to reach the detector, is analyzed. This is an advantage for determining the amount of NiO ejected at the air/Ni-YSZ interface, as the results will be limited by line of sight to the surface. This is in contrast to energy dispersive x-ray analysis (EDX), which detects species that are as much as 1 μm below the surface.

Therefore, in this study, Ni-YSZ layers, coated with a thin YSZ electrolyte layer, as shown schematically in Figure 3.1, were first reduced from the NiO state, then oxidized fully at 900, 800, 700 or 600°C, and then examined initially by top-down SEM analysis, as shown in Figure 5.3A to D, respectively. While the NiO and YSZ phases cannot be distinguished in these 2500X magnification secondary electron images (Figure 5.4), the images do indicate that the

XPS analysis would be performed on relatively uniform surfaces. Thus, the morphology of the NiO-YSZ surfaces should not introduce any significant artifacts in the XPS quantification of the amount of Ni and O present on the air-side of the samples. XPS analysis should thus establish whether a greater proportion of NiO particles are pushed out of the Ni-YSZ layer on the air side when oxidation occurs at low temperatures (homogeneous Ni oxidation) versus higher temperatures (graded Ni oxidation).

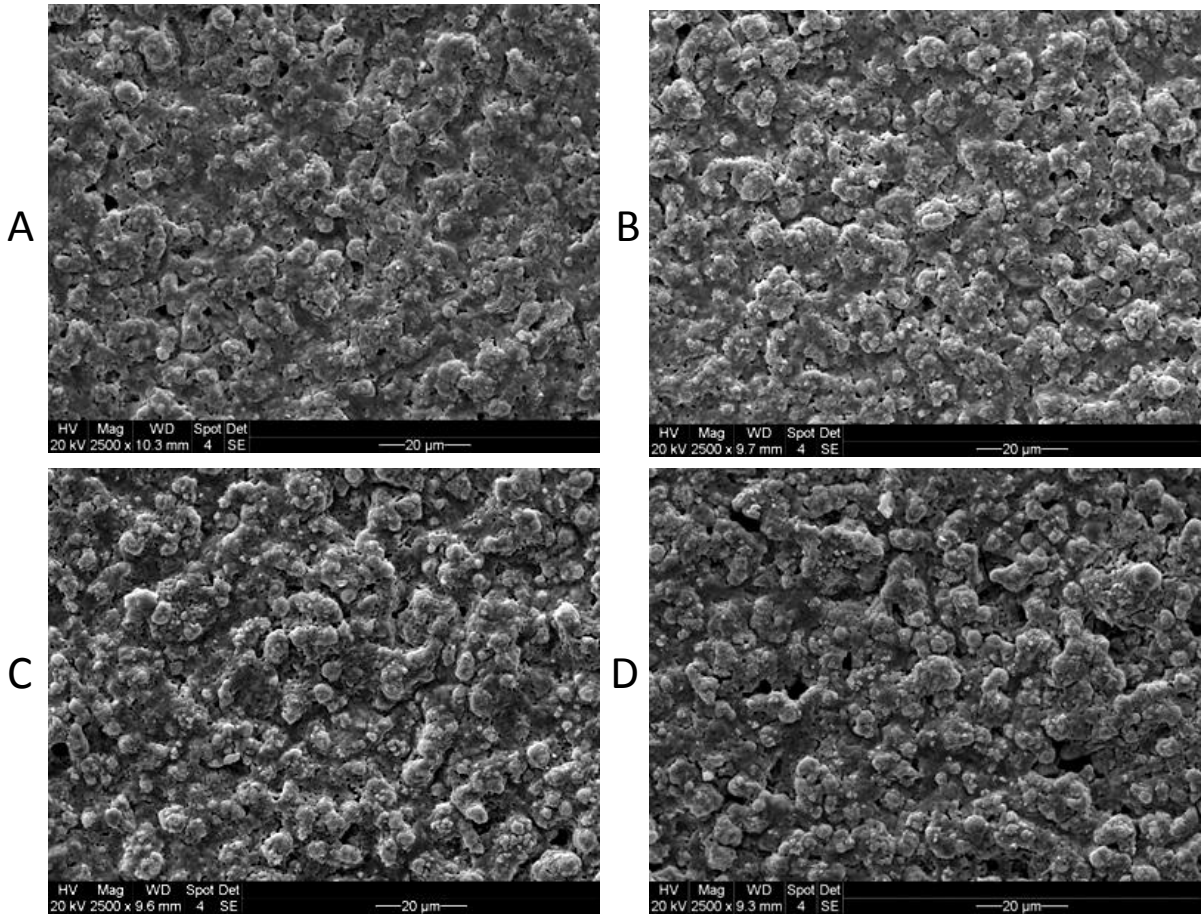

Figure 5.4. SEM image of Ni-YSZ surface after reduction in 10% H_2-He and then oxidation in 20% O_2-He at (A) 900, (B) 800, (C) 700 and (D) 600°C.

An XPS wide energy survey spectrum of the typical Ni-YSZ ASL surface (Figure 5.4) is shown in Figure 5.5 (in this case, for a sample in the as-received oxidized state), and Y, Zr, O, and Ni can be seen, as expected. The presence of carbon in this spectrum is due to adventitious carbon originating from the vacuum system of the instrument. A summary of the elements detected and their relative quantities for each of the samples studied here is presented in Table 5.1. The first column shows the conditions used for Ni-YSZ oxidation, columns 2-6 give the relative at% of each of the elements detected, columns 7-9 provide the at% with C and O omitted, and column 10 gives the ratio of Ni to the total amount of Y and Zr present.

It is first noted in Table 5.1 that, in all cases, the relative amount of NiO detected at the surface after a single redox cycle is enhanced in comparison with that for the as-received sample. Second, it is clearly seen that the amount of NiO detected on the Ni-YSZ anode layer surface for the samples oxidized at 600 and 700°C is larger than the amount of NiO detected for anodes oxidized at 800 and 900°C. This trend is seen even more clearly from the Ni:(Y+Zr) ratio, given in column 10 in Table 5.1, for samples oxidized at 600 and 700ºC, being ~0.4, while for samples oxidized between 800 and 900ºC, the Ni:(Y+Zr) ratio is ~0.6.

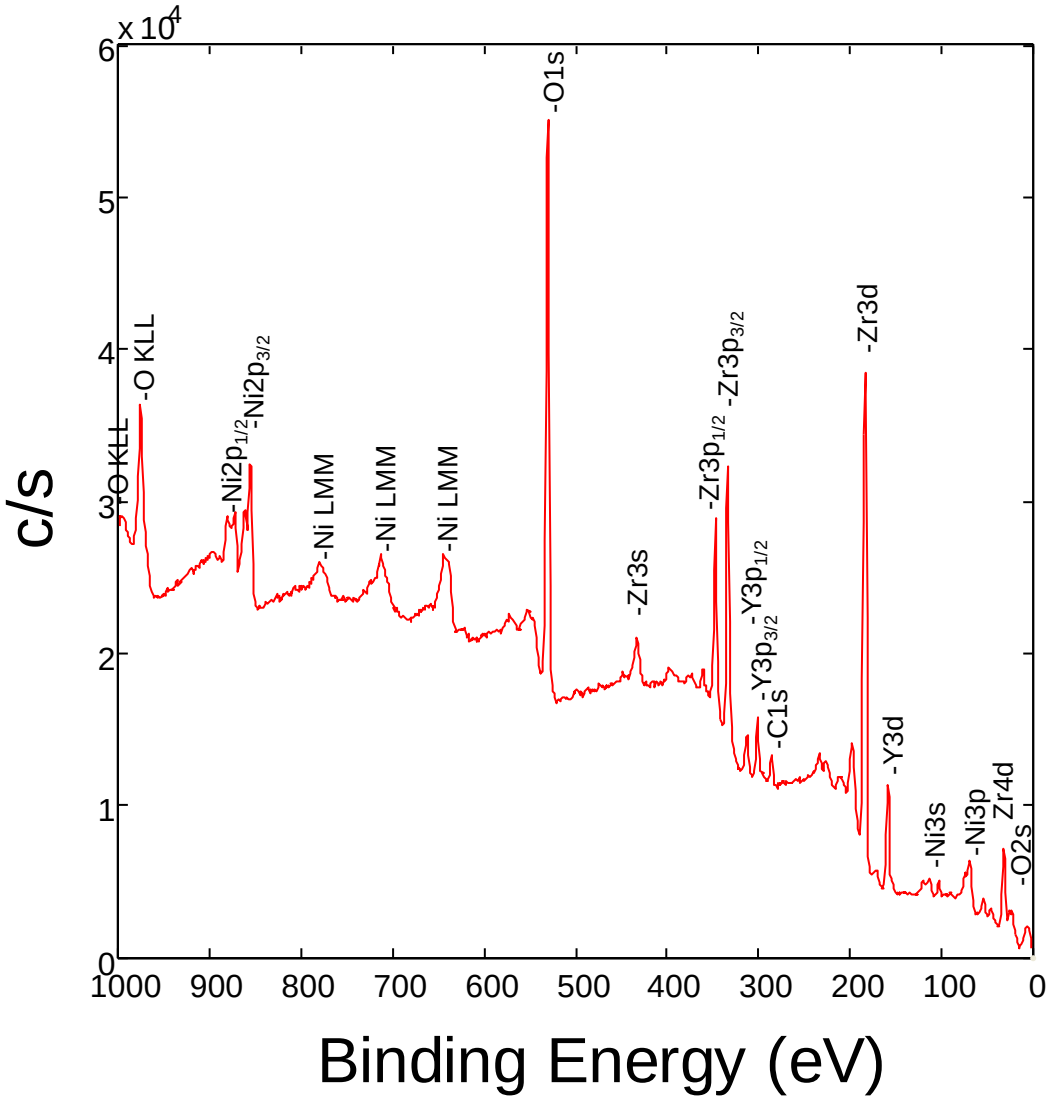

Figure 5.5. XPS wide energy survey spectrum of air-side of Ni-YSZ supported sample (Figure 3.1) in the as-received (oxidized) state.

Table 5.1. Summary of elemental concentrations of Ni-YSZ surface, detected using XPS.

Oxidation Temp. (˚C)	At% of Elements Detected [#]					At% without C and O [*]			Ratio of
	C	O	Ni	Y	Zr	Ni	Y	Zr	Ni:(Y+Zr)
As Rec.	35.9	45.5	2.4	3.4	12.8	13	18	70	0.15
900	11.1	60.8	9.1	3.7	15.3	33	13	54	0.48
800	10.1	62.1	8.2	3.2	16.1	30	12	59	0.43
700	10.1	62.8	10.5	3.3	13.4	39	12	49	0.63
600	9.7	61.5	11.4	3.3	14.1	40	12	49	0.65

[#] From XPS peak area measurements and using the corresponding sensitivity factor.

[*] From XPS peak area measurements and the corresponding sensitivity factor, after removing the C and O signals from the calculation.

Figure 5.6 shows the Ni 2p spectra for all four samples. The position of the Ni $2p_{3/2}$ peak at 854 ± 0.2 eV and the presence of two shake-up peaks at 856 and 861 eV on the higher binding energy side of the main Ni $2p_{3/2}$ peak is an indication of the presence of NiO in the samples (141). The expected spectrum for metallic Ni has been added to Figure 5.6, showing that metallic Ni has a peak at 852.7 eV and its XPS signal does not have any shake-up peaks. Ni_2O_3 is likely also present in increasing concentrations as the oxidation temperature is lowered, as was discussed in Section 2.5.1, with a peak that typically appears at 857 eV (142). However, there is no evidence of this peak in Figure 5.6, likely because the concentration of Ni_2O_3 in NiO that is calcined at 600°C will be less than 0.5% (143). The spectra for Zr and Y (not shown in Figure 5.6) correspond to their oxidized states, with the peak binding energies being typical for Zr^{4+} and Y^{3+} and no major differences seen between samples.

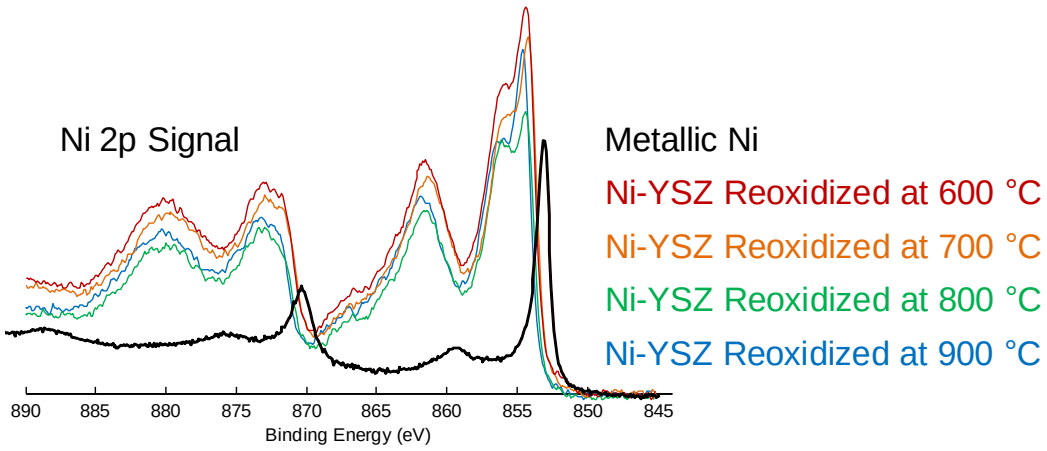

Figure 5.6. XPS spectra, showing the Ni2p peaks for as-received NiO-YSZ samples, reduced and then re-oxidized at 600 to 900°C, as well as the expected XPS spectrum for metallic Ni.

The XPS results (Table 5.1) clearly show that there is a significantly higher NiO content at the air-side of the Ni-YSZ anode layer when the sample was oxidized at low temperatures (600 and 700˚C) vs. at higher temperatures (800 and 900˚C). As the low temperature oxidation conditions have been shown (Chapter 4) to be correlated with the more homogeneous oxidation of the Ni in the anode layer, with no gradient in the NiO content into the depth of the Ni-YSZ layer present at any time over the course of the oxidation process, this argues that the ejection of NiO out of the anode layer helps to prevent stresses from building up on the thin YSZ electrolyte. In the next section, the goal will be to determine whether pre-oxidation at 600˚C will force enough NiO out of a Ni-YSZ anode (containing an AFL) at the air/anode interface to decrease cracking severity in the thin YSZ electrolyte layer, which is co-sintered on the anode layers (Figure 3.1), during subsequent air exposures at 600 to 900˚C.

5.3.3 Pre-Oxidation of Ni-YSZ Anodes at 600˚C to Minimize Redox Cycling Damage

For clarity, the process of re-oxidizing a fully reduced Ni-YSZ anode prior to the onset of normal system operation (or possibly even before the cells are assembled into stacks) for the purpose of preventing electrolyte cracking during subsequent accidental anode air exposure is referred to here as a "pre-oxidation" cycle. The pre-oxidation step could involve multiple oxidation-reduction cycles at 600˚C in 20% O_2, and in Table 5.2, all air exposure cycles to a safe oxidation depth (i.e., where it is known that the electrolyte will not crack), prior to an oxidation cycle to a higher oxidation depth, are still considered to be part of the pre-oxidation step.

5.3.4 Effect of Pre-Oxidation Cycling on Subsequent Air Exposure Damage at 600°C

It was previously shown in Chapter 4 that, for a freshly manufactured Ni-YSZ anode-supported cell, the maximum tolerable oxidation depth (percentage of oxidation of the anode layer Ni content) of a cell, oxidized at 600°C in 20% O_2-He without any electrolyte cracking (in all trials) was ~74%. In the present work, this was confirmed by first fully reducing and then re-oxidizing all of the samples (15 samples, with no cathode attached, as seen in Figure 3.1) to between 74 and 78% oxidation depth at 600°C in 20% O_2-He in a TGA. The electrolyte surface was examined (from the top of the sample depicted in Figure 3.1) using optical microscopy, as cracks in the electrolyte can typically be seen at 150X magnification. The entire electrolyte surface required careful examination, however, as it was often found that only a single crack would propagate across the electrolyte surface if an oxidation cycle went even slightly over its maximum tolerable oxidation depth. Of the ten samples oxidized to 74%, none exhibited any

cracks, whereas the samples oxidized to 75 (2 samples), 76 (1 sample) and 78% (2 samples) all exhibited one or more electrolyte cracks.

Following the re-reduction of the 10 samples that exhibited no electrolyte cracking (but each was exposed to one pre-oxidation cycle), a second oxidation cycle was then carried out to 80 ± 5% oxidation depth at 600°C in air (20% O_2-He), cooled, and inspected (optical microscopy) to determine if the oxidation tolerance of the cell had changed. The results, as summarized in Table 5.2, indicate that the oxidation depth that could be tolerated in the second oxidation cycle (after the pre-oxidation cycle at 600˚C) did increase somewhat, from ~74% to ~80%. There was no deviation from this value from cell to cell (all cells were part of the same batch), as the electrolyte would consistently crack if the oxidation depth exceeded 80% in the second oxidation cycle. Thus, although the beneficial of pre-oxidation at 600˚C is seen to be minor, the oxidation tolerance of the Ni-YSZ anode layers co-sintered with an electrolyte did still increase by a small amount.

Of the 10 samples that were subjected to pre-oxidation cycles to an 80 ± 5% oxidation depth at 600°C, 5 cells were oxidized to ≤ 80 % and exhibited no cracks in the electrolyte after the second oxidation step. These 5 samples were then subjected to a third oxidation cycle (having experienced one pre-oxidation step to 74% and an earlier pre-oxidation step to 80%) to 81 ± 2% oxidation depth. Only the 2 cells subjected to an 80% oxidation depth did not crack and all of the remaining cells (two oxidized to 81% and one to 83% oxidation depth) exhibited electrolyte cracking. The final two samples were subjected to 7 more pre-oxidation cycles to an 80% oxidation depth (all at 600°C in 20% O_2-He), confirmed to be crack-free, and then oxidized to 81%, after which a crack was found in the electrolyte of both samples (Table 5.2).

Table 5.2. Summary of maximum oxidation depth that a YSZ electrolyte tolerated without cracking after various Ni-YSZ anode pre-oxidation treatments, all at 600˚C.

Sample	Number of Samples Tested	Pre-Oxidation Depth			Sample Oxidation Depth[#]	Oxidation Tolerance[*]
		Cycle 1	Cycle 2	Cycles 3-10		
"Fresh" Cell (No Pre-Oxidation)	15	-	-	-	74 to 78%	74%
1 Pre-Oxidation Cycle [†]	15	74	-	-	80 ± 5%	80%
2 Pre-Oxidation Cycles [†]	10	74	80	-	81 ± 1%	80%
10 Pre-Oxidation Cycles [†]	5	74	80	80	81 ± 0.5%	80%
20 Pre-Oxidation Cycles [†]	1	74	80	80	81%	80%
50% pO_2 Pre-Oxidation Cycles [†]	2	74	80	80	81%	80%

[#] Range of oxidation depths to which the samples were subjected.

[*] Allowable oxidation depth before YSZ cracking was observed.

[†] Pre-oxidation cycles involves one or more Ni partial oxidation steps of a Ni-YSZ anode at 600˚C, and this is followed by oxidation to the 'Final Oxidation Depth' to determine if the oxidation tolerance changes.

A fresh sample was then subjected to a pre-oxidation cycle that consisted of one cycle to 74% oxidation depth, followed by 20 cycles to an 80% oxidation depth, cooled, inspected to confirm that there were no cracks, and then subjected to oxidation at 81% depth. It was seen that the maximum oxidation depth that cells could tolerate without cracking during exposure to air at 600˚C remained at 80%. Multiple pre-oxidation cycles did not appear to have any beneficial effects on the tolerable oxidation depth of the Ni-YSZ ASL, even after as many as 20 pre-oxidation cycles.

A 50% O_2-He atmosphere was then examined as alternative conditions for the pre-oxidation step, since it was suggested in a Chapter 4 that the degree of homogeneity of the Ni

oxidation into the depth of the anode layer would then be higher. As it is hypothesized that increasing the homogeneity of the Ni oxidation will increase the amount of NiO ejected at the air/Ni-YSZ interface, this should also have increased the oxidation tolerance of the cell. However, it is seen in Table 5.2 that the exposure of the samples to this high pO_2 environment does not have any effect on the tolerable oxidation depth, which remained at ~80%. In consideration of the anode surface NiO content, determined by XPS (Figure 5.6, Table 5.1), this is not surprising, since there was no increase in NiO observed when reducing the temperature from 700 to 600˚C.

It can therefore be concluded that there is a minor benefit to a single pre-oxidation treatment step at 600˚C in increasing the tolerable oxidation depth of a Ni-YSZ anode-supported cell. For the cells used in this study, the oxidation tolerance was increased from 74 to 80% before the YSZ electrolyte will be seen to crack. There are, however, no obvious benefits to the use of multiple pre-oxidation steps and, further, the use of higher pO_2 for the pre-oxidation cycle also demonstrated that it has no additional benefit to the oxidation tolerance of the cell in subsequent oxidation cycles. This suggests that the majority of the NiO that is ejected out of the anode-air interface does so in the first oxidation cycle.

The source of this increase in oxidation tolerance is proposed to be due to the small change in the Ni content in the surface region of the anode, which, if left within the pore structure, would have increased the overall internal stress in the anode layer. It has been demonstrated here that increasing the number of pre-oxidation cycles does not improve the oxidation tolerance of the cell at 600˚C after the first cycle. Thus it is likely that it is not possible to eject more NiO out of the anode surface, as the NiO particles would have had to be extracted from the inner regions of the anode layer.

5.3.5 Effect of Pre-Oxidation Cycles on Subsequent Air Exposure Damage at 800°C

When Ni-YSZ anode-supported cells are oxidized under conditions that result in a graded Ni oxidation throughout the anode (high temperature or low pO_2) it was shown previously (Chapter 4) that the oxidation tolerance is very low. Under these conditions, cracks that run parallel to the edge of the cell develop when < 50% of the Ni in the anode is oxidized and propagate across the electrolyte surface when only 60% of the Ni is oxidized (Chapter 4). These first cracks form because air can penetrate from the sides of the sectioned fragments, as was illustrated schematically in Figure 5.1, and it is likely that they form because the local oxidation depth is > 74% even though the overall anode oxidation depth is < 50%, a hypothesis that will be shown to be true in Chapter 6.

It has been demonstrated above that the oxidation tolerance of a homogeneously oxidized fresh sample can be improved from ~74% to ~80% after a single pre-oxidation cycle (at 600˚C), likely because of NiO particle ejection out of the anode-air interface during the oxidation process. Since NiO particle ejection occurs at all anode-air interfaces, including the sample edges (Figure 5.1), a pre-oxidation cycle should have, in theory, a large effect on the formation of these edge cracks, since the internal stresses in the anode in this region should then have been significantly lowered. Thus, the oxidation tolerance of a cell should be dramatically improved when exposed to oxidation conditions that lead to a NiO gradient.

In this work, the effect of a pre-oxidation cycle on electrolyte cracking characteristics at 800˚C is investigated. Two fresh samples (Figure 3.1) were prepared and then oxidized using two different procedures. Figure 5.7 shows the electrolyte surface of first sample after it was subjected to one full (100% of Ni) oxidation cycle at 800°C. It can be seen that the electrolyte cracks at the edges of the sample, in Figure 5.7A, are primarily parallel to the edge of the sample

(left side) with many cracks seen that are perpendicular to the edge of the sample. These latter cracks where shown in Chapter 4 to propagate from one parallel crack to another and, since these cracks do not propagate straight through the parallel cracks (i.e., they are offset), it is evident that the parallel cracks formed first. In the central regions of the sample, in Figure 5.7B, it can be seen that the electrolyte surface has many cracks that randomly propagate across the electrolyte surface, with many very wide cracks that are evidence of the severity of the degradation.

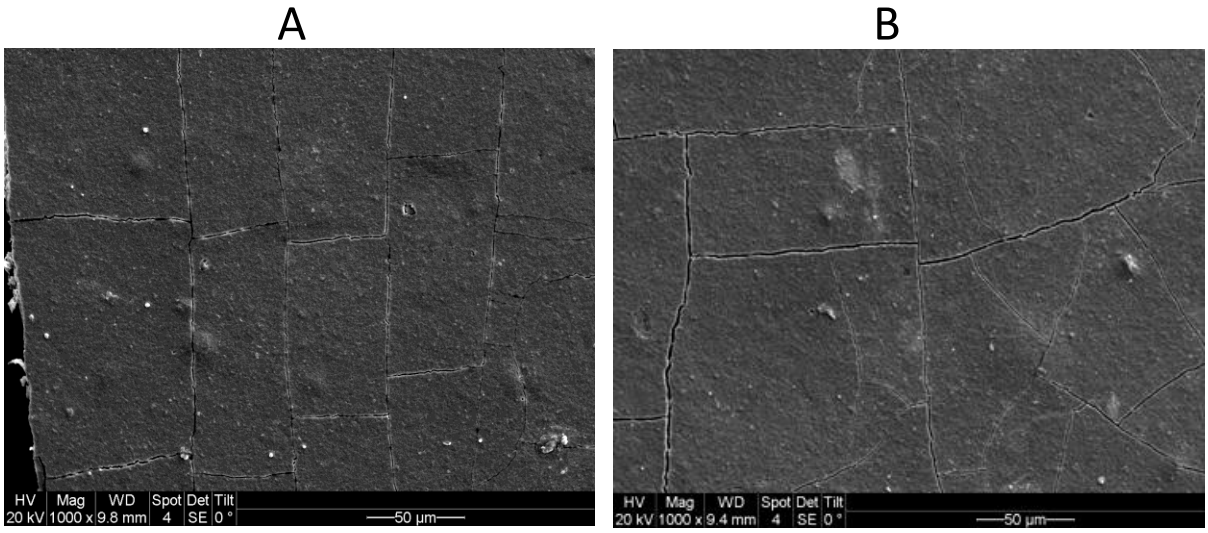

Figure 5.7. Cracks seen on the electrolyte surface (top down view of the sample in the orientation depicted in Figure 3.1) of a sample that was subjected to a full (100% of Ni) oxidation cycle at 800°C, with SEM images shown at (A) the edge of sample and (B) in the central area of the electrolyte surface.

Figure 5.8 shows the electrolyte of the second fresh sample (Figure 3.1), which was subjected to a single pre-oxidation cycle at 600°C (to 74% oxidation depth, in the same fashion as discussed in Section 3.1), followed by the full oxidation of the Ni in the anode at 800°C. It can

be seen in Figure 5.8A that there are still cracks parallel to the sample edge (left side), except that there are only two, in comparison with 5 cracks for the sample oxidized at 800˚C without a pre-oxidation cycle (Figure 5.7A). In Figure 5.8B, it can be seen that the cracks that randomly propagate through the central regions of the electrolyte are narrower than those in the sample that was not pre-oxidized (Figure 5.7B) and there also appears to be fewer cracks produced overall.

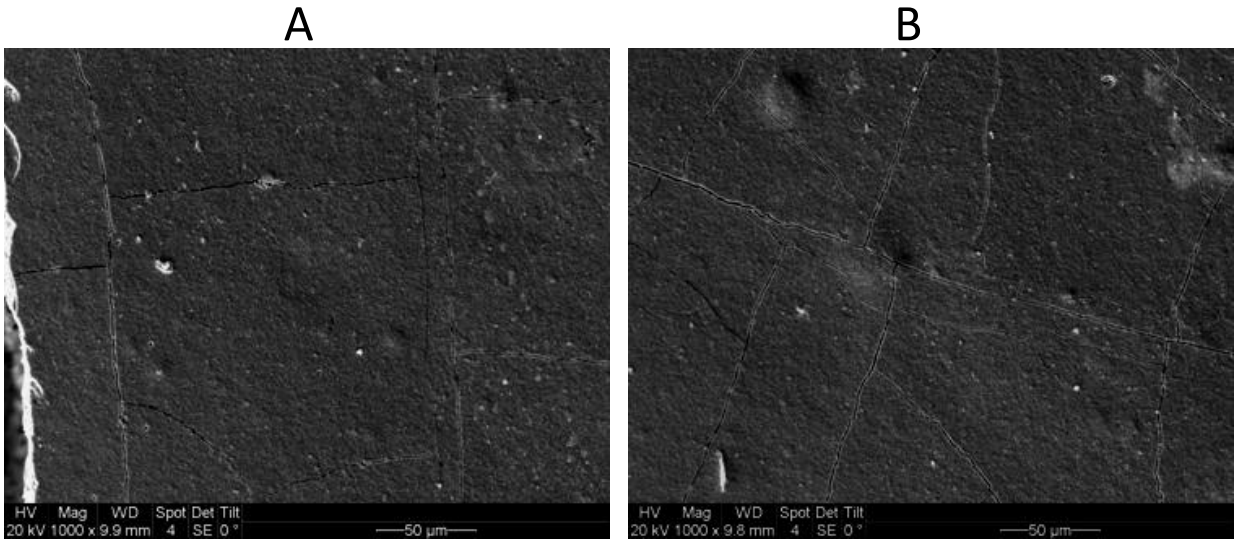

Figure 5.8. Cracks seen on the electrolyte surface (top down view of the sample in the orientation depicted in Figure 3.1) of a sample that was subjected to one pre-oxidation cycle to an oxidation depth of 74% at 600°C, followed by a full oxidation cycle at 800˚C, with SEM images shown at (A) the edge of sample and (B) in the central area of the electrolyte surface.

In fact, in the central regions of the electrolyte, the total number of cracks (of any length) visible in the SEM image decreases from 22 to 13, when comparing those formed on a sample that had not been pre-oxidized (Figure 5.7B) versus one that has (Figure 5.8B), respectively. This

decrease in the number of cracks in the viewable area of the micrograph, in addition to the narrower crack widths in the sample that was pre-oxidized at 600°C (in Figure 5.8B vs. Figure 5.7B), demonstrates that, overall, there is an obvious decrease in the severity of electrolyte degradation.

However, while the oxidation tolerance at 800˚C may have been improved with a pre-oxidation cycle at 600˚C, any amount of cracking of the electrolyte can be very harmful to the life and performance of an anode-supported SOFC. Thus, it is necessary to determine if the pre-oxidation step has improved the oxidation tolerance of an Ni-YSZ anode-supported cell. Once again, fresh samples were prepared and subjected to a pre-oxidation step at 600°C, followed by partial oxidations (40 to 60%) at 800˚C in air. Not surprisingly, similar to the case in Figure 5.8A, the severity of the degradation is lower, as it is observed that the number of parallel cracks is lowered to 2 (versus the 5 that are normally observed). However, in each case, cracks parallel to the edge of the sample formed at only a 40% oxidation depth, indicating that the oxidation tolerance had not been improved.

To maximize the extent of NiO ejection out of the anode-air interface, 20 pre-oxidation cycles were applied, using a 74% depth of oxidation in the first cycle and 80% in the remaining 19 cycles, all at 600˚C and in 50% O_2-He. (these cells were cooled and inspected with optical microscopy to ensure that they were crack-free, and then re-heated to 800˚C). Although in Section 5.3.4, a similar pre-oxidation procedure was unsuccessful in improving the tolerance at 600˚C, it was theorized that, since the first cracks to form are at the edges of the sample (Figure 5.8A), this procedure could have more success at 800˚C.

It can be seen in Figure 5.9A that, for a sample that was oxidized to a 50% oxidation depth at 800˚C after 20 pre-oxidation cycles at 600°C, there are only two cracks that propagate

parallel to the sample edge (at the bottom of the image), as compared with five cracks in the electrolyte of the fresh sample that had been oxidized to 50% without the application of a pre-oxidation procedure (Figure 5.9B). Once again, the number of cracks has decreased, as was also seen after a single pre-oxidation step at 600°C to a 74% oxidation depth in Figure 5.8A and B.

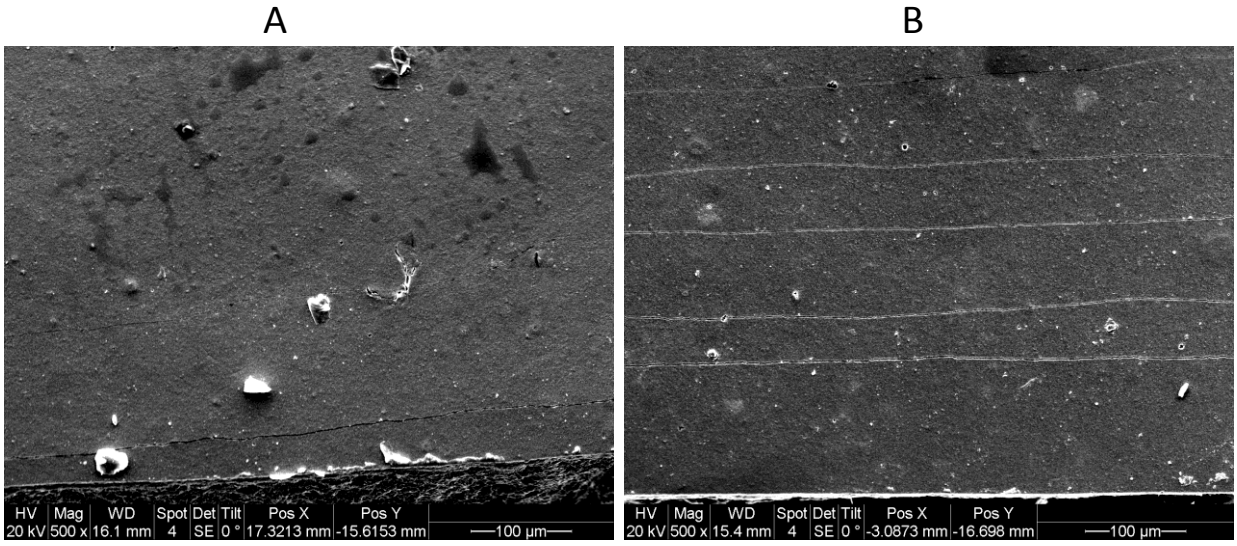

Figure 5.9. Cracks seen in the YSZ electrolyte of a Ni-YSZ ASL/YSZ sample that was air-exposed to a 50% oxidation depth at 800°C in 20%O_2-He, comparing images after (A) 20 pre-oxidation cycles at 600°C in 50%O_2-He and (B) without a pre-oxidation treatment.

There is therefore no observed change in the oxidation tolerance of a sample that undergoes Ni oxidation when exposed to conditions that lead to a gradient in the NiO content throughout an anode (e.g., > 700˚C). This conclusion is based on the narrow definition of oxidation tolerance used in this work, i.e., the highest oxidation depth that can be tolerated before cracks begin to appear. While the oxidation depth of the sample has not been improved

with pre-oxidation cycling, it is noted that the severity of the observed electrolyte cracking during Ni-YSZ oxidation at 800°C was almost halved. This may be enough to extend the life of an operating fuel cell in some situations.

5.4 Summary

When a Ni-YSZ (yttria-stabilized zirconia) anode-supported solid oxide fuel cell (SOFC) is inadvertently exposed to air, the outcome can be the catastrophic degradation of the cells, resulting from the 70% volume expansion of Ni as it forms NiO. The most critical degradation mechanism in high porosity Ni-YSZ anodes has been found to be cracking of the thin YSZ electrolyte layer. It had previously been observed that the more homogeneous the oxidation of Ni in the anode (the lower the gradient of NiO content into the depth of the anode layer over the course of oxidation from 0 to 100% NiO), the lower the degree of degradation observed (fewer and narrower cracks).

The reason that the homogeneously oxidized anode produces fewer cracks was theorized to result from the ejection of NiO particles out to the surface of the anode during air exposure, thus relieving some of the internal stresses. XPS analysis was used here to determine the NiO content on the outer surface of a Ni-YSZ anode-support layer, specifically monitoring the ratio of NiO content relative to Y and Zr (Ni:(Y+Zr)). It is confirmed that the Ni:(Y+Zr) ratio at the anode-air interface is increased when the Ni-YSZ anode is exposed to oxidizing conditions that lead to a homogeneous Ni/NiO content throughout the anode for the entire duration of the oxidation cycle.

It is also shown here that samples that were pre-oxidized in a single step at 600°C to a ~74% oxidation depth, i.e., the maximum amount of the Ni phase that can be oxidized without

inducing any electrolyte cracking, were crack-free and undamaged up to an oxidation depth of 80% at 600˚C. This increase of ~6% in the oxidation tolerance of the Ni-YSZ anode layer is not a very large improvement, but it could still represent the difference between saving or damaging a cell in some situations.

When the pre-oxidation approach at 600˚C was applied prior to full anode oxidation at 800°C, the cracks that were produced in the electrolyte were less severe (narrower and fewer in number) than when no pre-oxidation treatment was used. However, the cracks still appeared when < 50% of the Ni in the anode had been oxidized, similar to the case in the absence of any pre-oxidation steps and the oxidation tolerance of the sample had, therefore, not improved.

While the use of a pre-oxidation procedure does not result in an improvement of the oxidation tolerance of the sample in subsequent oxidation cycles at 800°C, the severity of the degradation of the electrolyte (crack quantity and width) is lowered (by 50%). This decrease in the crack severity could be significant if the performance degradation (due to fuel and air leakage through the electrolyte cracks) of the air exposed fuel cell suffers does not reach a critical magnitude. The lifespan of the cell could therefore be increased for a cell that was prepared with a pre-oxidation procedure versus a cell that was not pre-oxidized.

Chapter Six: **Raman Spectroscopy Study of Partially Oxidized Ni-YSZ Anodes in SOFCs**[‡]

6.1 Introduction

In Chapter 4, it was noted that electrolyte cracking during Ni oxidation cycles was more severe (larger crack width and higher number of total number of cracks) as the isothermal oxidation temperature was increased. This increase in crack severity was correlated with a steeper NiO content gradient through the anode thickness over the course of air exposure. The microscopy techniques used in Chapter 4 to map the NiO:Ni ratio through a 50% oxidized Ni-YSZ anode support layer were only qualitative and prone to large errors in interpretation. A more quantitative technique was therefore needed. Raman spectroscopy has recently been gaining acceptance in quantifying composition, oxidation state, and surface speciation of SOFC components and has been used in both *in situ* and *ex situ* studies (111). Here, it is shown that Raman spectroscopy data can be relatively easily and rapidly acquired (compared with microscopy) for Ni-YSZ anaodes and that the NiO content in the cross-section of a partially oxidized anode layer can be reliably determined.

6.2 Experimental Methods

For the purpose of the work carried out in this chapter, ASC-1 cells were used, as described in Section 3.1.1. All redox cycles were carried out inside a TGA, as detailed in

[‡] To be published as J.L. Young, R. Mahar and V.I. Birss, TBA. Dr. Mahar (Dept. of Physics, Imperial College London) provided training in the use of the Raman spectrometer, spectra deconvolution, and provided useful feedback on this chapter for eventual publication.

Sections 3.2 and 3.2.3. Sections 3.4.1 and 3.4.2 describe the analysis that was carried out by SEM and XPS, respectively, and the procedure used for Raman spectroscopy is detailed in Section 3.4.3.

6.3 Results and Discussion

6.3.1 General Characteristics of Ni-YSZ SOFC Anodes After Full and Partial Oxidation

Figure 6.1A and B show the backscattered electron SEM cross-sectional views of a polished Ni-YSZ anode (57% by mass NiO, balance YSZ, total anode thickness is 1 mm) in the as-received (fully oxidized) and fully reduced (in 10% H_2-He at 800°C) states, respectively. The electrolyte, which is approximately 10 μm thick, is at the top of each image. The anode layer adjacent to the electrolyte is ~20 μm thick and was fabricated using a fine starting powder (0.5 μm) and is thus referred to as the anode functionalized layer (AFL). The AFL has a porosity that is estimated by SEM (Figure 6.1A and B, respectively) to be 22% in the oxidized state and 30% after NiO reduction. In comparison, the anode support layer (ASL), which is the dominant layer in the images in Figure 6.1, was fabricated using a 1 μm average particle size and has a porosity of roughly 30% after firing and 38% after reduction.

The change in mass with time as the anodes in this study were oxidized in a TGA is shown in Figure 6.2A for oxidation temperatures of 600, 700, 800 and 900°C. At 700-900°C, it can be seen that the extent of oxidation increases linearly with time until ~50% of the Ni in the anode is oxidized. At 900°C, it is seen in Figure 6.2A that the deviation from linearity is not significant, while at 700 and 800°C, the deviation from linearity is quite noticeable after 60% of the Ni has been oxidized. At 600°C, the TGA plot is roughly linear until ~30% of the Ni has been oxidized before clearly becoming non-linear.

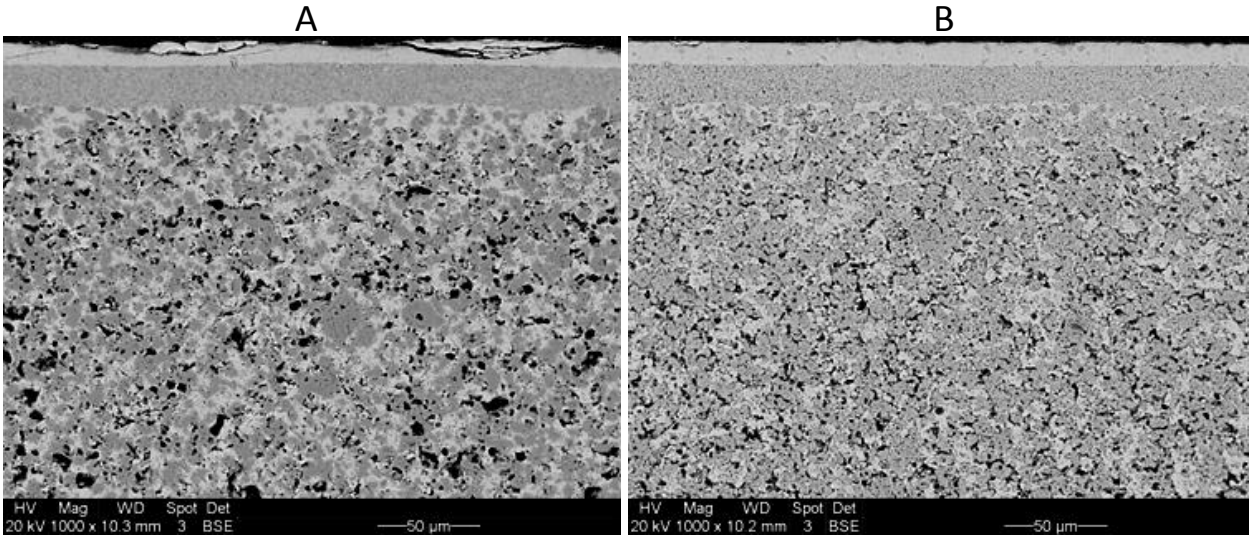

Figure 6.1. Backscattered SEM images of a polished cross-sectional Ni-YSZ/YSZ sample, showing the YSZ electrolyte (top 10 µm), the AFL (20 µm thick and adjacent to the electrolyte), and the thick ASL layer (the rest of the image) (A) after manufacture and thus in the oxidized state and (B) after full reduction in 10% H_2-He at 800°C.

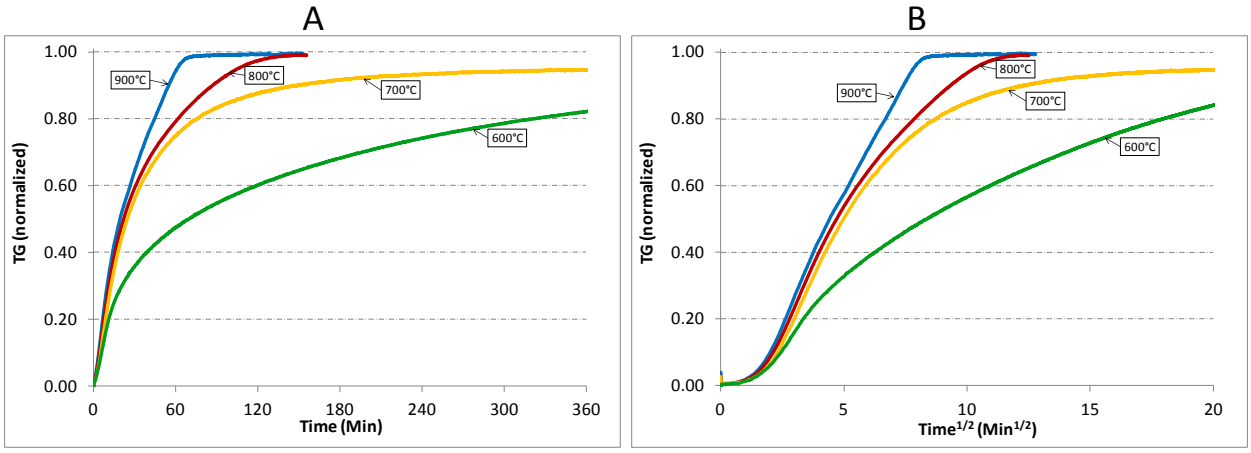

Figure 6.2. (A) Mass gain during exposure of a 200-250 mg fragment of the anode-supported Ni-YSZ/YSZ sample to air as a function of temperature, with (B) showing a parabolic kinetics plot of the data in (A).

When the data of Figure 6.2A are plotted in a manner consistent with parabolic kinetics (Figure 6.2B), linearity in the mass gain versus time plot is only observed at 900°C, with two slopes seen before and after ~50% oxidation. The activation energy calculated from the most linear portion of each curve is 34 $kJ \cdot mol^{-1}$, which is much lower than that measured by others, with the oxidation of small (5 μm) Ni particles exhibiting an activation energy of 145 $kJ \cdot mol^{-1}$ (144) and large (158 μm) Ni particles having an activation energy of 174 $kJ \cdot mol^{-1}$ at < 800°C (145).

The fact that none of the standard kinetic laws, which typically apply for the oxidation of bulk metals (146), will fit the Ni-YSZ anode layer oxidation data can be explained. First, it is known (99; 139) that transport limitations within the porous anode layer microstructure, which will cause a gradient in the extent of oxidation into the layer, will alter the mass gain data and, in extreme cases, result in rectilinear growth kinetics (146). Second, it is also possible that differing oxide film morphologies that will form at different oxidation temperatures (81) are affecting oxidation rates on the Ni particle surfaces. Finally, it is possible that geometric factors, resulting from the variable shape and size of the Ni network of particles in the anode, are having an impact on these results.

Prior to mapping the gradient in NiO content, cells were partially oxidized to ~50% at a range of oxidation temperatures (600, 700, 800 and 900°C). Through trial and error, anode layers were partially oxidized (and then cooled rapidly to room temperature (7.5°C/min) in N_2-He) until a mass gain equivalent to 50% NiO was reached (typically in < 20 min). It can be seen in the TGA profiles in Figure 6.3 that the lowest extent of oxidation was 43% (at 700°C) and the highest was 54% (at 900°C). The delay in mass gain (Figure 6.3) is due to the 10 min N_2 purge

in addition to the time it takes oxygen to pass through the tubing to the sample holder in the TGA instrument.

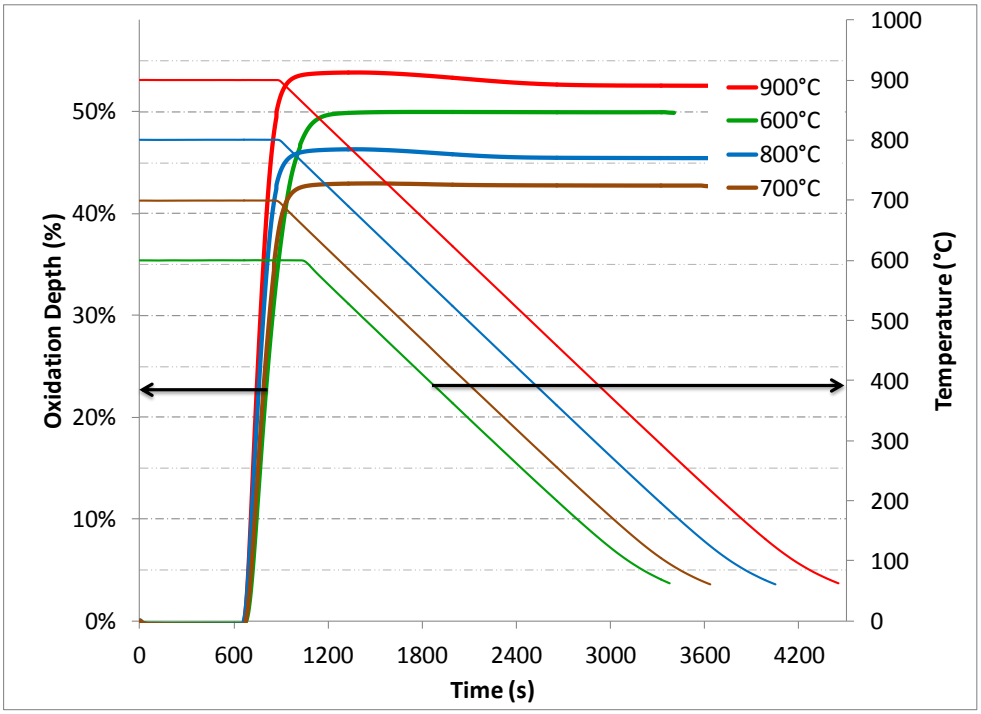

Figure 6.3. TGA profiles obtained during the partial oxidation (in 20% O_2-He) of Ni-YSZ anode support layers, followed by cool-down in 20% N_2-He.

6.3.2 Microscopic Methods to Determine Local NiO Concentration in Ni-YSZ Anodes

Optical microscopy images (40 X magnification) of the fully reduced anode (electrolyte on left) and the ~50% oxidized Ni-YSZ anode support layer cross-sections, attached to a thin, co-fired YSZ electrolyte layer (on right), are shown in Figure 6.4A to E, respectively. The fully reduced cell (Figure 6.4A) exhibits a relatively uniform distribution of bright (polished metallic phase), grey (YSZ and shallow pores) and black (deep pores) regions through the thickness of

anode layer. Samples that were partially oxidized at 800 and 900°C (Figure 6.4D and E, respectively) have higher concentration of the bright (metallic) phase deep inside the anode layer, near the electrolyte, and almost none in the outer regions of the anode. Conversely, at 700°C (Figure 6.4C), the anode appears to be more homogeneously oxidized, with a less predominant bright phase adjacent to the electrolyte, while after 50% oxidation at 600°C (Figure 6.4B), the reduced Ni phase appears to be homogeneously distributed across the thickness of the anode.

Comparing these samples (Figure 6.4A-E) to each other is difficult, due to the variations in the brightness and contrast between the images. In addition, because optical imaging is a low resolution technique, it is difficult to quantify the area occupied by small Ni particles. The images are dominated by large agglomerates that form as a result of the tape casting technique, which produces NiO and Ni particles with a diameter ranging from 2-5 μm and 1.5 to 3.7 μm, respectively, after sintering and reducing the NiO (115). Using higher magnifications to examine the smaller particles will not solve this problem, since this broad range of particle sizes, or "natural variability" inherent to these anode microstructures, can result in high error when compared to the overall cell average, especially if the area of analysis is very small.

Further complicating even a semi-quantitative interpretation of the optical images in Figure 6.4 is the differing density of Ni and NiO and a geometric effect that results from the presence of concentric spheres of partially oxidized particles (Ni particle core coated with a NiO shell). The density difference between Ni and NiO produces a 70% volume increase and any analysis will, thus, give a falsely high NiO content. This density difference was confirmed by a comparison of the images in Figure 6.4B-C with that of the fully reduced sample (Figure 6.4A), where it appears visually that the partially oxidized samples (50%, by TGA) are actually ca. 75%

oxidized. For random slices cut into concentric spheres, there is a large error, biased towards the dominant phase (> 50% by volume) (147). This geometric effect, arising from the presence of these concentric spheres, is confirmed by comparing Figure 6.4D-E, where it appears that the anode is fully reduced in the inner part of the anode (Ni dominated) and completely oxidized in the outer anode/air interfacial regions (NiO dominated).

Another feature in these images (Figure 6.4) that could potentially have been used to determine the Ni vs. NiO content into the depth of the anode layer is the porosity. When considering the significant volume change as the Ni particles are converted to NiO (70% volume increase), the resulting changes in porosity should be visible with SEM. However, the porosity of the anode is seen to range only between 30% and 38 % for the fully oxidized and fully reduced anode layers, respectively, in Figure 6.1. Thus, when considering the natural variability of the anode microstructure and the relatively large error (~5%) associated with determining percent porosity by using image software (e.g., ImageJ or AnalySIS), the differences in porosity between the oxidized and reduced samples (only 8%) are too small to track.

In addition, the microstructure of NiO, formed by Ni oxidation at 600 (Figure 6.5C) and 800˚C (Figure 6.5B), is quite different from that of an as-received anode (Figure 6.5A). The re-oxidized Ni particles can have a very cellular structure with tiny pores that would not be detected optically, as seen by comparing the SEM images in Figure 6.5 (A to C) for an as-received anode with images of anodes that were fully re-oxidized at 800°C and 600°C, respectively. Thus, measuring the cross-sectional porosity cannot be used to reliably determine the Ni:NiO ratio in these anode layers. For this reason, tracking the change in anode layer porosity is not a viable approach for determining the fraction of Ni converted to NiO in each region of the anode.

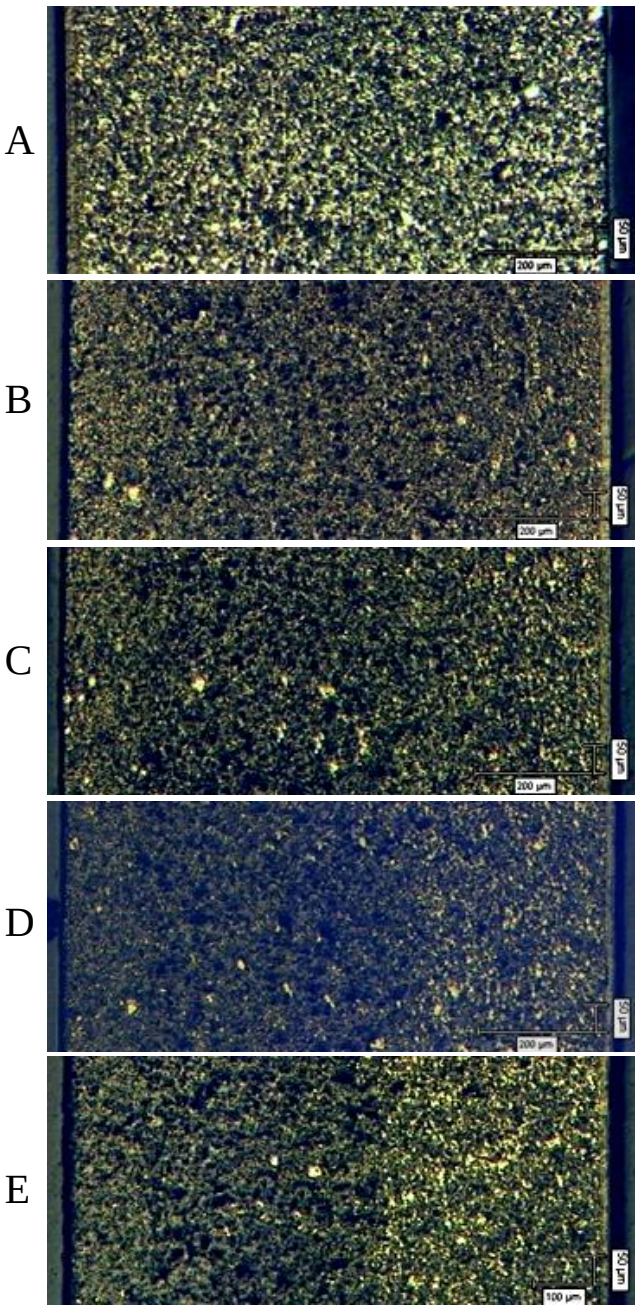

Figure 6.4. Optical images of polished cross-sections of Ni-YSZ anode support layer (on left in each image) attached to a thin YSZ layer (on right in each image) in the fully reduced state (A) and then after ~50 % oxidization in air at (B) 600, (C) 700, (D) 800 and (E) 900°C, showing Ni (white), NiO and YSZ (grey) regions as well as the open pores (black).

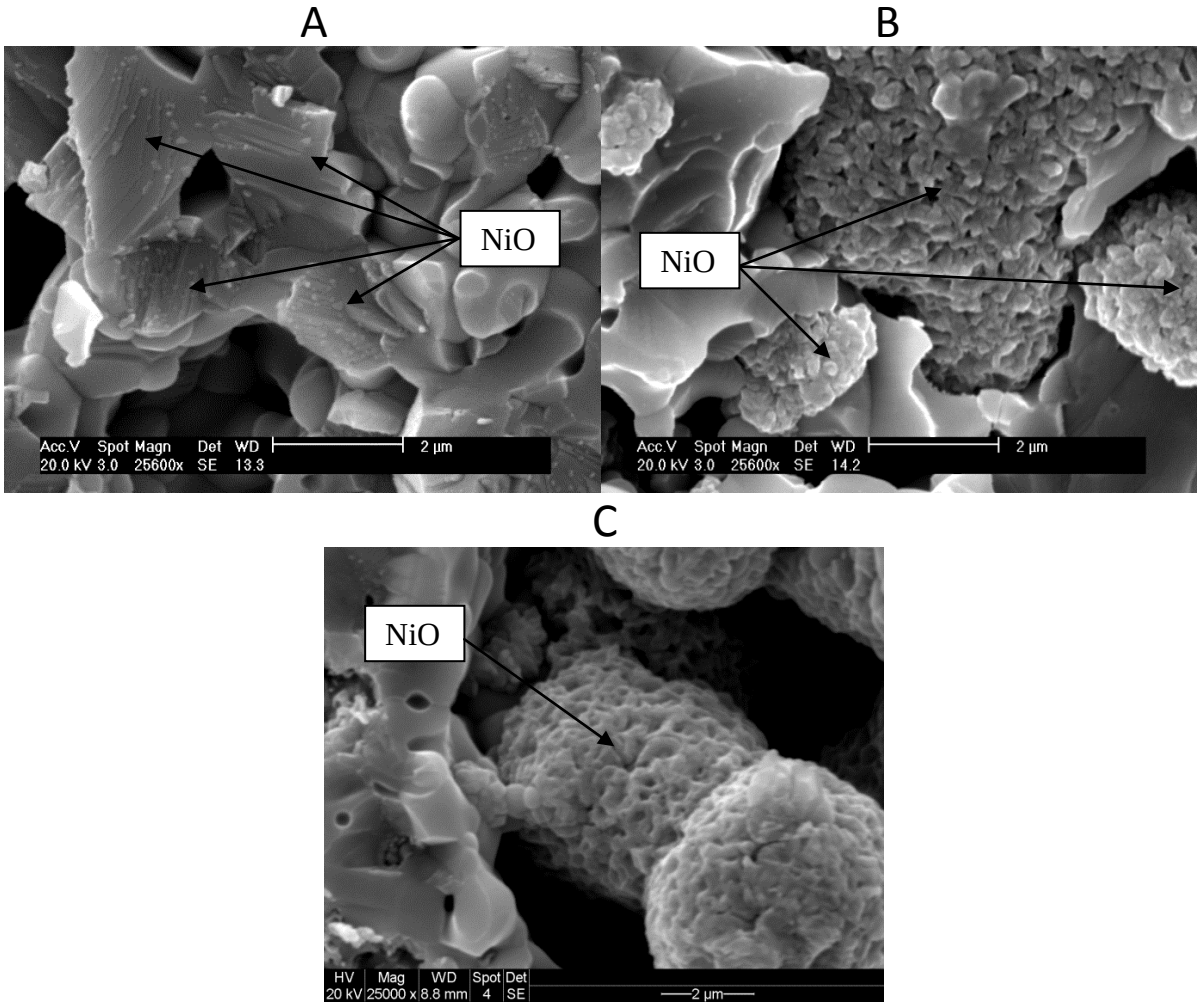

Figure 6.5. SEM images showing the morphology of NiO grains after (A) manufacture at 1450°C and after full re-oxidation of Ni particles at (B) 800°C and (C) 600°C.

SEM backscattered electron imaging was also employed in an effort to map Ni and NiO in anode layers in Chapter 4. These SEM images (Figure 4.5) do have the advantage that NiO appears grey and pores are dark grey to black, and, thus, these particles can be differentiated from the Ni and YSZ particles, but Ni and YSZ often have a contrast difference that is difficult to differentiate. In Chapter 4, multiple SEM images across the anode layer were combined to

form a composite image. Qualitatively, a decrease in the amount of NiO could be clearly seen, being much higher at the anode/air interface and decreasing towards the anode/electrolyte interface at 800 and 900°C, while at 600 and 700°C, the images showed a much more homogeneous Ni and NiO distribution (99). However, these SEM images ultimately have the same limitations as does light microscopy analysis. At low magnification, small features are missed and, at high magnification, there are additional errors present, since a smaller area is being sampled at any one time. A statistically relevant number of images in each zone must therefore be collected and analyzed in order to accurately determine the degree of oxidation in each location, making this technique challenging and highly time consuming.

Energy dispersive x-ray spectroscopy (EDX) has also been used in past studies (103) to track the oxygen content as a function of depth into a Ni/YSZ anode layer. These results can only be considered as qualitative, however, since there is always a considerable background oxygen signal, due to the large natural variability of the anode microstructure, which depends on the amount of YSZ that is included in the sampling area. In addition, errors in EDX analysis are known to be high and are the most significant for light elements, such as oxygen (118).

6.3.3 Raman Spectroscopic Study of NiO Content of Partially Oxidized Ni/YSZ Anodes

6.3.3.1 Raw Raman Spectroscopy Peak Area Data

Raman spectroscopy should have some distinct advantages over other techniques for quantitatively determining the degree of Ni oxidation into the depth of a Ni-YSZ anode support layer cross-section. While the penetration depth of the photons in NiO is not as large as for electrons (e.g., in EDX), the penetration depth should be sufficient to give an accurate value of the degree of Ni oxidation. Further, NiO, Y_2O_3 and ZrO_2 all have unique Raman signatures,

while Ni should give no response, as metals have a very shallow photon penetration (< 5 nm) and do not exhibit vibrational modes (137). Figure 6.6A shows a typical Raman analysis of a fully oxidized NiO-YSZ anode cross-section, revealing a zirconia-related peak at ~600 cm^{-1} and two NiO peaks at 1100 and 1500 cm^{-1} that represent the principal Raman mode and magnon peaks of NiO (126), respectively, as was shown in Section 2.7.3. For the fully reduced Ni/YSZ sample, Figure 6.6B shows that the YSZ peak remains, but that the NiO peaks have essentially disappeared, as expected. Figure 6.7A shows the Raman spectrum of the epoxy filler alone, showing significant background intensity, likely due to fluorescence, while Figure 6.7B shows the effect of the epoxy in the Ni-YSZ anode samples, revealing an increase in the background intensity and a greater number of sharp stray peaks. It is clear that the presence of the epoxy can have a significant impact on the peak fitting of the Ni-YSZ data. It was generally found that lower porosity (e.g., in the oxidized regions) resulted in less interference from the epoxy, while the reduced areas (higher porosity, more epoxy) showed more interference, as would be expected. The 1500 cm^{-1} NiO peak was highly variable in magnitude, as was also shown by others (125), so only the 1100 cm^{-1} peak was selected for the analysis carried out in the remainder of this chapter.

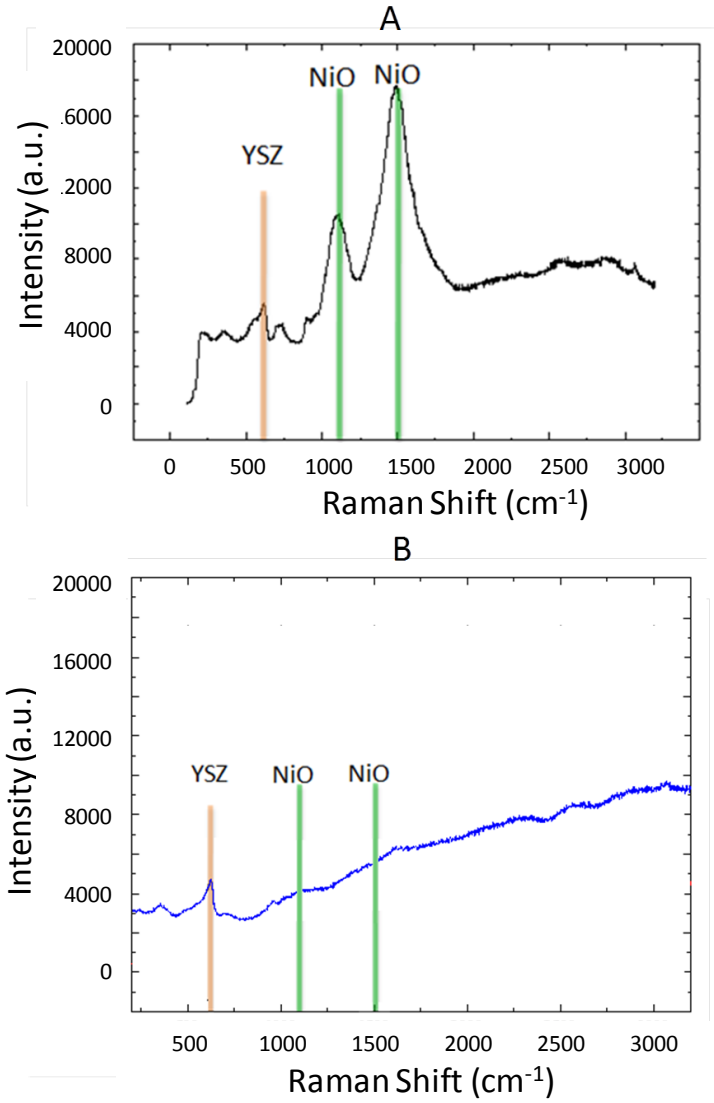

Figure 6.6. Raman spectra collected from cross-sections of (A) as-manufactured NiO-YSZ (i.e., in the fully oxidized state) and (B) of fully reduced Ni-YSZ (after reduction in H_2 at 800°C).

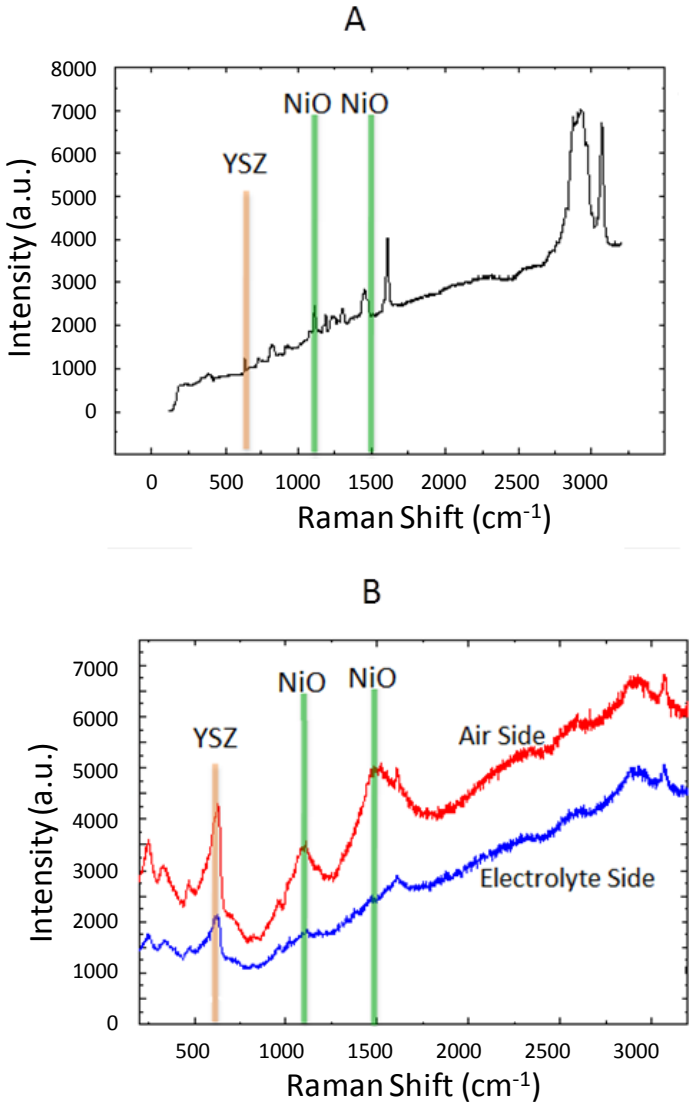

Figure 6.7. Raman spectrum of (A) epoxy, showing fluorescence, as is also seen in the background of the spectra (B) collected from an epoxy-mounted porous Ni-YSZ anode layer, partially oxidized (~50% by mass) at 900°C.

The raw NiO peak area (1100 cm^{-1}) maps for each of these samples are shown in Figure 6.8A to F. The Raman data were collected in raster-fashion across the anode layer at a constant depth, gradually moving towards the electrolyte (bottom side of each image), with a 5 µm

spacing between spectra, but with the 10 raster lines gradually penetrating through the thickness of the anode with a 20 μm spacing between lines. The 1100 cm^{-1} NiO peak area within each map, converted to color in Figure 6.8 (green indicates a high NiO content), was scaled in the same manner in each figure (with the exception of Figure 6.8A, which is scaled to allow the bright area to be viewed easier), where zero (black) indicates that there was no Raman signal (no NiO present) and an 8000 a.u. or greater peak area appears bright green (high NiO content). The overall first impression given by these Raman maps (Figure 6.8) is that there is a good qualitative match with the trends of the optical microscopy data, shown in Figure 6.4. A gradient in the NiO content can clearly be seen for samples with the Ni phase 50% oxidized at 700 to 900°C, but not for the fully reduced sample or the sample that was 50% oxidized at 600°C, for which the NiO peak area appears to be constant throughout the anode layer.

There are several features that immediately stand out in these NiO raw peak area maps. First, there is a large bright area nearly half-way down from the top of the Raman map of the fully oxidized sample (Figure 6.8A). As these samples were previously examined using SEM, the ~50 nm thick Au coating that was necessary for SEM analysis was polished off prior to the Raman analysis. This bright zone is likely a pore (or roughened area) that contains Au that was not removed in the polishing process. A Raman signal would not be expected from Au itself as metals have a very shallow photon penetration (< 5 nm) and do not exhibit vibrational modes (137). A thin Au film could easily block the Raman signal coming from the underlying NiO or, if some Au nanoparticles remained on the surface, the NiO signal could be enhanced due to surface enhance Raman scattering effects (148).

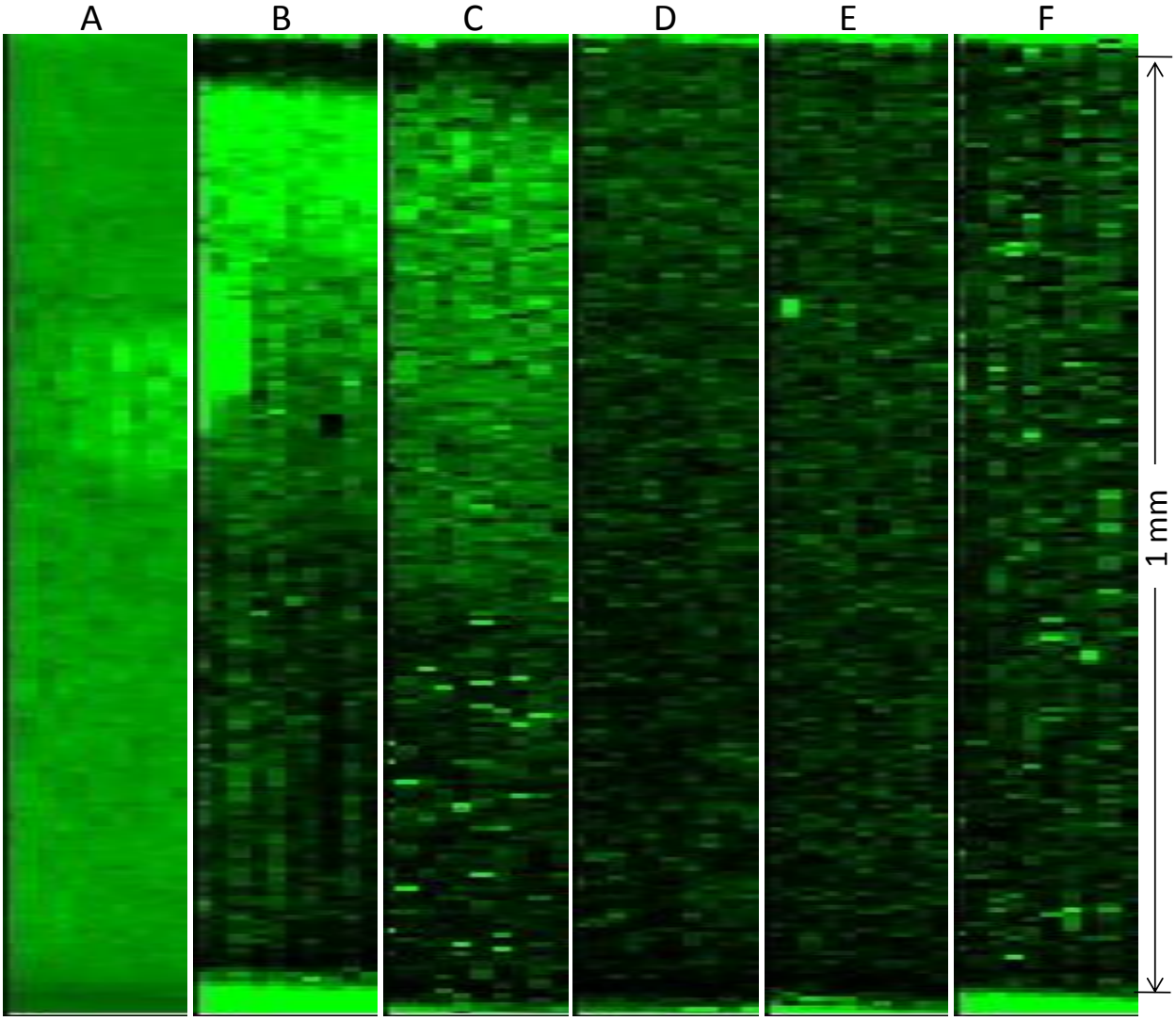

Figure 6.8. Cross-sectional Raman spectroscopy maps for the NiO 1100 cm^{-1} peak area for (A) a fully oxidized Ni-YSZ/YSZ sample, embedded in epoxy and polished, and for the same type of samples, but 50% oxidized (as determined by TGA mass measurements) at (B) 900, (C) 800, (D) 700, (E) 600°C, and (F) a sample that was fully reduced in H_2 at 800°C. All maps are normalized to the peak area of 8000 a.u., where a brighter green indicates a larger NiO 1100 cm^{-1} peak area.

It can also be seen in Figure 6.8 that the NiO signal is higher than expected in some regions (based on the optical data). Throughout the fully reduced sample (Figure 6.8F) and in the entire region near the electrolyte (inner 400 μm) in the Ni-YSZ samples that were partially oxidized at 800 and 900°C, for example, were not expected to exhibit an NiO signal (based on Figure 6.4). When adjacent spectra for the fully reduced and partially reoxidized (900˚C) samples (in the inner mostly metallic Ni region) are compared in Figure 6.9A and B, respectively, it can be seen that a small peak at 1100 cm^{-1} is seen in some spectra, but not others. For the fully reduced sample in Figure 6.9A, there are more spectra that do not exhibit the 1100 cm^{-1} peak. Interestingly, when the ten spectra are added together in Figure 6.9C, the resulting peak areas appear remarkably similar, even though the 50% oxidized 900˚C sample showed the 1100 cm^{-1} peak more consistently than did the fully reduced sample.

It was considered that the detection of NiO in regions where NiO was not expected may have been due to a small amount of NiO that has been trapped inside large Ni agglomerates during NiO reduction. It is known (74; 99) that reduction of NiO at 800°C will convert 99.5% of the NiO to Ni within 4 h, but full reduction to Ni is exceedingly slow. It is also possible that the anomalously high NiO peak area in some regions (Figure 6.8) arises from the presence of a thin (< 10 nm) oxide film that formed on the exposed Ni particle surfaces after the samples were removed from the TGA and exposed to air at room temperature. Thus, the peak area that is measured in these regions may not reflect the presence of NiO formed during the air exposure cycle in the TGA, but due to NiO that either did not reduce during H_2 exposure or formed at room temperature after removal from the TGA.

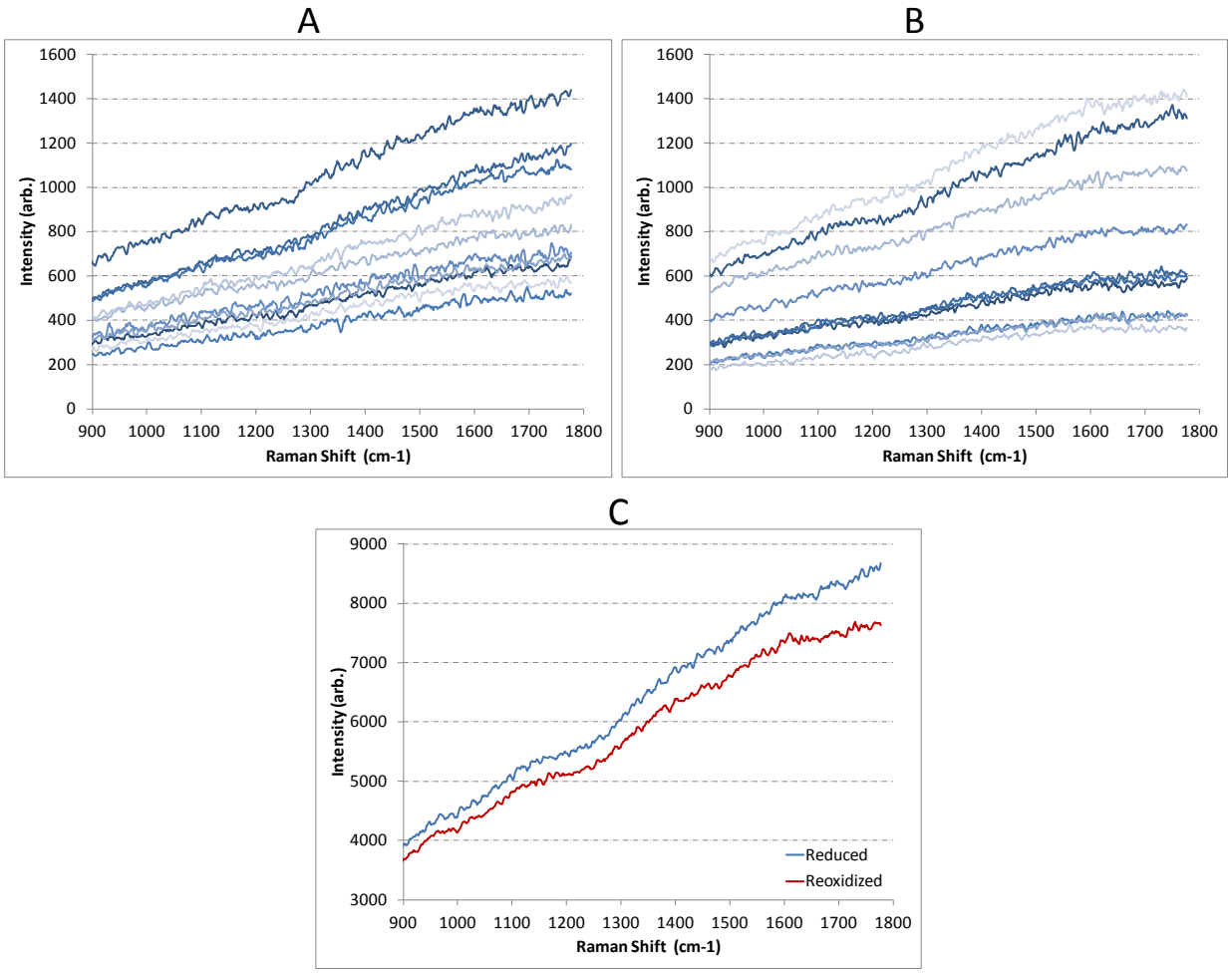

Figure 6.9. Raman spectra obtained from 10 adjacent locations in (A) within the fully reduced sample and (B) in the inner (less oxidized) region of the sample that was 54% oxidized at 900˚C. The ten spectra were then added together (C) in order to compare the overall oxidation depth of the two samples.

Finally, it is clear from Figure 6.8 that there are many locations where very bright (high NiO) and very dark (high Ni) spectra are seen immediately adjacent to each other. A closer examination of these spectra revealed that these differences in the area of the 1100 cm^{-1} NiO peaks are not real and are the result of spurious peak fits, as will be discussed further in Section

3.2. As can be seen in Figure 6.6B and Figure 6.9, there is a large amount of noise seen in some of the spectra and the peak fitting program was sometimes fitting the noise instead of the NiO peak area.

6.3.4 Processing Methods Used to Enhance the Quality of the Raman Peak Area Data

As discussed in Section 3.1, one of the main challenges related to the Raman work was the presence of spurious data points, largely due to sample fluorescence during spectra acquisition and also due to peak fitting program problems (resulting from variations in fluorescence and the peak area through the sample thickness). In order to allow a quantitative analysis of the Ni:NiO ratio to be carried out throughout the anode cross-section, best efforts were made to process the raw Raman data (Figure 6.8) to remove peak areas that are not real. As one example, in the case of the as-received sample in Figure 6.8A, most of the spectra are similar, with the majority of the spurious data seen in only one region of the anode cross-section, where it is suspected that some sputtered Au remains. Therefore, the removal of these spurious spectra without also removing reliable ones will show that the process is acceptable. If the criterion used to remove spectra are flawed, too many spectra will be removed and the remaining data could be expected to be more inconsistent (i.e. a higher standard deviation).

6.3.4.1 Fully Oxidized Ni-YSZ Anode Support Layer

The method of data processing is explained first for the as-received Ni-YSZ anode layer, which is fully oxidized, since the NiO signals would be the most pronounced and uniform into the depth of the anode layer in this case. Figure 6.10A shows the average NiO peak area that was obtained across the thickness of this anode with all of the spectra included. Each data point

represents the average 1100 cm^{-1} NiO peak area, obtained from the 10 spectra made at each at each 5 μm increment into the anode layer (i.e., each horizontal line of ten spectra in Figure 6.8A). These data points are plotted in Figure 6.10A as a function of distance from the air/anode interface (0 mm) towards the underlying electrolyte (1 mm). The trend line reflects the average of the 5 adjacent data points and the error bars represent the standard deviation of the 1100 cm^{-1} peak area in the 10 spectra examined.

It can be seen in Figure 6.10A for the fully oxidized anode that the NiO peak area remains relatively constant at each distance into the anode layer and that the standard deviation is quite low. However, consistent with what is observed visually in Figure 6.8A at 0.4 to 0.45 mm into the anode layer, an apparent increase in the NiO peak area is seen at this depth. As discussed above, this is likely due to the presence of the sputtered Au film in this region, which either blocks or enhances the underlying NiO signal, depending on the Au particle size. In any case, this results in a peak area with a high standard deviation.

In Figure 6.10B, it is observed that the majority of the spectra collected in the region where Au is present contain peaks with a Raman shift position that is higher than the 1100 cm^{-1} expected for NiO. Therefore, to remove these spectra from the results, the first criterion used was to keep only the NiO signals that are within the Raman shift range of 1090 to 1110 cm^{-1}. This led to the removal of 211 data points (of 2010 total) that came from spectra with shifts outside of this range, now giving the results shown in Figure 6.10C, for comparison with Figure 6.10A. It is seen in Figure 6.10C that the running average trend-line is smoother and the data now clearly have a lower standard deviation (smaller error bars).

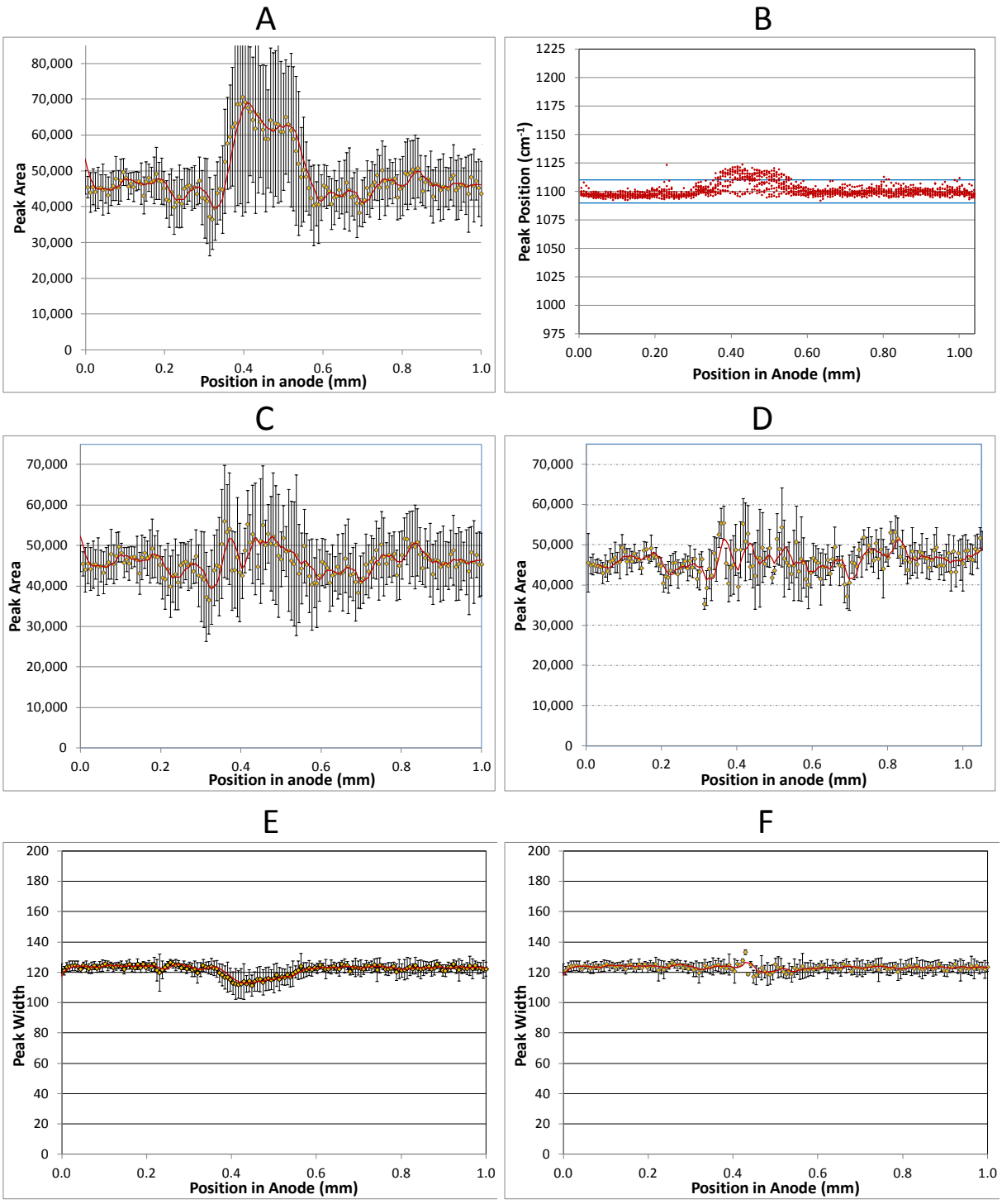
A
Peak Area
Position in anode (mm)
B
Peak Position (cm-1)
Position in Anode (mm)
C
Peak Area
Position in anode (mm)
D
Peak Area
Position in anode (mm)
E
Peak Width
Position in Anode (mm)
F
Peak Width
Position in Anode (mm)

Figure 6.10. Raman spectroscopy cross-sectional analysis of a fully oxidized NiO-YSZ/YSZ sample after manufacture at 1350°C, showing the NiO 1100 cm^{-1} (A) raw peak area data, (B) the Raman shift value, (C) peak area after removal of peaks outside a prescribed Raman shift window, (D) peak area after removal of areas that were significantly (> 1 standard deviation) too high or too low, (E) raw peak width data, and (F) peak width after the removal of spurious data. Each data point in these figures represents the average of 10 adjacent spectra, the error bars represent the standard deviation of the 10 adjacent spectra, and the red trendline represents a running average of 5 adjacent points (i.e., the average of 50 adjacent spectra).

To further improve the quality of the data, NiO peak areas that were greater than 1 standard deviation away from the mean peak area, all for the same distance into the anode support layer, were removed from the analysis. It can be seen in Figure 6.10D that, while the standard deviation improves, as should be expected, the trend line does not change significantly. It should be noted that the average NiO signal is ~45,000 in all cases, indicating that this method of data processing served only to smooth the data, rather than to perturb the NiO peak area.

The average width of the 1100 cm^{-1} NiO peak for the fully oxidized sample was also examined because it was noted that, after the removal of spurious spectra, the peak widths have a narrower distribution of values. Figure 6.10E and F show the peak width data for the as-received sample before and after, respectively, removal of peaks that were centered outside the Raman shift region of 1090 to 1110 cm^{-1}. It is seen that the NiO peak width for this fully oxidized sample is constant at 120 cm^{-1}, except for the region of Au contamination, where the peak width is narrowed. After removal of the spurious spectra (Figure 6.10F), the peak width was constant at

120 cm^{-1}. Thus, the method used for the analysis of the data in Figure 6.10 (for the fully oxidized NiO-YSZ sample) is considered successful and can now be employed for the remainder of the samples shown in Figure 6.8 (fully reduced and 50% oxidized at different temperatures).

6.3.4.2 Fully Reduced Ni-YSZ Anode Support Layer

The analysis of the Raman data for the fully reduced sample was particularly challenging, since the NiO peak area was small or nonexistent (Figure 6.8F and Figure 6.9A) and the interference from the epoxy matrix was expected to be more problematic due to the higher porosity of this sample. As an example, Figure 6.11 shows that, in some of the low NiO content areas, the peak fitting program (Wire 2.0) sometimes detected only a small peak area (1100 a.u.) when a NiO peak was clearly present (Figure 6.11A) and sometimes registered a very large peak area (6700 a.u.) when no obvious NiO peak could be seen (Figure 6.11B). Figure 6.12 shows the processed data for the fully reduced Ni-YSZ sample, using the same plots that were shown for the fully oxidized sample (Figure 6.10). Figure 6.12A shows the average peak area across the thickness of the fully reduced Ni-YSZ layer and, while some NiO is still detected, the magnitude and standard deviation associated with the peak area is very high. Figure 6.12B shows that the Raman shift position is much more scattered than seen in Figure 6.10B, being largely outside of the range of the typical NiO Raman shift position (1075 to 1125 cm^{-1}). This suggests that the majority of the NiO detected by Raman spectroscopy in this sample is spurious and that most spectra will be removed as the data is processed further.

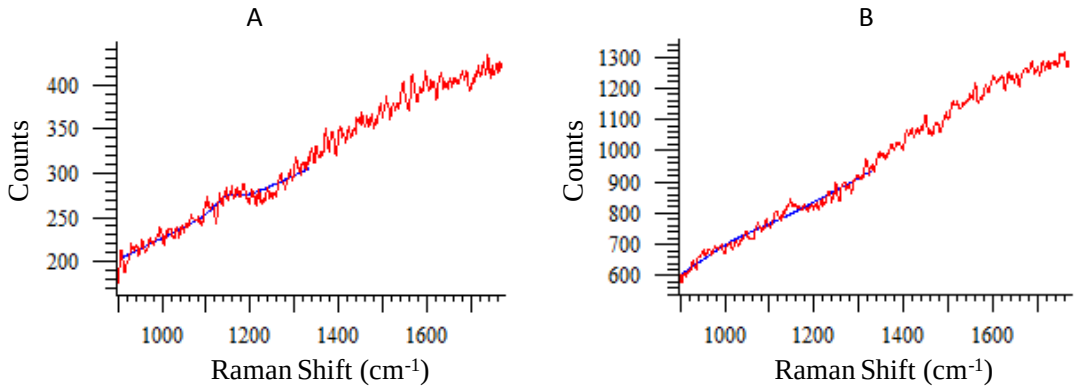

Figure 6.11. Example Raman spectra obtained for the fully reduced sample showing (A) a spectrum in which the 1100 cm^{-1} NiO peak can be clearly seen, but with a small peak area (1100 a.u.), and (B) a spectrum from a region that exhibited large fluorescence effects from the epoxy and no obvious 1100 cm^{-1} NiO peak, but a large NiO peak area (6700 a.u.) was measured.

Since it can be seen in Figure 6.10B that there is a cluster of spectra with a Raman shift position centered at ~1125 cm^{-1}, all of the peaks located within the Raman shift range of 1090 and 1150 cm^{-1} were included in the analysis, with the results shown in Figure 6.12C. The removal of spectra using this broader criterion than what was used in Figure 6.10 did not change the average peak area, which remained relatively high at ~2500 a.u. However, only 629 of the 2140 spectra were retained and the standard deviation was then still very large. Figure 6.12D shows the result after the removal of spectra with a peak area greater than 1 standard deviation from the mean, and only 429 spectra remain, thus making the interpretation of these results unreliable. The NiO peak width, before and after removal of the spurious spectra in Figure 6.12E and F, respectively, is ~80 cm^{-1} (with a high standard deviation), which is significantly lower than the ~120 cm^{-1} value seen for the fully oxidized anode in Figure 6.10.

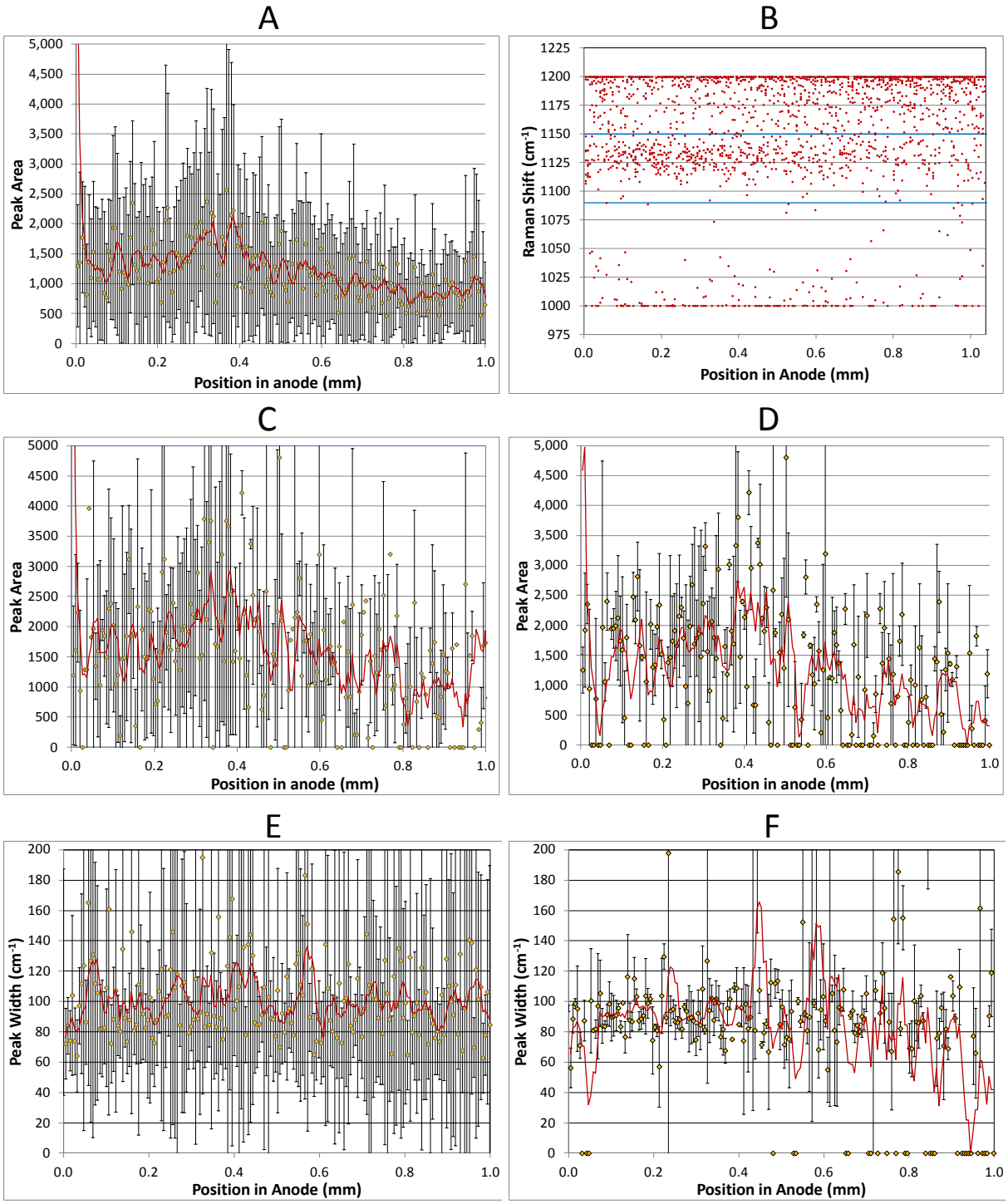
A
Peak Area
Position in anode (mm)
B
Raman Shift (cm-1)
Position in Anode (mm)
C
Peak Area
Position in anode (mm)
D
Peak Area
Position in anode (mm)
E
Peak Width (cm-1)
Position in Anode (mm)
F
Peak Width (cm-1)
Position in Anode (mm)

Figure 6.12. Raman spectroscopy cross-sectional analysis of an anode that was fully reduced at 800°C, showing the NiO 1100 cm^{-1} (A) raw peak area data, (B) Raman shift value, (C) peak area after removal of peaks outside a prescribed Raman shift window, (D) peak area after removal of areas that were significantly (> 1 standard deviation) too high or too low, (E) raw peak width data, and (F) the peak width after removal of spurious data. Each data point in these figures represents the average of 10 adjacent spectra, the error bars represent the standard deviation of those 10 adjacent spectra, and the red trendline represents a running average of 5 adjacent points (i.e., the average of 50 adjacent spectra).

In order to verify if there is a small NiO content in the fully reduced Ni-YSZ anode layer, x-ray photoelectron spectroscopy (XPS) was used to determine the NiO content, both on the exposed cross-sectional surface and into the depth of the sample. With no further surface preparation carried out (after Raman analysis in Figure 6.12), the surface was determined to be ~35% NiO, while after sputtering to remove ~10 nm of the surface material, the NiO content measured by XPS fell below the detectable limits of the instrument. This is consistent with the formation of a thin oxide scale on the exposed Ni particles in air at room temperature, but with essentially no measurable NiO content beneath the surface.

Raman spectroscopy is not expected to be sufficiently sensitive to detect the likely 2-3 nm thick NiO surface oxide scale on the surface of the cross-section. Also, since a scale of constant thickness should have a consistent impact on the 1100 cm^{-1} NiO peak area, which is not observed in Figure 6.9A, it is not likely that the small, but questionable, NiO signal that is observed in Figure 6.12 arises from the thin NiO scale on the exposed Ni particles, detected by XPS. Taken together, the high standard deviation associated with the NiO peaks collected from

the fully reduced sample, the lack of a 1100 cm^{-1} NiO peak in most spectra (Figure 6.12A), and the poor curve fitting results (Figure 6.11B), indicate clearly that the NiO peak area that is measured is spurious in nature.

It is likely that there are random locations within large agglomerates throughout the fully reduced specimen that contain NiO in the particle core, and these agglomerates would be exposed by polishing. These NiO peak areas will vary significantly because the agglomerate sizes would also be highly variable, with some agglomerates that are larger than 5 μm in diameter. However, the number of spectra that show the presence of NiO is very low (i.e., the Raman shift position is only at 1100 cm^{-1} in only 25% of the spectra) and the peak area of those that do suggest the presence of NiO could be quite high. It is concluded that the average NiO peak area measured for the fully reduced sample is not meaningful and therefore the NiO peak area cannot be used as the baseline value for a zero NiO content.

6.3.4.3 Ni-YSZ Anode Support Layer (50% Oxidized)

The data for the samples that were oxidized to a 50% level at 600 to 900˚C were processed using the same procedure as described above and are shown in their processed form in Figure 6.13 (similar to what is seen in D and F in both Figure 6.10 and Figure 6.12). The NiO gradient is observed to increase in slope as the oxidation temperature is increased. For the samples oxidized to 50% at 700 and 600°C (Figure 6.13C and D, respectively), the gradient is much less steep and the extent of Ni oxidation is spread more homogeneously into the depth of the anode layer, but there is still a small gradient seen in the sample partially oxidized at 600˚C.

A

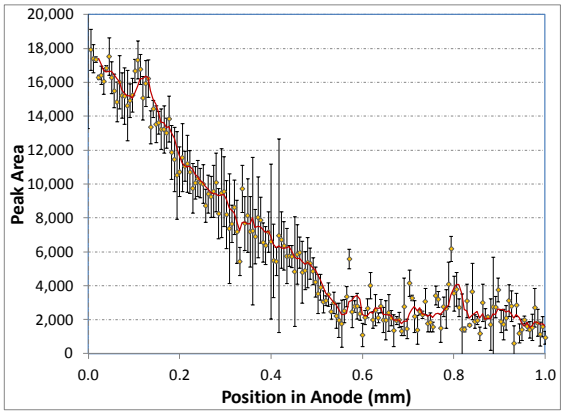
Peak Area
Position in Anode (mm)

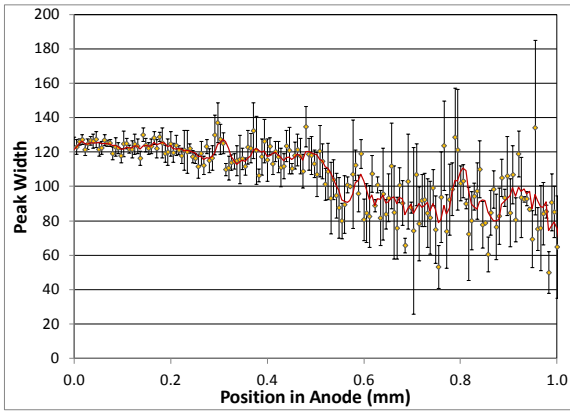
Peak Width
Position in Anode (mm)

B

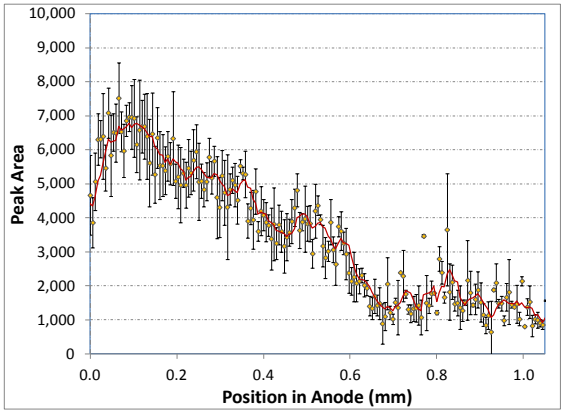
Peak Area
Position in Anode (mm)

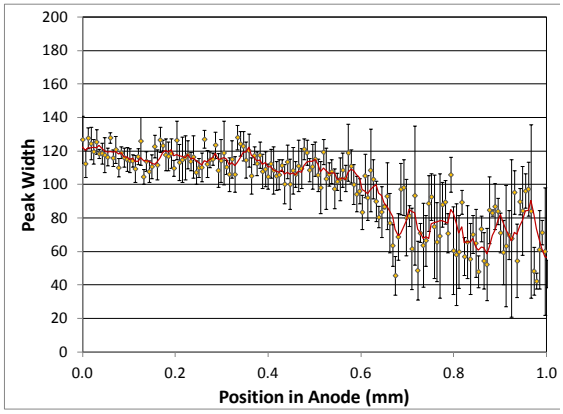
Peak Width
Position in Anode (mm)

C

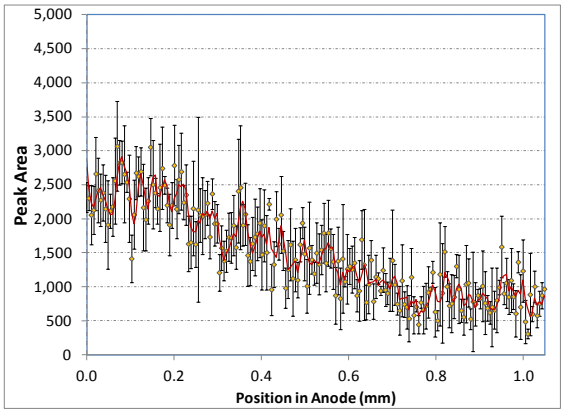
Peak Area
Position in Anode (mm)

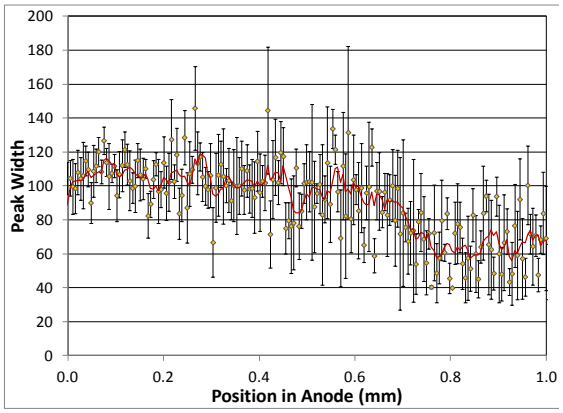
Peak Width
Position in Anode (mm)

D

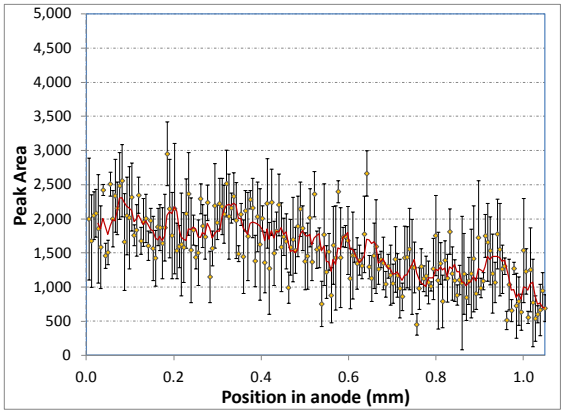
Peak Area
Position in anode (mm)

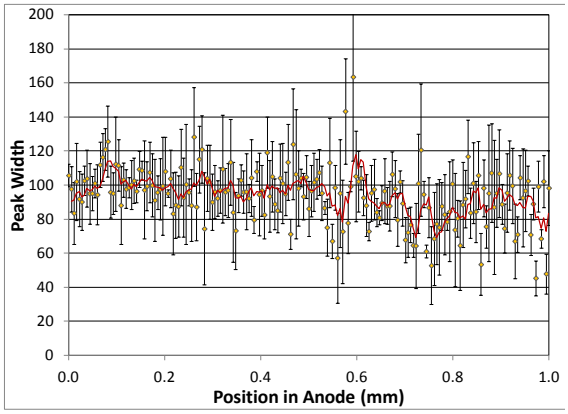
Peak Width
Position in Anode (mm)

Figure 6.13. Raman spectroscopy cross-sectional analysis of NiO concentration into the depth of a Ni-YSZ anode support layer that was partially oxidized (~50%) at (A) 900, (B) 800, (C) 700 and (D) 600°C, showing the NiO 1100 cm^{-1} peak area (left) and peak width (right) after full data processing.

The slopes of the gradients in Figure 6.13 are fully consistent with the raw data in Figure 6.8 for all oxidation temperatures. The gradients are also consistent with what is qualitatively observed in Figure 6.4, although the samples 50% oxidized at 800 and 900°C differ slightly. The gradient in NiO content that is seen in the optical cross-sectional microscope images (Figure 6.4D and E for 800 and 900˚C, respectively) appear to have a higher amount of NiO deeper into the anode layer that is followed by a steeper NiO gradient than is seen in Figure 6.13A and B. The difference that is observed is not significant and it is likely that this appearance exaggerated by the density difference between Ni and NiO (NiO is 70% larger by volume) and the problem of the sectioning of samples containing concentric spheres (shown to favor the dominant phase (147)). Thus, the gradients in the NiO content, observed in Figure 6.13A and B, are considered to be correct.

The Raman analysis has also allowed the quantification of the transition depth, i.e., the distance into the anode at which the predominantly NiO region converts to a predominantly Ni region, as summarized in Table 6.1. At 900˚C, Ni oxidation appears to have stopped at about 0.55 mm into the anode layer, while at 800°C, the gradient in the NiO concentration is seen (Figure 6.13B) to exhibit its transition at 0.6 mm into the anode. At 700°C, the transition from mostly NiO to mostly Ni occurs at 0.75 mm into the anode layer, while at 600°C, no transition point is seen. These results show that oxygen penetrates ever deeper into the anode

microstructure when the Ni-YSZ anode is exposed to air at lower temperatures, consistent with the less quantitative results, shown in Chapter 4.

Table 6.1. Summary of Raman Spectroscopy data (Figs. 10, 11 and 13).

Sample (Ox. Temp., Ox. Depth)	Depth Into Anode of Change of NiO Gradient[#] (mm)	Max/Min NiO Peak Area (x 10^3 a.u.)	Max. NiO Peak Width (Mean Raman Shift) (cm^{-1})	Min. NiO Peak Width (Mean Raman Shift) (cm^{-1})
A (1450˚C, 100%)	None	45/45	120 (1100)	120 (1100)
B (900˚C, 54%)	0.55	16/2	120 (1100)	90 (1110)
C (800˚C 46%)	0.6	7/1.5	120 (1100)	80 (1110)
D (700˚C 43%)	0.75	2.5/1	100 (1110)	80 (1110)
E (600˚C 50%)	None	2/1	90 (1110)	90 (1110)
F (N/A, 0%)	None	1.5/1.5	80 (1125)	80 (1125)

[#] Depth into the anode layer at which the gradient of the NiO content (Figures 10, 11 and 13) changes from a decreasing value to zero.

Interestingly, the peak width and peak position are also observed to change at this same transition point (i.e., at the depth at which the NiO gradient changes in Figure 6.13) at each temperature studied, as summarized in Table 6.1. The peak width decreases from 120 cm^{-1} to ~90 cm^{-1} and the peak position increases from 1100 to 1110 cm^{-1} at ~0.55 mm into the anode layer at 900˚C (Figure 6.13A). Likewise at 800˚C (Figure 6.13B), the peak width decreases from 120 cm^{-1} to 80 cm^{-1} and the peak position increases from 1100 to 1110 cm^{-1} when the gradient

changes at ~0.6 mm into the anode. At 700˚C (Figure 6.13C), the average peak width changes from 110 cm^{-1} to less than 50 cm^{-1} at 0.75 mm from the air ingress side of the cell, while at 600°C (Figure 6.13D), the peak width ranges from 90 to 60 cm^{-1}, but the peak position remains constant at 1110 cm^{-1} for all oxidation temperatures. The range of peak width and Raman shift positions that is observed for the four 50% oxidized samples (Figure 6.13) is between what is seen for the fully oxidized sample (120 and 1100 cm^{-1} in Figure 6.10B and F, respectively) and the fully reduced sample (60 and 1125 cm^{-1} in Figure 6.12B and F, respectively).

The changes in the Raman shift (peak position) and peak areas, shown in Table 6.1, could also be linked to changes in the Ni oxidation state (i.e., the stoichiometry of NiO) as a function of depth into each fully or partly oxidized Ni particle. This could be quite variable, considering the non-uniform conditions encountered in these anode layers. In the fully reduced sample, it is likely that any NiO retained in the core of a Ni particle is highly defective, with a higher Ni_2O_3 content. Likewise, a thin oxide layer coating a Ni particle is much more likely to have a high defect concentration, resulting in a higher Ni_2O_3 content. It has been in Section 2.5.1 that, when Ni is oxidized at lower temperatures (< 800°C), Ni_2O_3 is increasingly favored. Ni_2O_3 has a Ni-O bond length on the order of 2.047 versus 2.087 for NiO (149), which could cause a slight change in the oscillating dipole moment caused by the incident radiation. However, there are no published results for NiO to support this supposition.

Table 6.1 also gives the NiO peak width values, showing that they are 120 cm^{-1} for the fully oxidized sample and also for the outer regions of the anode layers that were partly oxidized at relatively high temperatures. Fully reduced Ni exhibits a peak width of 80 cm^{-1}. Consistent with this, the Raman shift is also always greater (and also has a wider distribution) in the deeper parts of the anode layers where the metallic Ni concentration is clearly higher. In Figure 6.14, the

combined spectra for 10 adjacent points (i.e., a summation of 10 spectra) near the anode surface (orange line) and near the electrolyte (red line) for an anode that was partially oxidized at 900°C are seen. The Raman shift and peak width data are indicated in the figure for each region of the sample, showing that the NiO peak is narrower and the Raman shift position is lower in the NiO-rich zone near the anode/air interface.

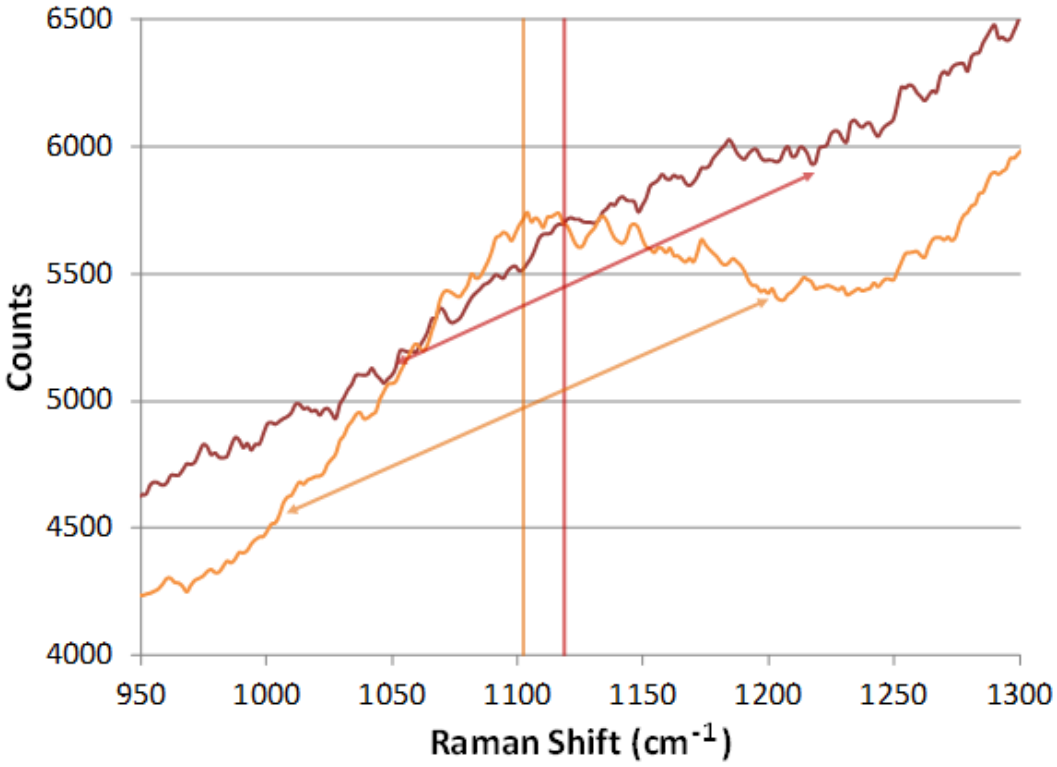

Figure 6.14. Combined spectra for 10 adjacent points near the anode surface (orange) and near the electrolyte (red) for an anode that was close to 50% oxidized at 900˚C.

It is also conceivable that the change in Raman shift position seen in Figure 6.14 is simply an artifact of the fluorescence from the epoxy, which could cause the high slope of the

baseline beneath the 1100 cm^{-1} peak. However, this shift may also be due to the thin NiO scale on the surface of the Ni particles that are exposed on the cross-sectioned surface. It has been shown (150) that, for very thin films, the Raman shift may be altered by the epitaxial growth of one material on the surface of another, especially if the substrate has a different crystal structure from the overlying material. Thus, in this case, very thin NiO layers may have NiO bond lengths that are distorted by the underlying Ni crystal structure.

6.3.5 Analysis of Raman Spectroscopy Determined Ni/NiO Depth Profiles

In terms of the fully oxidized (as-manufactured) sample, Table 6.1 shows that its average NiO peak area is much larger than for any of the other samples. This is peculiar, because the back-scattered SEM image of the cross-section of the sample that was 50% oxidized at 900°C in Figure 6.15, for example, shows that Ni is fully oxidized in the outer regions (50 μm) of the anode layer. In the image in Figure 6.15, Ni and YSZ are very difficult to distinguish, as both appear light grey or white. However, a light grey phase surrounded by a dark grey phase of constant thickness likely indicates a partially oxidized Ni particle and, by this criterion, the sample in Figure 6.15 is fully oxidized (dark grey with only a few suspected Ni core particles) in the outer (air side) 50 μm of the anode layer. Thus, the very high NiO signal for the as-manufactured (100 % NiO) sample does not match with what is seen for the NiO-rich regions of the partially oxidized samples.

It is possible that changes in the NiO morphology, which occur after Ni re-oxidation (Figure 6.5), are also responsible for some of the variations in the NiO peak areas seen in Table 1. A more cellular NiO structure that contains many micropores, as was seen in Figure 6.5B and C, would increase the roughness of the surface, which could effectively spread the Raman shifted

photons out over a larger area. This would lead to fewer photons returning through the objective lens of the microscope, potentially manifesting as a smaller peak area.

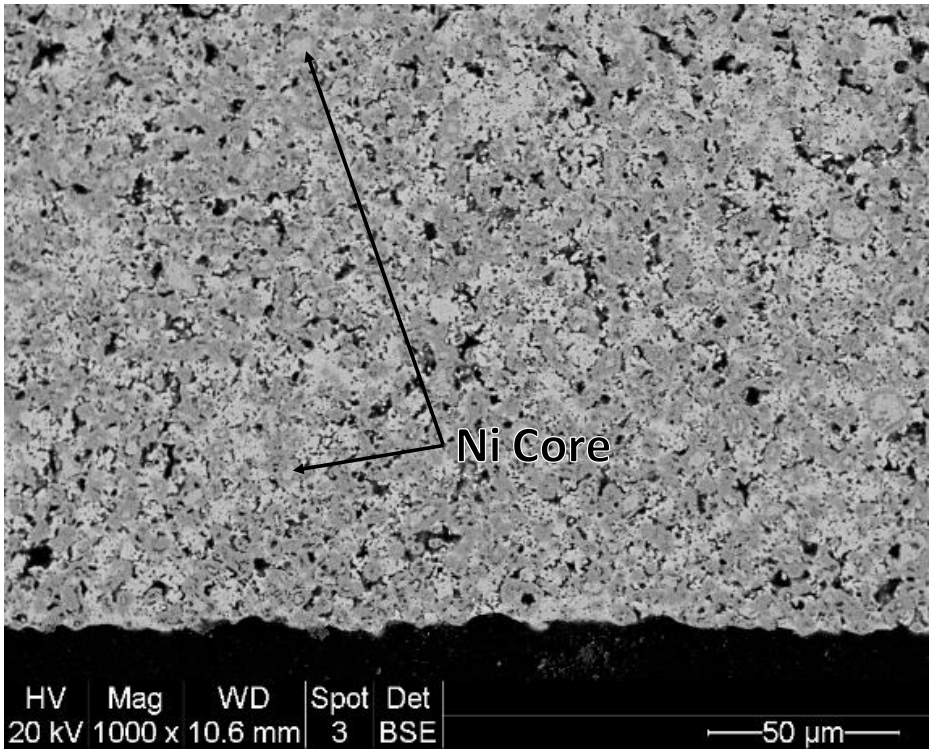

Figure 6.15. Backscattered electron SEM image of the outer (air ingress) side of a Ni-YSZ anode support layer, partially oxidized (54%) at 900°C. Ni and YSZ are difficult to distinguish (both are light grey or white), but NiO is the dark shade of grey. This sample appears to be 100% oxidized in the outer 50 µm surface region of the anode.

The large peak area differences in the NiO-rich regions may also result from the change in color (i.e., due to a change in Ni oxidation state) between the as-received sample (1450°C) and the sample re-oxidized at 600°C, which is quite dramatic, as seen in Figure 6.16. Even the sample re-oxidized at 900°C shows a small difference in color from the as-manufactured sample.

Indeed, oxygen-deficient NiO ranges in color from grey-green to grey and is commonly referred to as black nickel oxide, in contrast with stoichiometric NiO, which is green in color.

The observed differences in the NiO peak area between each sample (Table 1) could therefore be the result of a change in the absorption of incident photons due to changes in molar absorptivity of the various states of Ni oxide and due to a porous morphology that does not result in as much Raman scattered light returning back to the objective lens as a flat polished sample would. The most significant differences in morphology and color are between the as-manufactured (100% NiO) anodes and all of the 50% reoxidized samples. Thus the Raman data for the fully oxidized sample should not be compared directly (i.e., as a standard peak area for full oxidation) with the data obtained for the partially oxidized samples.

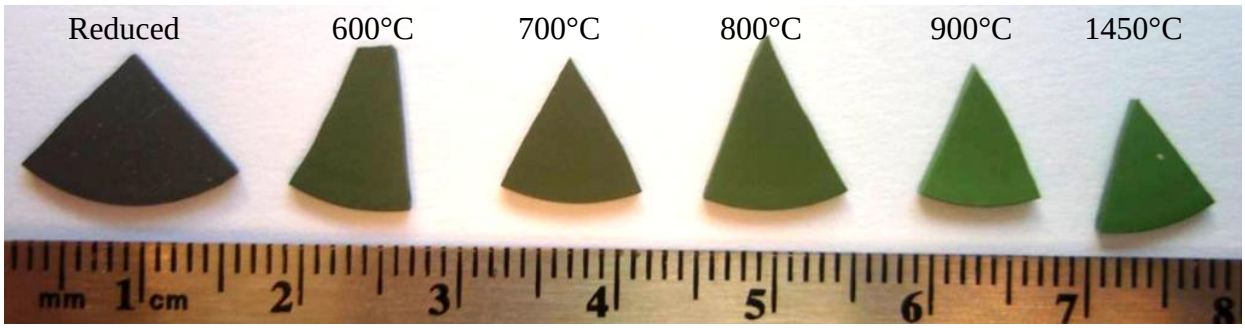

Figure 6.16. Color of fully oxidized Ni-YSZ anode samples as a function of oxidation temperature as compared to the reduced cell (on left) and a fully oxidized cell as-manufactured at 1450°C (on right), showing increasingly grey-green color as the temperature of oxidation is decreased.

In Figure 6.17, the peak area data for all of the 50% oxidized samples are combined together, showing that the total NiO content (equivalent to the total area beneath the curves),

which should be constant at ~50% at each oxidation temperature, varies greatly. This is related to the discussion above regarding why the NiO Raman signal varied between samples, probably best explained by changes in the defect chemistry (oxidation state) of Ni oxide, resulting in differences in color (Figure 6.16) as a function of the temperature of oxidation. As was shown in Table 1 and is clear from Figure 6.17 the total Ni oxide versus Ni content of the anode layer thus appears to decrease as the temperature of oxidation to 50% of the Ni content decreases. However, this is definitely not the case, as known from the TGA mass measurements in Figure 6.3.

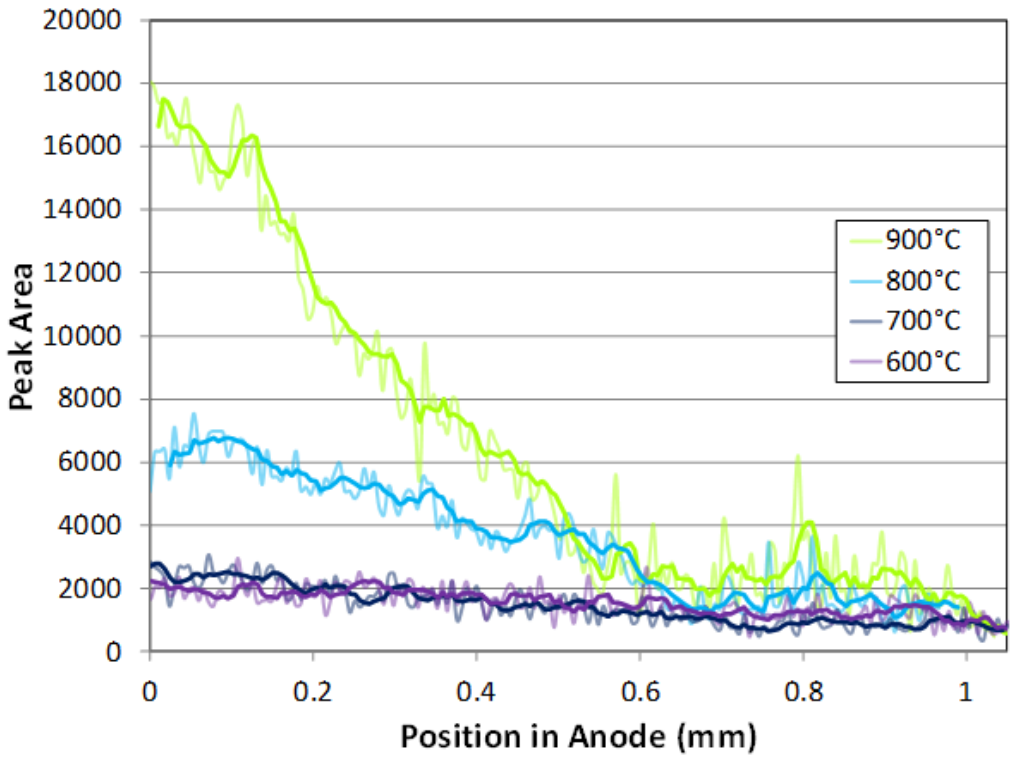

Figure 6.17. NiO peak area as a function of depth of Raman analysis into 50% oxidized Ni-YSZ anode support layers as a function of oxidation temperature.

While none of the factors that have been discussed above directly threatens the use of the Raman technique for accurately and quickly determining the gradient in the NiO content through the thickness of a partially oxidized Ni-YSZ anode layer (Figure 6.13, Table 1), it remains of interest to determine more precisely how much NiO vs. Ni is present as a function of distance into the anode. The data in Figure 6.17, therefore require adjustment to compensate for the factors (discussed above) that are likely affecting the yield from each sample differently. Therefore, to facilitate comparison, the Raman-determined gradients in the NiO peak area with depth into the anode (Figure 6.13) were linearized and then normalized to 100%, based on their known oxidation depth, as shown in Figure 6.13. The data for the as-manufactured 100% oxidized NiO-YSZ and the fully reduced sample were left out of this analysis for the reasons that were explained above.

The slope of the gradient in each sample was maintained as constant and the gradient line was adjusted up or down so that the area under it was equal to the known total oxidation depth of the cell (Figure 6.3), with the results shown in Figure 6.18. As was also discussed above (Figure 6.15), the outer 50 μm of the anode that was 50% oxidized at 900˚C is considered to be fully oxidized and the peak area in this region is considered as 100% in Figure 6.18, with no other adjustments made to it. It can now be seen in Figure 6.18 that the sample that was 50% oxidized at 900^{o}C again has the steepest NiO concentration gradient into the anode layer, with the lowest quantity of NiO seen closest to the electrolyte. In comparison, the 700 and 800^{o}C 50% oxidized samples appear now to have a similar NiO content to the 900˚C sample in the region closest to the electrolyte (Figure 6.18).

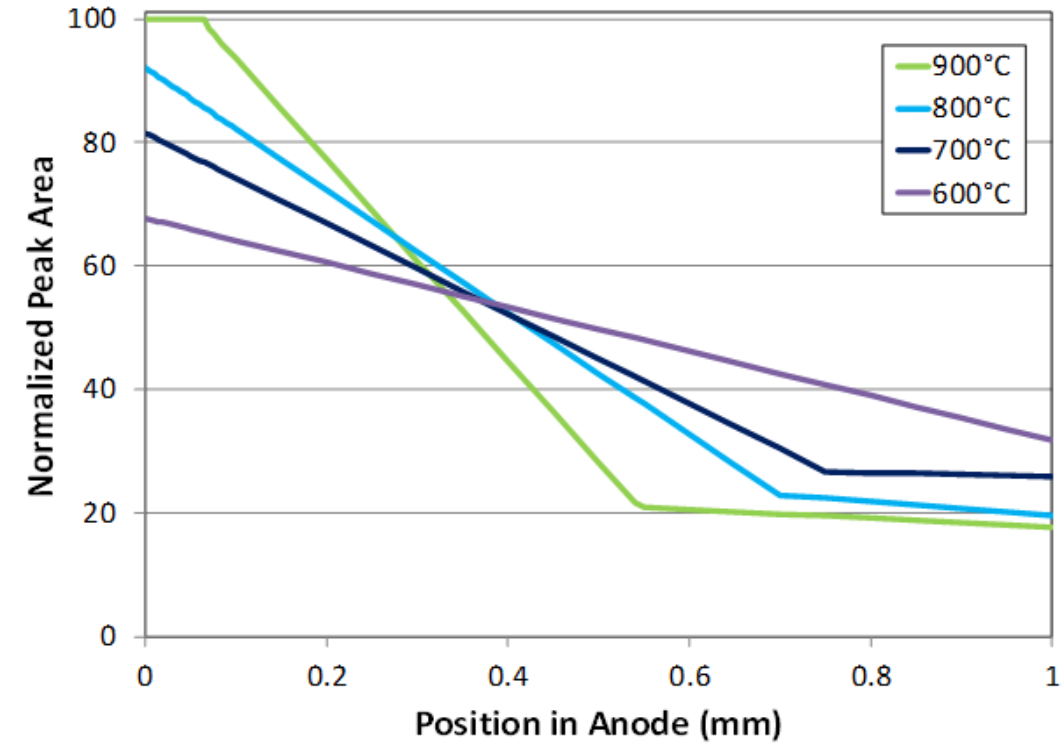

Figure 6.18. NiO peak area as a function of depth of Raman analysis into 50% oxidized Ni-YSZ anode support layers as a function of oxidation temperature, with the peak area data adjusted to match the actual oxidation depth from TGA data (Figure 6.3). The slopes were not adjusted.

It can be seen in Figure 6.18 that, with the adjustments made to Figure 6.17, the oxidation depth of the region adjacent to the electrolyte for the samples partially oxidized at 800 and 900˚C is now ~20%. In Chapter 4, this zone was considered to be unoxidized, but in a Ni-YSZ anode with an average Ni agglomerate diameter of 2 μm, the NiO scale thickness is < 100 nm thick when it is 20% oxidized. Since a layer this thin is difficult to see, SEM cannot be used to confirm if Raman derived gradient lines are correct. Therefore, XPS analysis was carried out in this

region of the 700, 800 and 900˚C samples and, after sputtering the surface of the cross-section and correcting for the volume and concentric sphere (147) errors, it was found that the NiO content was 32, 22 and 18%, respectively. These results agree very well with the adjusted results shown in Figure 6.18, arguing also for the validity of the data processing steps carried out.

6.4 Summary

In a prior study, it was found that the severity of cracking of the thin YSZ electrolyte in Ni-YSZ anode-supported solid oxide fuel cell (SOFC) specimens as a result of high temperature oxidation is correlated with the steepness of gradient of the NiO content into the anode layer over the course of air exposure. However, the use of microscopic methods to map the NiO content into the depth of the anode layer is time consuming and subject to high errors. Therefore, a new method for determining the NiO gradient through the anode layer was desired. Here, Raman spectroscopy mapping of the cross-sections of Ni-YSZ anode support layers, oxidized to 50% at various temperatures, was carried out to determine the NiO gradient more quantitatively.

After careful data processing to remove spurious Raman spectra, e.g., those affected by fluorescence of the epoxy filler or those spectra that resulted in a poor peak fit, it is shown that the NiO gradient at each oxidation temperature is linear, but with a slope that increases proportionally with temperature. When the anode layers were 50% oxidized, earlier imaging work had suggested that the inner regions (adjacent to the electrolyte) were in the metallic Ni form at 800 and 900°C. However, the Raman data suggest otherwise, giving extents of oxidation of ca. 20% in this region. This has been confirmed by X-ray photoelectron spectroscopy analysis, indicating that the amount of NiO present near the electrolyte in these two samples is 22 and 18%, respectively.

These results thus demonstrate that Raman spectroscopy, while requiring careful data processing in order to remove extraneous and incorrect spectral features, is a very good technique for quickly and accurately mapping the extent of Ni oxidation through the thickness of a Ni-YSZ anode layer. This also opens the door for modelers to better understand the complex oxidation process, involving gas transport issues as well as Ni oxide crystal growth kinetics, of Ni particles distributed in a thick, porous layer.

Chapter Seven: **In Operando Mass Measurements at High Temperatures: Protecting Ni-YSZ Anodes from Air Exposure Damage**

7.1 Introduction

An easily implemented approach for stopping (or at least slowing down) the formation of NiO during air exposure of Ni-YSZ anodes at high temperatures that has been considered previously (104; 108) involves the application of a negative bias to the anode during air exposure to electrochemically reduce NiO as it forms. However, as discussed in Section 2.6.1, it was not possible to conclusively show that NiO formation had been fully prevented. The primary aim of the present work was therefore to determine quantitatively and conclusively whether Ni oxidation in a Ni-YSZ cermet anode can be fully or partially prevented by the application of a reverse bias. Results obtained using both *ex situ* microscopy and a new *in operando* thermogravimetric analysis (TGA) method are presented here.

7.2 Experimental Methods

For the purpose of the results presented in this chapter, ESC-1 cells were used, as described in Section 3.1.3. All redox cycles were carried out in a TGA, as detailed in Section 3.2, with the *in operando* TGA procedure outlined in Section 3.2.5. Section 3.4.1 describes the analysis of the anode layers that was carried out by SEM and optical microscopy.

7.3 Results and Discussion

As discussed in Section 2.6.1, previous work (108) showed that the application of a cathodic potential (up to -350 mV vs. a Pt RE in a half-cell study) to a Ni-YSZ electrode during air exposure will result in a smaller polarization resistance (R_p) after H_2 was returned to the cell compartment, in comparison with the cell performance prior to air exposure. However, with the application of a negative current density of at least -15 mA/cm^2, it was demonstrated that the R_p of the anode will not improve (i.e., decrease) (108). Since an improvement in R_p has been correlated with Ni oxide formation followed by NiO reduction (74; 94), it was therefore concluded that the anode could be protected by the application of negative currents of this magnitude, but not at a cathodic voltage bias of only -350 mV.

However, when -350 mV potential was applied (vs. RE), the current density in air, which was initially -35 mA·cm^{-2}, continuously decreased to -10 mA·cm^{-2}, while at an applied current of -15 mA·cm^{-2}, the overpotential during air exposure slowly increased from -350 mV to a high of -1050 mV (108). These results suggested that the resistivity of the anode was increasing with time in air, which could indicate that Ni was slowly forming NiO. Thus, it was demonstrated that, with the use of only electrochemistry (108), it was not possible to determine with certainty if the Ni phase was being protected by the application of a reverse bias to the cell during air exposure. In the present work, both microscopy and *in operando* TGA methods were therefore used to help answer this question.

7.3.1 Ex Situ Analysis of Reverse-Biased, Air-Exposed Ni-YSZ Electrodes

Evidence of subtle microstructural changes (grain size, etc.) in the Ni phase after a full Ni oxidation/NiO reduction cycle, followed by a normal cell cool-down step, was shown in Chapter

4. However, in Figure 4.2, it can be seen that these changes in the Ni phase of an electrolyte-supported anode were subtle when viewing large agglomerates and impossible to see in small agglomerates. Further, it is likely that, due to the rapid sintering rate of Ni at 800°C, any evidence of these Ni surface alterations will very quickly disappear (73; 94).

An additional problem with the use of *ex situ* SEM analysis to identify subtle microstructural changes is that the surface morphology of Ni particles can likely also be altered as a result of partial or even localized Ni oxidation. Thus, even if Ni surface microstructural changes are found, it is impossible to determine if the evidence of localized oxidation is the result of a thin surface NiO layer (that would not be damaging to the cell) or if is the result of a full Ni oxidation. This approach was therefore not pursued further in the present work.

An alternative strategy for preparing and examining an electrolyte-supported cell *ex situ* was therefore necessary. To this end, two cells were subjected to the oxidation cycle described in Figure 3.8. One cell (the "biased" cell) had a -4 V bias applied to the Ni-YSZ electrode (vs. a Pt RE in 2-electrode configuration), and the other cell (the "unbiased" cell) was allowed to remain at the OCP during the 1 hour period of air exposure. Both cells were then rapidly cooled ($10^{o}C \cdot min^{-1}$) to room temperature in air, with the bias still applied in the case of the biased cell.

The cross-sectional optical image of these cells, after sectioning, mounting in epoxy, and polishing, is shown in Figure 7.1A and B for the unbiased and biased cells, respectively. In these optical micrographs (Figure 7.1), Ni can be distinguished from NiO and YSZ on the polished surface, due to its significantly more reflective surface after polishing. NiO is usually distinguishable from YSZ, as NiO has a green or black color versus the light grey color of YSZ, although a color camera was not used to collect the images shown in Figure 7.1. These images, which were obtained at 400X magnification, showing the YSZ electrolyte at the top, the 15 μm

thick Ni-YSZ WE between the yellow lines, and the Pt current collecting layer at the bottom of the image.

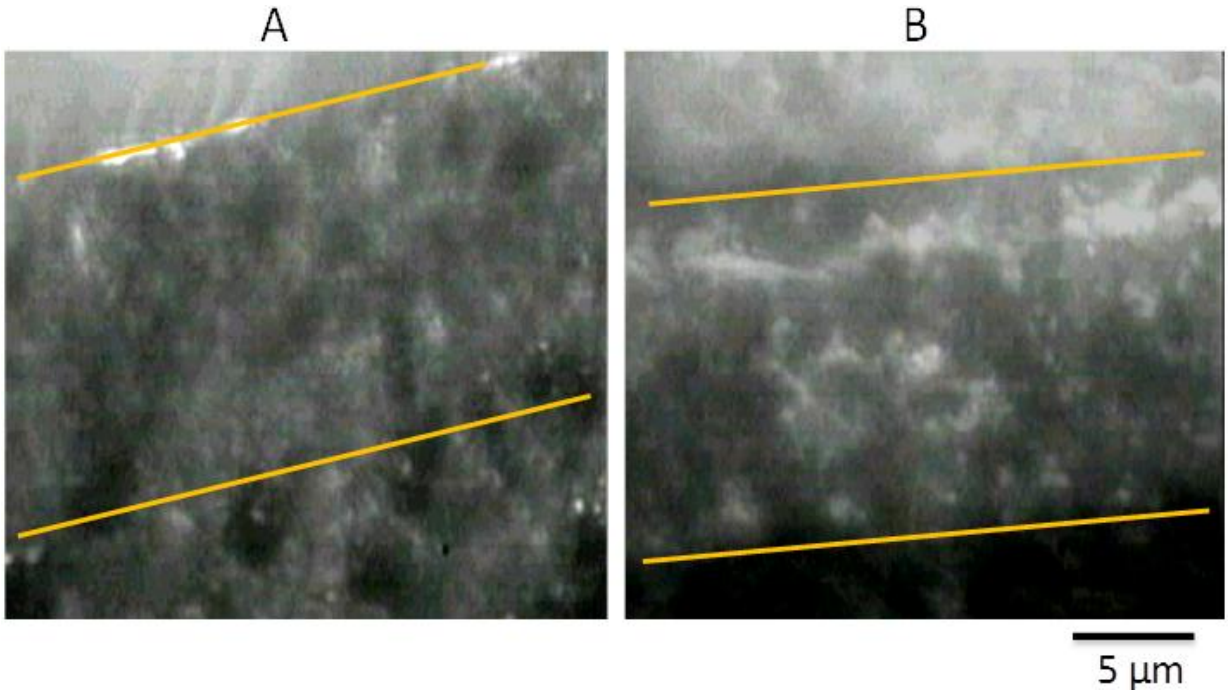

Figure 7.1. Optical microscope image (400X magnification) of the cross-section of two electrolyte-supported cells, for (A) the unbiased cell (the cell held at the OCP during air exposure at 800˚C) and (B) the biased cell (a -4 V cell bias was applied during air exposure at 800˚C and during rapid cooling to room temperature). Both samples were polished and thus the more reflective surfaces appear bright (Ni), less reflective surfaces appear grey (NiO and YSZ), and pores appear black. The Ni-YSZ electrode layers, encompassed by the yellow lines, are 15 µm thick, with the electrolyte layer shown at the top of the images.

While the quality of the images in Figure 7.1 is not very high at the magnification used, largely due to the highly porous electrode structure and also the inherent depth of field limitations of optical microscopy, distinctive changes in the Ni composition and distribution can

be seen. When comparing the unbiased cell (Figure 7.1A) to the biased cell (Figure 7.1B), more metallic (shiny) Ni regions are seen in the latter case. Qualitatively, these results do therefore indicate that some protection has been given to the Ni phase by the -4 V bias during air exposure. Further, there appears to be more metallic Ni near the electrolyte in the biased cell (top of the image) than deeper into the anode in Figure 7.1B, indicating that there may be more protection offered in the electrochemically active region near the electrolyte, as would be expected.

Scanning electron microscope (SEM) images of the unbiased cell (cooled after 1 h of air exposure in the open circuit, unbiased condition) are seen in Figure 7.2A (secondary electron) and B (backscattered electron), while the same types of images for the biased cell (cooled after 1 h in at a -4 V reverse bias in air) are seen in Figure 7.2C and D, respectively. When imaging via back-scattered SEM, NiO appears dark grey, Ni appears a very light grey, and YSZ appears white. The difference in contrast between Ni and YSZ can be minor in backscattered SEM images and thus these two phases are often very difficult to distinguish from one other.

As can be seen in the secondary electron images in Figure 7.2A and C, the Ni-YSZ electrode used has a high porosity. The biased sample (Figure 7.2C) appears to have a higher porosity after the air exposure and cool-down periods. This suggests that the cell is less oxidized, since the NiO occupies a ~70% greater volume than the equivalent amount of Ni. However, high errors result from the interpretation of high magnification SEM images because of the inherent variability of the morphology of Ni-YSZ anodes and because of variations in image contrast and brightness settings between image acquisitions.

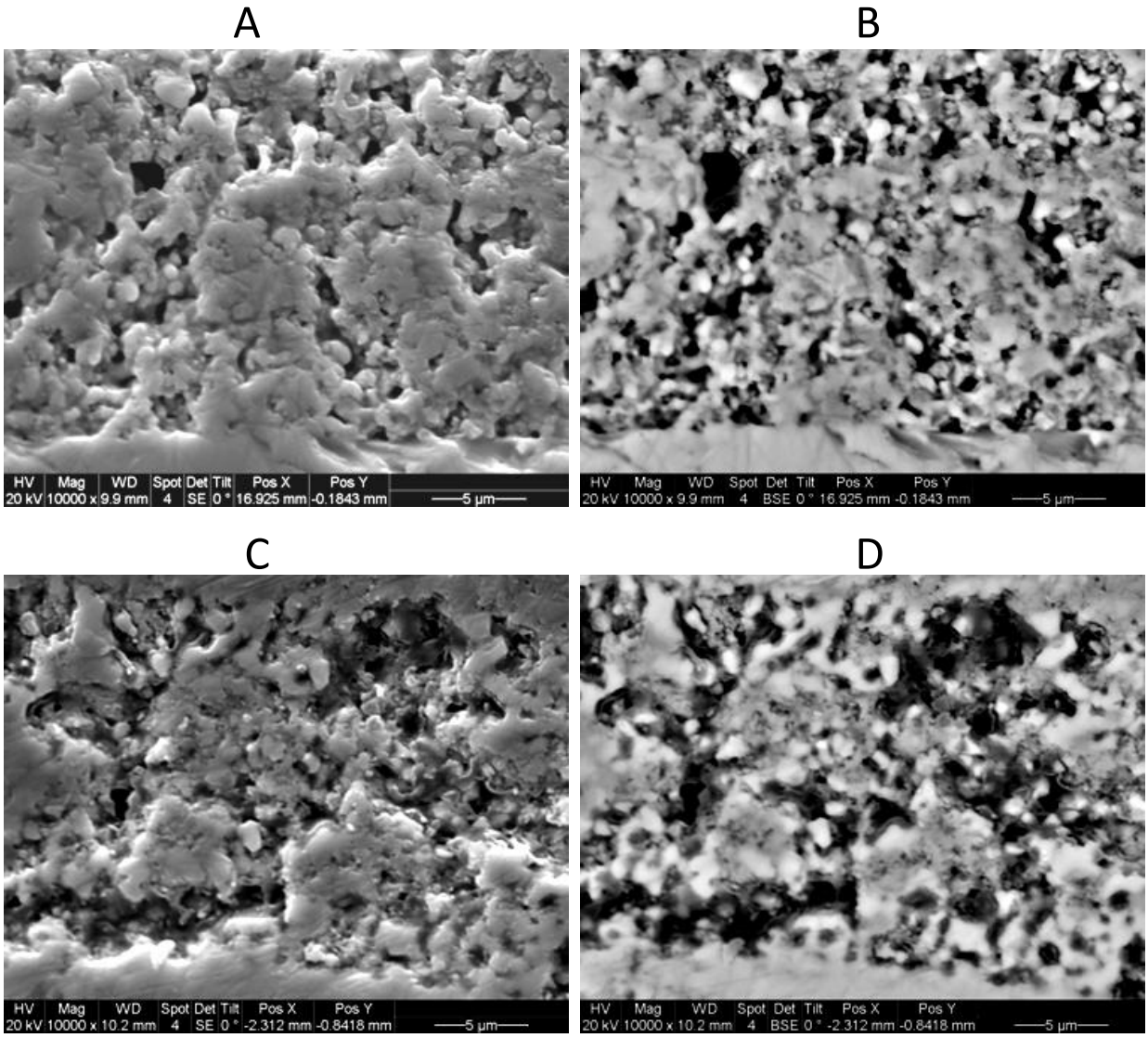

Figure 7.2. Polished anode cross-sections showing (A) a secondary electron image of the Ni-YSZ anode in the unbiased cell (the cell held at the OCP during air exposure at 800˚C and during the rapid cool-down), (B) a backscattered electron image of the same region as in (A), (C) a secondary electron image of the Ni-YSZ anode in the biased cell (a -4 V cell bias applied during air exposure at 800˚C and during the rapid cool-down, and (D) a backscattered electron image of the same region as in (C). In the backscattered images, NiO appears dark grey, but Ni (light grey) and YSZ (white) are difficult to distinguish.

In Figure 7.2B and D, the Ni (light grey) and YSZ (white) are difficult to distinguish from each other due to the similarity of the phase contrast in the images. NiO appears dark grey and it appears that the cell that was biased (Figure 7.2D) has a lower amount of NiO than the unbiased cell (Figure 7.2B). The white phase is YSZ, as confirmed by EDS (energy dispersive x-ray spectroscopy), but attempts to ascribe the light grey phase within the core of the dark grey phase surrounding it to metallic Ni were unsuccessful, as Zr could always be detected in addition to Ni in those sites. As with secondary electron images, there can be differences in the backscattered electron images due to differences in cell variability and due to difference in the contrast and brightness settings between images. However, there can also be significant errors due to the surface roughness of the sample. Surfaces that are very rough (i.e., porous), such as the microstructures seen in Figure 7.2A and C, make phase differentiation in the backscattered electron images very difficult, since surface roughness can obscure differences due to atomic number.

The cell cool-down process could also be causing a change to the Ni/NiO phase distribution in the biased cell. This could result because the current would be expected to decrease significantly as the temperature is decreased at a constant voltage bias. Thus, as the temperature is decreased, the degree of protection offered as the sample cools down is also lowered. Further complicating the interpretation of the results obtained from the biased cell is the condition of the cell once it had been cooled to room temperature. Although electrolyte cracks cannot be seen in Figure 7.1A or Figure 7.2C, the thick electrolyte of the biased cell was severely fractured and the cell was held together by the current collectors. This cracking could be the result of the rapid cooling rate employed or due to the application of a potential across the cell during cell cool-down.

The differences seen in the microstructure of the Ni-YSZ layers of the biased and unbiased cells, as seen by optical microscopy (Figure 7.1) and SEM analysis (Figure 7.2), are generally subtle and, as a result, are subject to very large errors in quantification. Overall, these many uncertainties demonstrate why post-analysis using *ex situ* microscopy methods to determine what fraction of the Ni phase (or of the individual Ni particles) in Ni-YSZ anodes may have been protected from oxidation is not very productive. While the results shown in Figure 7.1 do suggest that more Ni oxidation had occurred during OCP air exposure at 800˚C, vs. while under a -4 V bias, these results are still only qualitative. Thus, the *in operando* TGA method was investigated to achieve this goal more quantitatively.

7.3.2 In Operando 2-Electrode Half-Cell (Ni-YSZ WE, YSZ, Pt CE, H_2) Study in H_2 in the TGA

Our earlier EIS study (108) and the imaging results discussed above have suggested that a negative bias applied during air exposure can, at least partly, protect the Ni phase from oxidation during air exposure of Ni-YSZ anode layers at high temperatures. However, the prevention of cell performance activation by the negative bias, as inferred from the EIS data before and after air exposure (108), does not necessarily mean that no NiO had formed, and the optical imaging results in Figure 7.1 are also still quite qualitative. Thus, the goal here was to quantitatively monitor the mass of the cell *in operando* during negative polarization under various gas atmospheres, using a redesigned TGA sample holder to hold and connect to the cell (Figure 3.7).

To first ensure that reliable electrochemical data could be obtained from the cell test apparatus, situated inside the TGA chamber, an initial set of open-circuit EIS experiments, as well as cyclic voltammetry (CV), were carried out. The data obtained from this baseline study,

involving a 2-electrode half-cell configuration, could then be compared to the results obtained from conventional *ex situ* SOFC experiments (108), which utilize cells manufactured in exactly the same way. There are still some differences, however, that arise due to the requirements of the TGA, including longer Pt lead wires, Pt paste vs. Ni paste for WE current collection, and a lower overall pH_2. In the TGA, the backing gas (He that was 3% humidified through a bubbler) is required to protect the balance from harmful reactive gases. The 10% H_2-He, which is mixed with He prior to reaching the furnace, comprises 20% of the flow and results in an overall 2.5% H_2O-2% H_2-He gas composition (termed 'H_2' hereafter). This is a much lower pH_2 than employed in our normal electrochemical studies (108), which used 3% H_2O-H_2.

Electrochemical impedance spectroscopy (EIS) and cyclic voltammetric (CV) data were both collected from the cell located inside the TGA, all in the humidified H_2 environment at 800˚C. It can be seen in Figure 7.3A that R_p (the diameter of the arcs) is initially very high, but after running the CVs shown in Figure 7.3C, the cell became significantly activated, as seen in Figure 7.3B. The R_s and R_p values decreased from 7 $\Omega \cdot cm^2$ and 580 $\Omega \cdot cm^2$ to 6.8 $\Omega \cdot cm^2$ and 15.2 $\Omega \cdot cm^2$, respectively. It was noted that, if the cell was idle at open circuit for more than 6 h, R_p once again increased, which is typical of anode deactivation effects. In both Figure 7.3A and B, three arcs are seen (presumably one for the CE and two for the WE), although in Figure 7.3A, the high frequency arc is barely visible. The low frequency arc is seen to decrease the most in its diameter after CV cycling. This suggests that the majority of the cell activation (Figure 7.3 A and 6B) is likely due to gas transport phenomena, since it has been reported (151) that these low frequency arcs for Ni-YSZ anodes in humidified H_2 may be due to gas diffusion limitations within the pores of the anode. In these *in operando* TGA experiments, it is quite likely that the

low pH_2 used is responsible for this large initial arc, rather than being a characteristic of the Ni-YSZ anode layer itself.

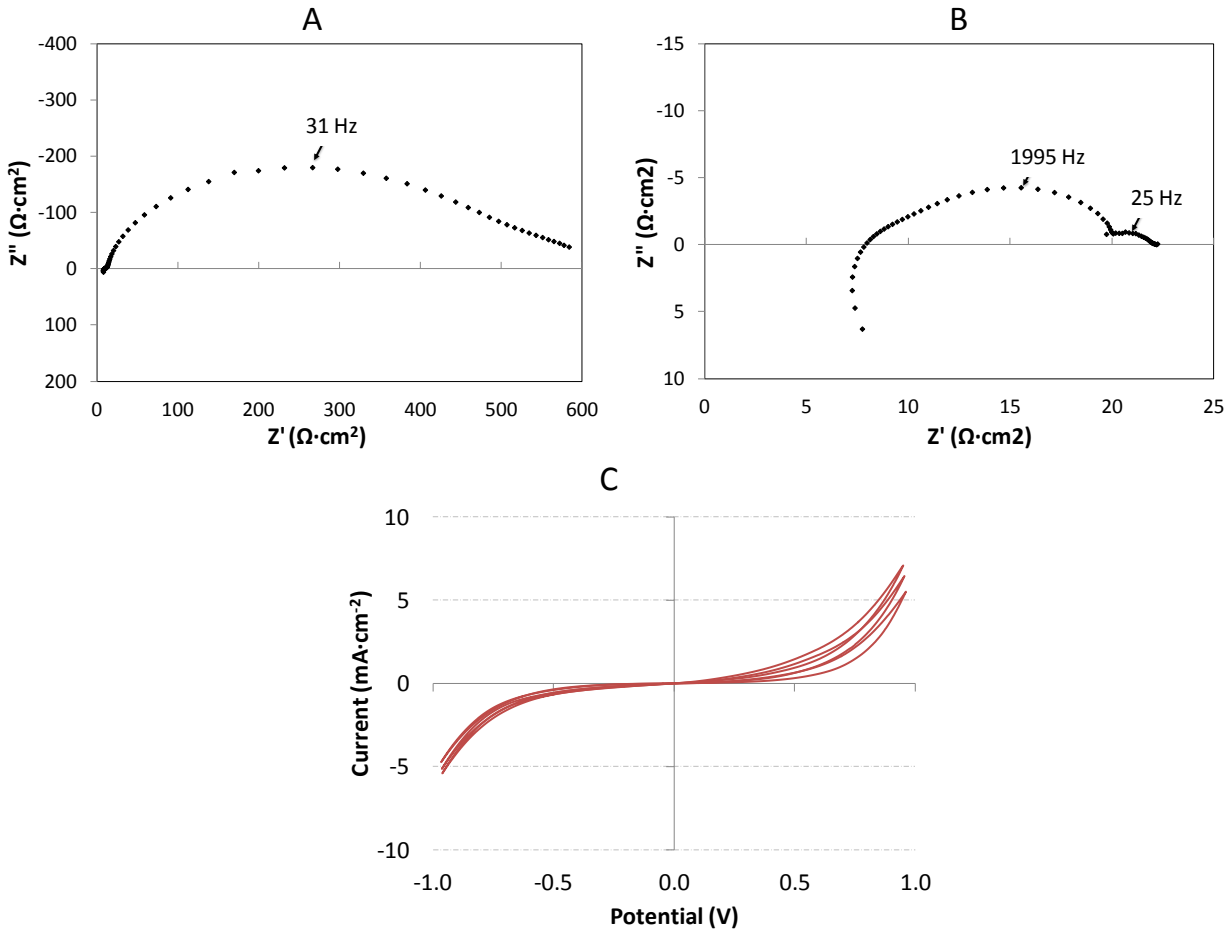

Figure 7.3. 2-electrode half-cell impedance spectroscopy response (A,B) in 2.5% H_2O-2% H_2-He (A) before and (B) after running the cyclic voltammograms (10 mV/s) shown in (C), all for an electrolyte-supported cell with Ni-YSZ as the WE and Pt as the CE at 800°C.

The 7 Ω·cm^2 R_s and 15.2 Ω·cm^2 R_p (vs. CE) values that are seen after CV activation (Figure 7.3B) compare reasonably well with the values of 1.6 Ω·cm^2 for R_s and 8.7 Ω·cm^2 for R_p (vs. RE) that were obtained in 3-electrode half-cell electrochemical studies prior to any exposure

to air (108). It was expected that R_s would be still higher in the present work, since the Pt leads used in the TGA holder were quite long (~60 cm with 5 junctions that connect various lengths of Cu and Pt wire before the cell is reached) and thin (< 0.5 mm diameter). In addition, while the Pt counter electrodes used were very similar in both studies, the current collectors attached to the Ni-YSZ WE differed. Here, Pt paste was used, while Ni paste (attached with a compressive force) was used in prior studies (108). The high R_p values and relatively low CV currents, seen in Figure 7.3, are thus not unexpected, since R_p includes the reaction at the Pt CE.

To ensure that the measured mass changes would reflect only the extent of oxidation of the Ni-based anode when exposed to air, all of the remaining components (CE, current collectors, etc.) were composed of Pt or YSZ, as neither of these materials should be influenced by pO_2 changes at temperatures up to 800°C. Thus, when the cell was exposed only to a humidified H_2 atmosphere, either at the OCP or under a bias, no mass changes were expected, as there are no predicted bulk reactions of Ni, Pt or YSZ with H_2. However, unexpectedly, Figure 7.4 shows that a small mass loss is seen when the cell was biased either positively or negatively at voltages of -1.5 V or larger vs. the Pt CE in the 2.5% H_2O-2% H_2-He environment. The apparent mass loss is very rapid (and reversible), with the magnitude of the mass loss increasing as the applied bias increases. This same apparent mass loss phenomenon was also seen when biasing a symmetrical cell, consisting of Pt as both the working and counter electrodes.

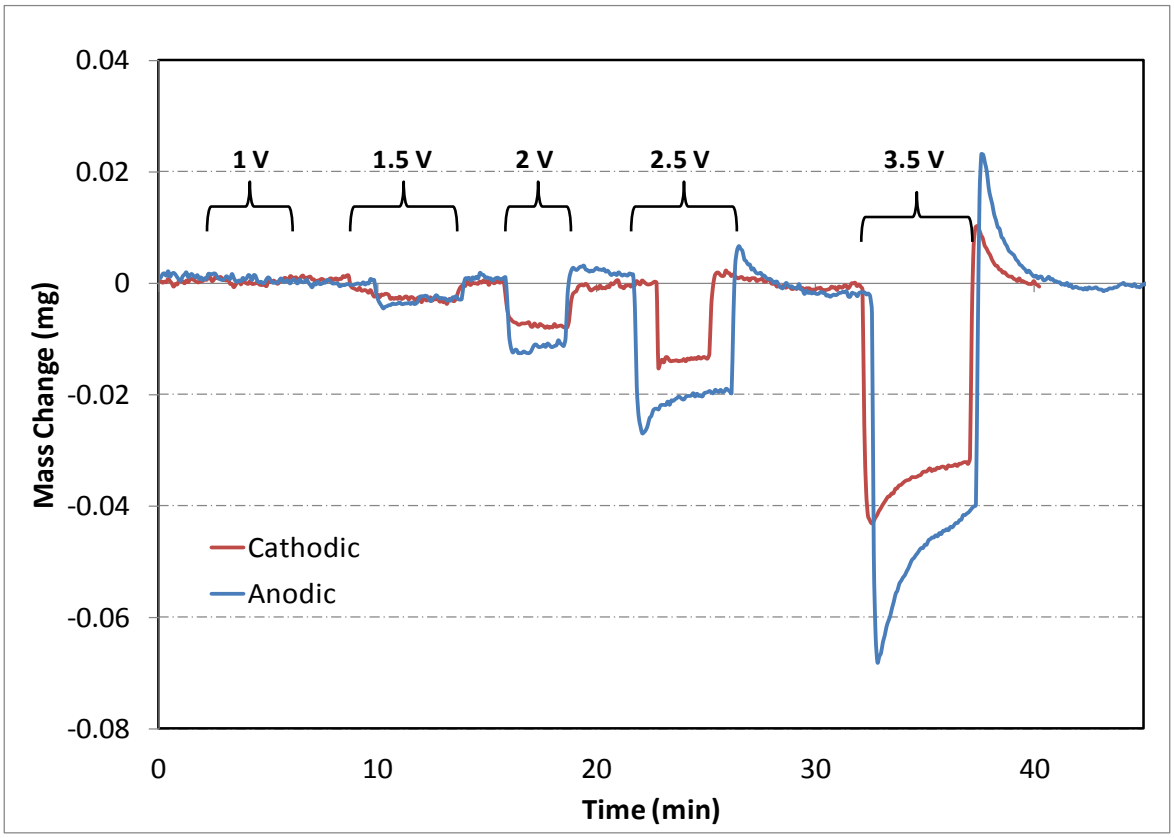

Figure 7.4. Mass changes of 0.5 g cell seen after application of either a negative (red) or positive (blue) potential to the Ni-YSZ working electrode vs. the Pt paste counter electrode in 2.5% H_2O-2% H_2-He at 800°C (the H_2 atmosphere remains unchanged in this experiment). The periods of time during which a potential was applied to the cell are indicated, with the cell being at open circuit at all other times.

The mass losses seen in Figure 7.4 in the H_2 environment may simply be an artifact of the system, arising from inductive and/or magnetic effects within the TGA resulting from current flow through the cell, for example. On the other hand, if the mass loss trends in Figure 7.4 are chemical in nature, several explanations may apply. Since the observed mass changes (Figure 7.4) are all quite small (5-70 μg) in relation to the mass of the complete cell (~500 mg), one

possibility is that, whichever electrode is biased positively loses the H_2 from its surface that is deposited at the OCP. Alternatively, during steam reduction (Reaction 7.1) in this humidified H_2 environment, it is conceivable that some YSZ reduction may occur (Reaction 7.2).

$$H_2O + 2e^- \rightarrow H_2 + O^{2-} \quad \textbf{(7.1)}$$

$$Zr(IV)O_2 + e- \rightarrow Zr(III)O_{1.5} + 0.5\ O^{2-} \quad \textbf{(7.2)}$$

Thus, at applied potentials of 1.5 V or larger, the YSZ electrolyte situated just adjacent to the negatively biased WE may undergo a small amount of reduction (undergoing a small change in its surface O^{2-} vacancy concentration), thus causing an overall cell mass loss. As the observed mass change (Figure 7.4) is < 0.02% of the mass of the electrolyte layer and as the mass changes are very rapid (i.e., no long diffusion pathways are present), this would indicate that only the YSZ interfaced with the WE is being reduced, rather than the YSZ bulk.

It is also seen in Figure 7.4 that, after a +2.5 and +3.5 V (anodic) potential has been applied to the Ni-YSZ WE vs. the Pt CE, the initial mass loss is followed by a small, slow mass gain. When the cathodic bias is switched off, the cell gains some mass for a period of time and then loses it again. This may be evidence for the electrochemical oxidation of Ni at these high positive biases, as would be expected. If the applied anodic potential is held for too long, the cell is observed to fail due to anode layer delamination.

Overall, the electrochemical activity of the electrolyte-supported cell *in operando* in the TGA is sufficient for the purpose of this work, with cell losses in this 2-electrode study that are only minimally larger than was seen in our previous 3-electrode electrochemical study in 3%H_2O-H_2. The small mass loss seen whenever the WE is polarized, either positively or

negatively (Figure 7.4), is much smaller than the mass changes seen when air is introduced into the TGA chamber and NiO is formed, as will be shown below.

7.3.3 In Operando Reverse-Bias Studies in Air and H_2 Atmospheres in the TGA

7.3.3.1 Mass Changes During Air Exposure Under Reverse Bias Cell Voltage Conditions

For each new cell, baseline electrochemical testing was first carried out in 2.5% H_2O-2% H_2-He ('H_2'), to ensure that the cell was functioning correctly. A voltage was applied to the WE (vs. CE) and, after another 15 min, of H_2 flow, the furnace was purged for 30 min in 2.5%H_2O-20% N_2-He ('N_2'), followed by 1 h in 2.5%H_2O-20% O_2-He ('air'), another 30 min in N_2, and finally a return to H_2, after which the cell was returned to the OCP condition (as depicted in Figure 3.8). Figure 7.5 shows the mass gain (red solid lines) vs. time plots (set to zero at t = 0) obtained at three different negative biases of the Ni-YSZ electrode vs. the Pt CE (-0.5 V, -1.5 V, and -3 V in Figure 7.5A to C, respectively), with the results always compared to the mass gain that was seen at the OCP (red hatched lines) in the same gas environments. Further, the current that flowed through the cell at each negative voltage bias as the gas environment was changed was monitored and is shown by the black line (right hand axis) in Figure 7.5.

A

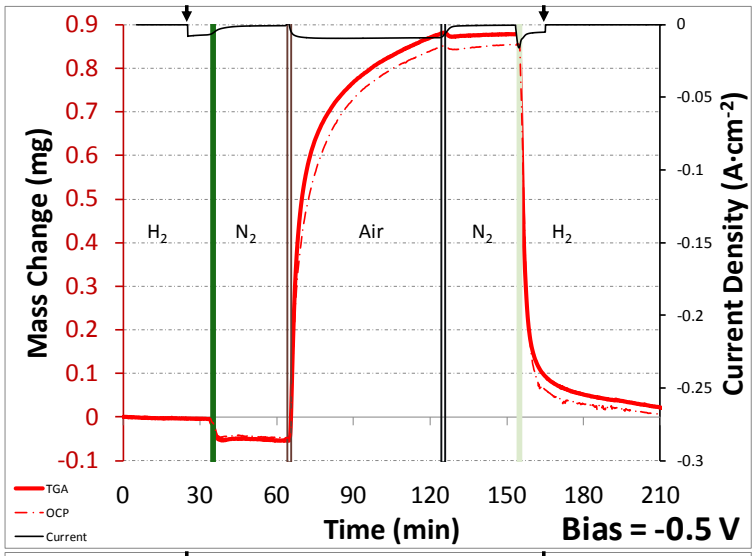
Mass Change (mg)
Current Density (A·cm-2)
H2
N2
Air
N2
H2
TGA
OCP
Current
Time (min)
Bias = -0.5 V

B

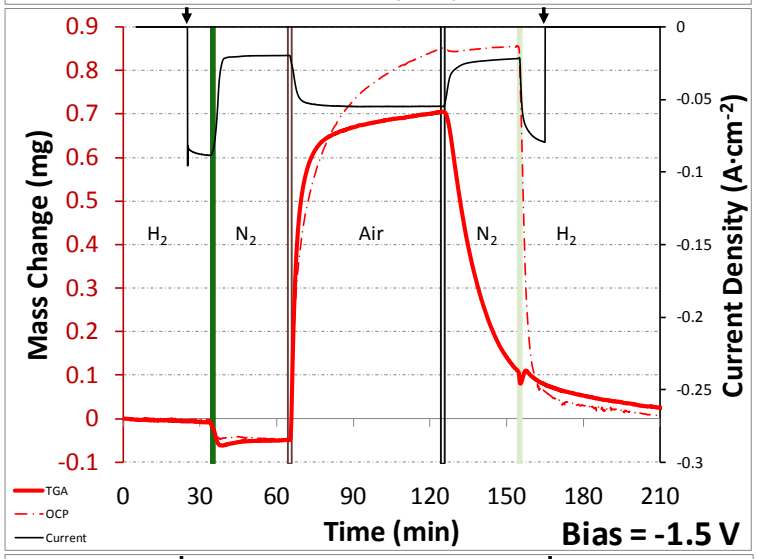
Mass Change (mg)
Current Density (A·cm-2)
H2
N2
Air
N2
H2
TGA
OCP
Current
Time (min)
Bias = -1.5 V

C

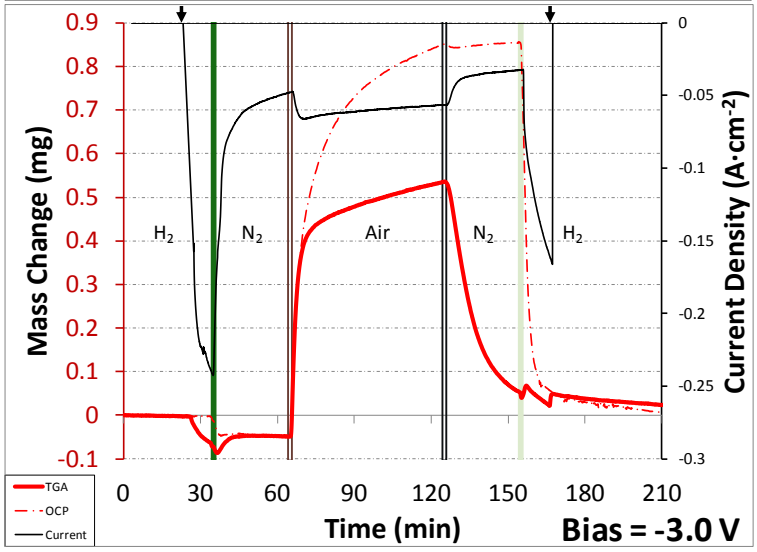
Mass Change (mg)
Current Density (A·cm-2)
H2
N2
Air
N2
H2
TGA
OCP
Current
Time (min)
Bias = -3.0 V

Figure 7.5. Mass change (solid red lines, left axis) and output current (black line, right axis) measured during an oxidation/reduction cycle with a cathodic bias (indicated by arrows) of (A) -0.5 V, (B) -1.5 V, and (C) -3 V applied to the Ni-YSZ electrode vs. the Pt CE. The mass change during an oxidation cycle/reduction cycle at the open circuit potential is also shown (red dashed line) and the changes in gas atmosphere are depicted by vertical lines (green for H_2/N_2 transitions and grey lines for N_2/O_2 changes).

At the OCP (red hatched line, Figure 7.5A to C), the cell mass, which is stable in H_2, is seen to decrease rapidly at the onset of the N_2 purge. When N_2 replaces air at 120 min in Figure 7.5A, the mass drops by ~10 μg. It is not clear what is causing this ~50 μg mass loss in N_2 (also seen under the negatively biased conditions in Figure 7.5), but this may reflect the desorption of surface species or, more likely, it is simply the result of a perturbation caused by a slight gas buoyancy change from H_2 to N_2. Fortunately, this small mass loss produces a baseline error of only < 5% of the total mass gain seen in air. Following the purge, air flow begins and the mass increases to ~0.85 g after 1 h of exposure. The mass change expected for the complete oxidation of all of the Ni in the anode (i.e., 100% oxidation) was 0.90 mg, based on the initial mass loss of the cell observed during its first reduction in H_2 and, thus, the cell is ~95% oxidized after 1 h of air exposure at the OCP.

During the cell bias, the expected reactions are changing, depending on the gas environment that surrounds the cell. Under H_2 conditions, it would be expected that the Ni-YSZ electrode could reduce steam, as shown in Reaction 7.1, while the oxidation process at Pt would be the reverse of Reaction 7.1, as shown in Reaction 7.3. In N_2, steam reduction (Reaction 7.1) is likely the cathodic reaction at the Ni-YSZ electrode. However, there is no H_2 present for

oxidation at the Pt anode (Reaction 7.3), and the formation of O_2 via Reaction 7.5 is therefore the most likely reaction taking place at the CE. Lastly, in air, the most likely reactions occurring at NiO-YSZ electrode are Ni (Reaction 7.6) and oxygen reduction (Reaction 7.4) and steam reduction (Reaction 7.1), to a much lesser extent. The reaction that likely takes place at the Pt CE is O_2 formation (Reaction 7.5).

$$H_2 + O^{2-} \rightarrow H_2O + 2\ e^- \quad \textbf{(7.3)}$$

$$O_2 + 4e^- \rightarrow 2O^{2-} \quad \textbf{(7.4)}$$

$$2\ O^{2-} \rightarrow O_2 + 4\ e^- \quad \textbf{(7.5)}$$

$$NiO + 2\ e^- \rightarrow Ni + O^{2-} \quad \textbf{(7.6)}$$

7.3.3.1.1 Ni Oxidation Protection by Application of a -0.5 V Bias

It is seen in Figure 7.5A that the current density in humidified H_2 (2.5% H_2O-2% H_2-He) (solid black line, right axis) increases to -7 mA·cm^2 within 5 s of electrode polarization at -0.5 V vs. the Pt CE. At the onset of the N_2 purge (humidified), the current density decreases to a very low value of < 1 mA·cm^{-2}, both before (30 to 60 min) and after (120 to 150 min) the air exposure period (Figure 7.5A). In the humidified air environment (Figure 7.5A), the current density increases to -9 mA·cm^{-2} and remains constant from the beginning to the end of the air exposure phase. When the cell is returned to a reducing (H_2) environment at 150 min, the current density initially rises to -13 mA·cm^{-2} before slowly (requiring ~4 min) returning back to -5.3 mA·cm^{-2} (Figure 7.5A). This observation of a initial high performance in H_2 is interesting, because it was also observed an earlier 3-electrode study with a -150 and -350 mV cathodic bias applied vs. the RE (108).

It can be seen in Figure 7.5 that, with the smallest cathodic cell voltage bias (-0.5 V) applied when air exposure is started (at 60 min), the mass gain observed due to Ni oxidation did not diminish in comparison with the mass gain seen at the OCP (dashed red). In fact, the final cell mass gain is ~0.02 mg larger than what was seen at the OCP, indicative of some drift in the TGA response. Other work (106; 105) has determined that the Ni/NiO reduction potential is -0.655 V vs. RE at 950°C in a high vacuum. Thus, it is apparent that a bias of -0.5 V is insufficient to protect the Ni-YSZ anode from oxidation under these *in operando* conditions. Further, Reaction 7.5 will typically not occur at such low potentials and it is therefore challenging to understand what electrochemical reactions could produce the -9 $mA \cdot cm^{-2}$ currents.

7.3.3.1.2 Ni Oxidation Protection by Application of a -1.5 V Bias

When the negative voltage bias was increased to -1.5 V (vs. the Pt CE) in the H_2 environment (Figure 7.5B), before air exposure (< 30 min), the cell current density in H_2 is relatively steady at -88 $mA \cdot cm^{-2}$. After oxidation, the current density is slow to recover and is only -80 $mA \cdot cm^{-2}$ after 15 min with a bias applied. The current density in this case is never given enough time to stabilize, although it is clearly still increasing and could have reached the initial cell current density, given more time.

During the first N_2 purge (30-60 min), the current density is seen to be relatively stable at -20 $mA \cdot cm^{-2}$ (Figure 7.5B). Contrary to the -0.5 V cell bias experiment (Figure 7.5A), O_2 evolution (Reaction 7.4) can now occur at the Pt CE as the cell bias (-1.5 V) is sufficiently high. This is consistent with the much higher current density that is observed here (Figure 7.5B). Of interest, during the N_2 purge that follows the air exposure stage of the cycle (120-150 min), the

current density is initially much higher at -30 $mA \cdot cm^{-2}$ before slowly decreasing to -22 $mA \cdot cm^{-2}$ over the 30 min purge time.

In air, the current density increases to -53 $mA \cdot cm^{-2}$ after 5 min and then slowly increases to -55 $mA \cdot cm^{-2}$ over the final 55 min of air exposure (60 to 120 min in Figure 7.5B). Figure 7.5B shows that Ni oxidizes rapidly at first (55% oxidation depth after 5 min), before shifting to a much slower oxidation rate (gaining only 50 μg in the final 50 min of air exposure) when ~75% of the Ni is oxidized. The maximum mass gain during the 1 h oxidation cycle (Figure 7.5B) is seen to be lower than at the OCP (red hatched line) conditions, reaching only ~80% of the full mass gain. While a steady-state mass does not appear to be reached after 60 min of air exposure (at t = 120 min on Figure 7.5B), with the Ni continuing to oxidize at ~1 $\mu g \cdot min^{-1}$, this cannot be interpreted because instrument drift is also observed (i.e., the final mass at t = 210 min is ~20 μg higher than the initial mass at t = 0 in Figure 7.5B). Thus, a bias of -1.5 V does serve to prevent the full oxidation of the Ni component of the WE during air exposure.

A very interesting and important feature that is seen in Figure 7.5B is that, during the N_2 purge after the cell has been oxidized to 80% during the air exposure phase, the cell begins to rapidly lose mass. NiO reduces to metallic Ni as soon as the air is replaced with N_2 at t = 120 min. In fact, the NiO in the WE is almost fully reduced (only 10% NiO remains at 150 min) by the time the cell is returned to the H_2 environment. Contrary to the case at -0.5 V (Figure 7.5A), these results indicate that a -1.5 V cell bias is sufficient to bring the Ni-YSZ electrode negative of the Ni/NiO equilibrium potential and, in the very low pO_2 (N_2) environment, the NiO quickly reduces.

It is also noteworthy that, after N_2 replaces air at 120 min, the currents are higher than those passed in N_2 before air exposure, with 7 C passed in the first purge and 8.6 C passed in the

second. The coulombic efficiency for NiO reduction during the second purge is therefore 10%, which is a good result. If it is assumed, however, that the charge passed during the first purge is due to Reaction 7.1, and that the same rate for Reaction 7.1 will apply in the second N_2 purge, then the charge passed in the first purge can be subtracted from that passed in the second purge. Thus, with the assumption that only the charge that is passed in the second purge that is in excess of the charge passed in the first purge is involved in NiO reduction (Reaction 7.6), then the efficiency improves to 60%, which is a very good result. In reality, the efficiency could not be this high, as it is likely that H_2 is building up in the WE pores due to steam reduction (Reaction 7.1), and this newly formed H_2 will also participate in the NiO reduction.

7.3.3.1.3 Ni Oxidation Protection by Application of a -3.0 V Bias

When the negative voltage bias applied to the Ni-YSZ anode was increased even further to -3 V, the current density (due primarily to steam reduction, Reaction 7.1) in the first H_2 exposure phase (up to 30 min) increases with time (from -220 to -240 $mA \cdot cm^{-2}$). Similar to what was seen at a -1.5 V bias, the current density only increases to -165 $mA \cdot cm^{-2}$ by the end of the 15 min period with the -3 V bias applied in H_2 (after the N_2 purge is completed at t = 150 min). The current was still increasing when the cell was switched off and, thus, could have reached the values seen at early times (< 30 min).

Once again, the current densities in N_2 are lower than in H_2, both before (30-60 min) and after (120-150 min) air exposure. As the same cathodic reactions are occurring in both cases, this suggests that the electrochemistry at the Pt CE is dominating the cell current, with Reaction 7.5 being more sluggish than Reaction 7.3. The current density during the first N_2 purge at a -3 V applied potential never stabilizes, decreasing constantly to a minimum of -47 $mA \cdot cm^{-2}$, at which

point, the air exposure phase begins. It is uncertain if there is an influence outside of the reactions that have been highlighted (Reaction 7.1 to 7.6), since a line can be drawn through both N_2 purges that shows that the resultant current density is constantly decreasing. In the second N_2 purge (120 to 150 min), the current density decreases from -39 to -32 $mA \cdot cm^{-2}$.

When the cell is exposed to air during the -3 V bias, the cell current density, in Figure 7.5C, decreases from 65 to 55 $mA \cdot cm^{-2}$ during the 1 h air exposure period. This decrease in current density appears to follow the general trend to a lower current density that is seen during the two N_2 exposure phases. In Figure 7.5C, it can also be seen that the extent of Ni oxidation was lowered even more during air exposure (vs. what was seen at a -1.5 V bias in Figure 7.5B). Only ~65% of the Ni in the anode was oxidized within the 1 h air exposure cycle, where, once again, it is seen that 50% of the Ni oxidizes in only 5 min of air exposure. The oxidation rate then slows to a lower and constant rate (~2 $\mu g \cdot min^{-1}$), resulting in a ~65% oxidation depth at the end of the 1 h air exposure period. While this rate is faster than what was observed with a -1.5 V bias, this may occur because there is more metallic Ni remaining (Figure 7.5C) and not because there is a lowered amount of protection given to the Ni at the higher bias.

As was the case in the -1.5 V bias experiment (Figure 7.5B), the -3 V biased Ni-YSZ electrode also experiences a significant mass loss (Figure 7.5C) as soon as N_2 is returned to the TGA chamber after the completion of the air exposure phase (at t = 120 min). NiO is once again quickly reduced, with the observed NiO content decreasing from 65 to 5% during the 30 min N_2 purge phase. In this case (Figure 7.5C), the coulombic efficiency calculated from the total charge passed (8.6 C) and the amount of NiO that is reduced (60%) during the N_2 purge (between t = 120 and t = 150 min) is once again ~10%.

7.3.3.2 Summary of Results at -0.5 to -3.0 V Cell Bias

While a direct measurement of the mass change could not be made in earlier work (108), the decrease in the resultant current output (65 to 55 $mA \cdot cm^{-2}$) with time during the oxidation cycle were similar to the present study. The decrease in current density suggests that the resistance of the cell is increasing, which, in turn suggests the slow but continuous formation of NiO (due to less conductive NiO replacing the more conductive Ni). Thus, it is shown (Figure 7.5) clearly indicate that, while full (100%) protection from Ni oxidation was never observed, a Ni-YSZ anode can be at least partially protected from oxidation during air exposure by the application of a negative cell voltage. A negative bias of -1.5 V or more is needed to begin to prevent Ni oxidation in a 20% O_2 environment, as the Ni-YSZ anode potential must be made negative of the Ni/NiO equilibrium potential.

Further, it has been shown that, in low pO_2 atmospheres (in N_2), a negative bias of -1.5 V is sufficient to fully reduce NiO, either by direct electron transfer or by reduction with H_2 generated during steam reduction. This suggests that, in practice, Ni could be kept in the metallic state during the inadvertent exposure of Ni-YSZ anodes to slow air leaks and low pO_2 environments by applying a negative bias as low as -1.5 V (vs. the Pt CE). Because all of the experimental purge phases were carried out using humidified N_2, however, it is not known with certainty if NiO is reduced directly (Reaction 7.6) or as a secondary reaction after steam reaction (Reaction 7.1) first liberates H_2. As discussed in Section 3.1.2, the charge that is passed during the second N_2 purge (after Ni is oxidized in the air exposure phase) does match up well with the amount of NiO that is reduced (i.e., the coulombic efficiency is high), but future experiments will be necessary to determine if this is the case.

7.3.3.3 Mass Changes During Air Exposure Under Reverse Bias Currents

The use of a cathodic potential applied to the Ni-YSZ electrode to prevent full Ni oxidation in high pO_2 has been quantitatively demonstrated in the previous section to lower the amount of Ni oxidized during air exposure. However, in earlier work (108), the use of a reverse current flow was shown to be more successful in preventing Ni oxidation, as gauged from the EIS response. Thus, the use of a negative current bias was also examined here using the *in operando* TGA technique. Figure 7.6 (solid red line) shows the mass change/time profile for three different applied current densities (-13, -131 and -262 mA cm^{-2} in A to C, respectively), in comparison with the OCP data (red dashed line), also shown in Figure 7.5, and with the cell voltage shown in the black line (right hand axis). In this case, the smaller the cell voltage, the more active the cell.

7.3.3.3.1 Summary of Results at -13 mA·cm^{-2} Bias

With the application of a relatively small current of -13 mA·cm^{-2} (-5 mA at a 0.38 cm^2 electrode) to the cell, the potential in H_2 decreases from a stable value of -1.6 V to -2.3 V when the N_2 purge begins (Figure 7.6A). In air, a fairly low cell voltage is seen (quickly reaching 0.5 V vs. Pt CE), lower than seen in the H_2 and N_2 environments, indicative of the higher cell activity in the air environment. After the air exposure phase, the potential during the N_2 purge increases from 1.0 to 1.8 V during the 30 min period (between t = 120 and t = 150 min) and when H_2 is returned to the furnace chamber (at t = 150 min), the potential slowly increases from 1.2 to 1.7 V over the 15 min until the reverse bias is turned off.

A

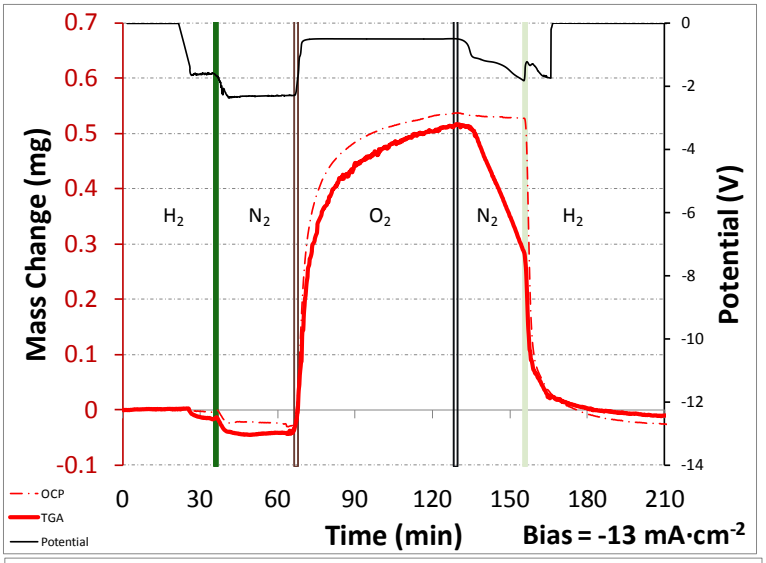
Mass Change (mg)
Potential (V)
H2
N2
O2
N2
H2
OCP
TGA
Potential
Time (min)
Bias = -13 mA·cm-2

B

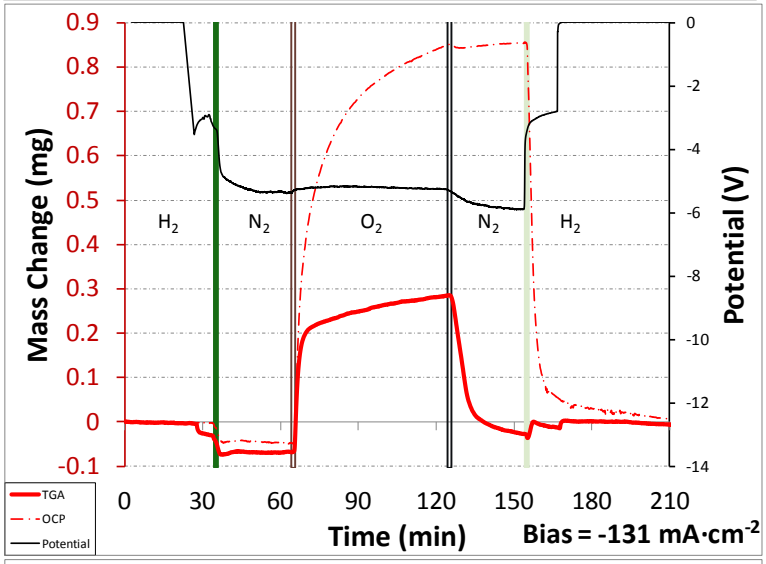
Mass Change (mg)
Potential (V)
H2
N2
O2
N2
H2
TGA
OCP
Potential
Time (min)
Bias = -131 mA·cm-2

C

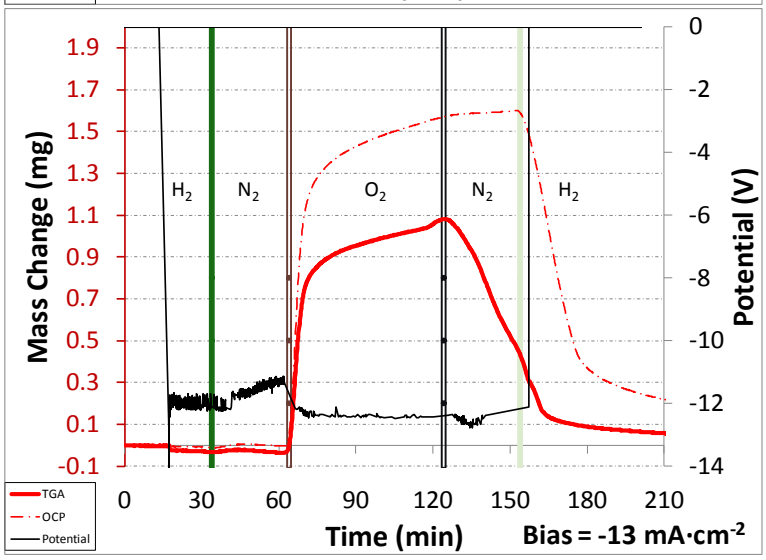
Mass Change (mg)
Potential (V)
H2
N2
O2
N2
H2
TGA
OCP
Potential
Time (min)
Bias = -13 mA·cm-2

Figure 7.6. Mass change (solid red lines, left axis) and output potential (black line, right axis) during an oxidation/reduction cycle with a negative bias of (A) -13, (B) 131, and (C) 262 mA·cm^{-2} applied to the Ni-YSZ electrode vs. the Pt CE. The mass change during an oxidation cycle/reduction cycle at the open circuit potential is also shown (red dashed line) and the changes in gas atmosphere are depicted by vertical lines (green for H_2/N_2 transitions and grey lines for N_2/O_2 changes).

The cell voltage of 0.5 V, seen during air exposure at -13 mA·cm^{-2}, makes the results in Figure 7.6A comparable to those in Figure 7.5A, where -0.5 V was applied during the air exposure cycle. Under the conditions of Figure 7.6A, a small amount of protection is seen to be offered to the Ni-YSZ electrode from oxidation, with ~95% of the Ni in the anode being oxidized during the 60 min period of air exposure, as compared to no protection offered when a bias of -0.5 V was applied. The slightly higher degree of protection given to the Ni electrode in Figure 7.6A (negative current) vs. in Figure 7.5A (negative voltage) may be due to cell variability, as only -9.1 mA·cm^{-2} is seen to flow at the -0.5 V bias condition in Figure 7.5A, vs. the -13 mA.cm^{-2} current density used here.

Importantly, when N_2 was returned to the cell environment (120 min) (Figure 7.6A), NiO began to slowly reduce, which was not seen in Figure 7.5A at a cell bias of -0.5 V. As discussed in Section 3.1, NiO may reduce directly by Reaction 7.6 or via H_2 that has been generated by steam reduction (Reaction 7.1). After 30 min of N_2 exposure, ~40% of the NiO has been reduced to Ni, with the rest of the NiO reduced quickly when N_2 is replaced with H_2 at 150 min (Figure 7.6A). During the N_2 purge, before and after air exposure, it is seen that the voltage was roughly 2 V (t = 30 to t = 60 min), but only 1.6 V for several minutes (t = 120 to t = 150 min) before

stabilizing back at 2 V afterwards. This shows that the presence of NiO in the WE was enhances the performance, likely through the action of Reaction 7.6 concurrently with Reaction 7.1.

7.3.3.3.2 Summary of Results at -131 mA·cm^{-2} Bias

When a significantly larger negative current bias of -131 mA·cm^{-2} (-50 mA at a 0.38 cm^2 electrode) was applied, it can be seen in Figure 7.6B that the potential increases from -2.9 V in H_2 to -5.3 V in the first N_2 purge (at t = 30 min). After the air purge, the potential in N_2 (from t = 120 min to t = 150 min) is again -5.3 V, but it increases marginally to -5.8 V following the reduction of all of the NiO that remains in the WE. After H_2 was introduced into the cell chamber, the potential returned to the -2.9 V value that it was before the air exposure phase.

It can also be seen in Figure 7.6B that the degree of protection given to the cell from Ni oxidation is quite significant. Now, the cell potential, which increases from -5.16 to -5.25 V during the air exposure phase, is larger than any of the negative voltage biases used in Figure 7.5. Under the conditions of Figure 7.6B, only ~34% of the Ni in the electrode was oxidized during the 1 h air exposure period. Unlike the mass gain observed at -13 mA·cm^{-2} (Figure 7.6A), but similar to that seen for negative cell voltages of -1.5 and -3 V (Figure 7.5B and C, respectively), the mass gain/time profile suddenly changes slope, with the Ni oxidizing much more slowly, gaining only 80 μg over the final 55 min of air exposure. The initial mass gain during air exposure in Figure 7.6B is rapid at first, following the trend seen at the OCP, and then a slow increase in mass is seen from 0.44 to 0.54 mg, for the remainder of the 1 h period.

Thus, similar to what was seen in Figure 7.5C, Ni oxidation is again not fully prevented, but the depth of oxidation has been greatly diminished by the applied negative current bias. Once

again, when the second N_2 purge begins, the NiO begins to be reduced, although in this case, the NiO remaining in the anode is fully reduced within the first 10 min of the onset of the N_2 purge.

7.3.3.3.3 Summary of Results at -262 mA·cm^{-2} Bias

In order to determine if the mass gain could be stopped completely, an extremely high current density of -262 mA·cm^{-2} (-100 mA at a 0.38 cm^2 electrode) was applied. After most of the attempts at applying such high reverse-bias current densities, the majority of the cells were damaged irrecoverably. The example in Figure 7.6C is for one case in which the cell did survive. It has been reported (152) that, with increasing applied potentials, the electronic conductivity of YSZ can compensate for oxygen-starved conditions and, thus, it is possible that the electrolyte is short-circuiting under these high current conditions. As a result, it may be the high rates of O_2 evolution that cause cell failure (e.g., through electrode delamination at the Pt CE) in this situation (153).

As can be seen in Figure 7.6C, the potential very high at -12 V and, even when the gases surrounding the cell are changed, this value remains at approximately -12 V. This suggests that the limits of the gas (or ion) transport for the cell have been reached. For electrolyte-supported cells at 800°C, it is not surprising that there would be a limit to the magnitude of the negative current or potential that can be applied to a cell. It can be seen in Figure 7.6C, that when the applied cathodic current is this high, the degree of protection that is given to the cell is not proportionately better, as 66% of the Ni content of the anode was converted to NiO with a -262 mA cm^{-2} current density (Figure 7.6C) versus 34% with a -131 mA·cm^{-2} current density (Figure 7.6B).

7.3.3.4 Comparison of Effect of Negative Potentials vs. Negative Current Densities in Preventing Ni Oxide Formation

A summary of mass gain, coulombs passed and coulombic efficiency (the coulombs that would be needed to reduce the Ni that remains in metallic state versus the total number of coulombs passed) after 1 h of air exposure with either a negative voltage or current applied to the Ni-YSZ electrode (vs. the Pt CE) is given in Table 7.1. Based on the present *in operando* electrochemical study in the TGA, it is clear that the application of a cathodic current or potential to an Ni-YSZ anode during air exposure does not provide full protection from oxidation in air. It can be seen from Table 7.1 that the best protection (62%) is offered when using a sufficiently large current density (obtained under the conditions in Figure 7.6B), thus ensuring a constant flux of oxygen ions through the electrolyte.

In Figure 7.7A and B, which show the percent protection offered versus the applied (or resultant) current density and versus the applied (or resultant) potentials, respectively, show that the relationship between the protection given and the magnitude of the bias is linear in both cases. This is an indication of the inter-related nature of these two variables. The relationship between the magnitude of the applied bias and the percent of the Ni phase protected from oxidation fails when the sample biased at -260 $mA \cdot cm^{-2}$. It is possible that this sample was damaged, but it can be seen in the inset of Figure 7.7A that, when considering the fraction of the Ni mass that was oxidized, the protection offered is still comparable to what was achieved at -130 $mA \cdot cm^{-2}$. The low degree of protection is therefore the result of the high mass of Ni that is present in this electrode. Thus, the current that passes is closely related to the mass of Ni that is protected. Related to the optical microscope observations in Figure 7.1, this strongly suggests that Ni is protected in the active area of the cell nearest to the electrolyte.

Table 7.1. Summary of results obtained during reverse bias protection of Ni-YSZ electrodes in air at 800˚C.

Applied Bias vs. Pt (Voltage or Current)	Measured Output (Current or Voltage)	Mass Gain (%)	Ni Protected (mg)	Coulombs Passed (C)	Coulombic Efficiency # (%)
-0.5 V	-8.9 $mA \cdot cm^{-2}$	100	0.000	12	0.0%
-1.5 V	-56 to -52 $mA \cdot cm^{-2}$	80	0.170	76	1.5%
-3 V	-67 to -57 $mA \cdot cm^{-2}$	63	0.315	87	2.4%
-13.1 $mA \cdot cm^{-2}$	-0.50 V	96	0.022	18	0.8%
-131 $mA \cdot cm^{-2}$	-5.15 to -5.25 V	38	0.528	184	1.9%
-262 $mA \cdot cm^{-2}$	-12.1 to -12.4 V	66	0.561	368	1.0%

the coulombs that would be needed to reduce the Ni that remains in metallic state in the anode layer versus the total number of coulombs passed.

It is noted in Table 7.1 that the coulombic efficiency associated with the protection of Ni from oxidation by the application of a reverse bias, in air, is quite low, reaching a maximum of 2.4% (at -3 V), but it should also be noted that this is highly dependent on how long the Ni-YSZ electrode is exposed to air. This is because, for the majority of the time of reverse bias, the cell mass hardly changes. For example, at -131 $mA \cdot cm^{-2}$ (Figure 7.6B), if air exposure had been stopped after 30 min, the efficiency would have been 12.8%, while if it had been carried on for a 2 h air cycle, the efficiency would have dropped to below 1.2%. However, in the relatively low pO_2 of ~10^{-6} atm, associated with the N_2 gas environment, the average coulombic efficiency is 10%. Further, when the charge passed during the first N_2 purge (prior to air exposure) is

subtracted from the charge passed in N_2 after the air exposure (i.e., assuming that this is charge passed due to steam reduction at the Ni-YSZ electrode), the coulombic efficiency associated with just the prevention of NiO formation approaches 60%.

Another positive consequence of the observed NiO reduction during the N_2 purge, as seen after the simulated air flow is stopped and inert N_2 flow begins in Figure 7.5 and Figure 7.6, is that at a low pO_2 gas concentration, the Ni-YSZ anode could likely be fully protected from oxidation at -13 $mA \cdot cm^{-2}$ or -1.5 V. Since it would be expected that most of the air ingress into the cell would result from slow leaks through seals and back through the afterburner, these relatively small biases should be sufficient to fully protect a Ni-YSZ anode. Even so, thicker cells would need to be tested to determine if there is a limitation in the anode layer thickness that can be protected.

One other point to note is that Ni continues to oxidize slowly with time even when the highest cathodic biases are applied to the Ni-YSZ electrode in simulated air (Figure 7.5B and C, Figure 7.6A and B). This suggests that, in still higher pO_2 conditions, the cell would likely not be protected from oxidation for significantly long periods of time. While for most applications, this limit to the time period over which a cell can be protected is likely not a problem, future work focusing on longer term testing is still necessary in order to determine the limits of the protection offered to Ni-YSZ anodes by a reverse bias during variable pO_2 exposures.

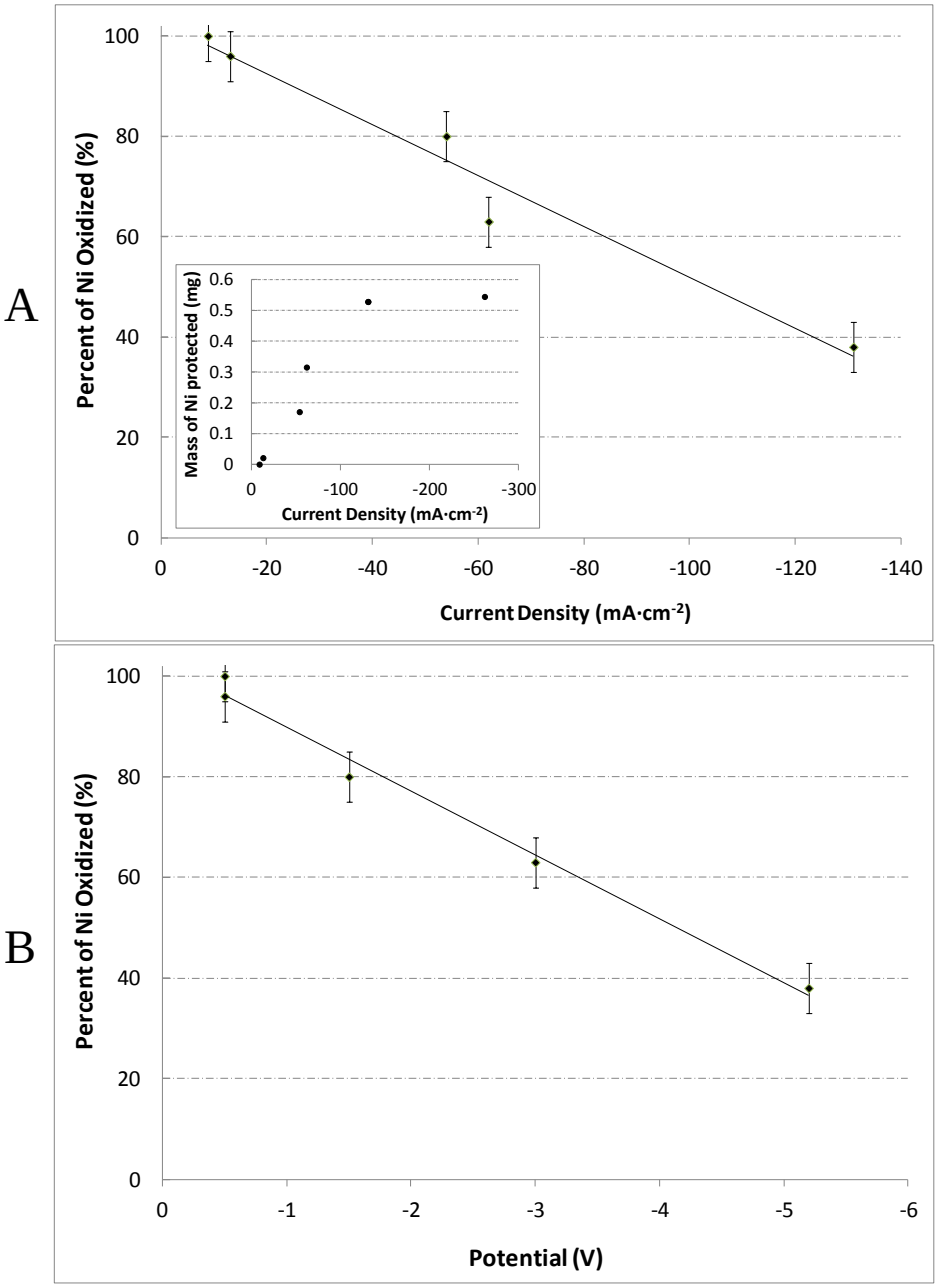

Figure 7.7. Relationship between the percent Ni oxidized and the negative (A) current density and (B) potential applied to the Ni-YSZ electrode vs. the CE. Each graph shows a line of best fit. The inset in (A) shows the relationship between the mass of Ni protected and the applied current density employed.

The development of the *in operando* TGA in the present work also has great promise for the study of a number of other SOFC processes, including the reversal of coking or sulfur-poisoning, determination of the accumulation rate of coke during half-cell operation, and monitoring the oxidation state of mixed conducting anode materials during half-cell operation for the determination of the redox stability of these materials. Finally, this technique could also be used to investigate mass changes during gas phase corrosion and potentially in sensors, especially when the sensing phenomena are related to the adsorption of, or reaction with, gases that can be introduced into a TGA.

7.4 Summary

Based on this first-time *in operando* electrochemical study in the TGA, it is clear that the application of either a cathodic current or potential to a Ni-YSZ electrode during air exposure can prevent the oxidation of a fraction of the Ni phase, as long as the cell voltage is greater than ca. -1 V. However, this method does not provide full protection from oxidation in air, with a maximum of 62% protection obtained when a reverse current density of -131 $mA \cdot cm^{-2}$ was used. Importantly, there is a linear relationship between the current density (and cell potential) and the percent of Ni protected, confirming that the protection is electrochemical in nature. Although the coulombic efficiency after 1 h of reverse bias is quite low in air (< 3 %), the efficiency could be higher (> 10%) if the reverse bias were applied for shorter times. It is also noted that, in air, the Ni-YSZ electrode continues to slowly oxidize, even with a negative bias applied, and thus longer term studies are necessary to determine how well the negative bias would work in the longer term.

In N_2, after the oxidation cycle, if the bias is > -1 V, the NiO in the anode will begin to reduce to Ni. The reduction could result from either the direct reduction of NiO or by reduction via the H_2 that is formed during the reduction of steam that is present in the humidified N_2 flow. It has also been found that the efficiency of NiO reduction is quite good (10%, based on the raw currents passed, or 60%, when the H_2O reduction and leakage currents are subtracted) in the low pO_2 environment of the humidified N_2 flow. This suggests that the reverse bias technique may be very effective in preventing degradation caused by slow air leaks or low pO_2 sources, although more work is needed to confirm this. Overall, the *in operando* TGA technique has quantitatively determined the oxidation depth of a Ni-YSZ electrode exposed to air with a reverse bias and shows promise of being an excellent tool for many other applications.

Chapter Eight: **Reversing Sulfur Poisoning of Ni-YSZ SOFC Anodes with Air Exposure and a Reverse Cell Bias**

8.1 Introduction

It was demonstrated in Chapter 7 that a Ni-YSZ electrode, exposed to air at high temperatures with a reverse bias applied, does not oxidize to the same extent as when the electrode is exposed to air at the OCP (open circuit potential). The primary aim of the work described in this chapter is therefore to use the *in operando* thermogravimetric analysis (TGA) to determine if this technique could serve to protect the Ni phase from oxidation while also removing adsorbed S-species, which result from exposure to low levels of H_2S. Under these conditions, the adsorbed S-species (S_{ads}) should be oxidized (Reaction 8.1) while Ni should be protected from oxidation by the action of Reaction 8.2.

$$S_{ads} + O_2 \rightarrow SO_2 \qquad \textbf{(8.1)}$$

$$NiO + 2\ e^- \rightarrow Ni + O^{2-} \qquad \textbf{(8.2)}$$

8.2 Experimental Methods

For the purpose of the work described in this chapter, ESC-1 cells were used, as described in Section 3.1.3. All redox cycles were carried out inside a TGA, as detailed in Section 3.2, with the in operando TGA procedure outlined in Sections 3.2.5 and 0.

8.3 Results and Discussion

8.3.1 In Operando S-poisoning Inside the TGA

It is known that Ni catalyst poisoning in SOFC anodes by H_2S is rapid at typical operating temperatures (700-1000°C) (39), but it is also known that H_2S can adsorb to most available surfaces, including the stainless steel tubing leading to the furnace and to the walls of the furnace itself (154). Thus, it was necessary to first ensure that the Ni-YSZ electrode could be fully poisoned in the inside the TGA apparatus described in Section 3.2.5, since the supply line for the 5 ppm H_2S - 10% H_2-He is long and as there are many Pt components within the cell holder apparatus.

In the first two poisoning experiments, the cell was exposed to H_2S at the OCP and with +1 V applied to the Ni-YSZ electrode (vs. the Pt CE). The +1 V potential was chosen based on previous *in operando* experiments (Chapter 7) that showed that the losses of the electrodes are relatively high in the *in operando* TGA apparatus. The current density at a +1 V polarization of the Ni-YSZ WE (vs. CE) in a half-cell configuration (both electrodes were exposed to the same gas atmosphere) was therefore monitored for the full duration of the H_2S poisoning cycle, along with electrochemical impedance spectroscopy (EIS) every 2 h. The mass change was also monitored prior to and during the H_2S exposure period in these *in operando* experiments. However, due to the small thickness (~30 μm) and the low Ni surface area (> 1 μm average particle size) of the Ni-YSZ layer, it was not expected that the change in mass due to the adsorption of S to the surface would be detectable above the TGA noise (~1 μg) or the daily cyclic mass changes observed (up to 100 μg).

Figure 8.1 shows the current density passing through the cell (at +1 V vs. CE). It can be seen that the current density decreases after the H_2 gas environment is switched to 1 ppm H_2S at

time 0 h, with the most rapid decrease in the current density occurring in the first 5-10 h. This was faster than expected, since, as described above, the long supply lines could delay H_2S ingress into the cell chamber. However, this is followed by a period of relatively constant decline in the cell performance, which could reflect the fact that the initial pH_2S was actually somewhat lower than 1 ppm due to adsorption on the H_2S supply lines, etc. Thus, the actual concentration of H_2S that reaches the Ni-YSZ anode is likely increasing gradually to the 1 ppm value.

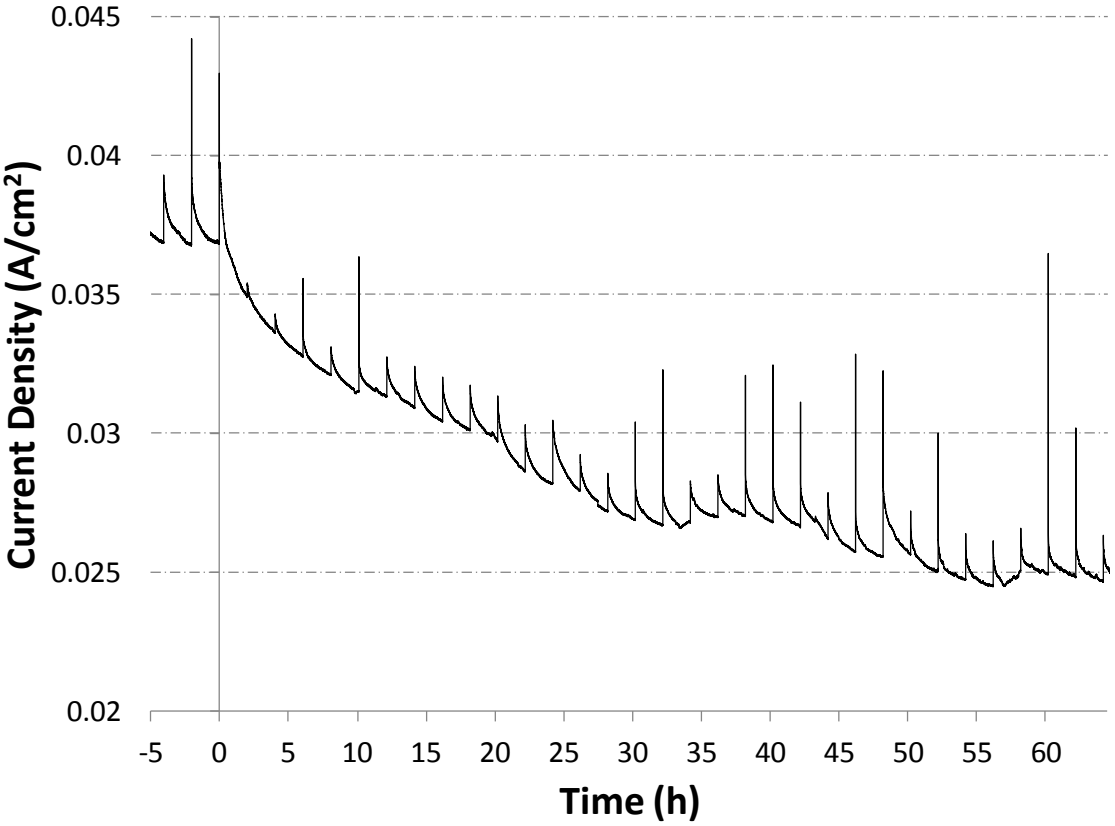

Figure 8.1. Current density at 800°C at a 1 V potential between the Ni-YSZ WE and the Pt CE. The gas composition changes from 2.5% H_2O-2% H_2-He to 1 ppm H_2S-2.5% H_2O-2% H_2-He at t = 0. Apparent spikes in current are due to a pause in the applied potential in order to perform impedance spectroscopy at the open circuit potential.

The performance of the cell is seen in Figure 8.1 to stabilize after 55 h of exposure to 1 ppm H_2S at a current density of 25 $mA \cdot cm^{-2}$. This reflects a 32% drop in cell performance, which is high in comparison with literature (41) losses when a H_2S concentration of only ~1 ppm is introduced. However, considering that no reference electrode was used in this half-cell study, it is likely that there is poisoning not only of the Ni-YSZ working electrode, but also of the Pt counter electrode, which will then also contribute to the observed loss in the current density.

The open circuit EIS response, seen in Figure 8.2, correlates well with the decrease in performance observed in Figure 8.1. The polarization resistance (R_p) increases rapidly in the first 5-10 h, followed by a much more gradual increase in R_p until the cell performance stabilizes after 55 h. It is expected that there are at least 3 arcs present for the reactions occurring at the two electrodes, although ascribing arcs to different cell processes can be difficult and is not the focus of the work presented here. The frequency maximum of the dominant arc is seen to decrease from 125 Hz, at the onset of 1 ppm H_2S exposure (0 h), to 80 Hz, after H_2S flow is stopped (60 h). The values of the resistances of the cell, as determined by EIS, are summarized in Table 8.1. For the purpose of performing the circuit fitting, the high frequency inductor (L) and the series resistance (R_s) were assumed to be constant and were thus fixed at the pre-poisoned (0 h) values. This is because, as seen in Figure 8.2, the cell is usually not at equilibrium when the EIS measurement is begun, due to the +1 V applied potential.

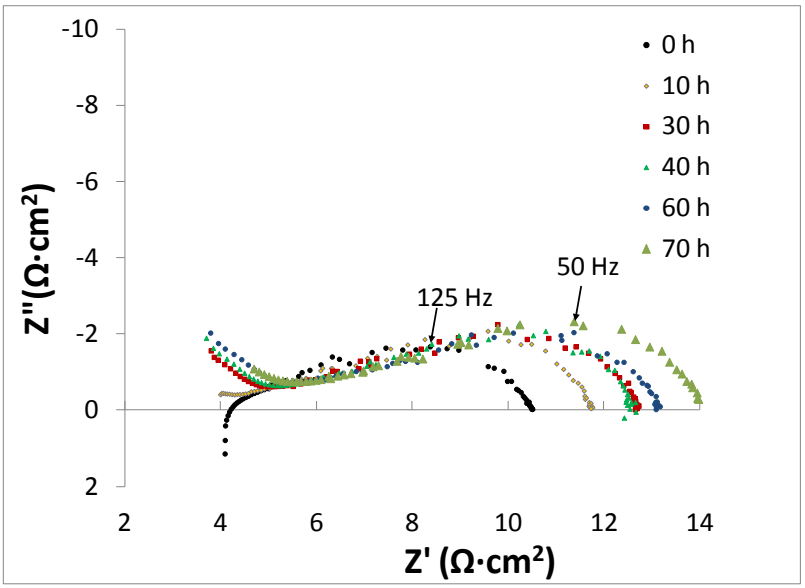

Figure 8.2. Selected open circuit EIS results during 65 h of exposure of the half-cell to 1 ppm H_2S at 800°C. Measurements were made in a 2-electrode configuration (Ni-YSZ WE and Pt CE) at the OCP using a 10 mV amplitude. The frequency at the maximum of the low frequency arcs for the 0 h and 60 h results are indicated.

Table 8.1. Polarization resistance after S-poisoning.

Time (h)	R_s [#] ($\Omega \cdot cm^2$)	R_p (Total) ($\Omega \cdot cm^2$)
0	3.7	6.8
10	3.7	8.2
30	3.7	9.1
40	3.7	8.8
60	3.7	9.5
70	3.7	10.5

[#] R_s is calculated for time = 0 h, but fixed for all other EIS analyses.

8.3.2 Attempts at In Operando Recovery of S-Poisoned Ni-YSZ Anode in H_2 at the OCP

The cell examined in Section 1.1 was then exposed to another 48 h of 1 ppm H_2S at 800˚C, for a total of 120 h of H_2S exposure. It can be seen in Figure 8.3 that R_p has increased only marginally from 10.5 (Figure 8.2 and Table 8.1) to 11.0 $\Omega \cdot cm^2$ (Rs is still assumed to be constant at 3.7 $\Omega \cdot cm^2$, since there is evidence that the cell is not at equilibrium), indicating that the cell was only slightly further S-poisoned by the additional 48 h of exposure to H_2S at the OCP. This good stability is consistent with the fact that the coverage of adsorbed S on Ni should reach a steady-state value that depends entirely on the operating temperature, and thus the degree of poisoning should not increase continuously (10).

This second period of H_2S exposure was then followed by 48 h of OCP H_2 exposure, for a total time of 168 h of H_2S exposure, with the final 96 h having been at the OCP. In the H_2 atmosphere, it is expected that the Ni-YSZ anode would slowly recover from the S-poisoning (40) and thus R_p should slowly decrease. However, this is not seen in Figure 8.3, where Rp is still 11.0 $\Omega \cdot cm^2$ after 48 h of H_2 exposure. This may indicate that H_2S is still adsorbed to the walls of the fuel supply lines, etc., and that it is only slowly desorbing and passing through the cell environment. This experiment was repeated 5 times, and it was found that recovery could not be achieved under these OCP conditions inside the TGA.

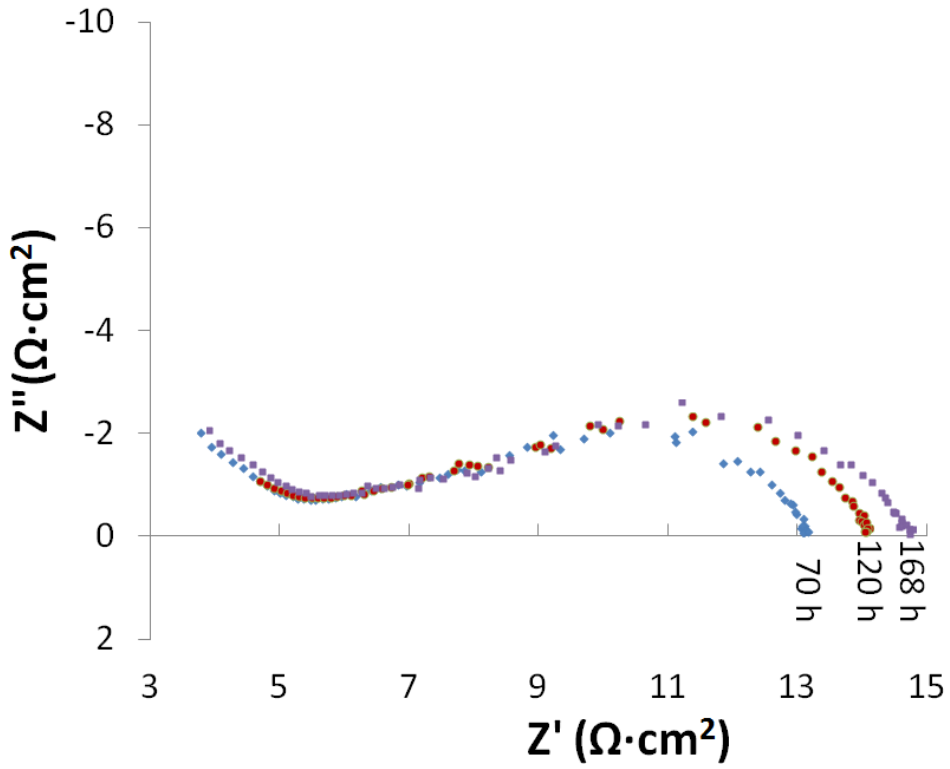

Figure 8.3. EIS response of a 2-electrode half-cell with a Ni-YSZ working electrode and Pt counter electrode after poisoning (70 h) in a 1 ppm H_2S-2.5% H_2O-2% H_2-He gas environment, after another 50 h at the OCP in a 1 ppm H_2S-2.5% H_2O-2% H_2-He, and after maintaining that same cell at the OCP for another 48 h in a 2.5% H_2O-2% H_2-He gas environment (total 168 h).

8.3.3 In Operando Recovery of S-Poisoned Ni-YSZ Anode by Air Exposure with Reverse Bias Applied

It is known that poisoning of Ni-YSZ anodes, resulting from fuel contamination by S-compounds (e.g., H_2S), can be reversed by air exposure at high temperatures (112). In addition, it is known from our previous study (Chapter 7) that a reverse bias applied to a Ni-YSZ anode during air exposure can partially prevent the Ni oxidation reaction. However, it is not clear if the

effectiveness of the air exposure cycle as a means of removing adsorbed S will be hampered by an applied reverse bias. On the plus side, the AFL, the region that is most prone to cause damage to the electrolyte when it oxidizes, is the region where the reverse bias will be most pronounced, as seen in Chapter 7. On the other hand, while it is known that some NiO will still form during the reverse bias in air (Chapter 7), it is not clear whether NiO formation is a necessary step for ensuring the removal of adsorbed S.

The goal of this work was thus to determine if S-poisoning of a Ni-YSZ anode can be reversed with air exposure under a negative bias, while also establishing how much air purging is required before the electrode recovers. Thus, following the Ni-YSZ anode S-poisoning in 1 ppm H_2S for 120 hours and a flow of 10% H_2-He for 48 h to clear the long supply lines of H_2S, as was described above, sequential air purges of 5, 15 and 30 min duration were carried out sequentially. A bias of -4 V potential was applied to the Ni-YSZ WE, since it was shown (Chapter 7) that this could maintain the anode at a maximum of 65% oxidized and yet was not too large for the electrolyte-supported cell to withstand.

In Figure 8.4A, it can be seen that, similar to the results in Chapter 7, when H_2 was switched off and N_2 switched on, there is an immediate mass loss (solid red line, left axis) and the current density (solid black line, right axis) decreases. When air is introduced, the mass begins to increase and the current density begins to decrease, which then reverse once the air purge is turned off after 5 min. Finally, when H_2 is returned to the anode chamber, the mass of the cell slowly returns to its initial condition. The mass gain that is observed is equivalent to only 37% of Ni oxidation when compared to the OCP mass gain (dashed red line, left axis).

The largest difference between this trial and the work in Chapter 7 is that, here, the current density of the cell in N_2 appears to be higher than in air. Some inconsistency was

observed from cell to cell, but in the three cells that were S-poisoned, all three exhibited a better performance in N_2. It is uncertain if the adsorbed S is playing a role here, since the current density had decreased to 0.3 $mA \cdot cm^{-2}$ in the N_2 purge that follows the air purge, although it is still increasing slowly. The first N_2 purge in a subsequent poisoning experiment using the same cell show that the current density returns to 0.4 $mA \cdot cm^{-2}$ on the re-poisoned cell, which suggests that S may indeed be playing a role.

In Figure 8.4B, the results for a 15 min air purge are seen to be almost identical to the results shown for a 5 min purge (Figure 8.4A). The difference is that more mass is gained, since the mass had not stabilized after only a 5 min purge, as was seen in Figure 8.4A. With a longer (15 min) air purge, the mass gain is equivalent to only 54% of the Ni in the anode being oxidized and, in this case, the current density decreases rapidly to 90 $mA \cdot cm^{-2}$ and then decreases to 87 $mA \cdot cm^{-2}$ at the end of the air purge.

Similar results are obtained for a 30 min air purge, as can be seen in Figure 8.4C, where the total mass gain is 71% and the rate of mass gain appeared to be slowing. The protection offered by the reverse bias does not match the level of protection that was obtained in Chapter 7. Thus, although the cell is better performing with respect to the current density output, it is likely that this cell is less efficient than others (Chapter 7) that have been examined with this technique. Regardless, when the air purge begins, the current density quickly decreases to 90 $mA \cdot cm^{-2}$ and then steadily decreases to 83 $mA \cdot cm^{-2}$ by the end of the 30 min air purge, which suggests that the resistance of the cell has steadily increased (due to Ni oxidation).

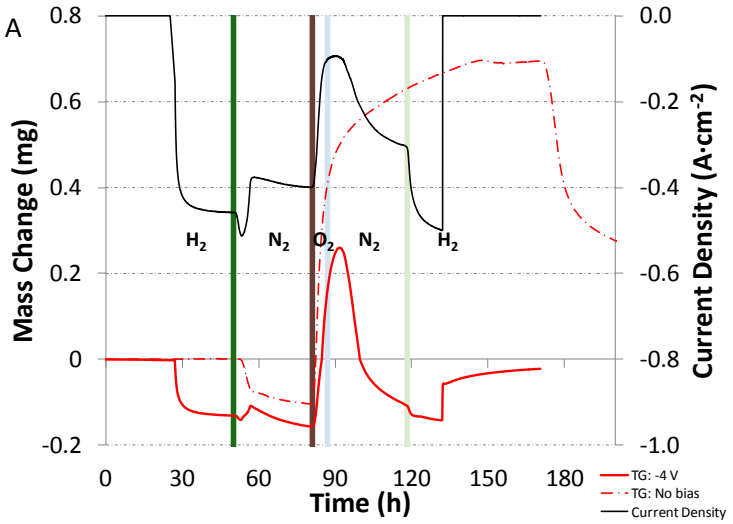
A
Mass Change (mg)
Current Density (A·cm-2)
Time (h)
H2
N2
O2
N2
H2
TG: -4 V
TG: No bias
Current Density

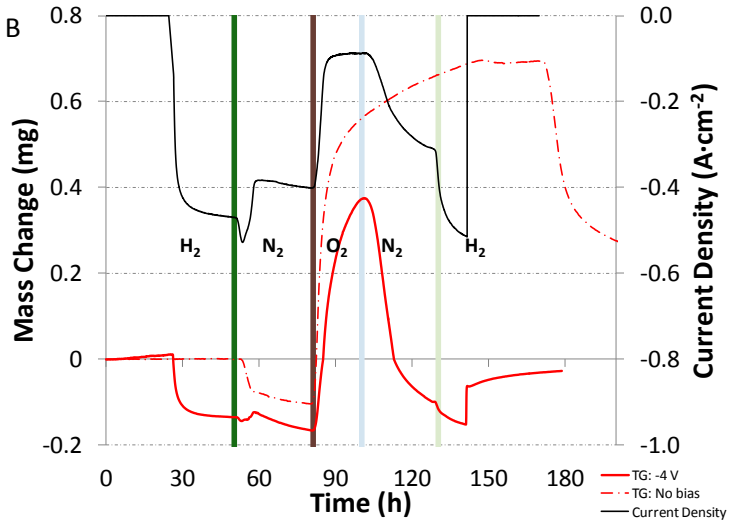
B
Mass Change (mg)
Current Density (A·cm-2)
Time (h)
H2
N2
O2
N2
H2
TG: -4 V
TG: No bias
Current Density

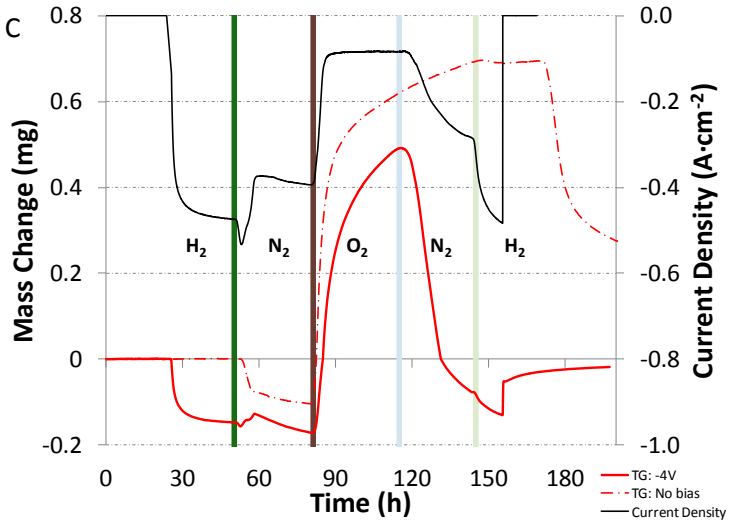
C
Mass Change (mg)
Current Density (A·cm-2)
Time (h)
H2
N2
O2
N2
H2
TG: -4V
TG: No bias
Current Density

Figure 8.4. Mass change (solid red line, left axis) and output current density (black line, right axis) during an oxidation/reduction cycle with a cathodic bias of -4 V applied to the Ni-YSZ electrode (that had previously been exposed to H_2S for 120 h) vs. the Pt CE (A) 5 min, (B) 15 min, and (C) 30 min. The mass change during an oxidation cycle/reduction cycle at the open circuit potential is also shown (red dashed line) and the changes in gas atmosphere are depicted by vertical lines (green for H_2/N_2 transitions and grey lines for N_2/O_2 changes).

When H_2 flow resumes after the air purge, in each case, it is noted that the final cell mass in each case (Figure 8.4) is lower than the initial cell mass in H_2, but this is not indicative of S removal. As discussed in Section 1, the *in operando* TGA technique, while very sensitive, cannot detect the small mass associated with adsorbed H_2S or its removal. Therefore, this difference in the final mass is merely an artifact of the TGA slowly returning to its original mass following the application of a high voltage bias to the cell, as was also seen in Chapter 7.

Since the mass change due to the loss of adsorbed S is too small to be detected at these thin (30 μm) Ni-YSZ electrodes (Figure 8.1), the performance of the cell must be used to determine if the air purge with a reverse bias had successfully removed the S-species. Figure 8.5 and Table 8.2 show the EIS data, comparing the cell performance after 5 and 15 min air purges (30 min data are not shown, but a similar R_p is seen as for the 15 min sample, as shown in Table 2) to the performance prior to H_2S exposure (0 h, Figure 8.2) and after the anode was fully S-poisoned (168 h, Figure 8.3).

It can be seen in Figure 8.5 (and Table 8.2) that the cell does not recover from S-poisoning after a 5 min air purge, which has resulted in the oxidation of ~37% of the Ni in the

electrode. However, after a 15 min air purge with a -4 V reverse bias applied, ~54% of the Ni has been oxidized and the cell has now recovered fully to its original S-free performance. These results are very significant. While an *ex situ* microscopic study in Section 7.3.1 had shown evidence that there was preferential protection in the more electrochemically active regions of the electrode, i.e., closest to the electrolyte, this result provides further evidence that this is the case. While it was suggested in previous studies (99) that the outer region will oxidize rapidly in Ni-YSZ anode-supported cells, in thin (30 μm) anodes, the oxidation is homogeneous throughout the electrode. This was also shown during the OCP *ex situ* cell oxidation test (99).

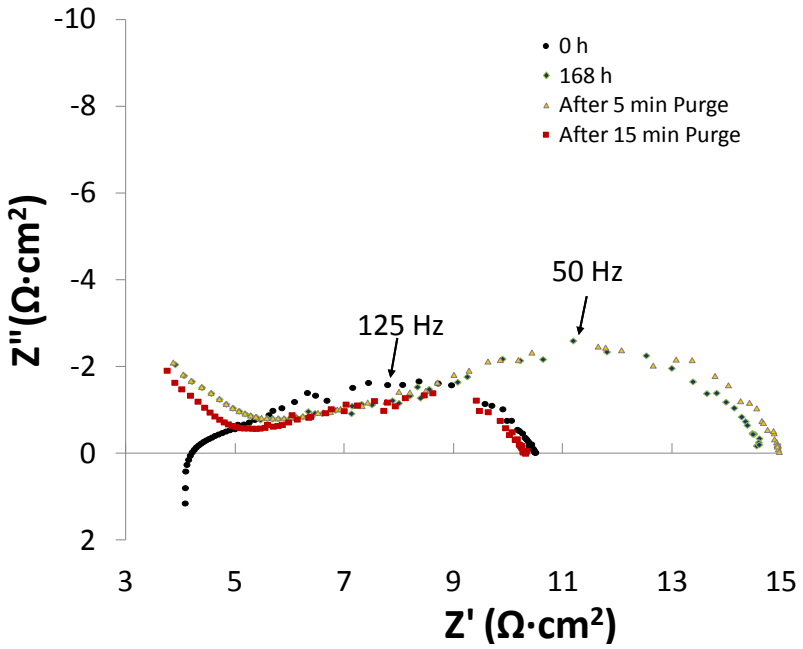

Figure 8.5. EIS spectra of 2-electrode half-cell with a Ni-YSZ working electrode and Pt counter electrode of a fresh cell (at 0 h) and that same cell after full S-poisoning in 1 ppm H_2S (at 168 h) and air purged with a -4 V bias applied to the Ni-YSZ working electrode for 5 and 15 min.

Since there was no recovery from S-poisoning after a 5 min air purge, there is evidence that some surface Ni oxidation in the active area of the cell may be necessary in order to oxidize the S and remove it from the Ni surface. The electrode is only 15 μm thick and the porosity is estimated to be > 35%, so air should penetrate though the full thickness of the anode if 37% of the Ni in the anode can oxidize in such a short time. Thus, further work is not only necessary to determine if O_2 can penetrate the active region of a thick (~1 mm) anode support layer to reverse S-poisoning before a critical amount of Ni has oxidized, but also to determine if this observation is real.

Table 8.2. Polarization resistance after S-poisoning and recovery using an air purge with a -4 V bias applied to the Ni-YSZ WE.

Time (h)	R_s[#] ($\Omega \cdot cm^2$)	R_p (Total) ($\Omega \cdot cm^2$)
0	3.7	6.8
168 h	3.7	11.0
5 min Purge	3.7	11.3
15 min Purge	3.7	6.6
30 min Purge	3.7	6.7

[#] R_s was determined by best-fit to the circuit at time = 0 and was then fixed at this value for all other times.

8.4 Summary

The primary aim of this work was to determine if a Ni-YSZ anode protected from oxidation by the application of a negative bias would also reverse the S-poisoning that results from H_2S exposure. It was determined that the exposure of a Ni-YSZ anode to 1 ppm H_2S *in operando* in a TGA would not show a mass change due to S adsorption, consistent with the low surface area of the Ni and the small thickness of the anode layer (30 μm). Electrochemical impedance spectroscopy, however, showed a 30% loss in performance, confirming that the cell was poisoned after 65 h with a 1 V applied potential.

Air exposure with a simultaneous reverse bias of -4 V was then used to both protect the Ni phase from oxidation and to oxidize the adsorbed S on the Ni surface. It was shown that a short 5 min air purge (with a bias), which oxidized only 37% of the Ni, did not reverse S-poisoning, while a 15 min air purge (with a bias) that oxidized 54% of the Ni fully reversed S-poisoning. This indicates that the reverse bias is protecting predominantly the Ni that is located in the region adjacent to the electrolyte, as would be expected, and that surface Ni oxidation in the active region of the cell is necessary to recover a cell from catalyst deactivation due to S-poisoning.

Chapter Nine: **Conclusions and Future Work**

9.1 Conclusions

It has been demonstrated by current solid oxide fuel cell (SOFC) development trends that anode-supported Ni-yttria stabilized zirconia (YSZ) cell architectures are the current state-of-the-art when it comes to cost and performance. However, the lifetime of anode-supported SOFCs is presently too short and in order to extend the lifetime, the anode resistance to sulphur (S) poisoning, coking, and oxidation of the Ni phase must be improved. Also, since it is known that S-poisoning and coking can be reversed with an oxidation cycle, if damage due to Ni oxidation with air exposure can be minimized, then this approach can be used to remove impurities and deposits.

At the onset of the work carried out in Chapter 4, it was known that the primary and most critical degradation mechanism of high porosity Ni-YSZ anodes is cracking of the thin YSZ electrolyte layer. This arises because, when a Ni-YSZ (yttria-stabilized zirconia) anode-supported SOFC is inadvertently exposed to air, a 70% volume expansion occurs because NiO is much less dense than Ni. The aim of the research in Chapter 4 was therefore to gain a better understanding of the mechanisms of cell degradation due to air exposure and to determine the conditions under which an anode-supported cell could safely be exposed to air.

In this work, it was demonstrated that, as the temperature is increased and pO_2 is lowered, the Ni oxidation kinetics diverge from parabolic, first to mixed parabolic and then to rectilinear as the oxidation conditions become more extreme. The first electrolyte cracks to form are near, and parallel to, the cell edges for anodes that were partially oxidized to $\geq 50\%$ at 800°C. These

types of cracks do not form at lower temperatures (≤ 700°C). It was also shown that degradation to the electrolyte is more severe as the temperature is increased from 600 to 900˚C. The most severe cracks seen in this study resulted when the pO_2 was decreased to ~0.1%.

A careful analysis of the NiO distribution as a function of depth into Ni-YSZ anode support layer that were partially oxidized by air exposure at various temperatures, was carried out. The distribution is homogeneous when the anode layer was partially oxidized at relatively low temperatures (600˚C). However, it was shown for the first time in this work that a gradient in the NiO content develops into the anode support layer, with more NiO seen in the outer regions of the anode and less deep inside the layer, for anodes that had been partially oxidized at higher temperatures (700 to 900˚C). Further, when air exposure was done at 800˚C in low pO_2 conditions (~0.1% O_2), the largest gradient in the NiO content of the anode support layer was seen. Thus, the severity of electrolyte degradation observed in Chapter 4 was shown to correlate with the steepness of the NiO gradient seen in the anode layer, which is a very important diagnostic. Further, it was shown that, in a high pO_2 oxidation environment, cell cracking is less severe than at normal pO_2. As there should be higher local temperatures generated in the oxidizing regions of the anode with higher O_2 availability, this showed conclusively and uniquely that thermal shock and creep can be ruled out as mechanisms of cell cracking after Ni oxidation.

It was also qualitatively shown in Chapter 4 that, the more homogeneous the distribution of NiO into the anode layer, i.e., the least damaging the oxidation conditions were, the more evidence was seen for the enrichment of NiO at the Ni-YSZ anode/air interface. This suggested that the expulsion of some of the NiO particles from the bulk of the anode out onto the outer anode/air surface may relieve the internal stresses in the anode and minimize YSZ electrolyte

cracking. The aim of the study presented in Chapter 5, therefore, was to confirm the enrichment in the NiO at the ASL/air interface under these safer air exposure conditions, and then to take advantage of this knowledge by applying a novel "pre-oxidation" step to the cell in order to make it more oxidation tolerant.

It was confirmed by x-ray photoelectron spectroscopy (XPS) analysis that the Ni:(Y+Zr) ratio at the anode-air interface is indeed higher when the Ni-YSZ anode is exposed to the least damaging oxidizing conditions. The oxidation tolerance, i.e., the maximum amount of the Ni phase that can be oxidized without inducing any electrolyte cracking, of a fresh sample is 74% at 600˚C, as confirmed by careful TGA investigation. The oxidation tolerance increases to 80% after the second oxidation of the sample at 600˚C after it has been subjected to a "pre-oxidization cycle", in which a sample was oxidized to a ~74% oxidation depth at 600°C. Multiple pre-oxidation cycles, however, had no further beneficial effect on the oxidation tolerance of the sample. Even so, this work showed that the oxidation tolerance of a Ni-YSZ based cell, operated at 600˚C, could be increased with the use of a pre-oxidation step, without modifying the manufacturing procedure of the cells.

The oxidation tolerance of a fresh sample oxidized at 800˚C is < 50%. The oxidation tolerance does not increase after a second oxidation step at 800˚C (i.e., after it has been subjected to a pre-oxidation cycle to 74% at 600˚C). However, the cracks that were produced in the electrolyte were less severe (narrower and fewer in number) than when no pre-oxidation treatment was used. While the use of a pre-oxidation procedure does not result in an improvement of the oxidation tolerance of the sample in subsequent oxidation cycles at 800°C, the severity of the degradation of the electrolyte (crack quantity and width) is definitely lowered (by 50%). This decrease in the crack severity as a result of the application of pre-oxidation

cycles is an important new development, which could be significant if the lifespan of the cell is extended for any duration.

In Chapter 6, the aim of the study was to map the gradient in NiO content into the depth of a partially oxidized Ni-YSZ anode layer more quantitatively. Since the severity of cracking of the thin YSZ electrolyte in Ni-YSZ anode-supported SOFC specimens during oxidation was correlated in Chapter 4 with the steepness of the NiO gradient that develops, modelling the oxidation process could provide further insight into this phenomenon. Microscopic methods for mapping the NiO distribution into the depth of the anode layer is time consuming and subject to high errors. In Chapter 6, Raman spectroscopy was used for the first time to map the NiO gradient quickly and quantitatively.

Over the course of the study presented in Chapter 6, it was found that a 20X objective lens was superior (to the 50X) for the Raman analysis of the NiO distribution due to the larger area of the sample from which Raman shifted photons could then be collected (2.5 μm vs. 1 μm), giving a higher signal to noise ratio, although this came at the cost of a smaller NiO Raman peak area (at 1100 cm^{-1}). Even so, the Raman data required careful processing to remove spurious Raman signals and to deal with various background issues. Once these were dealt with, it was confirmed that a gradient in the NiO distribution into the anode layer is present when air exposure of Ni-YSZ anodes is carried out under conditions that lead to significant YSZ cracking. The gradient in the NiO distribution was confirmed to increase proportionally with the air exposure temperature, which is a very important outcome of this thesis work. Furthermore, the Raman spectroscopic data revealed that the inner regions of oxidized anodes (near the YSZ electrolyte) that were 50% oxidized overall, at 800 and 900°C, were ~20% NiO. This was not expected, based on SEM analysis in Chapter 4, which suggested that only Ni metal was present

in this region. XPS analysis confirmed that the amount of NiO present near the electrolyte for these two samples is 22 and 18% (at 700 and 800˚C, respectively). These results thus demonstrate that Raman spectroscopy, while requiring careful data processing in order to remove extraneous and incorrect spectral features, is a very good technique for quickly and accurately mapping the extent of Ni oxidation through the thickness of a Ni-YSZ anode layer.

Another key goal of this work was to develop an easily implemented approach for stopping (or at least significantly slowing down) the formation of NiO during air exposure of Ni-YSZ anode layers at high temperatures. It was shown in our previous work that the application of a reverse bias (a negative bias applied to the Ni-YSZ anode) during air exposure could potentially protect Ni from Ni oxidation. However, these earlier results were inconclusive as it was not possible to "see" what was happening in the cell during an oxidation cycle with a reverse bias applied. The primary aim of the work presented in Chapter 7 was therefore to determine quantitatively and conclusively whether the Ni component of a Ni-YSZ cermet anode could be protected from oxidation by reverse biasing the cell during air exposure at SOFC operating temperatures.

An *ex situ* microscopy study was first carried out to determine if and where Ni was protected. Qualitatively, it appeared that some protection was conferred to the Ni phase in the anode using a negative current or voltage bias. Further, the results suggested that Ni that is located near to the electrolyte is protected preferentially as compared with the rest of the electrode. However, the poor depth of field and contrast differences between the microscopic images did not allow quantification of the level of protection offered to the Ni in the electrode. Thus, an entirely new technique was developed, allowing the mass of the Ni-YSZ anode layer to be tracked while under electrochemical control in Chapter 7. A unique cell test apparatus was

thus developed that allowed electrochemical half-cell experiments to be performed *in operando* inside a TGA instrument.

Preliminary electrochemical results *in operando* inside the TGA indicated that good electrochemical results could be achieved. The application of either a negative current or potential to a Ni-YSZ electrode during air exposure at 800˚C was shown conclusively to prevent the oxidation of a significant fraction of the Ni phase, as long as the cell voltage is greater than -1.5 V or the current is greater than -13 $mA \cdot cm^{-2}$. It was also shown that both a reverse current density or reverse bias potential are linearly related to the percent of Ni protected from oxidation, up to a maximum current density of -131 $mA \cdot cm^{-2}$. A maximum of just over 60% protection of the Ni phase from oxidation was achieved when a reverse current density of -131 $mA \cdot cm^{-2}$ was used in an air environment at 800˚C, which was a very positive outcome. Importantly, increasing the current any further was shown to damage an electrolyte-supported cell.

In the N_2 environment in the *in operando* TGA experiments, it was also shown that a negative bias of $\geq$ -1.5 V or -13 $mA \cdot cm^{-2}$, applied to a fully oxidized Ni-YSZ anode, could serve to quickly and completely reduce the NiO to Ni. The occurs either through the direct reduction of NiO by electrons or by reduction via the H_2 that is formed during the reduction of steam that is present in the humidified N_2 flow. The efficiency of NiO reduction during reverse biasing of the Ni-YSZ anode in the low pO_2 humidified N_2 environment is quite high (12%, based on the raw currents passed, or 60%, when the H_2O reduction and leakage currents are subtracted). These results in the N_2 environment are very important, indicating that the reverse bias technique may be effective in preventing degradation caused by slow air leaks or low pO_2 sources, although more work is needed to confirm this.

Overall, the *in operando* TGA technique, developed for the first time in this thesis work, has allowed the quantitative determination of the extent of oxidation of a Ni-YSZ electrode exposed to air at high temperatures with a reverse bias also applied. This method shows great promise of being an excellent tool for many other applications.

It was demonstrated in Chapter 7 that a Ni-YSZ electrode, exposed to air at high temperatures with a reverse bias applied, will not oxidize to the same extent as when the electrode is exposed to air at the OCP (open circuit potential). It is also known that an air purge can remove S and C species from the Ni surface. Another objective of the thesis work was therefore to determine if the applied negative bias could be used to protect a Ni-YSZ anode from oxidation at the same time as air is introduced in order to reverse S-poisoning that results from H_2S exposure.

Although adsorbed S-species on a thin, small anode layer were shown here to be undetectable by TGA, impedance spectroscopy showed conclusively that the onset of poisoning was rapid but that full saturation coverage of the Ni surface by S-species takes several days. A short 5 min air purge (with a -4 V bias applied vs. CE), which resulted in only 37% of the Ni in a Ni-YSZ anode layer being oxidized at 800˚C, did not serve to reverse S-poisoning. However, a 15 min air purge (with a -4 V bias applied vs. CE), still allowing only 54% of the Ni to be oxidized, did successfully reverse S-poisoning. This indicates that the reverse bias is predominantly protecting the Ni located in the region adjacent to the electrolyte, as was also indicated in Chapter 7. These results also suggest that it may be necessary to oxidize the Ni surface in the active region of the cell in order to recover the cell from catalyst deactivation due to S-poisoning. Overall, the application of a negative bias during air exposure was shown here, for the first time, to prevent a damaging extent of Ni oxidation from occurring while also

removing S-species. It is possible that this may also serve to prevent coking, or to remove coke, from Ni-based anodes when operated at high temperatures in hydrocarbon-rich fuels.

9.2 Future Work

There are many key areas of this thesis work that should be studied further, both to further improve the understanding of the Ni oxidation degradation mechanisms and also to improve the understanding and implementation of the reverse bias technique, as follows:

1. The use of a pre-oxidation cycle has been shown to improve the oxidation tolerance of the cell and it is known that increasing the temperature of oxidation to > 700˚C will decrease the extent of cell cracking. The following study could be carried out:
    a. By partially reducing the newly manufactured cells and then etching a small portion of the Ni from the cell edge region, it may be possible to increase the oxidation tolerance of the cell dramatically without altering the performance of the anode in most of the active region of the cell.
2. The use of Raman spectroscopy has been demonstrated to allow mapping of the NiO gradients in cell cross-sections. The following studies can now be carried out.
    a. Samples with varying oxidation depth should be analyzed in order to fully validate the Raman mapping technique, especially to determine NiO gradients.
    b. Raman spectroscopy could also now be used to analyze samples that have been oxidized at different pO_2 and temperatures.
3. *In operando* TGA has been demonstrated as a viable technique for determining the oxidation depth of the anode during air exposure with a reverse bias applied.

a. Other variables, such as pO_2, temperature and length of air exposure can now be studied.
b. Anode-supported cells, which are difficult to work with due to the difficulty of applying a counter electrode, etc., could now be studied with this technique to determine if reverse bias will protect these cells from degradation.
c. A preliminary *in situ* Raman spectroscopy study was carried out at Imperial College London with Drs. Mahar and Offer. However, while the initial results were promising, more work is necessary to determine if the Ni in the anode is preferentially protected, particularly in the region adjacent to the electrolyte.
d. A coke-tolerant cell test apparatus could now be developed that can determine coking rates and coke removal using this *in operando* technique.
e. This technique can also be used to study the oxidation tolerance and degradation mechanisms of anode-supported cells, caused by the electrochemical oxidation of the anode (i.e., due to anodic potentials that are too high and begin to oxidize Ni in the active region of the cell).

References

1. Kruszelnicki, Karl S. Fuel Cells 1. *ABC Science.* [Online] December 7, 2006. http://www.abc.net.au/science/articles/2006/12/07/741247.htm.
2. Grove, W. R. 1839, The London and Edinburgh Philosophical Magazine and Journal of Science, Vol. 14, pp. 127-130.
3. Grove, W. R. 1842, The London and Edinburgh Philosophical Magazine and Journal of Science, Vol. 21, pp. 417-420.
4. Ostwald, W. 1894, Zeitschrift für Physikalische Chemie, Vol. 15, pp. 4009-4021.
5. Mobius, Hans-Heinrich. 1997, Journal of Solid State Electrochemistry, Vol. 1, pp. 2-16.
6. Oniciu, L. *Fuel Cells.* Kent : Abacus Press, 1976.
7. Marbán, Gregorio and Teresa Valdés-Solís. 2007, International Journal of Hydrogen Energy, Vol. 32, pp. 1625-1637.
8. Neef, H.-J. 2009, Energy, Vol. 34, pp. 327-333.
9. Beychok, Milton R. 1973, The Oil and Gas Journal, Vol. 71, pp. 53–56.
10. Galea, N. M., E. S. Kadantsev and T. Ziegler. 2007, Journal of Physical Chemistry, Vol. 111, pp. 14457-14468.
11. Morris, A. E. *Freed.* San Diego, CA : Thermart Software, 2007.
12. Schroeder, Daniel V. *An Introduction to Thermal Physics.* s.l. : Addison Wesley, 2000.
13. Beér, János M. 2007, Progress in Energy and Combustion Science, Vol. 33, pp. 107-134.
14. Amrollahi, Zeinab, Paul Andreas, Marchioro Ystad, Ivar S. Ertesvåg and Olav Bolland. 2012, International Journal of Greenhouse Gas Control, Vol. 8, pp. 1–11.
15. Giuffrida, Antonio, Matteo C. Romano and Giovanni Lozza. 2013, Energy, Vol. 53, pp. 221–229.
16. Choudhury, Arnab, H. Chandra and A. Arora. 2013, Renewable and Sustainable Energy Reviews, Vol. 20, pp. 430-442.
17. James, Brian D., Kevin N. Baum and Andrew. Arlington : Strategic Analysis Inc., 2012.
18. Mani, A. and V. Birss. 2012, Journal of Electroanalytical Chemistry, Vol. 687, pp. 102-110.
19. Fray, Derek. http://www.doitpoms.ac.uk/tlplib/fuel-cells/types.php. [Online] University of Cambridge, April 2006. [Cited: August 25, 2013.]
20. Brandon, N.P. S., Skinner and B.C.H. Steele. 2003, Annual Review of Materials Research, Vol. 33, pp. 183 -213.
21. Jiao, Kui, Yibo Zhou, Qing Du, Yan Yin, Shuhai Yu and Xianguo Li. 2013, Applied Energy, Vol. 104, pp. 21-41.
22. Raissi, A. T., A. Banerjee and K. G. Sheinkopf. 1997. IEEE Proceedings of the 1997 32nd Intersociety Energy Conversion Engineering Conference. Vol. 3/4, p. 1953.
23. Ho, Jonathan C., Ewe-Chai Saw, Louis Y.Y. Lu and John S. Liu. 2014, Technological Forecasting and Social Change, Vol. 82, pp. 66-79.

24. de Souza, S., S. J. Visco and L. C. de Jonghe. 1997, Journal of the Electrochemical Society, Vol. 144, pp. L35-L37.
25. Kawada, T. and H. Yokokawa. 1997, Key Engineering Materials - Electrical properties of oxide materials, Vol. 125/126, pp. 187-248.
26. Atkinson, A. , S. Barnett, R. J. Gorte, J. T. S. Irvine, A. J. McEvoy, M. Mogensen, S. C. Singhal and J. Vohs. 2004, Nature Materials, Vol. 3, pp. 17-27.
27. Baur, E. and H. Preis. 1937, Z. Electrochem., Vol. 43, pp. 727-732.
28. Khandkar, A. C. and A. V. Joshi. Interface. s.l. : The Electrochemical Society, 1993, pp. 26-35.
29. Etsell, T. H. and S. N. Flengas. 1970, Chemical Reviews, Vol. 70, pp. 339-376.
30. Volicer, B. and S. Tello. http://faculty.uml.edu/ndeluca/84.334/topics/topic2.htm. *Umass Lowell Class Connections.* [Online] University of Massachusetts Lowell, 1998. [Cited: August 30, 2013.]
31. Cai, Z., T. N. Lan, S. Wang and M. Dokiya. 2002, Solid State Ionics, Vols. 152-153, pp. 583-590.
32. Millikena, C., S. Guruswamy and A. Khandkar. 1999, Journal of the Electrochemical Society, Vol. 146, pp. 872-882 .
33. Badwal, S. P. S. D. Fini, F. T. Ciacchi, C. Munnings, J. A. Kimptonb and J. Drennan. 2013, Journal of Materials Chemistry A: Materials for energy and sustainability .
34. Richter, Jörg, Peter Holtappels, Thomas Graule, Tetsuro Nakamura and Ludwig J. Gauckler. 2009, Monatsh Chem, Vol. 140, pp. 985–999.
35. Shi-Zhen, Zhu, W. Q. Ming, X. D. Guo. 1994, Journal of Rare Earths, Vol. 12, p. 28.
36. Cava, R. J. http://www.princeton.edu/~cavalab/tutorials/public/structures/perovskites.html. *Cava Lab: Solid State Chemistry Research Group.* [Online] [Cited: August 29, 2013.]
37. Spacil, H. S. Electrical device including nickel-containing stabilized zirconia electrolye. *Electrical device including nickel-containing stabilized zirconia electrolye. 3,503,809* US, 1970.
38. Zhu, W.Z. and S.C. Deevi. 2003, Materials Science and Engineering A, Vol. 362, pp. 228–239.
39. Zha, S., Z. Cheng and M. Liu. 2007, Journal of the Electrochemical Society, Vol. 154, pp. B201-B206.
40. Birss, V., L. Deleebeeck, S. Paulson and T. Smith. Montreal, Canada : ECS Transactions, 2011. SOFC XII. Vol. 35, pp. 1445-1454.
41. Matsuzaki, Y. and I. Yasuda. 2000, Solid State Ionics, Vol. 132, pp. 261-269.
42. Kishimoto, H., Y. Xiong, K. Yamaji, T. Horita, N. Sakai, M. E. Brito and H. Yokokawa. 2007, Journal of Chemical Engineering of Japan, Vol. 40, pp. 1178-1182.
43. Lussier, A., S. Sofie, J. Dvorak and Y. U. Idzerd. 2008, International Journal of Hydrogen Energy, Vol. 33, pp. 3945-3951.
44. Cowin, Peter I., Christophe T. G. Petit, Rong Lan, John T. S. Irvine, and Shanwen Tao. 2011, Advanced Energy Materials, Vol. 1, pp. 314-332.
45. Kurokawa, H., T. Z. Sholklapper, C. P. Jacobson, L. D. De Longhe and S. J. Visco. 2007, Electrochemical and Solid State Letters, Vol. 10, pp. B135-B138.

46. Yang, Lei, YongMan Choi, Wentao Qin, Haiyan Chen, Kevin Blinn, Mingfei Liu, Ping Liu, Jianming Bai, Trevor A. Tyson, and Meilin Liu. 2011, Nature Communications, Vol. 2, pp. 357-366.
47. Jiang, San Ping. 2006, Materials Science and Engineering: A, Vol. 418, pp. 199-210.
48. Rahaman, Mohamed N. *Sintering of Ceramics.* New York : CRC Press, 2007.
49. Stochiniol, G., E. Syskakis and A. Naoumidis. 1995, Journal of the American Ceramic Society, Vol. 78, pp. 929-932.
50. Eguchi, K., T. Setoguchi and H. Arai. 1991, Vacuum, Vol. 42, pp. 1061-1065.
51. Hui, Rob, Zhenwei Wang, Olivera Kesler, Lars Rose, Jasna Jankovic, Sing Yick, Radenka Maric and Dave Ghosh. 2007, Journal of Power Sources, Vol. 170, pp. 308-323.
52. Kendall, K., N. McNalfor, W. J. Clegg and J. D. Birchall. 1990, British Ceramic Proceedings, Vol. 45, p. 79.
53. Kellet, B. J. and F. F. Lange. 1990, Advanced Ceramic Processing and Technology, Vol. 1, p. 1.
54. Julbe, A., C. Guizard, A. Larbot, L. Cot and A. Giroir-Fendler. 1993, Journal of Membrane Science, Vol. 77, p. 137.
55. Minh, N. Q. 1993, Journal of the American Ceramic Society, Vol. 76, pp. 563-588.
56. Shaigan, Nima, Wei Qu, Douglas G. Ivey, Weixing Chen. 2010, Journal of Power Sources, Vol. 195, pp. 1529-1542.
57. Singh, Raj N. 2006, Journal of Materials Engineering and Performance, Vol. 15, pp. 422-426.
58. Balachandran, U., Dorris, S.E., Picciolo, J. J., Poeppel, R.B., McPheeters, C.C., Minh, N.Q. 1989. Proceedings of the 24th Intersociety Energy Conversion Engineering Conference. Vol. 3, pp. 1541-1545.
59. Yokokawa, Harumi. Overview of Intermediate-Temperature Solid. [book auth.] T. Ishihara. *Perovskite Oxide for Solid Oxide Fuel Cells.* s.l. : Springer Science-Business Media, LLC, 2009, 2, pp. 17-43.
60. Huang, Kevin and Subhash C. Singhal. 2013, Journal of Power Sources, Vol. 237, pp. 84-97.
61. Minh, Nguyen Q. 2004, Solid State Ionics, Vol. 174, pp. 271-277.
62. Cassidy, M., K. Kendall and G. Lindsay. Oberrohrdorf, Switzerland : s.n., 1993. Proceedings fo the 1st European Solid Oxide Fuel Cell Forum. pp. 577-586.
63. Minh, N. Q. and R. A. Gibson. Lucerne, Switzerland : s.n., 1993. Proceedings of the 1st European Solid Oxide Fuel Cell Forum. pp. 587-596.
64. Kim, Haekyoung, Young Min Park, Ju Hee Kim and HyunWoo Jin. 2011, ECS Transactions, Vol. 35, pp. 2147-2150 .
65. Virkar, Anil V., Jong Chen, Cameron W. Tanner and Jai-Woh Kim. 2000, Solid State Ionics, Vol. 131, pp. 198-198.
66. Couse, Stephen. *US 8,067,129 B2* United States, 2011.
67. Simwonis, S., F. Tietz and D. Stöver. 2000, Solid State Ionics, Vol. 132, pp. 241-251.
68. Cassidy, M., G. Lindsay and K. Kendall. 1996, Journal of Power Sources, Vol. 61, pp. 189-192.
69. Fouquet, D., A. C. Muller, A. Webber and E. Ivers-Tiffée. 2003, Ionics, Vol. 8, pp. 103-108.

70. Stathis, G., D. Simwonis, F. Tietz, A. Moropoulou and A. Naoumides. 2002, Journal of Materials Research, Vol. 17, p. 951.
71. Waldbillig, D., A. Wood and D. G. Ivey. 2005, Solid State Ionics, Vol. 176, p. 847.
72. Tikekar, N., T. Armstrong and A. Virkar. 2006, Journal of the Electrochemical Society, Vol. 153, p. A654.
73. Laurencin, J., G. Delette, O. Sicardy, S. Rosini and F. Lefebvre-Joud. 2010, Journal of Power Sources, Vol. 195, pp. 2747-2753.
74. Young, J. L., V. Vedaharathinam, S. Kung, S. Xia, V. I. Birss. Nara, Japan : The Electrochemical Society, 2007. ECS Transactions. Vol. 7, pp. 1511-1519.
75. Sarataradis, D. and A. Atkinson. 2007, Fuel Cells, Vol. 7, pp. 246-258.
76. Van Vlack, L. *Nickel Oxide.* New York : INCO, The International Nickel Company, Inc., 1980. pp. 18-20.
77. Popescu, Ionel, Eleni Heracleous, Zinovia Skoufa, Angeliki Lemonidou and Ioan-Cezar Marcu. 2014, Physical Chemistry, Chemical Physics, Vol. 16, pp. 4962-4970.
78. Atkinson, A., R. I. Taylor and P. D. Goode. 1979, Oxidation of Metals, Vol. 13, pp. 519-543.
79. Atkinson, A., A.E. Hugues and A. Hammou. 1981, Philosophical Magazine A, Vol. 43, pp. 1071–1091.
80. Evans, U. R. *Corrosion and Oxidation of Metals.* London : Arnold, 1960.
81. Peraldi, R., D. Monceau and B. Pieraggi. 2002, Oxidation of Metals, Vol. 58, pp. 249-273.
82. Zhang, Y., B. Liu, B. Tu, Y. Dong and M. Cheng. 2005, Solid State Ionics, Vol. 176, p. 2193.
83. Waldbillig, D., A. Wood and D. G. Ivey. 2005, Journal of Power Sources, Vol. 145, pp. 206-215.
84. Bradford, S. A. *Corrosion Control.* New York : Van Nostrand Reinhold, 1993.
85. Jeangros, Q., T. W. Hansen, J. B. Wagner, C. D. Damsgaard, R. E. Dunin-Borkowski, C. Hebert, J. Van herle and A. Hessler-Wyser. 2013, Journal of Materials Science, Vol. 48, pp. 2893–2907.
86. Richardson, J. T., R. Scates and M. V. Twigg. 2003, Applied Catalysis, A: General, Vol. 246, p. 137.
87. Rodriguez, J. A., J. C. Hanson, A. I. Frenkel, J. Y. Kim and M. Perez. 2002, Journal of the American Ceramic Society, Vol. 124, p. 346.
88. Szekely, J. and J. W. Evans. 1970, Chemical Engineering Science, Vol. 25, pp. 1091-1107.
89. Utigaard, T., M. Wu, G. Plascencia and T. Marin. 2005, Chemical Engineering Science, Vol. 60, pp. 2061-2068.
90. Malzbender, J., E. Wessel and R. W. Steinbrech. 2004, Ceramic Engineering and Science Proceedings, Vol. 25, pp. 387-392.
91. Kondoh, J., H. Shiota, K. Kawachi and T. Nakatani. 2004, Journal of Alloys and Compounds, Vol. 365, pp. 253-258.
92. Klemenso, T., C. C. Appel and M. Mogensen. 2005, Journal of the Electrochemical Society, Vol. 152, pp. A2182-A2192.
93. Grahl-Madsen, L., P. Larsen, N. Bonanos, J. Engell and S. Linderoth. 2006, Journal of Materials Science, Vol. 41, pp. 1097-1107.

94. Klemenso, K. and M. Mogensen. 2007, Journal of the American Ceramic Society, Vol. 90, pp. 3582–3588.
95. Kim, S., H. Moon, S. Hyum, J. Moon, J. Kim and H. Lee. 2006, Solid State Ionics, Vol. 177, pp. 931-938.
96. Kong, J., K. Sun, D. Zhou, N. Zhang, J. Qiao. 2006, Rare Metals, Vol. 25, pp. 300–304.
97. Klemenso, T., C. Chung, P.H. Larson, M. Mogensen ,. 2005, Journal of the Electrochemical Society, Vol. 152, pp. A2186–A2192.
98. Faes, A., A. Nakajo, A. Hessler-Wyser, D. Dubois, A. Brisse, S. Modena, J. Van Herle. 2009, Journal of Power Sources, Vol. 193, pp. 55–64.
99. Young, J. L. and V. I. Birss. 2011, Journal of Power Sources, Vol. 196, pp. 7126-7135.
100. Waldbillig, D., A. Wood and D. G. Ivey. 2007, Journal of the Electrochemical Society, Vol. 154, p. B133 .
101. Pihlatie, M., T. Ramos, A. Kaiser. 2009, Journal of Power Sources, Vol. 193, pp. 322–330.
102. Wood, A., M. Pastula, D. Waldbillig and D. G. Ivey. 2006, Journal of the Electrochemical Society, Vol. 153, pp. A1929-A1934.
103. Vedasri, V., J. L. Young and V. I. Birss. 2010, Journal of Power Sources, Vol. 195, pp. 5534-5542.
104. Mukerjee, Subhasish, Keegan Grieve, Kevin M. James. *US6,620,535* United States, 2003.
105. Yang, C. Y. and W. E. O'Grady. 1982, Journal of Vacuum Science and Technology, Vol. 20, p. 925.
106. Yang, C. Y. and H. S. Isaacs. 1981, Journal of Electroanalytical Chemistry, Vol. 123, p. 411.
107. Van Manen, P. A., R. Weewer adn J. H. W. de Wit. 1992, Journal of the Electrochemical Society, Vol. 139, pp. 1130-1134.
108. Young, Jason L., Vedasri Vedharathinam and Viola I. Birss. 2011, ECS Transactions, Vol. 35, pp. 1697-1706 .
109. Worrell, W. L. and J. L. Iskoe. Belgirate, Italy : s.n., 1972. Proceedings of the NATO sponsored Advanced Study Institute of Fast Ion Transport in Solids, Solid State Batteries and Devices. pp. 513-521.
110. Kim, T., G. Liu, M. Boaro, S.-I. Lee, J. M. Vohs, R. J. Gorte, O. H. Al-Madhi and B. O. Dabbousi. 2006, Journal of Power Sources, Vol. 155, pp. 231-238.
111. Pomfret, M. B., J. C. Owrutsky and R. A. Walker. 2006, Journal of Physical Chemistry, B, Vol. 110, pp. 17305-17308.
112. Wang, J. H. and M. Liu. 2008, Journal of Power Sources, Vol. 176, pp. 23-30.
113. Hepola, J. and P. Simell. 1997, Applied Catalysis, B:, Vol. 14, pp. 305-321.
114. Underwood, E. E. *Quantitative stereology.* New York : Addison-Wesley Pub. Co., 1970.
115. Jiang, S. P., Y. Y. Duan and J. G. Love. 2002, Journal of the Electrochemical Society, Vol. 149, p. A1175.
116. Chayes, Felix. 1989, Mathematical Geology, Vol. 21, pp. 319-329.
117. Lara-Curzio, E. an M. Radovic. Oak Ridge, Tennessee : Oak Ridge National Laboratory, 2003. Annual Report.

118. Williams, David B. and C. Barry Carter. *Transmission Electron Microscopy.* New York : Springer, 2009.
119. Hertz, H. 1887, Annalen der Physik , Vol. 267 , pp. 983–1000.
120. Siegbahn, K. and K. I. Edvarson. 1956, Nuclear Physics , Vol. 1, pp. 137–159.
121. Carlson, T. A. 1982, Interface Anal, Vol. 4, pp. 125–134.
122. Raman, C. V. and K. S. Krishnan. 1928, Nature, Vol. 121, pp. 501-502.
123. Kneipp, Katrin, Harald Kneipp, Irving Itzkan, Ramachandra R. Dasari and Michael S. Feld. 1999, Chemical Reviews, Vol. 99, pp. 2957–2976.
124. Roth, W. L. 1958, Physical Review B, Vol. 110, pp. 1333--1341.
125. Mironova-Ulmane, N., A. Kuzmin, I. Sildos and M. Pars. 2011, Central European Journal of Physics, Vol. 9, pp. 1096-1099.
126. Dietz, R. E., G. I. Parisot and A. E. Meixner. 1971, Physical Review, B, Vol. 4, pp. 2302-2310.
127. Broido, A. 1969, Journal of Polymer Science A-2: Polymer Physics, Vol. 7, pp. 1761–1773.
128. Angrist, S. W. *Direct Energy Conversion.* Boston : Allyn and Bacon, 1982.
129. Kettani, M. A. *Direct Energy Conversion.* London : Addison-Wesley Publishing Company, 1970.
130. MacDonald, J. Ross. *Impedance Spectroscopy: Emphasizing Solid Materials and Systems.* Toronto : John Wiley and Sons, 1987.
131. Bockris, John O'M. and Amulya K. N. Reddy. *Electrochemistry, 2B: Electrodics in Chemistry, Engineering, Biology, and Environmental Science.* New York : Kluwer Academic Publishers, 2000.
132. Primdahl, S. and M. Mogensen. 1999, Journal of the Electrochemical Society, Vol. 146, pp. 2827-2833 .
133. Ammosov, R. M., N. V. Marukov and A. V. Nikitin. 1988, Measurement Techniques, Vol. 31, pp. 560-561.
134. Hesse, R., T. Chasse, P. Streubel and R. Szargan. 2004, Surface and Interface Analysis, Vol. 36, pp. 1373-1383.
135. Mohai, Miklós. *Thesis: Development and Applications of Quantitative X-ray Photoelectron Spectroscopy.* Hungarian Academy of Sciences. Budapest : s.n., 2005.
136. ULVAC PHI PHI5000 VersaProbe: Part 1 Measurement Manual. [Online] 1.30E, 2013/08/30. http://park.itc.u-tokyo.ac.jp/hpx/VersaProbe/000_VersaProbeManual_Part01_2013_08_30_130E_optimized.pdf.
137. Lewis, Ian R. and Howell Edwards. *Handbook of Raman Spectoscopy.* Google eBook : CRC Press, 2001.
138. Wang, Q. I., D. D. Allred adn L. V. Knight. 1995, Journal of Raman Spectroscopy, Vol. 26, pp. 1039-1043.
139. Ettler, M., G. Blass, N.H. Menzler. 2007, Fuel Cells, Vol. 7, pp. 349–355.
140. Pihlatie, Mikko, Andreas Kaiser, and Mogens Mogensen. 2012, Solid State Ionics, Vols. 222-223, pp. 38-46.
141. Klein, Joseph C. and David M. Hercules. 1983, Journal of Catalysis, Vol. 82, pp. 424-441.
142. Lee, D. H., S. Y. Yoon, D. H. Yoon and S. J. Suh. 2004, Journal of the Korean Physical Society, Vol. 44, pp. 1079-1082.

143. Illis, A., G. C. Nowlan and H. J. Koehler. 1970, Canada Minerals and Metals Bulletin, Vol. 73, pp. 49-53.
144. Karmhag, R., G. A. Niklasson and M. Nygren. 1999, Journal of Applied Physics, Vol. 85, pp. 1186-1191.
145. Karmhag, R., G. A. Niklasson and M. Nygren. 1999, Journal of Materials Research, Vol. 14, pp. 3051-3058.
146. Fromhold, A. T. *Theory of Metal Oxidation: Volume 1 - Fundamentals.* New York : North-Holland PublishingCompany, 1976.
147. Chayes, Felix. 1989, Mathematical Geology, Vol. 20, pp. 319-329.
148. Campion, A. and P. Kambhampati. 1998, Chemical Society Reviews, Vol. 27, pp. 241-250.
149. Gao, Ling-Ling, Yan Liu, Xu-Yan Lv, Jian-Feng Liu, and Tuo-Ping Hu. 2012, International Journal of Inorganic Chemistry, Vol. 2012.
150. Shen, J. L., I. M. Chang, Y. M. Shu, Y. F. Chen, S. Z. Chang and S. C. Lee. 1994, Phys. Rev. B, Vol. 50, pp. 1678–1683.
151. Zhu, Huayang, Alexander Kromp, Andre Leonide, Ellen Ivers-Tiffée, Olaf Deutschmann and Robert J. Kee. 2012, Journal of the Electrochemical Society, Vol. 159, pp. F255-F266.
152. Hauch, A., S. D. Ebbesen, S. H. Jensen and M. Mogensen. 2008, Journal of The Electrochemical Society, Vol. 155, pp. B1184-B1193.
153. Minh, N. Q. and M. B. Mogensen. 2013, Interface, Vol. 22, pp. 55-62.
154. Brosha, E. L., T. Rockward, F. A. Iribe and F. H. Garzon. 2009, ECS Transactions, Vol. 17, pp. 369-381.

Appendix A: Copyright License

ELSEVIER LICENSE
TERMS AND CONDITIONS
Feb 24, 2014

This is a License Agreement between Jason Young ("You") and Elsevier ("Elsevier") provided by Copyright Clearance Center ("CCC"). The license consists of your order details, the terms and conditions provided by Elsevier, and the payment terms and conditions.

All payments must be made in full to CCC. For payment instructions, please see information listed at the bottom of this form.

Supplier	Elsevier Limited The Boulevard,Langford Lane Kidlington,Oxford,OX5 1GB,UK
Registered Company Number	1982084
Customer name	Jason Young
Customer address	2500 University Drive, NW Calgary, AB T2N 1N4
License number	3335540753201
License date	Feb 24, 2014
Licensed content publisher	Elsevier
Licensed content publication	Journal of Power Sources
Licensed content title	Crack severity in relation to non-homogeneous Ni oxidation in anode-supported solid oxide fuel cells
Licensed content author	J.L. Young,V.I. Birss
Licensed content date	1 September 2011
Licensed content volume number	196
Licensed content issue number	17
Number of pages	10
Start Page	7126
End Page	7135
Type of Use	reuse in a thesis/dissertation
Portion	full article
Format	both print and electronic

Are you the author of this Elsevier article?	Yes
Will you be translating?	No
Title of your thesis/dissertation	Understanding and Preventing Ni Oxidation in Ni-YSZ Anode-Supported SOFCs
Expected completion date	Mar 2014
Estimated size (number of pages)	250
Elsevier VAT number	GB 494 6272 12
Permissions price	0.00 USD
VAT/Local Sales Tax	0.00 USD / 0.00 GBP
Total	0.00 USD

Terms and Conditions

INTRODUCTION

1. The publisher for this copyrighted material is Elsevier. Byclicking "accept" in connection with completing this licensingtransaction, you agree that the following terms and conditions apply to thistransaction (along with the Billing and Payment terms and conditionsestablished by Copyright Clearance Center, Inc. ("CCC"), at the timethat you opened your Rightslink account and that are available at any time at http://myaccount.copyright.com).

Licensing material from an Elsevier book: A hyper-text link must be includedto the Elsevier homepage at http://www.elsevier.com . Allcontent posted to the web site must maintain the copyright information line onthe bottom of each image.

Posting licensed content on Electronic reserve: In addition to the above the following clausesare applicable: The web site must be password-protected and made available onlyto bona fide students registered on a relevant course. This permission isgranted for 1 year only. You may obtain a new license for future websiteposting.

For journal authors: the following clauses are applicable inaddition to the above: Permission granted is limited to the author acceptedmanuscript version* of your paper.

***Accepted Author Manuscript (AAM) Definition:** An accepted authormanuscript (AAM) is the author's version of the manuscript of an article thathas been accepted for publication and which may include any author-incorporatedchanges suggested through the processes of submission processing, peer review,and editor-author communications. AAMs do not include other publishervalue-added contributions such as copy-editing, formatting, technicalenhancements and (if relevant) pagination.

21. **Other Conditions**:

v1.7

If you would like to pay for this license now, please remit this license along with your payment made payable to "COPYRIGHT CLEARANCE CENTER" otherwise you will be invoiced within 48 hours of the license date. Payment should be in the form of a check or money order referencing your account number and this invoice number RLNK501234672.
Once you receive your invoice for this order, you may pay your invoice by credit card. Please follow instructions provided at that time.

Make Payment To:
Copyright Clearance Center
Dept 001
P.O. Box 843006
Boston, MA 02284-3006

For suggestions or comments regarding this order, contact RightsLink Customer Support: customercare@copyright.com or +1-877-622-5543 (toll free in the US) or +1-978-646-2777.

Gratis licenses (referencing $0 in the Total field) are free. Please retain this printable license for your reference. No payment is required.

SPRINGER LICENSE
TERMS AND CONDITIONS
Feb 24, 2014

This is a License Agreement between Jason Young ("You") and Springer ("Springer") provided by Copyright Clearance Center ("CCC"). The license consists of your order details, the terms and conditions provided by Springer, and the payment terms and conditions.

All payments must be made in full to CCC. For payment instructions, please see information listed at the bottom of this form.

License Number	3335541442369
License date	Feb 24, 2014
Licensed content publisher	Springer
Licensed content publication	Journal of Materials Science (full set)
Licensed content title	Reduction of nickel oxide particles by hydrogen studied in an environmental TEM
Licensed content author	Q. Jeangros
Licensed content date	Jan 1, 2012
Volume number	48
Issue number	7
Type of Use	Thesis/Dissertation
Portion	Figures
Author of this Springer article	No
Order reference number	F2.7
Title of your thesis / dissertation	Understanding and Preventing Ni Oxidation in Ni-YSZ Anode-Supported SOFCs
Expected completion date	Mar 2014
Estimated size(pages)	250
Total	0.00 USD
Terms and Conditions	

Introduction
The publisher for this copyrighted material is Springer Science + Business Media. By clicking "accept" in connection with completing this licensing transaction, you agree that

the following terms and conditions apply to this transaction (along with the Billing and Payment terms and conditions established by Copyright Clearance Center, Inc. ("CCC"), at the time that you opened your Rightslink account and that are available at any time at http://myaccount.copyright.com).

Limited License

With reference to your request to reprint in your thesis material on which Springer Science and Business Media control the copyright, permission is granted, free of charge, for the use indicated in your enquiry.

Licenses are for one-time use only with a maximum distribution equal to the number that you identified in the licensing process.

This License includes use in an electronic form, provided its password protected or on the university's intranet or repository, including UMI (according to the definition at the Sherpa website: http://www.sherpa.ac.uk/romeo/). For any other electronic use, please contact Springer at (permissions.dordrecht@springer.com or permissions.heidelberg@springer.com).

The material can only be used for the purpose of defending your thesis, and with a maximum of 100 extra copies in paper.

Although Springer holds copyright to the material and is entitled to negotiate on rights, this license is only valid, subject to a courtesy information to the author (address is given with the article/chapter) and provided it concerns original material which does not carry references to other sources (if material in question appears with credit to another source, authorization from that source is required as well).

Permission free of charge on this occasion does not prejudice any rights we might have to charge for reproduction of our copyrighted material in the future.

Altering/Modifying Material: Not Permitted
You may not alter or modify the material in any manner. Abbreviations, additions, deletions and/or any other alterations shall be made only with prior written authorization of the author(s) and/or Springer Science + Business Media. (Please contact Springer at (permissions.dordrecht@springer.com or permissions.heidelberg@springer.com)

Reservation of Rights
Springer Science + Business Media reserves all rights not specifically granted in the combination of (i) the license details provided by you and accepted in the course of this licensing transaction, (ii) these terms and conditions and (iii) CCC's Billing and Payment terms and conditions.

Copyright Notice:Disclaimer

You must include the following copyright and permission notice in connection with any reproduction of the licensed material: "Springer and the original publisher /journal title, volume, year of publication, page, chapter/article title, name(s) of author(s), figure number(s), original copyright notice) is given to the publication in which the material was originally published, by adding; with kind permission from Springer Science and Business Media"

Warranties: None

Example 1: Springer Science + Business Media makes no representations or warranties with respect to the licensed material.

Example 2: Springer Science + Business Media makes no representations or warranties with respect to the licensed material and adopts on its own behalf the limitations and disclaimers established by CCC on its behalf in its Billing and Payment terms and conditions for this licensing transaction.

Indemnity
You hereby indemnify and agree to hold harmless Springer Science + Business Media and CCC, and their respective officers, directors, employees and agents, from and against any and all claims arising out of your use of the licensed material other than as specifically authorized pursuant to this license.

No Transfer of License
This license is personal to you and may not be sublicensed, assigned, or transferred by you to any other person without Springer Science + Business Media's written permission.

No Amendment Except in Writing
This license may not be amended except in a writing signed by both parties (or, in the case of Springer Science + Business Media, by CCC on Springer Science + Business Media's behalf).

Objection to Contrary Terms
Springer Science + Business Media hereby objects to any terms contained in any purchase order, acknowledgment, check endorsement or other writing prepared by you, which terms are inconsistent with these terms and conditions or CCC's Billing and Payment terms and conditions. These terms and conditions, together with CCC's Billing and Payment terms and conditions (which are incorporated herein), comprise the entire agreement between you and Springer Science + Business Media (and CCC) concerning this licensing transaction. In the event of any conflict between your obligations established by these terms and conditions and those established by CCC's Billing and Payment terms and conditions, these terms and conditions shall control.

Jurisdiction
All disputes that may arise in connection with this present License, or the breach thereof,

shall be settled exclusively by arbitration, to be held in The Netherlands, in accordance with Dutch law, and to be conducted under the Rules of the 'Netherlands Arbitrage Instituut' (Netherlands Institute of Arbitration).***OR:***

All disputes that may arise in connection with this present License, or the breach thereof, shall be settled exclusively by arbitration, to be held in the Federal Republic of Germany, in accordance with German law.

Other terms and conditions:

v1.3

If you would like to pay for this license now, please remit this license along with your payment made payable to "COPYRIGHT CLEARANCE CENTER" otherwise you will be invoiced within 48 hours of the license date. Payment should be in the form of a check or money order referencing your account number and this invoice number RLNK501234676.
Once you receive your invoice for this order, you may pay your invoice by credit card. Please follow instructions provided at that time.

Make Payment To:
Copyright Clearance Center
Dept 001
P.O. Box 843006
Boston, MA 02284-3006

For suggestions or comments regarding this order, contact RightsLink Customer Support: customercare@copyright.com or +1-877-622-5543 (toll free in the US) or +1-978-646-2777.

Gratis licenses (referencing $0 in the Total field) are free. Please retain this printable license for your reference. No payment is required.
